technische universität
dortmund

Experiments and simulations on the structural and electrical properties of nano and micro structures on graphite surfaces produced by ion beam lithography

Dissertation for the doctoral degree of natural sciences at the faculty of physics at the Technische Universität Dortmund

Dipl.-Phys. Lukas Patryarcha
August 2011

Dissertation submitted – August 2011
PhD oral exam – September 2011

Examiners:

PD Dr. Hövel
Prof. Dr. Weis
Prof. Dr. Spaan
Dr. Siegmann

Contact:
Technische Universität Dortmund
Experimentelle Physik I
Otto-Hahn-Straße 4
44221 Dortmund, Germany
Gateway 29

Tel.: +49(0)231 / 755-3505
Fax: +49(0)231 / 755-3657
Homepage: http://e1.physik.tu-dortmund.de/e1anew/homepage_e1/

Index of contents

1. Introduction

This project was performed at the Technische Universität Dortmund at the institute of experimental physics EIa of the physics department. Under the supervision of Prof. Dr. M. Tolan and PD Dr. H. Hövel and in cooperation with the Raith GmbH and other partners, this project was performed from September 2008 until August 2011. During their diploma theses Dipl.-Phys. S. Balk and Dipl.-Phys. K. Bauer also worked on this project in the period from December 2008 to December 2009 and from November 2009 to November 2010.

In this project the production processes of nano and micro structures on graphite surfaces using ion beam lithography was investigated. Besides a direct production process using a high-dose irradiation a low-dose irradiation process was used for structure production. Additionally, the structural and electrical properties of the structures produced by both methods were investigated and compared to theory and to simulations. The investigation results show possibilities for an improvement of the ion beam lithography. Furthermore, the ion beam lithography was classified concerning the possibilities, advantages and disadvantages in comparison to other lithography methods.

Since most electrical components are manufactured by electron beam lithography on silicon wafers, the motivation for this project is the use of an alternative structuring method without the need of a resist for the structure production on an interesting and important material, the graphite. Graphite consists of several graphene layers. Graphene is a highly investigated material and a hot topic in recent science as the award of the Noble prize [1] and actual publications [2], [3], [4] or [5] show. Especially in the case of electrical components new ideas or materials have to be investigated to overcome future limitations for electrical devices [6] like the size limitation of about 10nm for electrical structures.

In cooperation with the Raith GmbH an ion beam lithography device, the ionLiNE, was used for structure production. Samples were prepared and structured using low-dose and high-dose irradiation processes at different kinetic ion energies. While at high ion doses the lattice atoms of the graphite bulk become sputtered or milled out of the sample surface, the production of structures using low-dose irradiation has to be combined with a subsequent oxidation process. For both methods critical ion doses were determined where the low-dose and the high-dose structure production processes are initialized. The critical parameters were also determined by simulations.

The structural properties were investigated concerning the resulting structure depth and width. Although, the structures produced by low-dose irradiation are more controllable concerning the structural properties, this production method has certain limitations for the structure depth that can be overcome using the high-dose production process. The advantages of both methods will probably be combined in future by an im-

proved method that is partially described in this work. The structural properties can also be determined by simulations of the ion impact into solids.

For applications in industry the electrical properties of the produced structures are interesting. In this context, four-probe measurements were performed on simple structures or rather conductors that were produced by both production methods. Experimental results show a difference between electrical bulk and electrical nano- and microstructure properties. The reason for this difference is the structure process itself that will change the lattice arrangement of the sample. Additionally, other influences on the electrical properties could be identified by experiments and by simulations for the potential and current distribution in the structures.

In this work the theoretical basics of the ion beam lithography will be discussed in chapter 2. In chapter 3 the devices used in this project will be presented. In chapter 4 the preparation and the properties of the graphite samples will be described in more detail. Thereafter, the results of the structure production and the structural properties of the structures produced by low-dose and high-dose irradiation will be presented in chapter 5. Furthermore, the results of the electrical measurements using four-probe measurements will be discussed in chapter 6. Finally, the project results will be summarized and a conclusion and an outlook will be given in chapter 7. There is a short chapter summary included at the end of all chapters that contains the most important aspects.

In the appendix the abbreviation list, the reference list, the word list, the acknowledgement and the affirmation are added. All used physical constants were found in references [7], [8] and are also listed in the appendix.

2. Ion beam lithography

In this chapter the basic principles of the ion beam lithography are discussed. Here, the theory of the interaction of ions with matter as a function of the kinetic ion energy is presented. Later, it will be shown by simulations how different ions behave in interaction with matter and how the interaction varies if the solid material is changed. To conclude this section, the ion beam lithography will be explained in more detail, improvements concerning the ion beam lithography in future and a brief summary of the chapter will be given.

2.1 Methods for surface modifications

For the production or modification of nano or micro structures interaction processes must be performed at an atomic or molecular scale. A solid is structured or modified at the nano- or micrometre scale, when material is added or removed from the sample or when the atomic lattice arrangement is changed.

A solid can be characterized by the categories crystalline, polycrystalline, quasi-crystalline, liquid crystalline and amorphous [9]. The categories arrange solids by their degree of atomic periodicity, so by their atomic arrangement and by the range of this arrangement. A crystalline solid has a completely periodic and ideally infinite atom arrangement. Many solids can be described by this ideal assumption where the atoms are connected by bond types like covalent bonds, Van der Waals interactions, ionic bonds, metallic bonds or by hydrogen bonds [10]. In this case the atoms mostly occupy fixed lattice positions in the solids.

In physics there are a variety of theoretical models to describe the potential distribution in solids so that certain physical properties can be explained. These properties are, for example, the electronic band structure and the electrical or the thermal conductivity. Some well-known theoretical potential models for the electronic structure determination are the tight binding model, the nearly free electron model, the Hartree-Fock model, the density functional approximation theory, the muffin tin potential model or the LCAO method [11], [12]. A potential model to describe the interaction between atoms or molecules by Van der Waals forces is the Lennard-Jones potential [9].

Depending on the bond type a certain amount of energy is required to remove or displace an atom from the solid or the lattice position. The total energy that is required for a structuring process or a structure modification can be applied, for example, by atom, ion or molecule collisions with lattice atoms. Also the energy transfer by friction or by thermal energy can suffice to remove atoms from their lattice position. In addition,

chemical processes can solute sample atoms. If incident atoms or ions will be implanted into the sample the atom arrangement in the sample lattice can be modified or destroyed so that the lattice atoms can be removed with less energy. The atom or molecule arrangement and the bond strength in some materials can be additionally changed by electron irradiation. This process is called the electron beam lithography. In this context, the electron irradiation changes a molecule arrangement so that chemical etching processes will be slowed or accelerated. In summary, various types of energy transfers are possible to structure or modify solids. Several structure production or modification methods are so-called lithography processes that are presented in the next subchapter.

2.2 Lithography processes

The production of nano and micro structures in modern research and in industry is known as lithography, although the term historically describes a printing technique using stone plates from the 19th century and the direct translation from the ancient Greek (λίθος (*lithos)*, „stone“ and γράφειν (*graphein)*, „to write“) points to this procedure like reported in reference [13]. In principle, modern lithography techniques have only one thing in common with this ancient art, namely the possibility to produce structures using a mask where the entire sample surface can be exposed in a single parallel process. Additionally, there is a serial process in which the structures are produced one after the other. In general, serial running lithography is much more time consuming than parallel running lithography. Lithography methods applied in research and industry can be categorized as follows and are listed, for example, in reference [14]:

- *Electron and ion beam lithography:* The ion beam lithography is a serial process in which atoms are sputtered at the sample surface by the use of focused ion beams. Therefore, this process is called the sputtering or the milling. With this method structures of a few nanometres in size can be produced. By using light ions the structure size can theoretically be decreased to 1nm [15]. When using electron beam lithography the surface is not structured immediately. The electrons are used to irradiate a substance called the resist. The irradiated resist areas will be solved more slowly (negative resist) or faster (positive resist) during a chemical etching process due to a lattice re-arrangement of atoms or molecules after the irradiation. Known resist materials are SU-8, a negative resist, and PMMA, polymethylmetacrylate, a positive resist [16].
- *Electron and ion projection techniques:* These techniques are parallel lithography processes in which electrons or ions are used. Here, the sample is irradiated over a large area using a mask and resist. The size of the structures may be a few nano meters.
- *Optical lithography, X-ray lithography, EUV lithography:* Besides the use of electrons or ions also radiation is used for structure production [17]. In these pro-

ceedings a resist is used that can be modified by radiation with different wavelengths.

- *Scanning probe microscopy processes:* In a serial method a scanning tunnelling microscope (STM) or an atomic force microscope (AFM) is used to produce structures on sample surfaces. Here, the tips of the devices are used for structure production. With these methods masks can be produced, which are used in a parallel lithography method [18]. The final structure size depends on the tip quality and can be a few nano meters.
- *Nano-imprint-lithography:* This method uses, for example, compression moulding to create a pattern in resist films [19]. The structure on the resist film can then be transferred on other materials and can be about 25nm to 10nm in diameter.

In this project ion beam lithography was used to create structures on a graphite surface by single charged gallium ions, whereby sputtering processes and ion implantations in addition with lattice defect creations and cascade collisions are important. In preparation for the explanation of the ion beam lithography the following subsections will discuss ion-matter-interactions in more detail.

2.3 Ions

Positive ions (cations) and negative ions (anions) are charged atoms with more or less electrons than protons [20]. Almost all elements presented in the periodic table [21] are usable for ion beam lithography. But the required energy for ionization, the availability of a material, chemical, electrical and thermal properties and the interaction process with matter limit the selection of atoms for this lithography method. Ions interact with other particles mainly due to their charge and their Coulomb potential. In the context of ion beam lithography the kinetic energy of the ion is also important due to different interaction mechanisms at different kinetic energies.

To ionize an atom the ionization energy is needed that depends on the electron configuration of the atoms. Historical investigations of N. Bohr [22], [23], W. Heisenberg [24], L. de Broglie, W. Pauli and E. Schrödinger [25] could explain the structure of atoms and so the energy levels electrons occupy. Consequently electrons occupy orbitals, which correspond to the probability distribution of electrons around the nucleus. Because of the Pauli exclusion principle and the Hund's rules [11], the electron configuration is determined by the quantum numbers (principal quantum number, azimuthal quantum number, magnetic quantum number, spin projection quantum number). These conditions divide the orbitals into s-(1x), p-(3x), d-(5x) and f-shells (7x). The first ionization energy which is necessary to remove an electron from an atom is shown in Figure 1 and listed in reference [26].

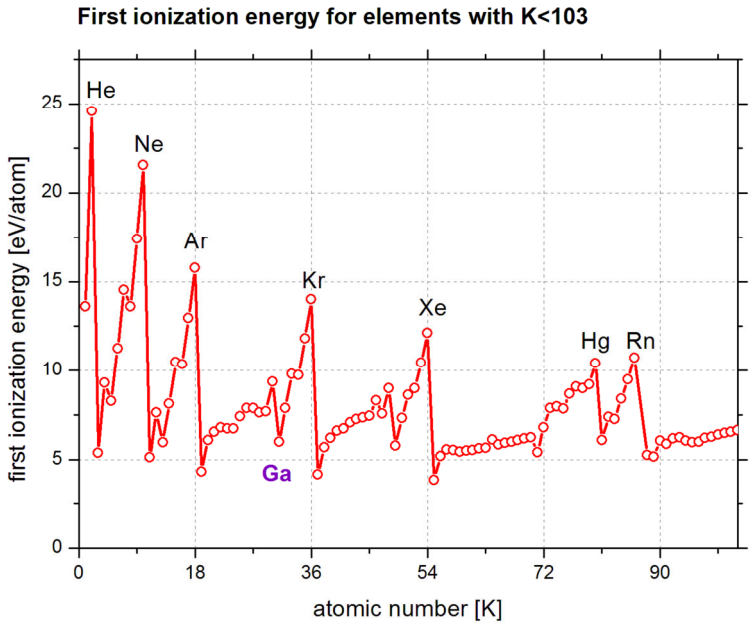

Figure 1: First ionization energy as a function of the atomic number K [26]. Especially atoms with fully occupied orbitals, as the main elements of the VII group (He, Ne, Ar, Kr, Xe, Rn), require higher first ionization energies. The first ionization energy of gallium atoms that are used in the ion beam facility of this project is highlighted (6.0eV).

2.3.1 Acceleration of ions in an electric field

In ion beam lithography ions are accelerated and focused onto a sample surface. By the acceleration of an ion with the charge of $n \cdot e$ (multiple of the elementary charge) in a potential field, the kinetic energy of the ions ΔE_{kin} changes as a function of the acceleration voltage U by

$$\Delta E_{kin} = n \cdot e \cdot U. \tag{1}$$

From relativistic physics the relationship between energy and mass increase Δm is known. With c as the velocity of light this results in

$$\Delta E_{kin} = \Delta m \cdot c^2. \tag{2}$$

For the mass increase of an accelerated ion in an electric field this leads to

$$\Delta m = \frac{n \cdot e \cdot U}{c^2}. \tag{3}$$

Since the resulting mass m equals the sum of the mass m_0 and the mass increase Δm the result for the mass ratio is

$$\frac{m}{m_0} = 1 + \frac{n \cdot e \cdot U}{m_0 \cdot c^2}. \tag{4}$$

Taking into account that the relativistic increase in mass of a particle depends on the speed v

$$\frac{m}{m_0} = \frac{1}{\sqrt{1 - \frac{v^2}{c^2}}} \tag{5}$$

the two equations can be combined so that the relativistic ion velocity as a function of the kinetic ion energy or acceleration voltage is given by

$$v = c \cdot \sqrt{1 - \frac{1}{\left(1 + \frac{n \cdot e \cdot U}{m_0 \cdot c^2}\right)^2}} = c \cdot \sqrt{1 - \left(\frac{m_0 \cdot c^2}{E_{kin} + m_0 \cdot c^2}\right)^2}. \tag{6}$$

Because of the small mass electrons are much faster at a certain kinetic energy in comparison to ions. Relativistic corrections at about 5% light speed have to be taken into account in electron beam lithography above kinetic energy of about 1keV and in ion beam lithography above 1-100MeV depending on the ion material for beam focussing as it is shown in Figure 2.

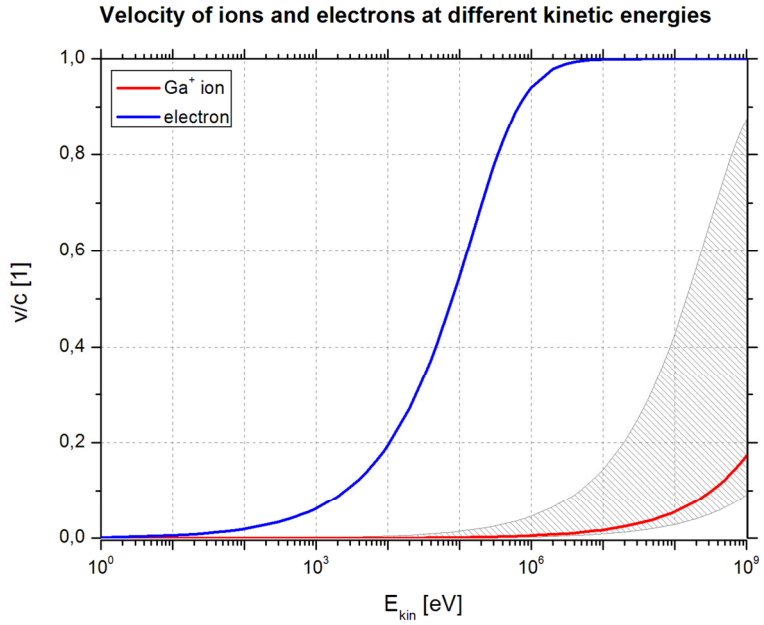

Figure 2: Speed of ions and electrons in proportion to the speed of light as a function of the kinetic energy. The grey-shaded area represents the distribution of velocity of all single charged ions. The velocity of a single charged Ga^+ ion has been highlighted.

As mentioned before, the interaction mechanism of incident ions and solids changes with the kinetic ion energy. The interaction effect will be discussed in the next subsection in detail.

2.4 Interaction mechanisms of ions with solids

In Figure 3 the interaction mechanisms of accelerated and single charged ions in solids are roughly listed like, for example, presented in reference [27]. It should be noted that the interaction processes are determined by the ion itself, its mass and charge, as well as by the physical sample properties, such as lattice arrangement and element composition of the target in addition to the kinetic energy.

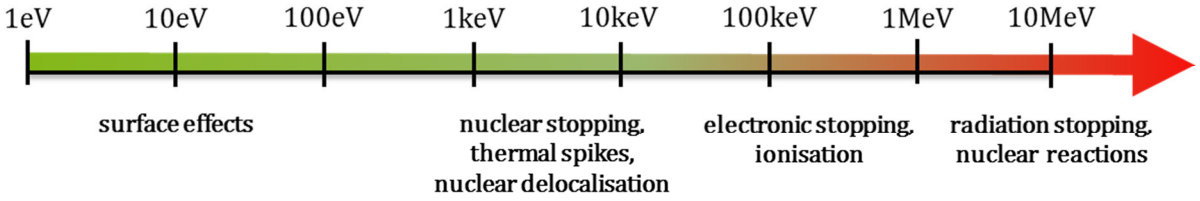

Figure 3: Rough description of the interaction mechanisms of ions with solids at different kinetic energies.

In the low-energy range the interaction mainly takes place between the ions and the sample surface, even if the energy is equivalent to most of the binding energy of chemical substances [9]. The incident ions cannot penetrate into the solids or transfer enough energy to nuclei in order to deform or destroy the sample lattice arrangement. In this energy range the ions mainly become adsorbed at the surface and diffusion and desorption processes occur. Not only single charged ions but also single charged atom clusters only interact with the sample surface at these low kinetic energies as other investigations of our group show [28]. It is important to mention, that multiple charged ions show other interaction processes. This is explained briefly in chapter 2.7. In this context, the potential energy of the ions, which is determined by the ion charge, can induce sputtering processes or a lattice deformation or destruction at even low kinetic energy as it is reported in reference [29]. For ion beam lithography single charged ions with low kinetic energy are not useful.

Above kinetic ion energies of 1keV the ions penetrate into the solid. Mainly Coulomb interactions and elastic collisions of ions with the lattice atoms occur. The interaction with the lattice atoms will reduce the kinetic ion energy until the ions are fully stopped and implanted into the solid. Because of the deceleration of the ions by Coulomb interaction and elastic collisions with lattice atoms this process is called the nuclear stopping. The energy the ions transfer to the solid lattice induces oscillations of the atoms that can be interpreted as thermal energy. The thermal energy can heat parts of the sample volume up to several thousand Kelvin. This effect is described by so-called thermal spikes and lasts a few picoseconds. More information on thermal spikes is given in references [30] and [31]. Thermal spikes can lead to local lattice destruction or to local sample melting. In addition, a sputter effect can be induced when the energy transfer is high enough to remove lattice atoms out of the sample surface.

Above kinetic ion energies of about 100keV interaction processes mainly occur between the ions and the sample electrons. This interaction increases as a function of the kinetic

ion energy and is dominant besides other interaction processes in the MeV energy range [32]. In this energy range ions become scattered during the interaction process with the electrons of the sample. In this energy region also strong ionization effects combined with radiation emission of the lattice atoms appear. Since the energy loss of ions mainly happens by the interaction with electrons this process is called the electronic stopping.

At energies above several MeV energy loss by radiation emission occurs. The energy loss by radiation strongly depends on the particle mass and is therefore only important for very light particles. For most ions the radiation stopping can therefore be ignored. In this context, this effect is mentioned for the sake of completeness. The energy loss by radiation emission is called radiation stopping but also the term bremsstrahlung is used in literature. Publications about the bremsstrahlung cross-section formulas or about a pair production induced by bremsstrahlung are shown in references [33] and [34]. Another effect is the emission of Čerenkov radiation which occurs for faster charged particles than the phase velocity of electromagnetic waves [35], [36]. Furthermore, at very high energies nuclear reactions or decays can appear.

The desired effect for ion beam lithography is the interaction of ions with lattice atoms during the nuclear stopping process. Since ions with high kinetic energy interact strongly with the sample electrons and lose kinetic energy, the ions first penetrate deep into the material before they start to interact with the lattice atoms in the nuclear stopping energy range. Lattice defects occur in deeper material regions for fast ions while slow ions will determine lattice defects or sputter effects near the sample surface as it is shown in Figure 4. Scattered lattice atoms are called recoils and can be able to scatter other lattice atoms after a sufficiently high energy transfer. In this case collision cascades can occur.

The scattering of the incident ions is smaller in the electronic than in the nuclear stopping energy range. This is due to a smaller cross section in the interaction of incident ions and electrons and due to a smaller mass ratio of electrons and ions in comparison to atoms and ions. Figure 4 was made by TRIM simulations that will be explained in more detail in chapter 2.6.2. It should be noted that not all sample properties like, for example, the lattice arrangement are fully implemented in the TRIM or SRIM simulations. Many lattice effects like the channelling [37] can, therefore, not be considered. Also the effect of multiple charged ions is not taken into account.

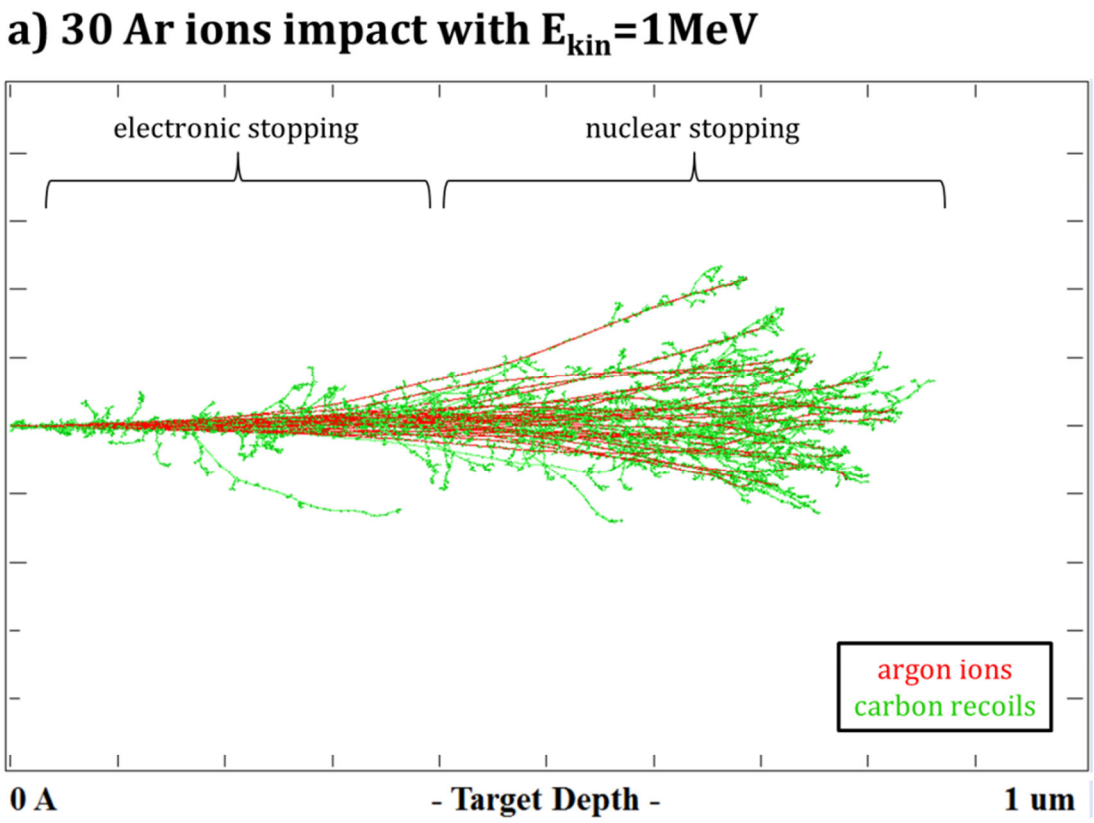

Figure 4: Nuclear and electronic stopping for the impact of argon ions with a kinetic ion energy of 100keV and 1MeV into a carbon solid calculated by the TRIM simulation that will be introduced in chapter 2.6.2. While the electronic stopping dominates for high kinetic ion energies, the nuclear stopping dominates after the kinetic ion energy has decreased to several keV. Both images are scaled different concerning the target depth.

2.5 Theory of the interaction processes of ions with solids

During the interaction of ions with electrons or lattice atoms the ions lose kinetic energy. This energy loss can be mathematically described as the stopping power $S(E)$ which is defined as the energy loss ΔE of the ions per distance Δx and is introduced for example in reference [38].

$$S(E) = -\frac{\Delta E}{\Delta x} \tag{7}$$

The stopping power is usually given in $[keV/cm]$ and refers to macroscopic systems. In addition to microscopic examination the stopping power is extended by the atomic density ρ $[kg/m^3]$ with

$$s(E) = -\frac{1}{\rho}\frac{\Delta E}{\Delta x} = \frac{1}{\rho}S(E) \tag{8}$$

in units of $[MeV \cdot cm^2/g]$. Usually, the stopping power is also given in units of $[MeV \cdot cm^2/mg]$. If the kinetic ion energy drops below the so-called threshold displacement energy, no interaction effects occur that are important for the ion beam lithography and the ions will be implanted into the solid [39]. The threshold displacement energy is specific for different solids. For typical solids the threshold displacement energy is in the order of 10-50eV like reported in [40] and [41]. Since the total stopping power is composed by the radiation, electronic and nuclear stopping this results in

$$S_G(E) = S_r(E) + S_e(E) + S_n(E) = -\left[\left(\frac{\Delta E}{\Delta x}\right)_r + \left(\frac{\Delta E}{\Delta x}\right)_e + \left(\frac{\Delta E}{\Delta x}\right)_n\right], \tag{9}$$

wherein the radiation stopping plays a minor role. It is possible to obtain the mean ion range R of a particle by integration

$$R = \int_E^0 \frac{1}{S_G(E)}\,dE = \int_E^0 \frac{1}{S_r(E) + S_e(E) + S_n(E)}\,dE \quad . \tag{10}$$

The stopping power can be plotted as a function of the range of the ions in matter. This plot is called the Bragg curve and can show theoretically the ion distribution of the implanted ions as a function of the ion range into a solid.

2.5.1 Electronic stopping

In the 1930s much research has been carried out to determine the stopping power and the ion-solid interaction. Based on the initial work of N. Bohr [42] in the year 1913 F. Bloch [43] and H. A. Bethe [44] have established the first equations for the stopping

power that is known as the Bethe-Bloch equation. This equation was then expanded using a shell and density correction and can be written as [45]

$$S_e(E) = -\frac{\Delta E}{\Delta x} = 4\pi N_a r_e^2 m_e c^2 \frac{\rho Z}{A}\frac{z^2}{\beta^2}\cdot\left[ln\left(\frac{\gamma^2\beta^2 m_e c^2}{I}\right) - \beta^2 - \frac{\delta}{2} - \frac{C}{Z}\right] \quad . \tag{11}$$

The parameters of the formula are: N_a: Avogadro constant, r_e: classical electron radius, m_e: electron mass, c: velocity of light, ρ: density of the absorbing medium, Z: atomic number of the absorbing medium, z: charge number of the incident particle, A: mass number of the absorbing medium, $\beta = v/c, \gamma = 1/\sqrt{1-\beta^2}$, δ: density effect correction term, C: shell correction term. Under this assumption the maximum energy that can be transferred to an electron by an incident ion with the mass M_1 is [46]

$$E_{max} = \frac{2\beta^2\gamma^2 m_e c^2}{1 + \frac{2\gamma m_e}{M_1} + \left(\frac{m_e}{M_1}\right)^2} \approx 2\beta^2\gamma^2 m_e c^2 \qquad for\ \gamma m_e \ll M \quad . \tag{12}$$

The Bethe-Bloch equation could explain experimental data obtained for the stopping power of ion velocities between 10MeV and 10GeV [46], but it fails for calculations of the stopping power of smaller or larger kinetic ion energies. Only after additional investigations a stopping power theory for ions with lower kinetic energies could be developed. Based on H. Bloch's work J. Lindhard proposed a parameterization of the stopping power and expanded Bloch's equation considering the Barkas effect and other corrections [47], [48]. In collaboration with M. Scharff and H. E. Schiott the LSS-Theory [49], [50] was developed. Finally, the additional work results can be summarized in a formula presented in [51].

$$S_e(E) = 8\pi e^2 a_0 \frac{Z_1^{\frac{7}{6}} Z_2}{\left(Z_1^{\frac{2}{3}} + Z_2^{\frac{2}{3}}\right)^{\frac{3}{2}}}\frac{v}{v_0} = 8\pi e^2 a_0 \frac{Z_1^{\frac{7}{6}} Z_2}{\left(Z_1^{\frac{2}{3}} + Z_2^{\frac{2}{3}}\right)^{\frac{3}{2}}}\sqrt{\frac{2E_{kin}}{M_1}} \tag{13}$$

Here are $a_0 = \hbar/(\alpha \cdot m_e c)$ the Bohr radius with $\hbar$ as the reduced Planck's constant and α as the Fine-structure constant, $Z_{1,2}$ the charge of the interacting particles (ions, electrons), $v = \sqrt{2E_{kin}/M_1}$ the velocity of the incident ion and $v_0 = e^2/\hbar$ the Bohr velocity.

At very low kinetic ion energy the interaction between the ions and lattice atoms is dominant and will be described in the next subchapter. For high kinetic ion energy radiation emission effects during the deceleration of charged ions known as bremsstrahlung occur. Both effects cannot be explained with the formulas of the electronic stopping process and have to be considered separately.

2.5.2 Nuclear stopping

The derivation of the nuclear stopping power is well described in reference [52] and will be explained here briefly where $S_n(E)$ equals the integral over the energy transfer $T(E_0, \theta(p, E_c))$ after a nuclear collision event with

$$S_n(E) = \int_0^\infty 2\pi \cdot T(E_0, \theta(p, E_c)) p \, dp \quad . \tag{14}$$

Here p equals all possible impact parameters, E_0 is the initial kinetic energy of the two particle system, E_c the kinetic energy of the two particle system and θ equals $\pi - \phi$ with ϕ as the deflection angle in the collision process. The energy transfer per collision is

$$T\big(E_0, \theta(p, E_c)\big) = E_0 \frac{4M_1M_2}{(M_1 + M_2)^2} sin^2\left(\frac{\theta(p, E_c)}{2}\right) \tag{15}$$

with $M_{1,2}$ as the mass of the incident ion and its collision partner. The integral then becomes

$$S_n(E) = \; 2\pi \cdot E_o \frac{4M_1M_2}{(M_1 + M_2)^2} \int_0^\infty sin^2\left(\frac{\theta(p, E_c)}{2}\right) p \, dp \quad . \tag{16}$$

Because the deflection angle depends on the interatomic potential $V(r)$ with r as the collision partner distance by

$$\theta(p, E_c) = \pi - 2 \int_{r_{min}}^\infty \frac{1}{r^2 \sqrt{1 - \frac{V(r)}{E_c} - \frac{p^2}{r^2}}} p \, dp \tag{17}$$

the integral can only be solved numerically since the interatomic potential cannot be described analytically. The potential is composed from the charge distribution of the core, the electron distribution of the ion and the solid and can be determined numerically by a so-called screening function $\Phi(r)$ with

$$V(r) = \frac{Z_1 Z_2 e^2}{r} \, \Phi(r) \quad . \tag{18}$$

On the basis of calculations J. F. Ziegler, J. P. Biersack and U. Littmark [53] found an approximation for the screening function that is known as the universal screening potential (USP) $\Phi(x)$.

$$\Phi(x) = 0.1818e^{-3.2x} + 0.5099e^{-0.9432x} + 0.2802e^{-0.4028x} + 0.02817e^{-0.2016x} \tag{19}$$

Here, $x = r/a_U$ and $a_U = 0.8854 \cdot 0.529\text{Å} \,/\, (Z_1^{0.23} + Z_2^{0.23})$. Additionally, a so-called dimensionless reduced energy ϵ has to be introduced that considers the dependence of the nuclear stopping power on the masses and charges of the incident ions and the solid atoms with

$$\epsilon = \frac{32.53 \cdot M_2 \cdot E_0}{Z_1 Z_2 \cdot (M_1 + M_2) \cdot (Z_1^{0.23} + Z_2^{0.23})} \quad . \tag{20}$$

The stopping power $S_n(\epsilon)$ in units of ϵ is then

$$S_n(\epsilon) = \begin{cases} \dfrac{\ln(1 + 1.1383\epsilon)}{2(\epsilon + 0.01321\epsilon^{0.21226} + 0.19593\epsilon^{0.5})} & \epsilon \leq 30 \\ \dfrac{\ln(\epsilon)}{2\epsilon} & \epsilon > 30 \end{cases} \quad . \tag{21}$$

Finally, the stopping power $S_n(E)$ in units of eV/(atom/cm²) is [52]

$$S_n(E_0) = \frac{8.462 \cdot 10^{-15} \cdot Z_1 \cdot Z_2 \cdot M_1}{(M_1 + M_2) \cdot (Z_1^{0.23} + Z_2^{0.23})} \cdot S_n(\epsilon) \quad . \tag{22}$$

2.5.3 Radiation stopping

The principles of the bremsstrahlung are known from electron-electron or positron-electron interactions and can be transferred to ion-electron interaction. In general, bremsstrahlung occurs due to the deflection of high-energy charged particles [46]. It has been investigated by N. Bohr and W. Heitler for electrons [54]. For ions the energy loss by bremsstrahlung can be described by the equation presented in reference [55].

$$S_r(E) = 4\alpha \cdot N_A \cdot \frac{Z^2}{A} \cdot z^2 \cdot \left(\frac{1}{4\pi\varepsilon_0} \cdot \frac{e^2}{mc^2}\right)^2 \cdot E \cdot ln\left[183 \cdot Z^{-\frac{1}{3}}\right] \tag{23}$$

Here, E is the energy of the ion before radiation emission, α the fine structure constant, N_A the Avogadro constant, Z the atomic number of the target, A the atomic weight of the target and z and m the charge number and the mass of the incident ion. In addition to the bremsstrahlung also other effects like the pair production occur [56]. Further research showed that under certain conditions the bremsstrahlung only counts a fraction for the stopping power and other effects can dominate in this high energy region [54]. Based on the theories described in this section and further investigations programs were developed to simulate the impact of ions into solids. Since some of these programs were used and compared with experimental data in this project, they should be presented in detail in the next subsection of this work.

2.6 Simulations of interaction processes – SRIM and TRIM

The deviated interaction processes received from the theoretical works on ion-solid interactions were used to simulate the ion impact into solids and the ion-solid interaction. Some of this programs are MELF-GOS [57] or the simulations ESTAR, PSTAR und ASTAR

of the National Institute of Standards and Technology [58] and, for example, SRIM(TRIM) programmed by J. F. Ziegler, M. D. Ziegler und J. P. Biersack which is explained in reference [59] or on the programmers' homepage [60] in more detail. Some of the programs can be used as freeware. Although, the programs may work with different algorithms and equations as it is described on appropriate references the simulated results only vary low among each simulation.

In this project the programs SRIM (The Stopping and Range of Ions in Matter) and TRIM (Transport of Ions in Matter) were used. Since the development and introduction of SRIM (TRIM) in the year 1985 the program has been continuously improved and expanded with new theoretical models and experimental data. The program SRIM version 2011 has an average accuracy of about 4.6% in comparison with experimental data for stopping power and approximately 69% (86%) of all measured data is in variation of 5% (10%) in comparison to SRIM calculations as it is reported on the programmers' homepage [60]. This program version was in beta phase during the calculations made in this project. For calculations the more bug free SRIM(TRIM) version 2008.04 was used.

2.6.1 SRIM – The Stopping and Range of Ions in Matter

The program SRIM simulates the electronic and nuclear stopping and the ion range of incident ions into a solid. The program is increasingly used in research. The simulated solids in this program can be composed of different elements. An integrated database helps to import a correction ratio of elements for the simulation of mixed materials. Furthermore, the database contains all important data for the calculation of a specific solid. Additionally, the pre-set values can be changed manually. Concerning an impact-ion the element name, the corresponding atomic number and the mean atomic weight have to be entered. The composition of the solid body is obtained by elements of the periodic table and takes into account what proportion of the solid state individual elements have. In this context, the element name, the atomic number and the average atomic weight have to be set for each element class. Furthermore, the density of the solid and its physical state have to be entered. The so-called compound correction takes into account the differences between elemental and bounded components such as H_2O instead of 2H and O or for other compounds in the database [61], [62]. Here, not only the masses of the compound elements of the solid are taken into account in the simulation, but also the bonds between the compound elements and the solid phase. Additionally, the compound correction also varies for light ions. Furthermore, the average ion range can be calculated and the so-called straggling that equals the square root of the variance of the ion range is explained in more detail in chapter 2.6.2. In this case lateral and longitudinal straggling relates to y-z- and x-z-projected ion range. To give an overview the stopping power, the range and straggling of different ions into a graphite solid are simulated and presented on the following pages. Graphite is implemented in the compound database of the SRIM simulation.

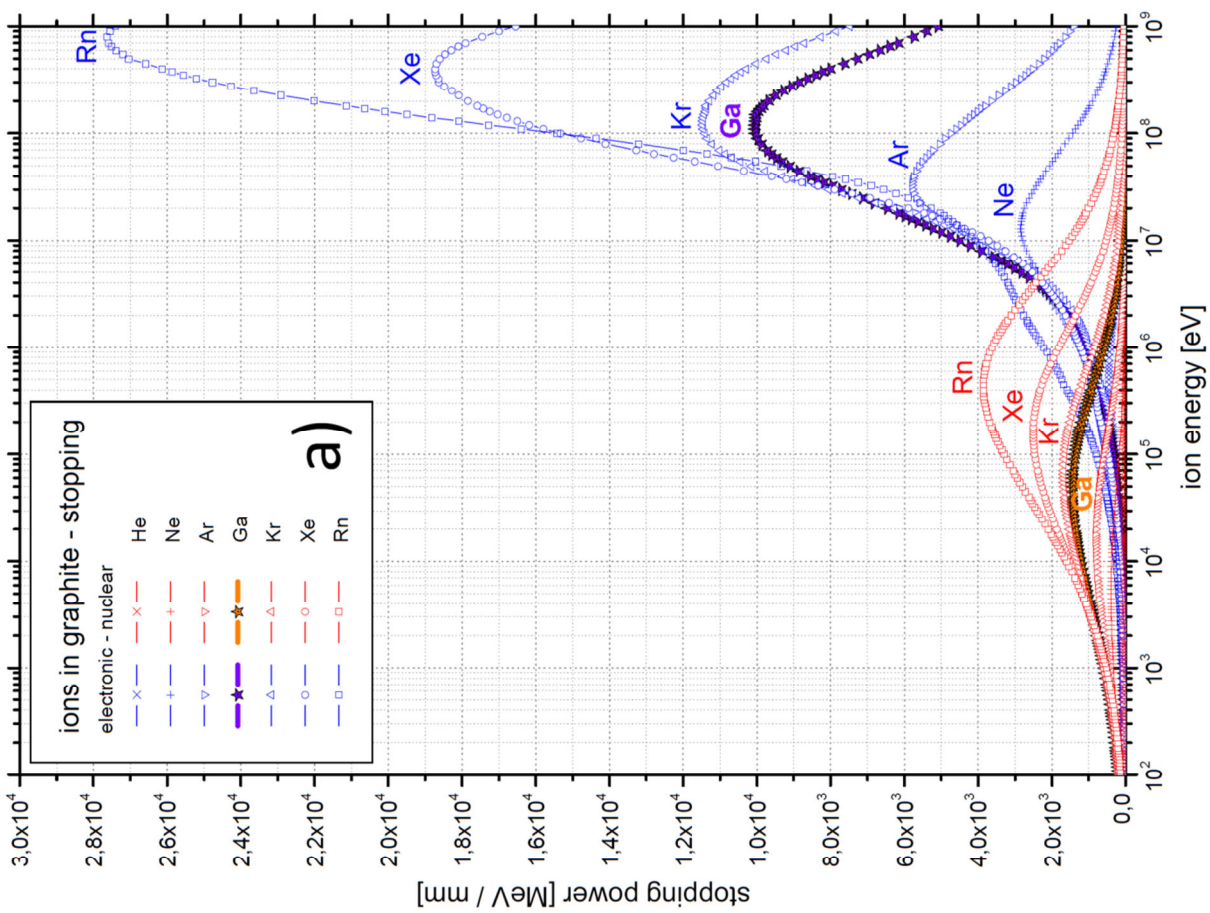
a)
ions in graphite - stopping
electronic - nuclear
He
Ne
Ar
Ga
Kr
Xe
Rn
stopping power [MeV / mm]
ion energy [eV]

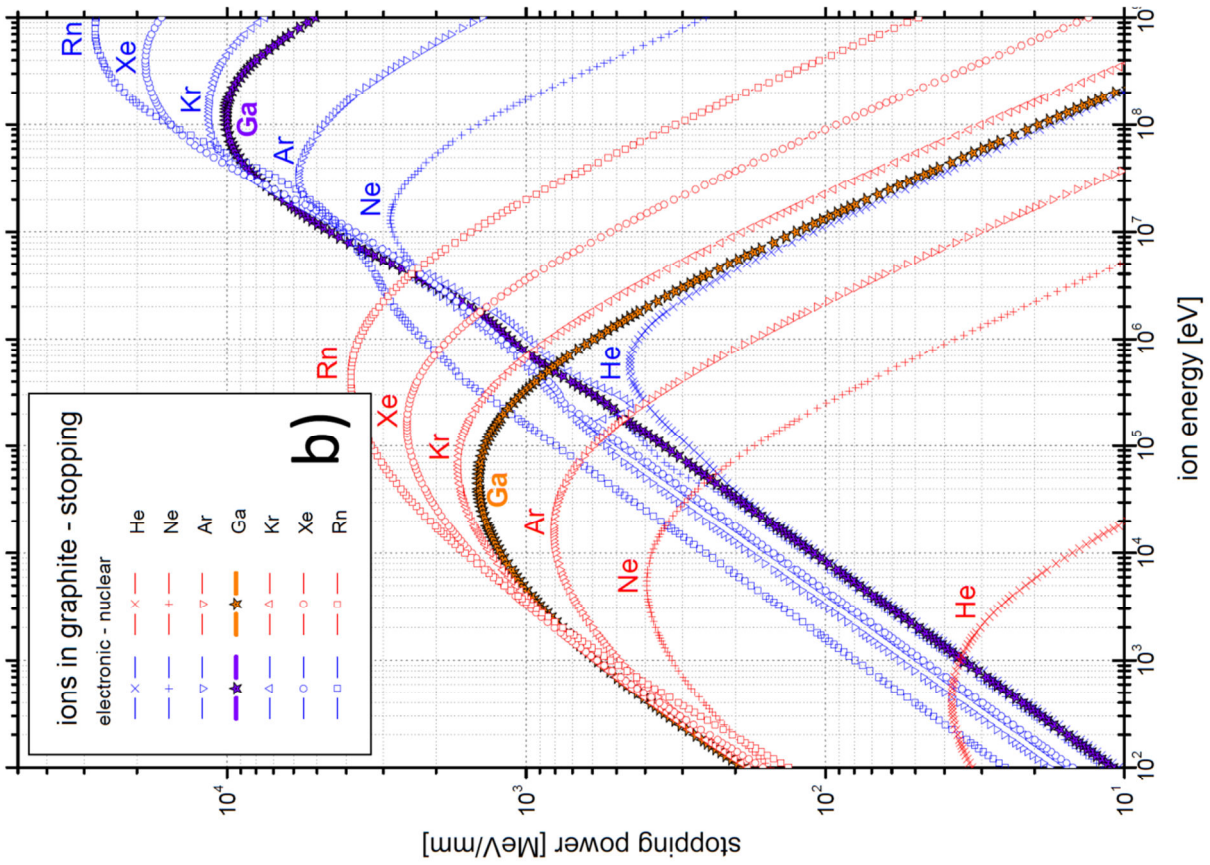
b)
ions in graphite - stopping
electronic - nuclear
He
Ne
Ar
Ga
Kr
Xe
Rn
stopping power [MeV/mm]
ion energy [eV]

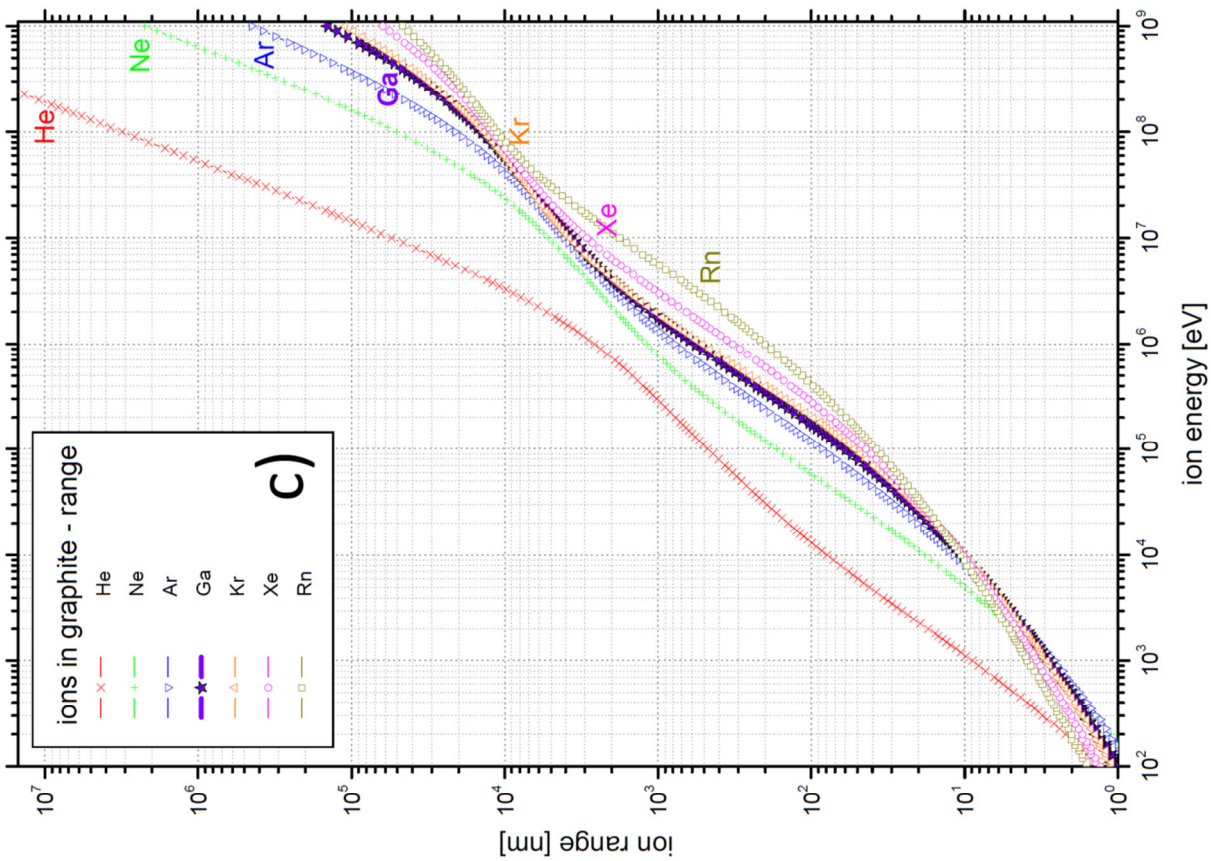
c)
ions in graphite - range
He
Ne
Ar
Ga
Kr
Xe
Rn
ion range [nm]
ion energy [eV]

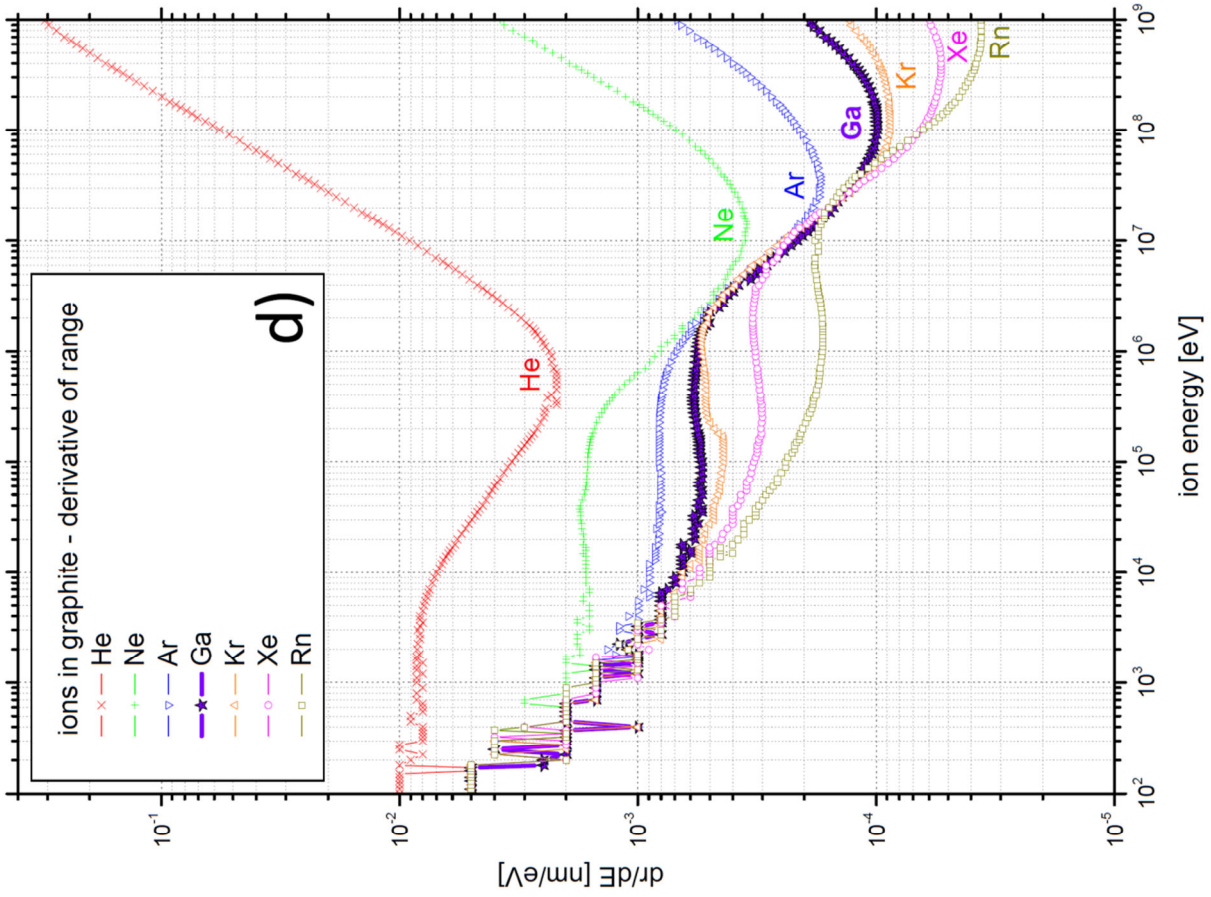
d)
ions in graphite - derivative of range
He
Ne
Ar
Ga
Kr
Xe
Rn
dr/dE [nm/eV]
ion energy [eV]

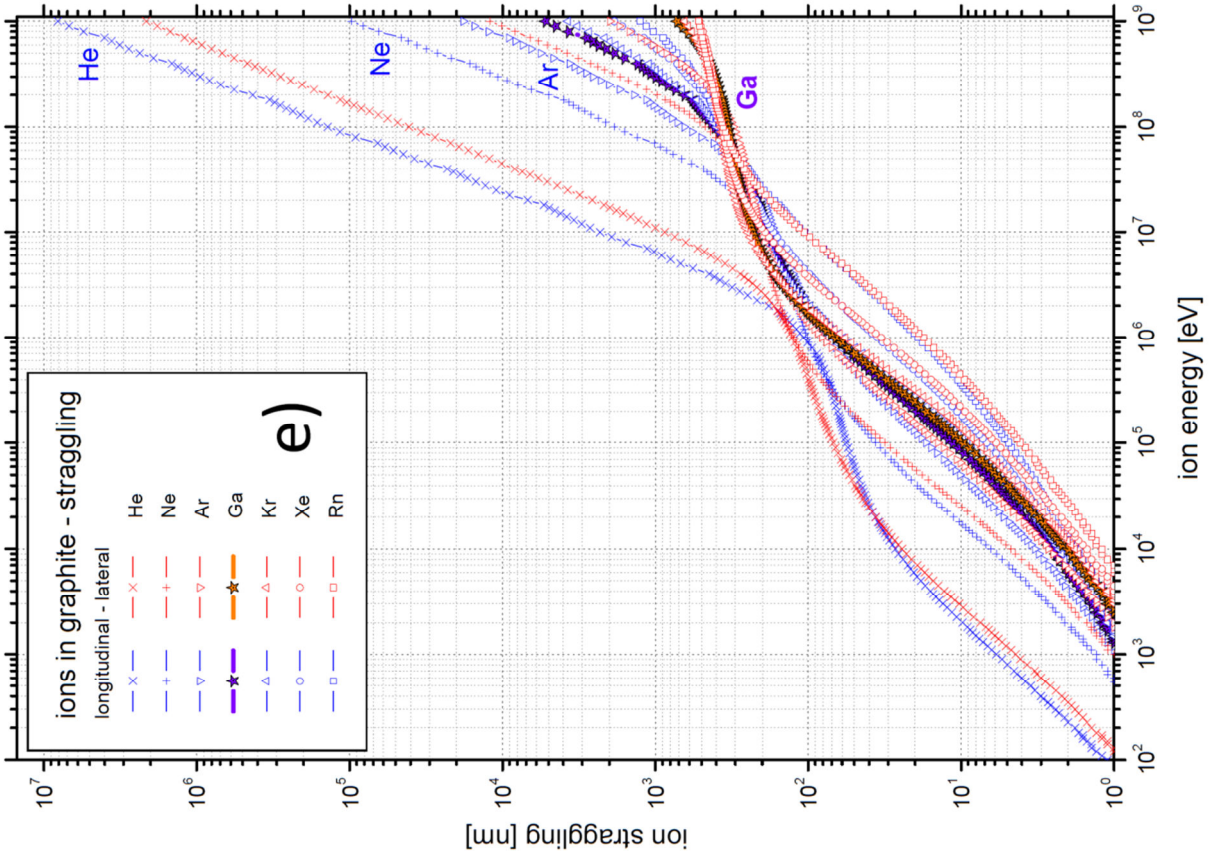

Figure 5: a)+b): Simulation results of the SRIM program on the electronic and nuclear stopping power for the impact of different ions into a graphite solid. In b) the stopping power is shown in logarithmic scale. c)-e): Calculated ion range, the derivative of the ion range and the ion straggling for the impact of different ions into a graphite solid.

In a) and b) of Figure 5 the nuclear and electronic stopping for the impact of different ions into graphite are shown in linear and logarithmic scale. For low kinetic ion energies the nuclear stopping dominates. At higher energies the nuclear stopping decreases and the electronic stopping power increases. The transition from nuclear to electronic stopping power shifts to higher kinetic ion energies with increasing ion atomic number. Also the maximum nuclear and electronic stopping shifts with increasing atomic number. The value of the maximum nuclear and electronic stopping rises as a function of the atomic number of the ions as it is shown in Figure 6.

The plots show the dependency of the maximum stopping power shift a) and the maximum stopping power value b) as a function of the ion atomic number. In both plots functions are added that describe the mathematical dependency. a) The peaks shift with the square of the atomic number. Here, the shift of the maximum electronic stopping rises faster with the atomic number, than the maximum nuclear stopping does like the equations in a) show. b) The value of the maximum stopping power increases linear with the atomic number. In c)-d) of Figure 6 the ion range, the range derivative of the ion range and the straggling are shown. Especially light ions penetrate deep into the solid material but also get scattered more in the solid as the straggling shows that equals the square root of the variance of the ion range. With increasing atomic number the ion range decreases due to the increasing ion masses. The straggling-plot also shows a strong de-

crease of the scattering process for heavy ions in the electronic stopping energy range. The derivative of the ion range decreases in the electronic stopping energy range and becomes a minimum at kinetic ion energies that correspond to the maximum electronic stopping power. The derivative is nearly constant for all ions in the nuclear stopping energy range. At energies of several eV the derivative of all simulated ions tend to 10nm/keV. On average, heavy ions do not penetrate solids as deep as light ions do at the same kinetic ion energies although the scattering of light ions in solids is much higher.

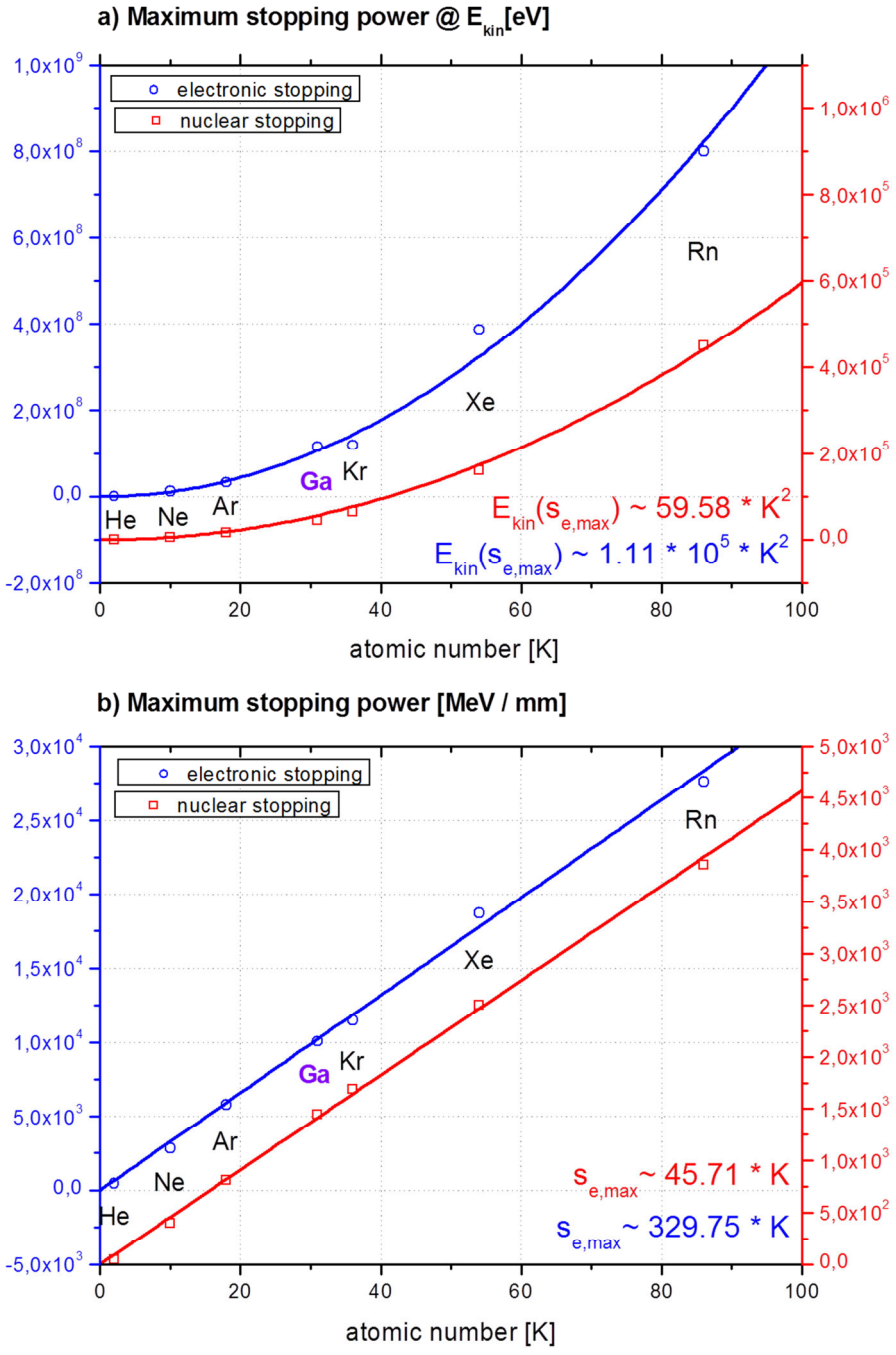

Figure 6: Maximum electronic and nuclear stopping at kinetic ion energies as a function of the ion atomic number a). In b) the value of the maximum electronic and nuclear stopping power is plotted as a function of the ion atomic number.

In additional simulations not the ion but the solid material was varied. The following plots show the impact of gallium ions into different solids. In this case also the impact into the compound materials GaAs and SiO_2 were simulated. As mentioned before, in the used simulation version compound corrections like the stopping correction for target chemistry and phase, the target composition and the target bonds are implemented in the simulations [61], [62]. The next plots are scaled just as the plots for the impact of different ions into graphite due to a better comparability.

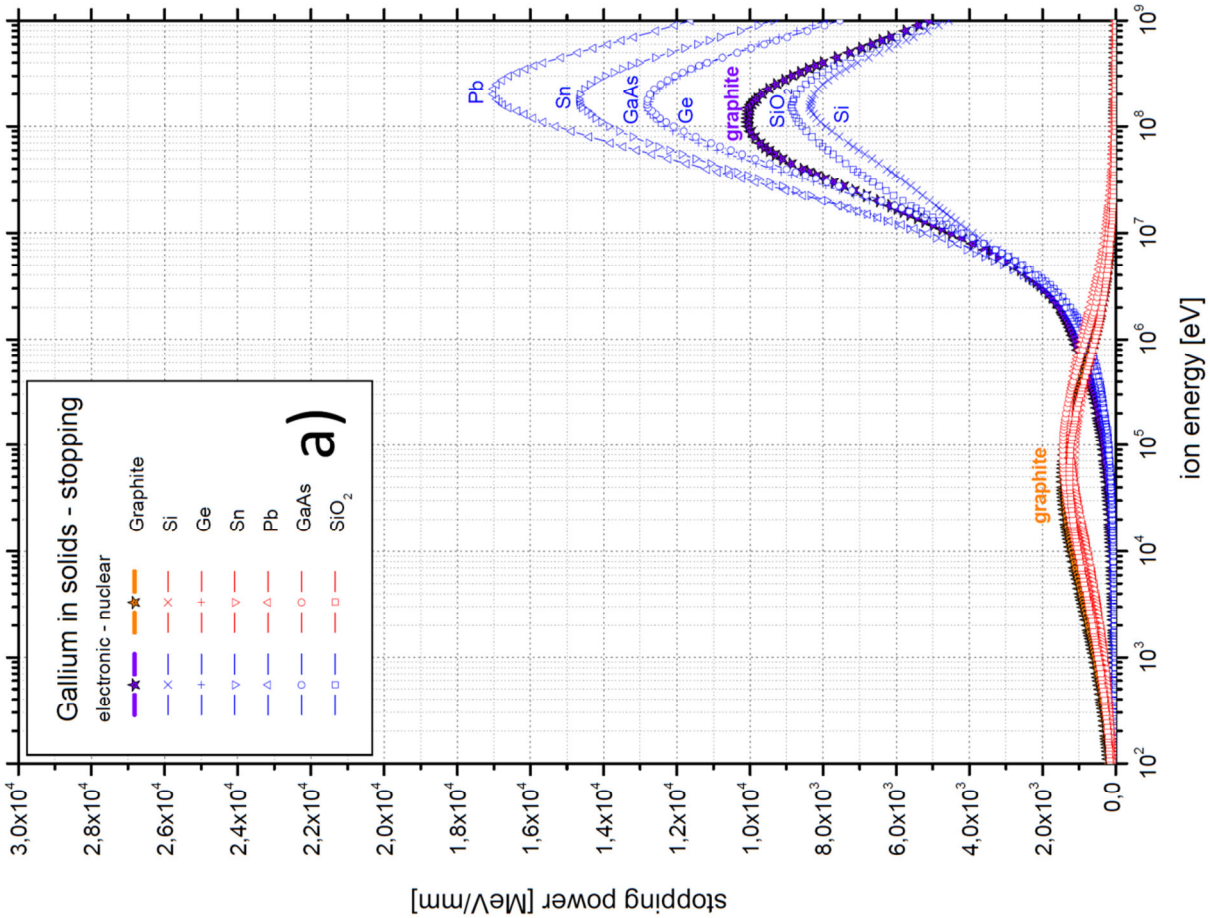

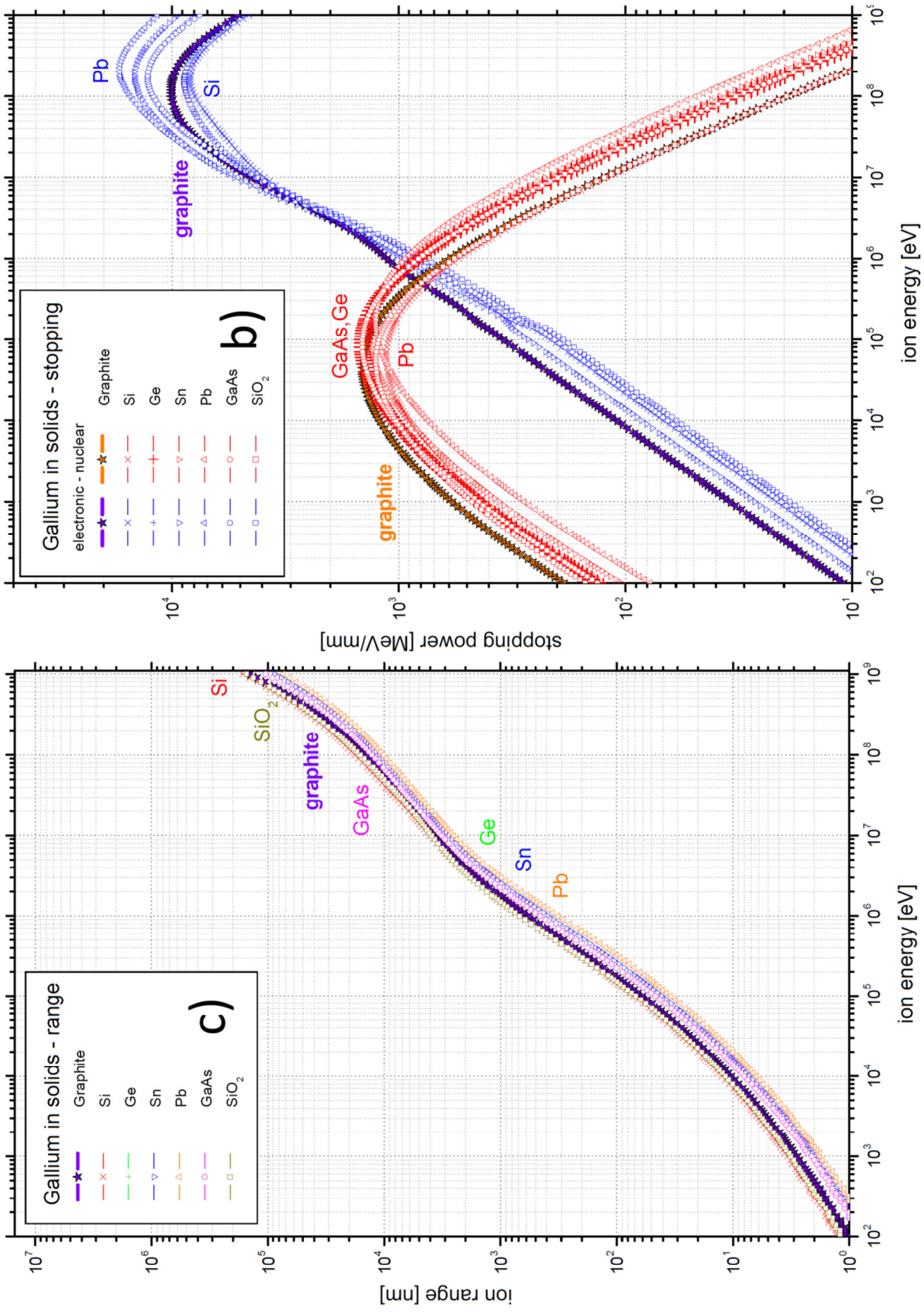
Gallium in solids - stopping
electronic - nuclear
Graphite
Si
Ge
Sn
Pb
GaAs
SiO2
b)
Pb
Si
graphite
GaAs,Ge
Pb
graphite
stopping power [MeV/mm]
ion energy [eV]
Gallium in solids - range
Graphite
Si
Ge
Sn
Pb
GaAs
SiO2
c)
Si
SiO2
graphite
GaAs
Ge
Sn
Pb
ion range [nm]
ion energy [eV]

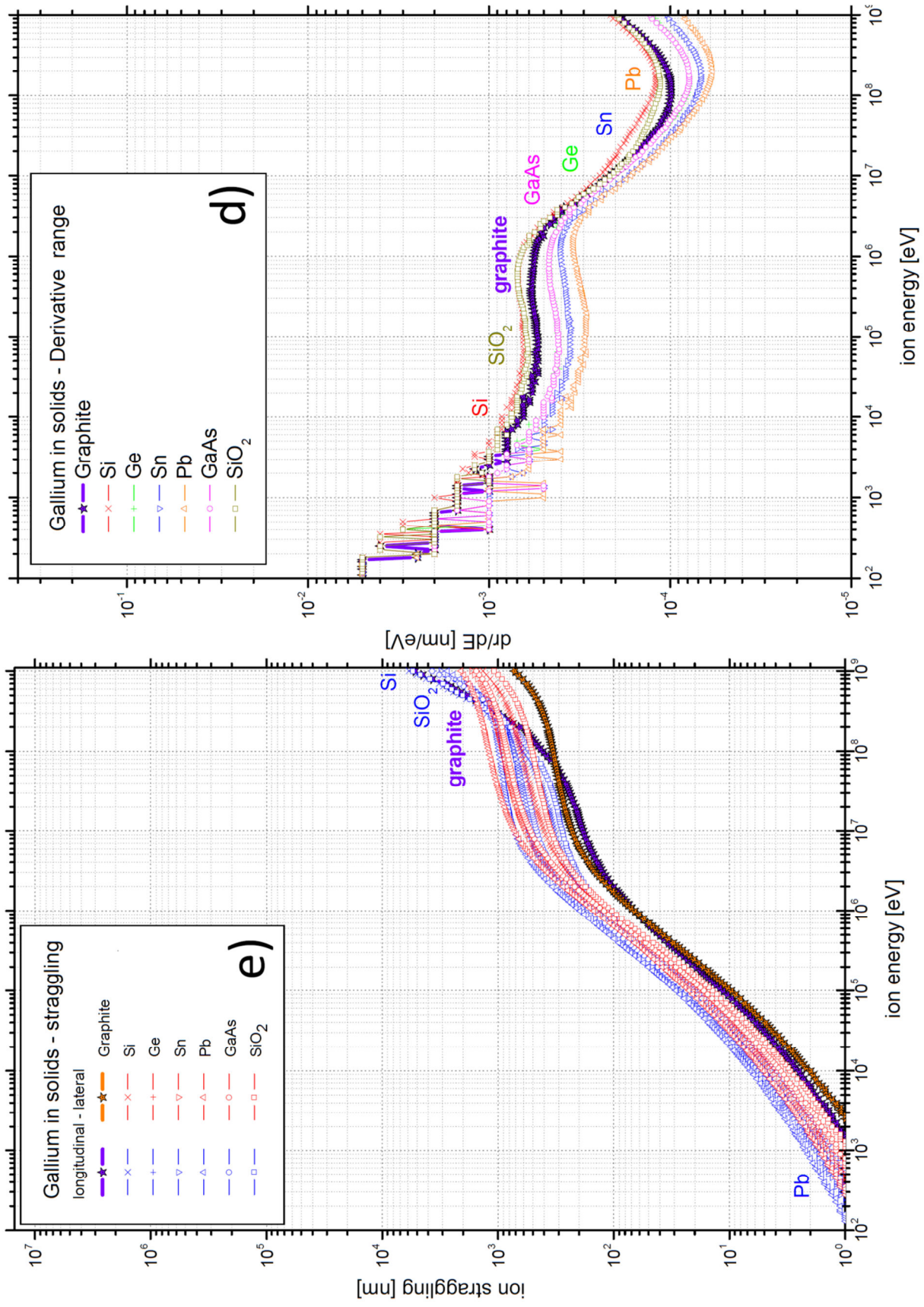

Figure 7: a)+b): Simulation results of the SRIM program on the electronic and nuclear stopping power for the impact of gallium ions into various solids. In b) the stopping power is shown in logarithmic scale. c)-e) Calculated ion range, the derivative of the ion range and the ion straggling for the impact of gallium ions into various solids.

Like all plots show, the variation of the electronic and stopping power, the ion range and the straggling is less for varying the solid material than varying the ion material. The plots a) and b) of Figure 7 in comparison to plots a) and b) of Figure 5 show that the electronic and nuclear stopping power for various solids are relatively close one to another. Because the simulations included only the results for one ion material this statement will perhaps not be valid for other ion materials. As plots a) and b) show there is also no meaningful dependency between the solid material and the maximum stopping power value or the maximum stopping power shift presented in Figure 8.

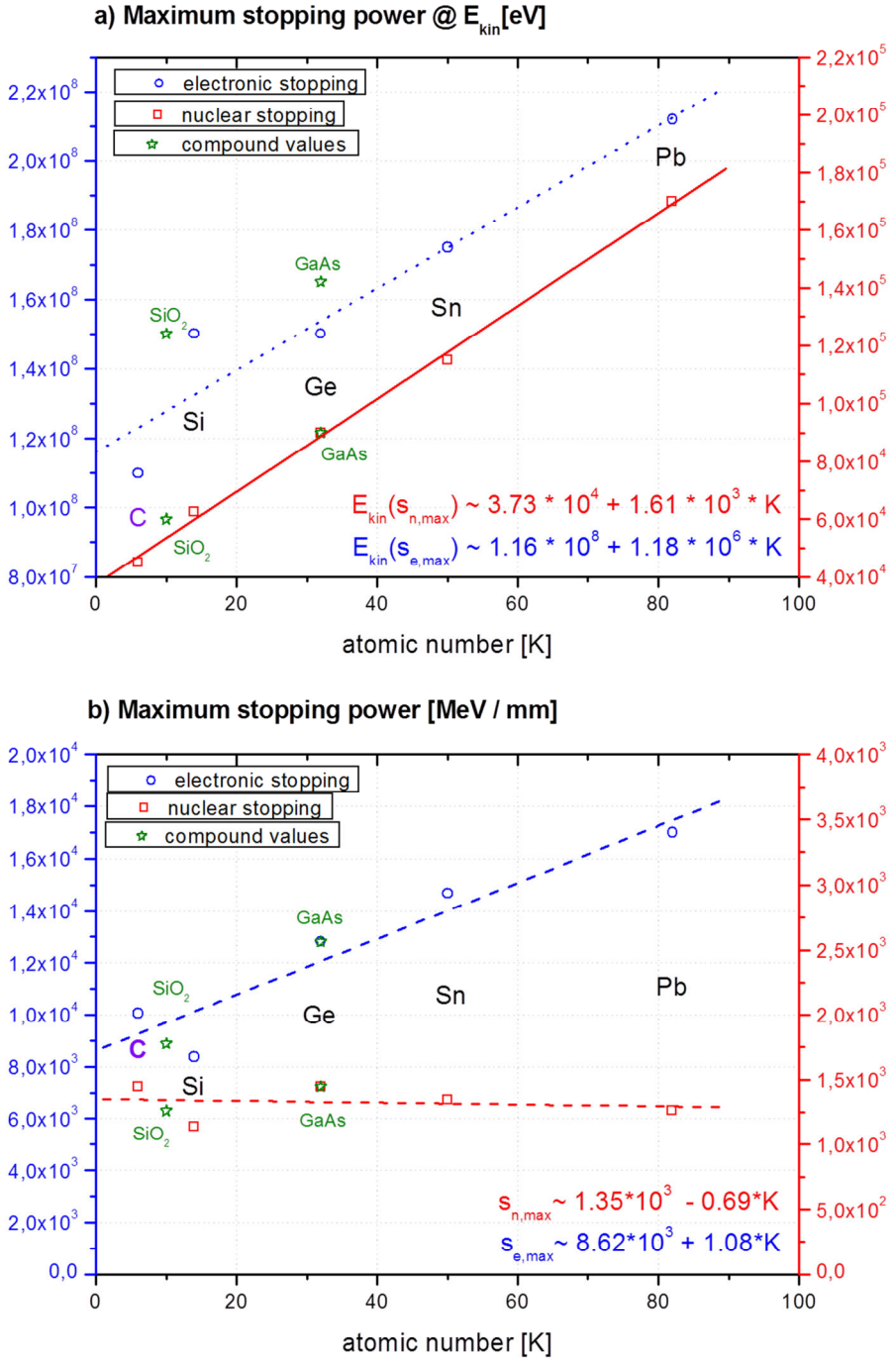

Figure 8: Maximum electronic and nuclear stopping at kinetic ion energies as a function of the ion atomic number a). In b) the value of the maximum electronic and nuclear stopping power is plotted as a function of the ion atomic number.

The plots show that the shift and the value of the stopping power rises as a function of the solid atomic number except for the nuclear stopping value (red line in b). The offset of the linear fits in a) and b) will probably be dependent on the solid material and will change for different materials.

The ion range and the derivative of the ion range, plots c) and d) of Figure 7, are nearly equal for various solid materials and different kinetic ion energies. Because the curves in c) and d) are nearly similar for the impact of gallium ions it can be assumed that the curves for another ion but various solid materials will also nearly be the same. Also the lateral and longitudinal straggling will only vary by one order of magnitude for different solid materials. In general the ion range and the straggling will not differ strongly for various solid materials.

Summarized, the used ion material in ion beam lithography strongly influences the ion range and the ion distribution, while the ion range and distribution will not change strongly for different solid materials.

It is important to mention that there is a difference between the calculated SRIM data and real measurement. In order to identify deviations between experiment and simulation a database with lots of experimental data is accessible on the programmers' homepage [63]. An overview of the impact of ions in carbon is shown in the following figure [64]. The figure shows the stopping power in the kinetic ion energy range of 1keV-100MeV. All plots are normed on aluminium. On the programmers' homepage there is no further reference to the normalisation on aluminium. Generally, the plots in the figure give a rough overview about the accuracy between SRIM and experiments.

The upper plot shows a good agreement for the nuclear stopping simulations with experimental data. In the lower plot a mean error of 6.7% for the ion impact into a carbon solid has been calculated. Depending on the ion material the deviation between experiment and simulation can be high.

There are several reasons for the deviation. Although, newer version of SRIM(TRIM) include corrections concerning the bonds between the atoms in solids, not all features of the lattice structure, especially the defect sites and the solid surface as well as impurities, are taken into account. Additionally, the impact of the ions is considered separately. After some ions have been implanted into the solid the next incident ions have to interact with a slightly deformed or changed solid concerning the atom arrangement and the implanted ions. The ion beam is assumed to be ideal. This means that there is neither a kinetic ion energy distribution nor a real ion beam diameter.

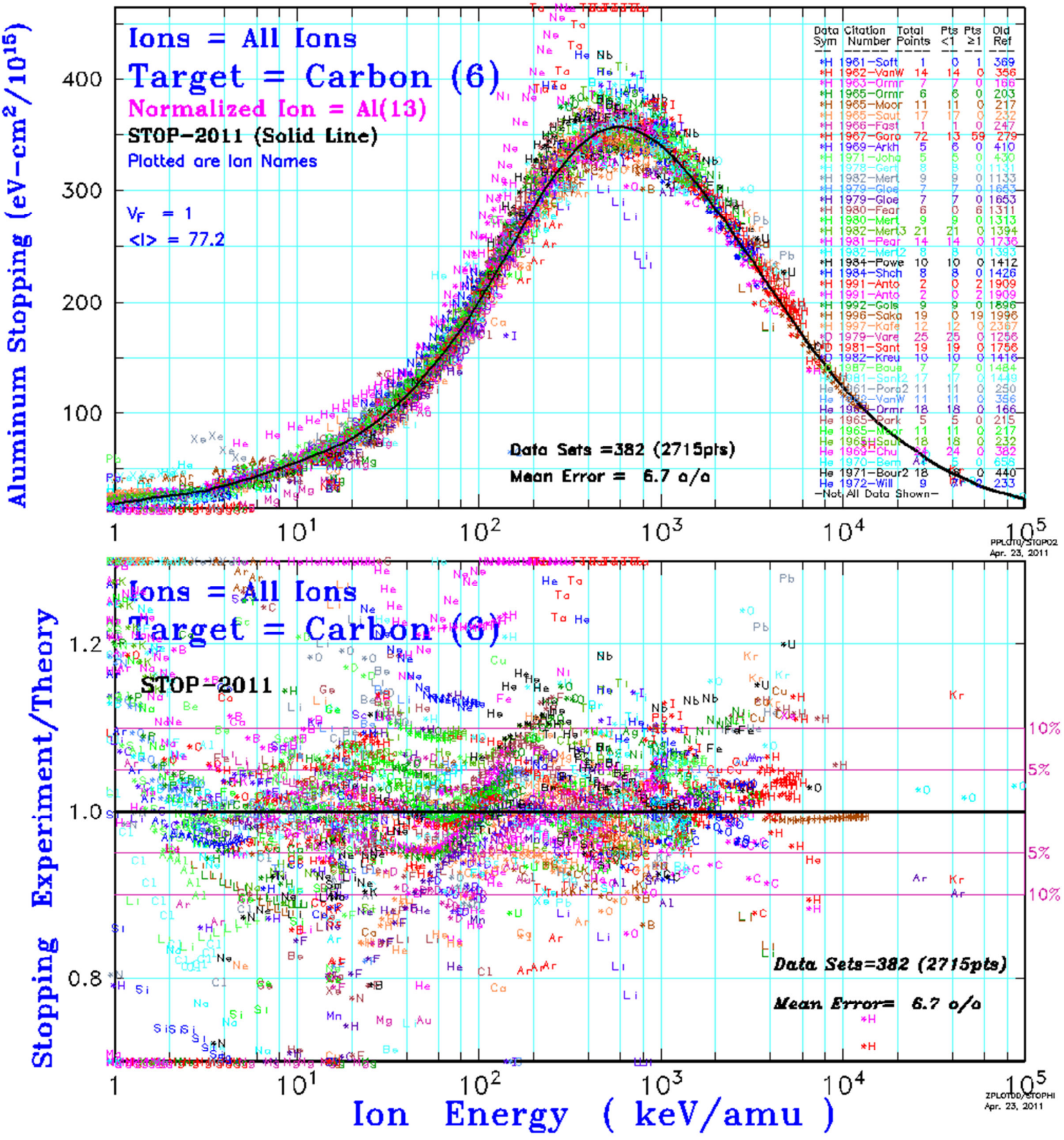

Figure 9: Comparison of SRIM simulations with experimental data [64]. The upper plot shows the simulated data normed on aluminium. Additionally, experimental data for many other ions is shown. The bottom plot shows the deviation of experimental and theoretical (simulated) data.

2.6.2 TRIM – Transport of Ions in Matter

With the TRIM program the transport and the trajectories of ions in solids can be simulated. Lattice atoms that have been removed from their lattice position due to an ion-atom collision are called recoils and can remove other lattice atoms at a sufficiently high energy transfer so that collision cascades can be initiated. By the removal of a lattice atom a lattice defect or a so-called vacancy is created. If recoils are completely removed from the solid the solid material becomes sputtered and cavities occur. The sputter process is also called "milling" in literature. The simulations of the ion and recoil trajectories are calculated dynamically in the TRIM simulation. The ion impacts are simulated one after the other. The implanted ions are not taken into account if a subsequent ion impact is simulated. For the calculation of the interaction process either a full damage cascade simulation or a speed improved Kinchin-Pease-analytic-method, which is described in references [65], [66], [67] and that only calculates the ion trajectories, can be chosen. The collisions are performed using a Monte-Carlo-simulation [68]. For the calculation of composite materials additional calculation methods were implemented based on reference [61] where also bonds between atoms were taken into account.

After an interaction process an ion with an initial kinetic energy of E_1 loses a part of its energy ΔE_1 and continues to move with the reduced kinetic energy E_2. There exists a so-called displacement energy E_d for lattice atoms which corresponds to the energy necessary to remove or displace a lattice atom. The surface binding energy E_b is the energy that has to be applied in order to remove a lattice atom from the solid. If the energy transfer to a lattice atom is greater than the displacement energy $\Delta E_1 > E_d$ the atom is removed from its lattice position. When the kinetic ion energy becomes smaller than the displacement energy E_d after the collision, the ion remains at the lattice site of the removed atom and loses its energy by lattice vibrations or phonons. But if, additionally, the energy of the removed atom is too small to leave its lattice site the ion occupies an interstitial position in the solid which leads to local lattice deformation. In this case, the energy of the ion and the atom is converted into phonons. A sputter effect is initialized when the energy of the incident ion E_1 is larger than the surface binding energy E_b of a lattice atoms and the fly path of the displaced or removed atom leads to a fully remove of the atom out of the solid. First, as discussed for the SRIM simulation, the necessary calculation parameters have to be set manually or they have to be imported from an internal database. Additionally to the element name, the atomic number, the atomic mass, the kinetic ion energy, the amount of impacting ions and their impact angle relative to the solid surface have to be entered. Also solid relevant parameters have to be set or imported. These parameters are the element name, their atomic number, the atomic weight, the solid density and the solid thickness. For compound materials the compound correction for calculations has to be imported. In addition, the solid can be built up from different layers with a specific thickness. The layers are stacked one on another and are simulated as ideal flat and infinitely extended. Furthermore, the state of matter for each layer should be established concerning solid or gas phase.

The dynamic calculation of the collision cascades as well as the ion trajectories happen along the x-y-z-axes in which the x-axis is perpendicular to the solid surface and is the flight direction of the ions. Besides the assessment of collision cascades on the x-y-, x-z- and y-z-planes other calculations or options can be set. These are the range distribution, the nuclear-recoil distribution, the lateral range distribution the ionization distribution, the phonon distribution the recoil energy distribution the collision distribution and the sputtering distribution. The simulation data of each calculation can be saved separately. Additionally, there are more parameters that can be calculated during the dynamic simulation. Apart from the lateral and longitudinal ranges a radial range is introduced in the TRIM simulation. The ranges and the square root of the variances, the straggling, are defined as reported in reference [69].

longitudinal range

$$R_p = \frac{\sum_{i=1}^{n} x_i}{n}$$

lateral range

$$R_y = \frac{\sum_{i=1}^{n} |y_i|}{n} \tag{24}$$

radial range

$$R_r = \frac{\sum_{i=1}^{n} \sqrt{y_i^2 + z_i^2}}{n}$$

longitudinal straggling

$$\sigma_p = \sqrt{\frac{\sum_{i=1}^{n} x_i^2}{n} - {R_p}^2}$$

lateral straggling

$$\sigma_y = \sqrt{\frac{\sum_{i=1}^{n} [(|y_i| + |z_i|)/2]^2}{n}} \tag{25}$$

radial straggling

$$\sigma_r = \sqrt{\frac{\sum_{i=1}^{n} y_i^2 + z_i^2}{n} - {R_r}^2}$$

Furthermore, the energy percentage distribution of the total energy into ionization, cavity production and phonon excitation by phonons and recoils is calculated as well as the sputtering yield in [atoms/ion] and the cavity production per ion. The simulations were carried out in the energy range of the nuclear stopping which constitutes the main effect in ion beam lithography. For the impact of 5000 ions with a kinetic energy of $E_{kin} = 40keV$ in graphite with the density of $\rho = 2.26\ g/cm^3$, the binding energy of $E_b = 7.41\ eV$ and the displacement energy of $E_d = 28eV$ the simulations were performed and the results for different ions in a graphite solid were listed in Figure 10. The red coloured lines correspond to ion trajectories while green coloured lines correspond to atom trajectories. In the following figure the parameters obtained from the TRIM simulations are listed. They are the range distribution of ions and recoils lateral longitudinal and radial and also the percentage distribution of the total ion or recoil energy for ionization processes cavity creation and phonon excitation. The values in the last two rows show how many lattice atoms are sputtered per incident ion and how many cavities are created per ion.

	ion stats	longitudinal	lateral	radial		energy loss	ionisation	vacancies	phonons		sputtering [atoms/ion]	Vacancies per ion
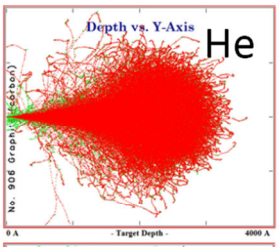	range [nm]	241.3	40.8	63.5		ions [%]	88.25	0.15	1.63		0.010	55.6
	straggle [nm]	40.9	51.2	33.5		recoil [%]	3.23	0.26	6.49			
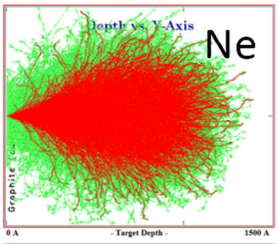	range [nm]	70.7	14.7	22.8		ions [%]	32.52	0.39	2.22		0.422	313.4
	straggle [nm]	21.9	18.7	12.7		recoil [%]	26.06	1.92	36.88			
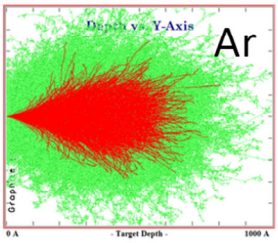	range [nm]	37.8	6.5	10.3		ions [%]	23.50	0.39	1.83		0.979	354.7
	straggle [nm]	10.8	8.2	5.6		recoil [%]	30.29	2.24	41.75			
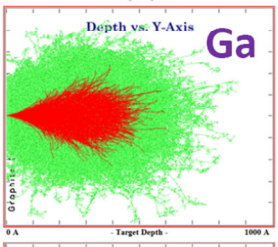	range [nm]	29.5	4.5	7.0		ions [%]	10.23	0.46	1.78		1.423	427.3
	straggle [nm]	7.4	5.6	3.8		recoil [%]	34.82	2.70	50.01			
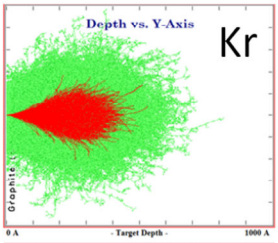	range [nm]	27.1	3.7	5.9		ions [%]	12.56	0.47	1.68		1.641	423.8
	straggle [nm]	6.0	4.7	3.2		recoil [%]	33.19	2.67	49.43			
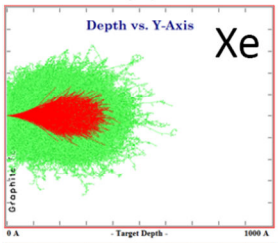	range [nm]	25.5	3.1	4.8		ions [%]	10.29	0.55	1.53		1.845	455.0
	straggle [nm]	4.3	3.8	2.5		recoil [%]	32.24	2.83	52.56			
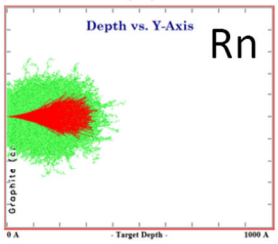	range [nm]	24.5	2.3	3.7		ions [%]	14.94	0.64	1.13		2.133	457.3
	straggle [nm]	2.8	2.9	1.9		recoil [%]	28.42	2.77	52.11			

Figure 10: TRIM simulation results on the impact of different ions with a kinetic energy of 40keV into a graphite solid. The figures show the trajectories of the ions (red) and the recoils (green). In the table the parameters obtained from the simulation such as the range, the energy distribution and the defect creation are shown. Collision figures for He and Ne were scaled differently. He: 400·400nm², Ne: 150·150nm², all others: 100·100nm².

While light elements only produce a few recoils through collision processes the ratio of ions to recoils increases for heavier elements. The figures show a decrease of the ion range for increasingly heavier ions that has already been seen in the SRIM simulations. In addition to the SRIM simulations TRIM can show that the most profound changes of the graphite lattice in deeper regions are mainly caused by ions for light-ion impact and by recoils for heavy-ion impact.

The TRIM simulation additionally shows that the width of the generated structure depends on the ion and recoil distribution in the solid and not only on the beam focus. The structure width in deeper regions is wider for light-ion impact than near the surface while the structure width for heavy-ion impact is constant near the surface and in deeper regions.

The longitudinal, lateral and radial ion range decreases with increasing ion atomic number. While for elements heavier than gallium the ranges nearly stay constant, the main range decrease happens for light ions or rather for helium to argon. For a kinetic ion energy of 40keV the longitudinal range of ions heavier than argon is about 25-40nm. Taking in account the recoil distribution the structure depth is 25-90nm. The lateral and radial width of the structures depends on the ion and recoil scattering. Although, the values for the lateral and radial ranges are small the resulting structure width in y- and z- direction will be much higher due to the recoil range especially for heavy incident ions. The structure width will be about three times higher than the values for the lateral and radial ion ranges. Also the straggling of the longitudinal, lateral and radial ion ranges decrease for increasing heavier incident ions.

For the energy transfer of incident ions and recoils into ionization energy, cavity production and phonon excitation only a small part of the energy is spent for cavity production (0.5-3.5%), while most of the energy is transferred into ionization (35%-90%) and phonon excitation (8-55%). The cavity production increases with increasing heavier ions, as the last column shows. The produced cavities per ion rate rises up to about 450 for heavy ions. The important sputtering yield for the milling effect in the ion beam lithography is very small, so that only up to about 2 atoms can be sputtered per ion if the incident ion is heavier than Xenon.

In an additional simulation series the impact of 5000 gallium ions at a kinetic ion energy of 40keV into different solids was simulated. The results of the simulation series is presented in the following figure. All data is scaled by $100 \cdot 100 nm^2$.

	ion stats	longitudinal	lateral	radial		energy loss	ionisation	vacancies	phonons		sputtering [atoms/ion]	Vacancies per ion
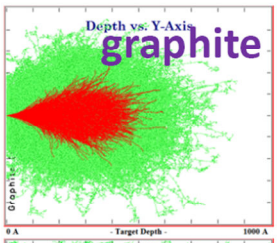	range [nm]	29.5	4.5	7.0		ions [%]	10.23	0.46	1.78		1.423	427.3
	straggle [nm]	7.4	5.6	3.8		recoil [%]	34.82	2.70	50.01			
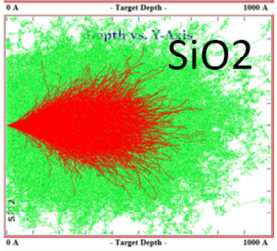	range [nm]	32.8	6.6	10.3		ions [%]	6.86	0.34	1.25		4.317	701.2
	straggle [nm]	10.7	8.4	5.9		recoil [%]	27.29	4.01	60.26		O: 3.3 Si: 1.0	
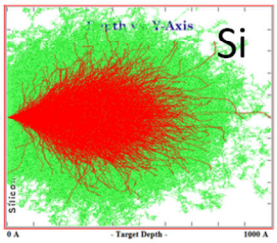	range [nm]	34.8	7.9	12.3		ions [%]	8.70	0.26	0.69		2.314	965.5
	straggle [nm]	12.9	10.1	7.3		recoil [%]	33.98	4.52	51.85			
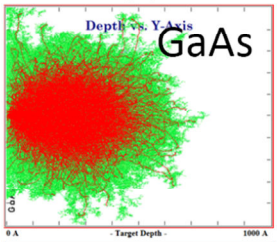	range [nm]	22.5	8.0	12.5		ions [%]	7.20	0.26	0.83		9.115	831.4
	straggle [nm]	11.9	10.5	7.8		recoil [%]	16.48	6.00	69.23		Ga:2.9 As: 6.3	
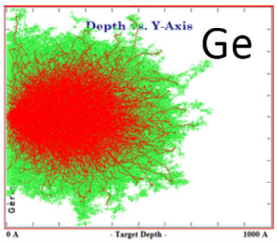	range [nm]	22.5	8.1	12.5		ions [%]	7.50	0.21	0.51		4.669	1422.9
	straggle [nm]	11.8	10.5	7.7		recoil [%]	16.75	6.96	68.07			
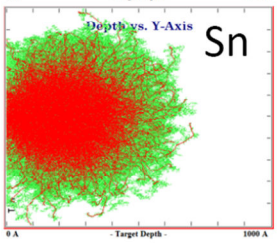	range [nm]	21.2	9.1	14.2		ions [%]	10.58	0.26	0.82		7.830	784.5
	straggle [nm]	12.1	11.8	8.6		recoil [%]	17.11	5.77	65.46			
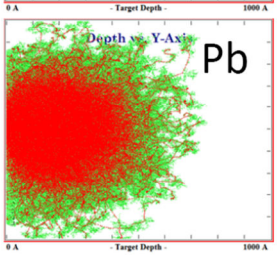	range [nm]	20.4	10.3	16.1		ions [%]	9.63	0.29	0.90		13.635	724.3
	straggle [nm]	12.3	13.2	9.5		recoil [%]	28.64	5.33	55.22			

Figure 11: TRIM simulations results on the impact of gallium ions with a kinetic energy of 40keV into different solids. The figures show the trajectories of the ions (red) and the recoils (green). In the table the parameters obtained from the simulation such as the range, the energy distribution and the defect creation are displayed. The scale of the data is 100·100nm².

Like in the SRIM simulation, the compound materials GaAs and SiO_2 were simulated in addition to pure solids.

As the SRIM simulation has already shown, the ion range distribution indicated by the red lines in the pictures is much more consistent after varying the solid material than the ion material. But the ion range does not decrease strictly with the solid material as the values for silicon and graphite show. Nevertheless, the scattering of the incident ions varies with the solid material especially near the sample surface. The ion distribution becomes more spherical with increasing heavier solid material. The recoil range decreases for heavy solid materials due to the mass of the recoils. Generally, the ion and recoil distribution is not dependent on the solid material. It seems that the lattice atom arrangement (graphite <-> diamond) has an important effect on the ion and recoil distribution. The distribution will then also be different for compound materials.

Although, the ion and recoil distribution is affected by the solid material, the longitudinal, lateral and radial ranges do not differ as strong as by varying the ion material. The simulations show a narrow longitudinal range distribution between 20-35nm. In average, the longitudinal ion range slightly decreases with increasing heavier solid material. On the other hand the lateral and radial ranges slightly increase with the mass of the solid atoms.

While most of the system energy is still spent on ionisation (24-45%) and phonon excitation (52-70%), a much higher part of the energy is spent on vacancy production (3-7%) especially for heavy solids. The larger vacancy production rate can also be obtained from the last column. One ion can produce up to 1423 vacancies for germanium solids. Also the sputtering yield increases for heavy solid atoms to a value of 13.6 atoms per ion for the impact of gallium ions into a lead solid at a kinetic ion energy of 40keV.

Best sputter results can be assumed for the impact of heavy ions into heavy solid materials. The structure width will decrease with increasing heavier ions. Both facts are important for a controlled structuring process of nano and micro structures.

It is important to remark that the TRIM simulation does not take into account a deformed solid after several ions have been implanted into the solid. Every new ion impact is simulated as the solid would be in its initial ground state. After the solid has been irradiated with a high-dose of ions the destruction and deformation of the solid lattice should be high enough, so that the most lattice atom bonds will be broken or changed and that less energy is needed to displace or even sputter lattice atoms. The effective sputter yield should rise for high-dose irradiation.

In the next subchapter the basics of the ion beam lithography will be presented briefly. The results of the SRIM and TRIM simulations will be taken into account for a short description of the irradiation process in ion beam lithography concerning a low-dose and a high-dose patterning. Additionally, in a short part, a theoretical improvement on the ion beam lithography will be discussed.

2.7 Basics and improvement of the ion beam lithography

In ion beam lithography ions are accelerated by their charge using an electric field. The accelerated ions can be focused onto a sample surface via electrical optics. Here, the beam width in the focus point can be a few nanometres in diameter depending on the technical design. The lithography must happen at near vacuum conditions, since the ions are scattered by molecules in the atmosphere. In order to produce a uniform structure in the nano or micro metre range the sample surface should be free of impurities.

Because the ion beam lithography is a serial structure production technique the focused beam has to be moved over the sample surface by a sample stage or by a deflection of the ion beam. On the basis of a structure plan the structures will be produced on the sample surface.

As already mentioned, the patterning process is mainly generated by sputtering or defect production processes. For ion beam lithography only the nuclear stopping energy range from keV to MeV is important. In this energy range the ion-solid interaction process mainly proceeds between ions and atoms. Structures of a few nanometres can be produced by ion beam lithography.

As the SRIM and TRIM simulations show the interaction processes, as well as the ion range, the ion and recoil distribution and the sputtering yield depend on the ion material. These factors directly influence the shape of the generated structures. In the case of ion implantation the ion and recoil distribution plays a major role. For high sputtering yields and compact structures heavy ions have to be used. The resulting structure width will be always a few nanometres bigger than the planned structure width due to the ion and recoil scattering. Also the average ion range will vary depending on the ion and solid material. The straggling describes the ion range distribution and equals the square root of the ion range variance.

Although, the choice of the sample material will optimize the form of the produced structures slightly and the sputtering yield strongly, in most cases the choice of the solid material is determined by the physical and electrical properties that have to be retained on the generated structures.

As the TRIM simulations show, the sputter yield is low but the experimental sputter yield should be higher after the solid has been irradiated with a high ion dose due to a rising deformation and destruction of the solid lattice. Nevertheless, a high amount of ions is needed in ion beam lithography to initialize sputter effects. For this reason, the irradiation process is separated into a low-dose and a high-dose irradiation. While for low ion doses mainly ions are implanted into the solid, at high ion doses the absolute sputter rate is high enough to create structures directly in a milling process. The low-dose and high-dose irradiation process is shown in the next figure schematically.

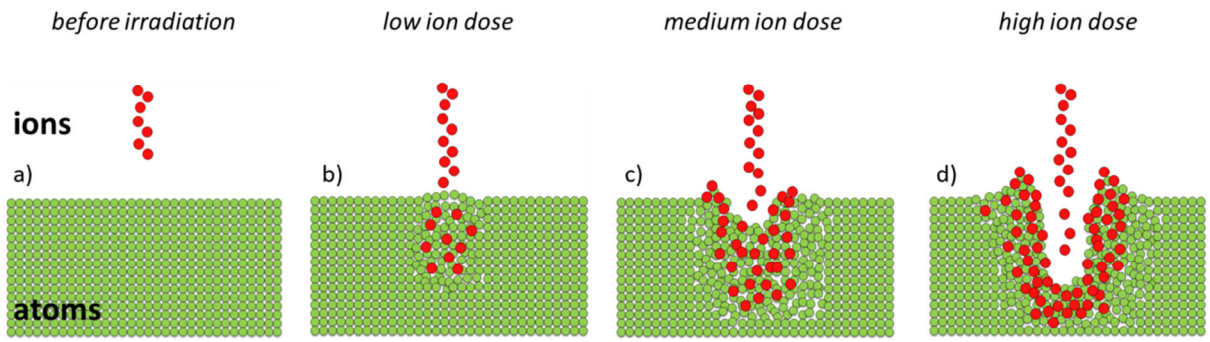

Figure 12: Schematic overview of the irradiation process at different ion doses. While for a low-dose irradiation b) mainly ions are implanted into the surface and the solid lattice becomes damaged and deformed, at higher doses the absolute sputter rate increases so that cavities are produced at the sample surface. For a high ion dose c) the cavity depth increases and many implanted ions and lattice atoms are sputtered. The edges go up due to a high ion and atom concentration in d).

The implantation of ions into the solids can be regarded as a kind of sample contamination. This is one of the biggest disadvantages of the ion beam lithography. Since the sputtering yield remains small at about 1-20 atoms per ion about as many ions are needed as atoms would be sputtered from the sample material. Already at low sputtering volumes $1.42 \cdot 10^9$ ions would be needed for the sputtering of a $500 \cdot 500 \cdot 50 nm^3$ volume. Certainly, many of the incident ions remain in the solid and only a few implanted ions would be sputtered by further incoming ions. As later experimental data will show the amount of implanted ions can be seen as accumulations at the cavity or structure edges. This border structure is heavily contaminated and destroyed by scattered ions and recoils. If the amount of edge destruction and contamination should be minimized it is necessary to use a low-dose irradiation process where structures will be generated in a subsequent oxidation process where mainly all destructed volumes will be removed from the solid surface. Since almost the entire defect area will be oxidized the purity and the lattice order of the created structures and edges will be very high. But for low-dose structuring the structure depth cannot be raised like for high-dose structuring using multiple structuring loops like later discussion in chapter 5 will show.

Besides the structure production by single charged ions, recent research deals with the interaction of highly charged ions with solids [29], [70], [71]. The high charge of the ions is equated with the potential energy of an ion. Due to the impact of a highly charged ion, the bonds of the lattice atoms are broken up by the emission of electrons from the charged ions, because the highly charged ions such as XE^{33+} have a very strong electron affinity. A single ion can break many bonds. The energy transfer of potential energy to the atoms is high enough to induce multiple sputter processes directly on the surface. The kinetic energy of the ions plays a minor role. In direct comparison, the sputtering yield by the use of highly charged ions is about two orders of magnitude larger than the sputtering yield of single charged ions. A suggestion would be to modify ion beam systems in the future to take advantage of the sputtering yield by the use of highly charged ions.

2.8 Chapter summary

For the production of nano and micro structures different lithography techniques are used where structures are produced by interaction processes with lattice atoms. The ion beam lithography is based on focusing ions on a sample surface. Ions are charged particles and can be accelerated in an electric field. The speed of accelerated ions will only become relativistic for kinetic ion energies of several MeV. The kinetic ion energy will be transferred in an interaction process to the solid.

The energy loss per path length in a solid is called stopping power. Here, a distinction is made between the electronic and the nuclear stopping power. The ions mainly interact by the Coulomb field of their charge with electrons and nuclei of the solid. While for energies in the MeV-GeV region the interaction of ions with solid electrons dominates with the associated processes such as ionization, radiation emission and scattering, ions with a kinetic energy of several keV mainly interact with lattice atoms of the solid. In this case lattice atoms can be displaced out of their lattice positions and will move as so-called recoils through the solid. At sufficiently high kinetic energy of the ions and recoils collision cascades can be initiated so that further atoms can be displaced or removed from the solid. If atoms are completely removed out of the solid a sputter process will start.

Based on the theoretical work on the stopping power programs such as SRIM and TRIM were created and can confirm most of the experimental data. The simulations show that the range and ion distribution in solids are mainly determined by the choice of the ion material where interaction processes are strongly dependent on the atomic number of the incident ions. There is only a slight dependency between the interaction processes and the atomic number of the solid material. Additionally, the bond type and the configuration of the solid material influence the interaction processes. The important process for the ion beam lithography is the interaction with lattice atoms. Because of the collision cascades and caused lattice damages the structured area is wider than the planned structure volume. Thus, the minimum feature size in ion beam lithography is limited to a minimum of a few nanometres. Generally, the sputtering yield by ion bombardment is very low. At low doses mainly ion implantation and lattice destruction occur. Only at high ion doses the absolute sputter rate will increase and material will be removed from the sample. But many incident ions will also contaminate the sample surface and especially the structured edges as experimental data shows. So, alternatively, a low-dose irradiation can be used to destroy or deform the solid lattice structure by the use of a few ions. The deformed or destroyed solid volume can be removed from the surface by a subsequent oxidation process. Both methods have advantages and disadvantages like a maximum possible structure or rather cavity depth. A higher sputtering yield could be achieved in future by the use of highly charged ions. The charge and energy exchange will mainly take place in the moment of the ion impact onto the surface for multiple charged ions. The resulting sputtering yield can be about hundred times larger in comparison to single charged ions.

3. Systems and equipment

The devices used in this project can be divided into the categories of structure production, structural analysis and electrical analysis. For the structure production an ion beam system of the Raith GmbH and an oxidation furnace were used among other devices. For the structural analysis mainly an atomic force microscope (AFM) was used. For the analysis on electrical structure properties, a four-point probe system was designed and started up. These devices and systems are described in detail in this chapter.

Besides the mentioned equipment other devices were used for structure production and analysis, which are only briefly described and can be classified in the equipment list as follows:

Structure production	**Applications**
3.1 – Ion beam facility - ionLiNE *Raith GmbH*	Structure production by gallium-ion bombardment with high or low ion doses
3.2 – Oxidation furnace *Gero GmbH*	Heater for structure production by oxidation with Ar-O_2 (2% O_2) mixed gas at 500°C
3.3 – Ozone-generator + UV-lamp *Dinies – Feinwerkt. + Elektronik*	Use of ozone as an oxidant for structure production at low temperatures of about 110°C
Structural analysis	**Applications**
3.4 – Atomic force microscope, AFM *TopoMetrix GmbH, Nanonics Ltd*	Quantitative structure analysis by mechanical scanning of surfaces using a tip
3.5 – Scanning tunnelling micr., STM *Omicron Nanotechnologie GmbH*	Quantitative structure analysis by electrical surface tracking of surfaces using a tip
3.6 – Scanning electron micr., SEM *Raith GmbH*	Qualitative and quantitative structure analysis by secondary electron detection
3.7 – Optical microscopes *Müller GmbH, Carl Zeiss AG*	Qualitative sample analysis and sample thickness measurements in the milli- and micrometre scale
Electrical analysis	**Applications**
3.8 – Four-point measuring device *Self-design*	Electrical analysis of generated structures or samples by four-point measurements
3.9 – SEM- four-point device *Omicron Nanotechnologie GmbH*	Combination of electron microscope and four-point measurement device for electrical analysis

Table 1: Overview of the used equipment in this project

Furthermore, the listed devices and systems for structure production and analysis in this work can be sorted according the operating scale in a scheme presented in the next figure.

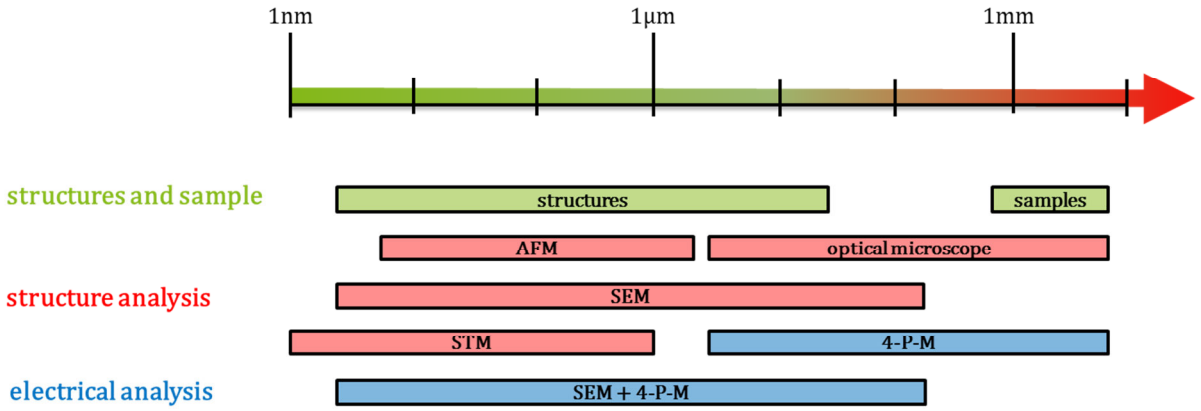

Figure 13: Approximated operating scale of the used devices and systems in comparison to the magnitude of the produced structure and sample size.

Nano- and micrometre sized structures were produced either directly by a milling process using high-dose irradiation or by low-dose irradiation and a subsequent oxidation process in an oxidation furnace at 500°C. Furthermore, attempts were made to establish the structure production at temperatures up to 110°C by using ozone as an oxidant.

For structure analysis most structures were examined with an AFM. For the examination of small structures an SEM or STM can be used for better resolution. Large structures can be measured by several AFM measurements or by optical microscopes. The SEM is also suitable for studying millimetre and micrometre size structures. While optical microscope and SEM images allow quantitative lateral information only qualitative information about the structure depth can be measured. For quantitative investigations concerning the structure depth an AFM or an STM have to be used.

For electrical measurements the structures have to be contacted by tips, which can apply an electrical current. The tips have to be free positionable on structures or sample surfaces for electrical properties determination. The self-designed four-point measuring device has an additional optical microscope and four micro manipulators included for the tip positioning. For even smaller, nanometre sized, structures an SEM-four-probe device of the Omicron Nanotechnology GmbH could be used for electrical investigations for a while.

The ionLiNE, the oxidation furnace, the AFM and the self-designed four-point-measuring device are described in detail in the next subchapters. These devices were mainly used during this project. Other used devices will be presented briefly.

3.1 The ion beam facility – ionLiNE

The ionLiNE of the Raith GmbH uses focused, single charged gallium ions to bombard a sample surface and to generate structures. The abbreviation for this machine is FIB-facility, which stands for “focused ion beams”. The system was designed by the Raith GmbH and their collaboration partners in the year 2001 and was then increasingly improved [72]. Since 2003 the system has been used in PhD and diploma projects by the faculty of physics of the Technische Universität Dortmund. A picture of the ionLiNE system is shown in the following figure.

Figure 14: Picture of the Raith GmbH ion beam facility [73]. Samples in the sample chamber can be bombarded by ions that are generated in the LMIS and focused with ion optic devices. The electronics and the vibration-damping system are located below the vacuum chamber. Additional electronics are in the system rack. Almost all tasks of the ionLiNE can be controlled with the computer.

The ion beam column, the most important component of the system, is located in a vacuum chamber, generates gallium ions and accelerates them as a focused ion beam with a few nanometres in diameter on the sample surface.

The sample is located in the main vacuum chamber or rather sample chamber. The chamber also includes an adjustable sample stage and two optical cameras for coarse positioning and an SEM for fine positioning of the sample. The SEM uses a detector to measure secondary electrons that are generated after the gallium ion irradiation on the sample surface.

The load lock is attached at the main chamber, where samples can be transferred in and out of the facility. The vacuum chamber and the load lock are pumped through an ion getter and a turbo molecular pump. The pressure in the main chamber will drop down to 10^{-7}mbar in operation mode.

The main electronics and the vibration damping systems are below the main chamber. Other electronic components, especially for the patterning processes, are in the system rack. The system operation can be controlled by a computer and a custom designed software. Important aspects concerning the ion beam facility are described in the following subchapters.

3.1.1 Ion beam generation

For the ion beam generation an LMIS, liquid metal ion source, is used [74], [75], [76]. Liquid metal is placed in a strong electric field. Because of the balance between surface tension and electrostatic forces a small cone-shaped metal tip is formed, where ion generation and emission is proceeded. Because of a small emission area when the liquid metal is placed at the needlepoint the generated ions can be accelerated and focused uniformly. The cone-shaped tip is called Taylor-Gilbert-Cone. It is named by G. I. Taylor and W. Gilbert that investigated the cone formation in their experimental and theoretical work [77], [78]. At the Taylor-Gilbert-Cone liquid metal flows due to capillary forces linear with the ion emission to the tip end so that ions can constantly be generated.

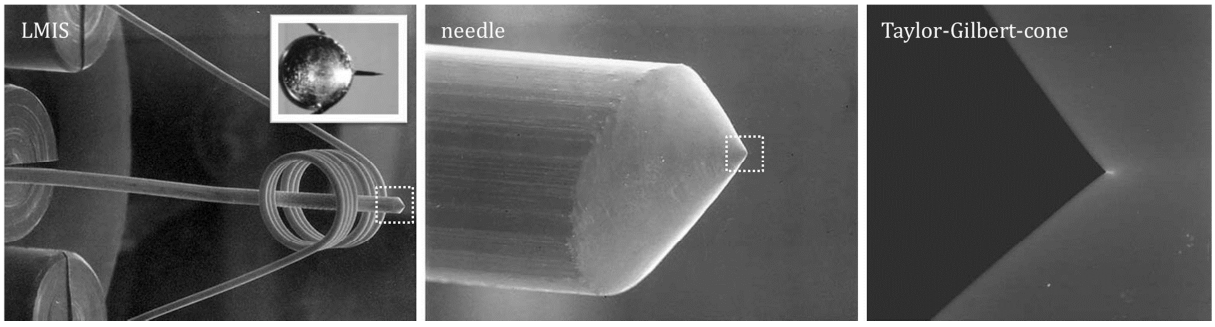

Figure 15: The LMIS [75]. A coiled wire is wetted with a liquid metal. The liquid metal is attracted by capillary forces to the tip end of a needle. Under the influence of an electric field a cone-shaped tip end is formed where ion generation and emission is proceeded.

An important point while using the LMIS is the liquefaction of the used metal. The heating process can worsen the vacuum conditions due to outgassing material. Therefore, many materials have been investigated for their use in the LMIS like for example presented in reference [79].

The advantage of gallium is a low melting temperature of 29.76°C, so that a heating process becomes almost unnecessary. In addition, gallium becomes mainly single charged in the LMIS so that most of the gallium ions will have the same kinetic energy after acceleration.

3.1.2 Ion beam focussing

The ions generated in the LMIS are accelerated and focused in the ion optics.

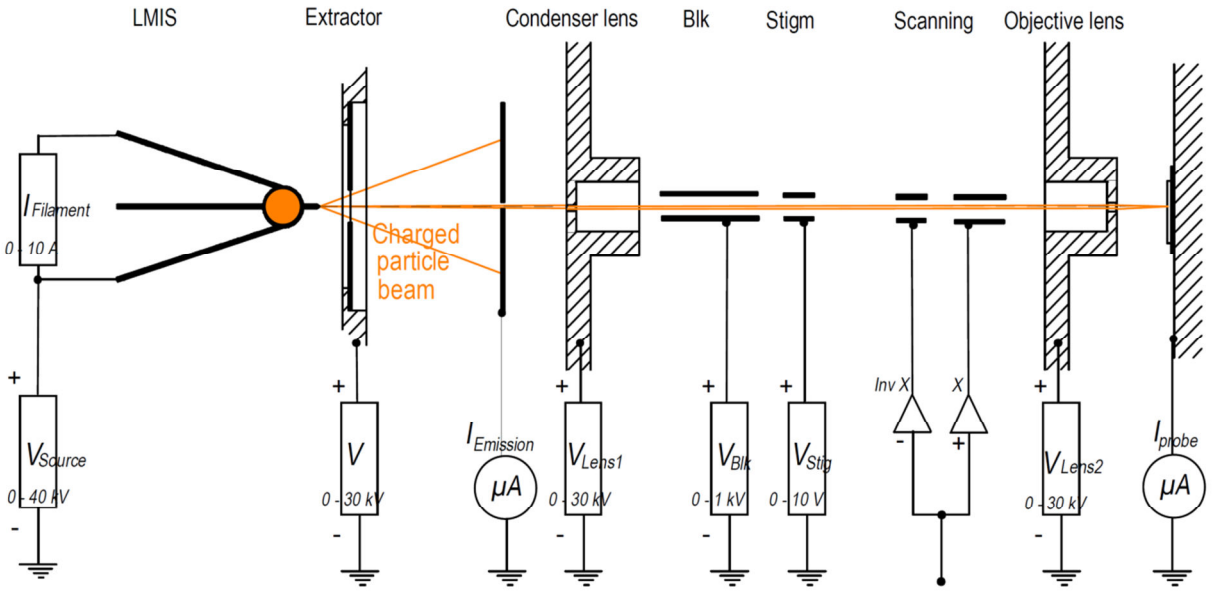

Figure 16: Ion optics in an ion beam facility [80]. The generated ions are accelerated by the extractor and focused by a lens and an aperture system onto the sample surface.

The acceleration of the LMIS ions happens via a voltage applied at the extractor. This component primarily controls the kinetic ion energy.

Since the ion beam diverges after passing the extractor, an aperture is included in the lens system to reduce the ion beam diameter. For this an orifice of 5-1000µm is located in the aperture centre. Ions that do not pass the orifice will be absorbed by the aperture. Using a small aperture with a small orifice the beam focus will increase while the ion intensity will decrease after passing the aperture. Small apertures are required for high resolution beam focussing. Since the aperture is continuously bombarded with ions an orifice enlargement or additional orifices appear on the aperture after excessive use. The aperture needs to be replaced regularly. Typical ion currents are in the range of 12-4000pA depending on the aperture size.

The next ion optics element is the condenser lens after the aperture that is used for beam guidance.

The blanker will turn away or blank the ion beam when the actual sample surface area should not be structured. Technically blanking the ion beam is more useful than the complete shutdown of the ion beam, since the shutdown takes several minutes in time but the blanking happens in milliseconds.

The stigmator corrects the astigmatism of the lens system and so the different foci for ions that move along the x-y-beam axis compared to the ions on the z-beam axis direction. The stigmator voltage settings can change the foci along the x-y- and the z-direction separately so that all beam ions will have the same focus.

The ion beam can be deflected along the x- and y-direction on the sample surface by the scanning device. The maximum deflection of the ion beam is technically limited to a 200x200µm² write field to minimize the incident angle and to exclude angular structure formation.

The objective lens focuses the ion beam before the ions reach the sample. The distance between the last lens and the sample surface is called the working distance and can be regulated by lowering or lifting the sample stage.

For surface patterning the ion beam has to be moved along the sample surface. In this context, two possibilities have been technically realized in the system. On the one hand the sample stage can be moved with up to 2nm accuracy using laser interferometer technology in x- and y-direction. Because the ion beam is fixed this mode is called the fixed beam moving stage (FBMS) mode. On the other hand a combination of beam deflection and sample stage movement can be used. After structures have been produced in a write field, the sample stage will move until the ion beam can expose another write field. The mode can be set manually in the ionLiNE software. During this project exclusively the second mode was used, a combination of beam deflection and sample stage movement.

It is important to notice that the beam is not homogeneous within the ion distribution. The ion intensity decreases rapidly at the outer ion beam radius. The ion distribution is similar to a Gaussian distribution. Depending on the used aperture the beam profile will additionally be changed [81].

3.1.3 Structuring methods and parameters

The structure plan is created by the system software. With this software, the so-called GDSII software, structures can be planned. They are composed of dots, lines and areas.

For the production of dots the ion beam is focused on a surface position for a pre-set time called the dwell time t_{dwell}. When the dot is created the ion beam will be deflected until the beam is positioned at another dot position.

If lines should be created several dots are produced along a line. The distance between the dots is called the step size d_{step}. The beam is moving while line writing from one dot to another and remains on every dot position for a duration time according the dwell time. In contrast to dot writing, the beam will not be blanked in line writing mode.

Areas are also produced by a variety of dots with constant distances between the dots along the x- and y-direction. In this context, a step size has to be set along the y-direction. It is beneficial to use the same step size along the x- and y-direction to obtain homogeneous dose distributions. Areas are produced by lines that are produced one after the other. Here, all lines can be generated either along the x-direction from “left” to

“right” or every second line will be produced from “right” to “left”. The second method will slightly decrease the irradiation as the ion beam has not to be moved back. Because the beam will not be blanked when changing a line less additional ions will be implanted by the second mode.

With the GDSII software various structures can be programmed. The entire writing area will be divided into several write fields. First, all structures within a write field will be produced. If a line or an area is located in more than one write field, the lines or areas will be divided, so that only parts of them will be created in the current write field. If the FBMS option is active there are no write fields, so that the structures will be created fully one after the other.

The deposited amount of ions or rather the deposited ion dose is determined by the ion current and the dwell time. Because the ion current will stay constant during the irradiation process the deposited ion dose is exclusively controlled by the dwell time. The dot-dose is the product of the ion current and the dwell time.

$$D_{dot} = I \cdot t_{dwell} \tag{26}$$

For line writing the step size is included in the formula.

$$D_{line} = \frac{D_{dot}}{d_{step}} = \frac{I \cdot t_{dwell}}{d_{step}} \tag{27}$$

The area dose is composed of the line-dose and the additional step size along the y-direction.

$$D_{area} = \frac{D_{line}}{d_{step2}} = \frac{I \cdot t_{dwell}}{d_{step} \cdot d_{step2}} \tag{28}$$

The amount of incident ions can be calculated by substituting the ion current with the charge transfer dQ per irradiation time dt. The charge transfer can be identified as the product of the amount of single loaded ions n multiplied with the elementary charge e. The dot, line and area dose can then be given in units of the number of incident ions by substituting

$$I \cdot t_{dwell} = \frac{dQ}{dt} \cdot t_{dwell} = \frac{n \cdot e}{t_{dwell}} \cdot t_{dwell} = n \cdot e \quad . \tag{29}$$

After measuring the ion current the needed dot-, line- and area-dose have to be set using the GDSII software. The values are global for all structures that have to be generated. If single structures should be created with a different dose, an individual dose factor can be set in the structure options that act multiplicatively with the global dose. By a dose factor of 2, for example, twice as much ion dose will be deposited in structures by doubling the dwell time.

3.1.4 Beam adjustment and structuring procedure

After the sample has been transferred, the beam has been activated, the structure plan has been created and the structure parameters have been set, the beam has to be adjusted before the structuring process can be started.

For this, the ion beam is focused on a free surface position. Using a software command a test dot will be generated on the sample surface. With the use of the SEM the test dot can be observed and the beam adjustments can be fine-tuned. First, the working distance is varied until the contrast of the test dot in the SEM image is optimized. Then the stigmator settings are optimized to improve the SEM image. The aperture position in the system can be changed so that less ions are scattered at the aperture hole which leads to an improved ion focus. Under these optimized settings a new dot has to be generated that should be smaller in diameter. This procedure has to be repeated until the beam focus is optimized (small dot) and the ion beam profile becomes uniform (circular dots).

Furthermore, the movement accuracy of the sample stage has to be optimized by a stage movement calibration if the original focus position is not reached after moving away and back. After a forward and backward movement the offset can be many nanometres. This error leads to structural distortion when structures are located in various write fields. To perform the calibration a dot has to be produced first. The calibration starts by a software script where the stage moves several microns away and back to the original position. If the milled dot is displaced out of the centre of the SEM image a correction can be set manually. This procedure is repeated for negative and positive x- and y-directions in several cycles.

Per drag and drop the structure plans can be inserted in a so-called position list. This list contains additionally parameters, settings and special commands. With the start button the instructions in the position list will be executed and the structuring process will begin automatically.

3.2 The oxidation furnace

For a low-dose irradiation the structures are not produced by sputtering or milling the surface. Only ions become implanted into the sample that deform or destroy the local lattice arrangement of the solid. The structures will only be produced during a subsequent oxidation process that mainly occurs on irradiated areas. The oxidation can only be performed if the sample material is oxidizable and the density of lattice destruction is high enough.

Besides the direct oxidation of carbon with oxygen to carbon monoxide at temperatures above 1200°C, that can be described by the formula

$$O_2(g) + 2C \rightarrow 2CO(adsorbed) \rightarrow 2CO(gas) \quad , \tag{30}$$

theoretical and experimental investigations [82], [83] predict other reaction mechanisms. Here, a reaction site S_a with a high reaction probability η_1 and a reaction site S_b with a low reaction probability η_2 are taken into account. While an oxygen atom can directly oxidize the carbon to carbon monoxide at the reaction site S_a, the other oxygen atom will be adsorbed on the surface and diffuses to site S_b where it can oxidize another carbon atom as it is reported in reference [82].

$$O_2(g) + S_a \rightarrow \begin{cases} CO(ads) \rightarrow CO(g) + S_a \\ O(ads) + S_b \rightarrow CO(ads) \rightarrow CO(g) + S_a \text{ or } S_b \end{cases} \tag{31}$$

The reaction of oxygen and carbon to carbon monoxide is of two orders of magnitude higher than the reaction to carbon dioxide. For the oxidation process an oxidation furnace of the Gero GmbH was used, which is shown in the following figure.

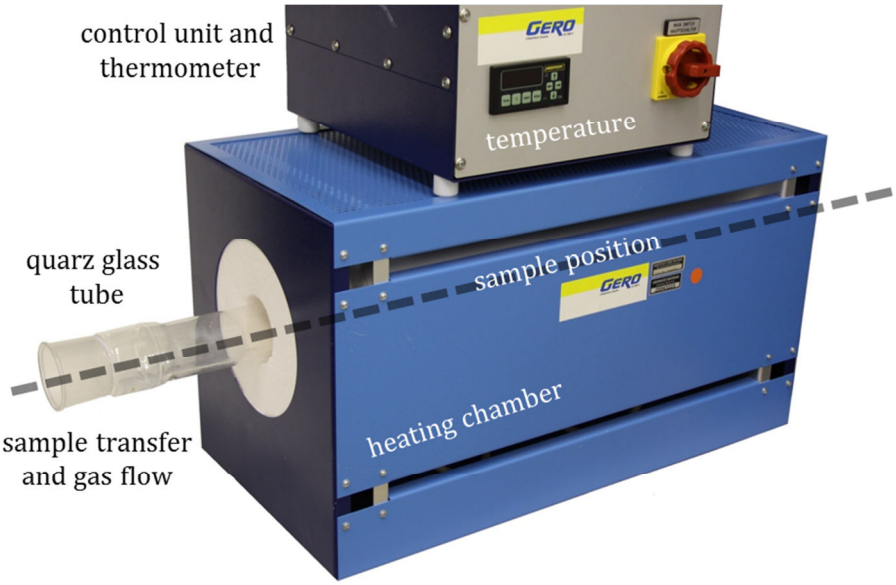

Figure 17: Image of the used oxidation furnace. The sample is placed in the centre of the glass tube. The furnace can heat samples up to 1200°C.

The oxygen mainly reacts with the defect areas and surface step edges. But also unstructured material apart from step edges will be slowly oxidized depending on the heating duration, the heating temperature and the used oxidation gas. For the oxidation an Ar-O_2 gas mixture with 2% oxygen was used.

3.2.1 Oxidation duration

The oxidation at defect sites or step edges can be described with an Arrhenius term presented, for example, in reference [84]. In this context, defect means surface points with missing lattice atoms. The oxidation process removes the graphite layer radially starting from a point defect. After a period of time t at a temperature T the point defect growth

results in a nano pit of a diameter D. Taking into account the activation energy E_a and the partial oxygen pressure p_{O_2} the pit diameter grows by [84]

$$D = C p_{O_2} t \cdot e^{-\frac{E_a}{RT}}. \tag{32}$$

The factor R is the gas constant and C is a function that describes the rate of the pit growth dependent on the defect density. For a graphite sample and an oxidation process within the basal planes, the function C equals $4 \cdot 10^3$nm mbar^{-1} for defect densities larger than 15/µm² [85]. The activation energy is $E_a = (127 \pm 3)$ kJ/mol [86]. For the Ar-O_2 gas mixture the partial oxygen pressure equals 20.265mbar. The nano pit diameter can now be calculated for different temperatures and oxidation times.

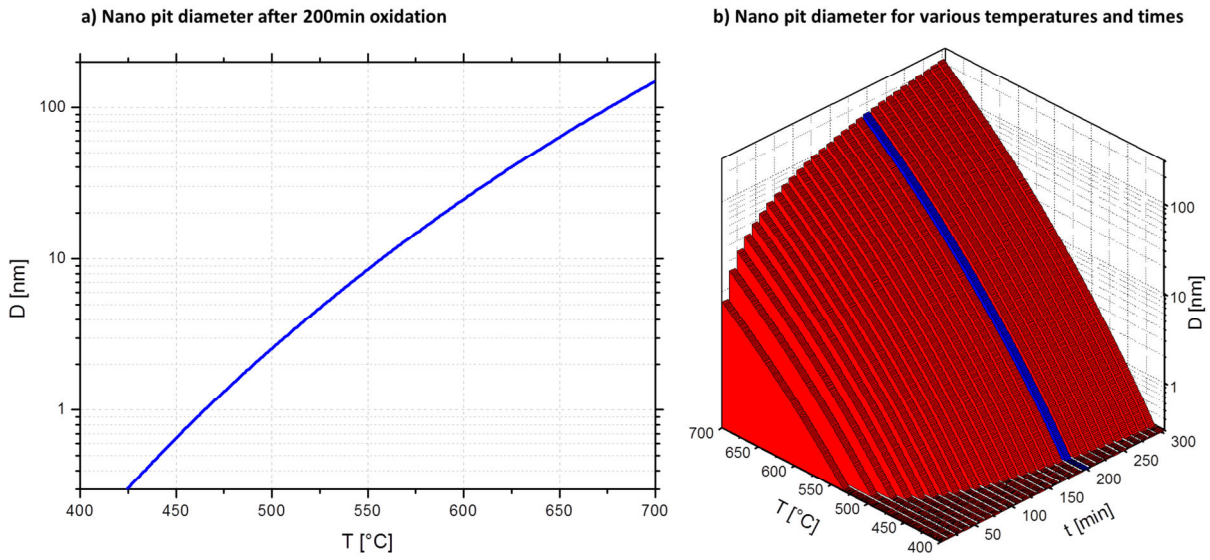

Figure 18: Nano pit diameter as a function of the temperature and the oxidation time assuming a monoatomic defect centre. a) The calculated diameter as a function of temperature after 200min heating in comparison to the pit diameter at different temperatures and heating times b).

The calculations refer to the oxidation of defect sites and step edges. The oxidation of irradiated areas runs parallel but faster. Ideally, the entire irradiated area should be oxidized, while the non-irradiated areas should not. The process duration and the heating temperature should be high enough to oxidize the irradiated material. The oxidation increases strongly with the temperature. On the other hand the temperature has to be low enough to not oxidize too much additional surface material. For that a oxidation time of 200min at 500°C was chosen where only 2.5nm additional edge material will be removed, as it is shown in Figure 18.

3.2.2 Oxidation procedure

Before the sample oxidation can be started, possible contaminations in the oxidation furnace have to be removed. For this the glass tube is heated without the sample to 1000°C to vaporize the contaminations. At the ends of the glass tube adapters can be

attached which are connected with gas bottles. While from one side of the tube nitrogen is inserted, the other side of the adapter contains a tube that leads to a water-filled wash bottle. During the heating process the nitrogen is passed through the tube so that vaporized contaminations will be blown into the water-filled wash bottle. The water-filled bottle prevents air to flow into the glass tube from one of the tube ends. During the heating process a sample holder and a small ceramic boat are heated, too, to clean them from contaminations.

When the glass tube has been heated up to 1000°C the heating process is stopped. With continuous nitrogen flow the glass tube centre has now to drop to 500°C before the sample can be inserted. For the sample transfer the adapter on the nitrogen side is removed and the sample is positioned in the ceramic boat at the centre of the glass tube. To minimize re-contaminations the sample transfer has to be done quickly.

To start the oxidation process the nitrogen is replaced by an argon-oxygen gas mixture with 2% oxygen. As mentioned before, the heating process will last 3h20min at 500°C and is checked regularly. After the heating process the sample will be removed from the oxidation furnace and the sample temperature will decrease rapidly so that the oxidation process will stop.

3.3 Ozone generator und ozone-lamp

At temperatures of 500°C heat sensitive samples can be destroyed in the oxidation furnace. One type of samples that will be destroyed is thin HOPG that is important for later electrical investigations and will be introduced in chapter 4.3.2. Therefore, an oxidation process was investigated to oxidize samples at much lower temperatures. In this case ozone, O_3, was used that is a strong oxidant so that structures should be produced at temperatures of about 110°C.

Since ozone is a highly reactive gas the investigation was carried out using an extractor hood. In principle, ozone is formed in the reaction of oxygen molecules at a molar reaction enthalpy of 286kJ by the reaction formula

$$3O_2 \rightarrow 2O_3 \quad . \tag{33}$$

The formation of ozone can be performed by gas discharge or by UV light absorption (λ<200nm) [87]. In this project an ozone generator and a UV lamp with emission wavelengths of λ=254nm and λ=185nm were used.

The ozone generator will produce and blow ozone over the sample surface or rather on the irradiated areas and the UV lamp will additionally produce ozone near the irradiated areas. For a higher reaction speed the sample was heated up to 110°C. This temperature does not destroy the mentioned thin HOPG samples that were used. A maximum tem-

perature of 110°C was determined in former experiments where the surface was observed at different temperatures with a high-resolution camera. The oxidation with ozone was performed in an aluminium case to protect the environment from harmful radiation and to increase the ozone concentration near the sample.

In several experiments samples were exposed under different ozone and temperature conditions. First, only the ozone generator was used. Second, the sample was heated additionally at different temperatures for various times. Third, the effect of the UV radiation by simultaneous heating of the sample was investigated. In a last experiment the samples were heated at 110°C, the UV lamp (13W lamp) was activated and the ozone generator produced 40 litres of ozone per hour for 6h.

3.4 Atomic force microscopy – AFM

In this project an atomic force microscope, AFM, was used to investigate the sample surface and structure topography. Besides the possibility to use an AFM of the Nanonics Ltd. at the Raith GmbH, an AFM of the TopoMetrix GmbH was used during the cooperation with the Department of Materials Engineering at the Technische Universität Dortmund. The AFM technique was developed by G. Binning, C. F. Quate and Ch. Gerber in 1985 [88] and has become a frequently used device for surface examination at the nano- and micrometre scale.

An atomic force microscope uses a nanometres thin tip to investigate the sample surface by the interaction of the tip with the sample surface. The tip is mounted on a so-called cantilever which deforms according to the attractive or repulsive forces between tip and surface. The tips can be bought with various modifications like special coatings or with different tip shapes depending on different applications. The used AFM tips bought at the NanoAndMore GmbH have an additional reflective aluminium coating at the cantilever backside and a sharp tip end with a diameter below 10nm.

The cantilever or rather tip is moved by piezoelectric crystals with an accuracy of a few nanometres. Areas of several square micrometres can be investigated. As mentioned before, the cantilever is deformed by the tip-surface interaction. The deformation can be detected by a laser system and will be registered by the electronics. This data can be used to calculate the surface topography of the scanned area. In the next figure a schematic overview of an AFM is shown.

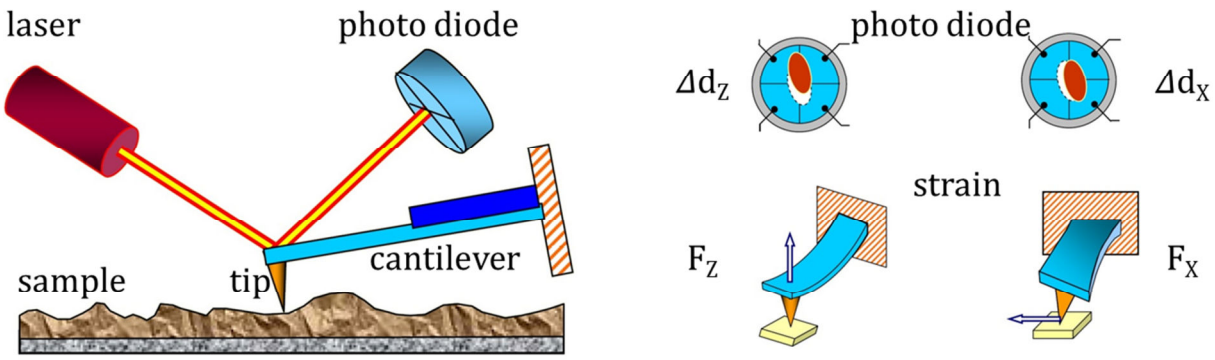

Figure 19: Schematic overview of an AFM [89]. While the tip is moved over the sample a photo diode can measure the beam deflection induced by the cantilever deformation. The sum of all scanned surface points can be used to calculate the surface topography of the investigated area.

3.4.1 AFM tips and cantilever

The AFM tip and the cantilever must fulfil certain requirements for the measurements in the nanometre scale. The cantilever itself consists mostly of silicon or silicon compounds such as silicon dioxide or silicon nitride. Some cantilevers are coated on the backside with reflective material like gold or aluminium to increase the laser light reflectivity.

The cantilever material determines the stiffness of the cantilever. The cantilever will be deformed when forces occur by bringing the tip close to the sample surface. The deflection or deformation is determined by the spring constant k_d and is proportional to the deformation force F_d as known from Hooke's law, where x is the deflection.

$$F_d(x) = k_d x \tag{34}$$

For special applications different cantilever types are needed where also the spring constant plays a major role. The tip end has to be sharp in order to obtain nanoscopic resolution. The tips are prepared by evaporation, irradiation and chemical or ion etching. The tip quality can be examined using an SEM like shown in the next figure.

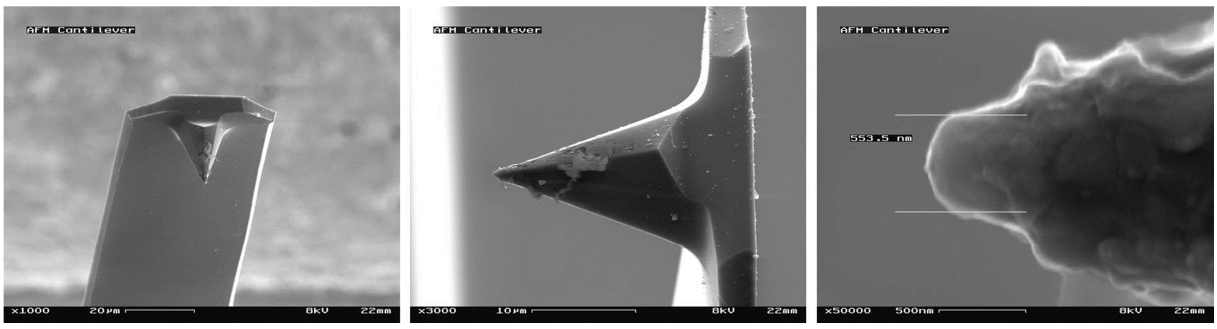

Figure 20: SEM images of an AFM tip [90]. The pyramid-shaped tip is mounted on a cantilever and has a tip end of a few nanometres in diameter. The geometry of the tip end determines the maximum possible resolution.

Depending on the tip shape some structure features cannot be investigated. Possible errors in measurements are shown schematically in the picture below.

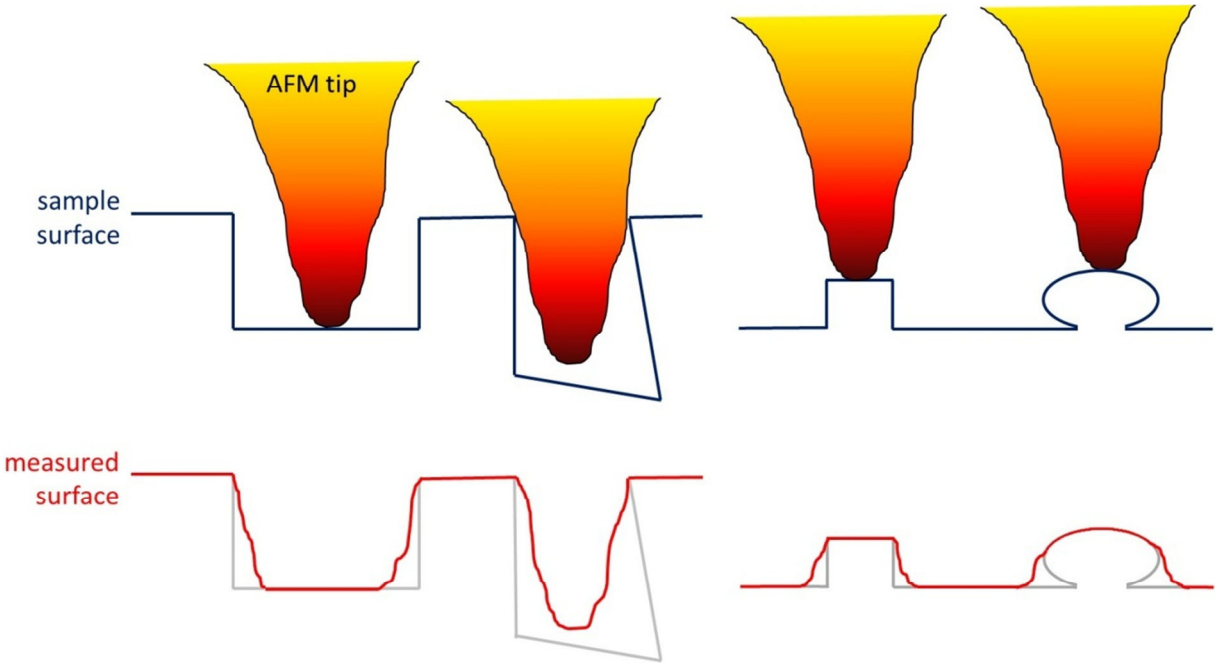

Figure 21: Possible differences between real and measured surface profiles.

While simple square structures can be investigated well, complex structure features in deeper regions cannot always be investigated. The width of nano pits can be determined by an evaluation of the upper structure edges. The structure depth can be measured if the tip reaches the bottom of the pit over a sufficiently large range. The structure depth cannot be determined if the tip does not reach the bottom of the cavity. Small, spherical or complex-shaped structures cannot be investigated well by AFM measurements.

For special applications the tips can be evaporated with gold or other conducting materials and are referred to as conductive AFM tips. Other special tips are diamond tips, molecule wetted tips, biological investigation tips or magnetic tips. Tips and cantilevers used in this project of the NanoAndMore GmbH are the Tap300Al-G.

3.4.2 Tip-sample interactions during AFM measurements

At distance of several nanometres between the tip and the sample surface mainly attractive forces occur while repulsive forces dominate after further approaching. These forces lead to the mentioned cantilever deformation and will be discussed in this subchapter.

The forces occur because of electrostatic, capillary and Van der Waals forces and also by the superposition of the electron wave functions of tip and sample atoms. While attractive forces mainly occur due to Van der Waals interaction, repulsive forces mainly occur

due to an electron wave function overlap of tip and surface electrons and because of the Pauli exclusion.

The Van der Waals interaction has a $1/r^6$ dependency where r is the tip-surface distance. It includes all inter- and intra-molecular interactions on permanent and induced dipoles and charge fluctuations. Van der Waals forces can be separated into dipole-dipole interactions, dipole-induced dipole forces and London's dispersion forces [91].

The superposition of the wave function or rather the Pauli exclusion leads to repulsive forces. Since the repulsion force is proportional to $1/r^{12}$ the entire force interaction can be qualitatively compared to a Lennard-Jones potential the resulting potential can be described by the formula [9]

$$U_r = \left(\frac{A}{r}\right)^{12} - \left(\frac{B}{r}\right)^{6} \quad . \tag{35}$$

The force can be calculated by –dU/dR. The dependency between the distance r and the force is shown in the next figure.

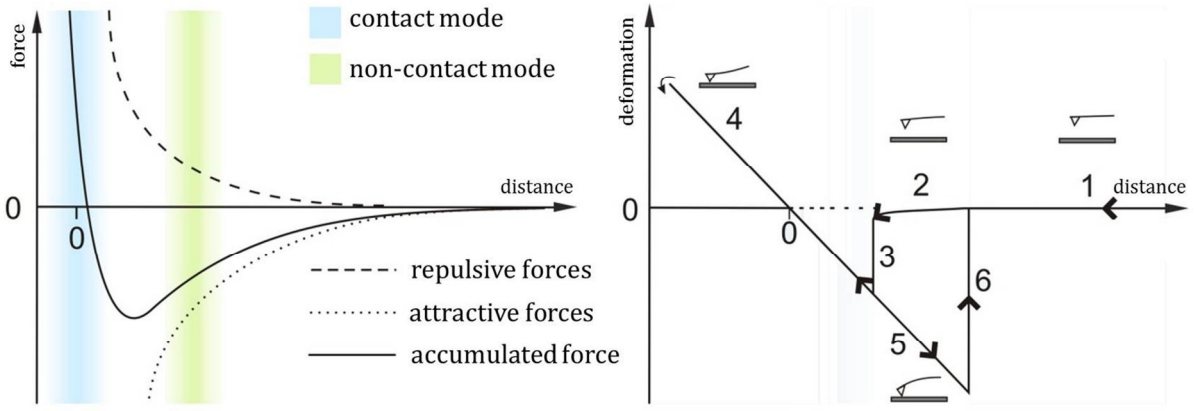

Figure 22: Forces between AFM tip and sample. When the tip approaches the sample surface mostly attractive forces occur, while repulsive forces start to dominate after further approaching. At a certain distance the rising attractive forces pull the tip to the sample surface and cause the cantilever to deform suddenly. The deformation stops when the tip is moved far away from the sample surface [92].

When the AFM tip is entering the attractive forces field the cantilever becomes slightly deflected like presented in Figure 22 in the right schema at point 2. If the cantilever is approached more the attractive forces will rise until a sudden deformation of the cantilever appears as shown in the right image at point 3. From now, the cantilever or rather the tip will be in contact with the surface and only repulsive forces appear. The sudden cantilever deformation during the approach can be clearly recorded by the electronics due to the laser deflection on the photo diode. The cantilever can be removed from the surface after moving back far enough like presented by points 5 and 6.

The AFM can be operated in different modes that use either the attractive or the repulsive forces. The modes are listed in the next figure.

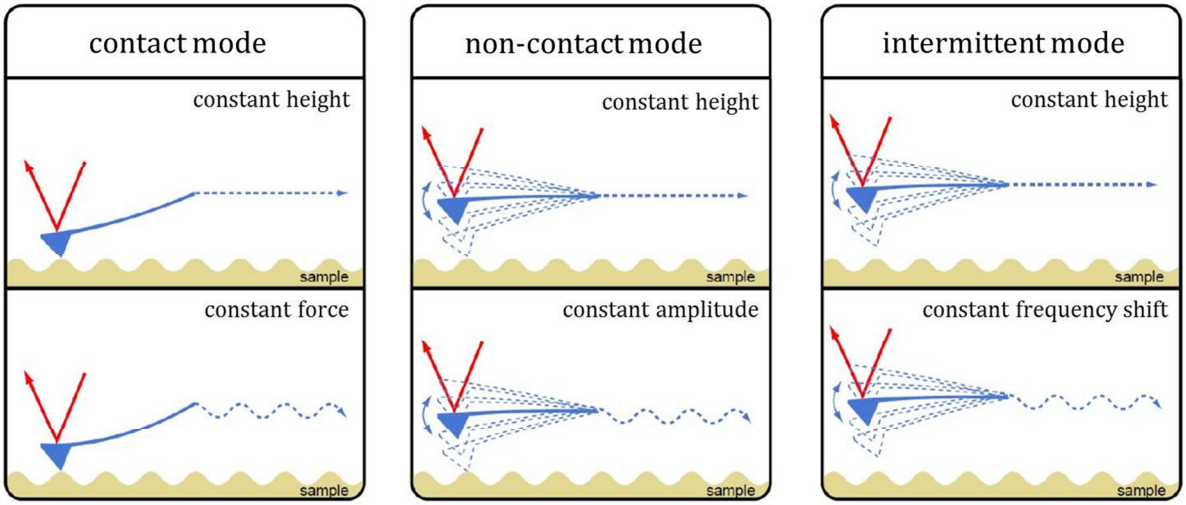

Figure 23: Overview of the measurement modes of an atomic force microscope. After approaching the tip to the sample repulsive forces in contact mode or attractive forces in non-contact mode are used for surface examination. In addition, the intermittent relationship as tapping mode can be used to exploit the advantages of both methods [92].

For repulsive forces the tip has a direct mechanical contact with the sample surface. In the contact mode the tip can either be moved at a constant height or at a constant force mode across the surface. For a constant height mode the deflection of the cantilever at every measuring point is detected by the photo diode. The deflection of the cantilever appears due to the changing repulsive forces. Another possibility for surface profile measurement is given by the constant force mode. In contact mode the resolution of the measurement is high, while the sample or the tip can be damaged due to too high repulsive forces and mechanic interaction.

For sensitive samples a non-contact mode is preferred. Here, the AFM tip is approached only until the attractive force field dominates so that the mechanical force becomes a thousand times smaller. As already mentioned, attractive forces can deflect the cantilever so that tip and sample will be in strong mechanical contact. In this case a stiff cantilever has to be used so that measurements can be applied in non-contact mode. The non-contact mode and the intermittent / tapping modes use a vibration excitation technique. The cantilever is excited in non-contact mode with a frequency greater than its resonant frequency. Here, the constant height or the constant amplitude mode can be applied. If the AFM tip is approached more to the surface while vibrating, the effective spring constant will decrease so that the resonance frequency and the vibrating amplitude will decrease. Thus, the tip will never get in contact with the surface.

The intermittent or rather tapping mode combines the advantages of both methods. Here, the excitation frequency is set below the resonance frequency of the cantilever, so that the effective spring constant increases for further tip approach during tip vibration. Thus, the AFM tip will be strongly attracted to the sample surface at the peak of the vibration and will come to mechanical contact with the surface for a moment. In summary, this mode provides high resolution measurements and can also be used in liquid medium.

3.4.3 Tip positioning by piezoelectric crystals

For nanometre precise positioning of the cantilever and the AFM tip piezoelectric crystals are used. Here, the piezoelectric effect is used that can be described as a mechanical deformation of the piezo crystals as a function of an applied electrical voltage or vice versa due to a dipole alignment within the piezoelectric crystals [93]. By applying a voltage the dipoles in the crystal will change their orientation. This results in a mechanical deformation of the crystal. This is called the inverse piezo effect. Or the dipoles will orientate because of a mechanical deformation so that a voltage can be measured at the piezo crystal which is called the direct piezo effect.

The arrangement of the dipoles in a piezo crystal and so the lattice symmetry is relevant for the strength of the piezoelectric effect. Materials that are used for piezo crystals are for example barium titanat [94], $BaTiO_3$, berlinit, $Al[PO_4]$ or the α-quartz. Piezoelectric crystals are also used as vibration quartz or as loudspeakers [95]. Besides the material properties the bulk diameters and the number of dipoles are crucial for the deformation strength.

For the positioning of the AFM tip in three dimensions either three piezo crystals or a single piezo tube is used. In a first approximation there is a linear relationship between mechanical deformation and electrical voltage in a piezoelectric crystal [93].

$$s = d \cdot E \tag{36}$$

Here, s corresponds to the relative length change $\Delta l/l$ in units of [Å/m], d corresponds to a deformation coefficient in [Å/V] and E is the electric field in [V/m]. The deviations from the ideal linear relationship result from piezo effects like the intrinsic nonlinearity, hysteresis, creep, cross coupling and aging. They will be explained briefly and are shown in the following figure.

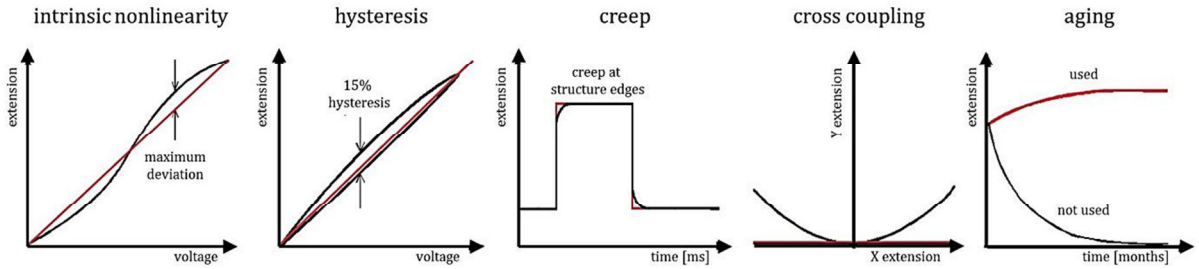

Figure 24: Overview on the five main error sources in the use of piezo electric crystals. The ideal behaviour of piezoelectric crystals is shown in red, while the real behaviour is indicated in black [93].

- *Intrinsic nonlinearity:* The expansion of the crystal is not linear with the applied voltage, but rather s-shaped, which mainly depends on the piezo material. The intrinsic nonlinearity leads to distortion of the measured image, which is highly visible in uniform structures, but cannot be determined in disordered structures. In

most cases the nonlinearity can be corrected by the help of calibration samples and by entering correction values in the AFM software.

- *Hysteresis:* Also hysteresis effects can distort the measurements. The hysteresis causes the piezoelectric crystals to have different deformation behaviour for expansion and relaxation. In this context, the measured data in forward direction has to be separated from the data measured in backward direction. For a data analysis the average values of all forward or backward measurements should always be calculated. The hysteresis increases with the extension of the piezo crystals and is highest at the maximum crystal expansion.
- *Creep:* The so-called creep occurs during sudden voltage changes at the piezoelectric crystals due to structural height differences, for example, in constant height mode measurements. The dipole re-orientation is not fast enough to follow structure height changes, so that structure edges will be measured imprecisely.
- *Cross coupling:* The cross coupling effect occurs when the deformation of a single piezo crystal also deforms other piezo crystals. Especially for piezo tubes that deform in all three dimensions a deformation in x- or y-direction will always include a deformation in z-direction. This cross coupling decreases the measurement accuracy, but can be corrected by most AFM software.
- *Aging:* Aging occurs when the piezoelectric crystals have not been used for an extensive period of time. Only after a regular re-use of the crystals the deformation as a function of the applied voltages will increase to the maximum value. At all, the aging effect is negligible when measurements are performed regularly.

The listed error can be compensated by software or calibration correction. Besides the mentioned piezo errors also external errors can distort the measurements and will be briefly mentioned in the next sub-chapter.

3.4.4 AFM measurements - external errors

The tip-to-sample interaction causes a deformation of the sample surface. In this context, sample layers near the surface will be attracted or pushed due to forces of about 10^{-7}N which is called the giant corrugation [96]. Especially in STM measurements this effect was widely investigated.

Some measurements have to be performed under vacuum conditions due to contaminations of the sample. Additionally, vibrations can cause errors during the AFM measurements and the tip or the sample can be damaged. So, most AFM devices must have or have a damping system.

For certain measurements in nanometre scale the measurement accuracy is reduced by atomic vibrations or by Brownian motion of the atoms. To increase the resolution some experiments have to be carried out under low temperature conditions by cooling the sample with liquid nitrogen or liquid helium at 77K or 4K.

3.4.5 Measuring procedure

In this project two different AFM devices were used. Since the measurements were mainly performed using the TopoMetrix AFM, the measurement procedure is described for this device.

The device consists of a bottom part that contains a vibration damping system and a sample holder where the sample can be moved roughly in the milli- or micrometre scale. The entire device is placed on a marble plate with rubber feet to improve the damping properties. The top part of the device contains electronics for the laser alignment. Additionally, laser-deflection mirrors, a camera, the cantilever holder and the piezo system are placed in the top part. By several screws the relative angle between cantilever and sample surface can be aligned.

The preparation for the measurement, the beam adjustment and the measurement process are technically and electronically simply as follows. After the top part of the device is removed, the sample can be placed on the sample holder in the lower part of the device. The top part is replaced and the camera, the cantilever-surface angle and the tip-surface distance are adjusted by screws or micro-step motors. The measurements are performed under standard conditions for temperature and pressure.

The tip is roughly approached to the sample surface by screws. Then the tip is approached by the piezo element electronically so that the tip-to-sample distance will be about 0.2mm. The laser is turned on and positioned on the backside of the cantilever to measure later cantilever deflections. The laser has to be positioned on the photo diode by mirrors until the laser signal at the diode is centred and at its maximum.

After the mechanic adjustment the parameters like scan size, scan speed and the scan resolution are set. Also the measure method can be chosen. In this project only the constant force mode at contact mode was used.

The final approach is performed fully automatic and will stop when a sudden cantilever deflection is registered due to attractive forces. Using the software a force-deflection curve is measured that will calibrate the subsequent measurements.

During the measuring process the surface field is scanned line by line. Every line is measured in the x-direction, the so-called fast scan direction. After every line the y-piezo moves the tip to the next line. The y-direction is called the slow scan direction. A scan resolution of up to 500 by 500 measuring points can be set. The minimum scan size is $1 \cdot 1 \mu m^2$ so that the measure point distance can be reduced to 20nm. The maximum scan field can be $150 \cdot 150 \mu m^2$.

The measured data was additionally calibrated with a calibration sample. The calibration was performed either using the HS-20MG or the HS-100MG calibration samples by “budget-sensors” that are functionalized with square and round structures with 20nm or 100nm gaps.

3.5 Scanning tunnelling microscopy – STM

Also for scanning tunnelling microscope measurements a tip is used at tip-to-sample distances of a few angstroms to investigate the surface topography. For the investigation the quantum mechanical tunnelling effect is used in STM. Here, a voltage is applied between the tip and the sample. At sufficient small tip-surface distances it is possible that electrons are transferred from the tip to the sample or other way round and an electric current will flow that is exponentially dependent on the tip-to-sample distance. If the currents and the corresponding distances are measured for several surface positions, a surface profile can be calculated. This surface profile equals the electronic surface density profile and can differ from the real surface. Since the STM uses electrical measurements the tip and the sample have to be electrically conductive materials.

3.5.1 Interaction processes between STM tip and sample surface

Both the electrons in the STM tip and the electrons in the sample surface occupy energy states which differ in their energy levels. If the tip-surface decreases to several angstroms the high energy occupying electrons will jump to equal unoccupied energy levels in the other material. This jump also happens at present potential barriers, like small tip-sample distances, and is called the tunnelling effect. Because the electron transfer happens from occupied to unoccupied levels of the same energy an elastic tunnelling effect is assumed. In classical physics this exchange is prohibited but can be explained by quantum physics using the wave function $\Psi(x)$ for electrons.

Using the Schrödinger equation the wave function $\Psi(x)$ can be calculated for electrons using continuity conditions at potential barriers. The continuity conditions describe an exponential decrease of the wave function amplitude $A_0 = |\Psi(x) \cdot \Psi^*(x)|^2$ within a potential barrier. If the amplitude does not decrease to zero $|A_1| > 0$ after the wave has passed the potential barrier, there exists a probability that the electron can overcome the barrier and tunnel to the energy levels of other materials. The transfer direction, from the tip to the sample or other way round, always happens from occupied to unoccupied same energy levels.

Because the transferred electrons can tunnel back to the energy levels in the original material it is necessary to apply a voltage between tip and sample. In this case, the Fermi energy level is always higher for one of the materials. The electrons will tunnel mainly in one direction and due to the applied voltage a current flow or rather an electrical circuit will be initiated. This current can be measured and stays constant for constant tip-surface distances.

Since the tunnelling probability and the wave function amplitude decrease exponentially in the potential barriers due to the continuity conditions a direct exponential relation-

ship between the tip-surface distance d and the current flow I exist. In the case of parallel and infinite metal plates at a distance d in vacuum the current I at small voltages U and a constant work function ϕ is [97]

$$I_T = \frac{e^2\sqrt{2m_e\phi}}{h^2} \cdot \frac{U}{d} \cdot e^{-\frac{4\pi\sqrt{2m_e\phi}}{h}d} \quad . \tag{37}$$

This equation can approximately be applied to most STM measurements. Therefore, the tunneling current mainly depends on the distance d. In the formula e is the elementary charge, m_e is the electron mass and h the Planck's constant. Because of the exponential decrease with the tip-to-surface distance STM measurements are very sensitive to distance variations. The current changes by one order of magnitude when the distance changes by 0.1nm.

In scanning tunnelling microscopy two methods are used that are already known from atomic force microscopy. In constant height mode the relative height is constant. In constant current mode the tip-surface distance is constant. In this context, the z-direction piezo regulates the relative tip height through all measurements. The deflection of the z-direction piezo of every point in the scanned field can be used to determine the surface topography. All realized measurements were made in constant current mode.

3.6 Scanning electron microscopy – SEM

In scanning electron microscopy - short SEM - the sample surface is irradiated with a focused electron beam that is moved along in a grid over an area of the sample surface. The interaction between the electrons with the sample leads to an electron and photon emission out of the sample surface that can be detected by special devices so that a qualitative surface profile can be provided. The SEM used in this project belongs to the Raith GmbH and is integrated in the eLiNE facility [98].

The electrons are generated by the heating of a bent wire that is typically made of tungsten. By wire heating the kinetic electron energy distribution is broad and the focus abilities are therefore limited. By the use of a field emission cathode in a field emission gun (FEG) the electrons are emitted by applying a high-voltage electric field. The kinetic energy spectrum of the electrons is much narrower so the focus abilities, the beam stability and the image quality are improved. The electrons are accelerated by voltages of a few keV and are focused using electric and magnetic lens systems.

The electrons and photons emitted from the sample surface are Auger electrons, secondary electrons, X-rays and the so-called bremsstrahlung. But also back scattered beam electrons can be measured by detectors.

There are several investigation methods like BSE (back scattered electrons), EDS and EDX (energy dispersive X-ray spectroscopy) and WDS or WDXRF (wavelength dispersive X-ray spectroscopy) [99] for surface analysis. One common investigation method is the detection of secondary electrons [100].

Secondary electrons are for example detected by an Everhart-Thornley detector [101], a scintillator-photomultiplier. Secondary electrons are primarily emitted from the top lattice layers of the sample surface. Depending on the angle between sample and incoming electrons the emission of secondary electrons varies and so the measured intensity does. Additionally, the interaction mechanisms at structure edges or at charged surface regions change the electron spectrum which increases the structure contrast for measured images.

SEM measurements detect the incoming electron intensity of all scanned surface points. The scanning grid can be square nanometres to square millimetres in size. Together with excellent resolution qualities the SEM is used in many applications. But in comparison to AFM or STM devices no structure depth information can be obtained.

The eLiNE system of the Raith GmbH has to work under vacuum conditions so that the beam electrons will not be absorbed by atmosphere molecules. The sample surface can be scanned fast enough so the observation can happen in real time. As charge effects play a major role in SEM the samples have to be electrically contacted or rather grounded.

3.7 Optical microscopes

Optical microscopes of the Müller GmbH and the Carl Zeiss AG were used for the analysis of the samples in milli- and micrometre scale. For structural investigations of produced nano structures could not be performed by optical microscopes due to a limited resolution. For micrometre sized structures the microscopes were used for contacting micro pads in electrical measurements as this will be described in further subchapters.

The minimum field sizes are $1000 \cdot 750 \mu m^2$ for the Müller and $70 \cdot 50 \mu m^2$ for the Carl Zeiss microscopes at resolutions of 1µm or rather 0.5µm.

The microscopes can operate using transmitted, reflected or diffuse light. By light scattering the position of the produced structures could be determined. Especially transmitted light could be used to investigate the thickness of thin samples. Additional calibrations enabled the evaluation of the sample thickness just by using optical microscopes. All microscopes were equipped with cameras, so that images of the investigations could be created and saved.

3.8 Four-point measuring device

A four-probe measuring device was designed for electrical investigations of micrometre sized structures. The design and the construction of the facility was first presented in reference [102].

For electrical measurements with the self-designed the structures had to be produced with 25·25µm² to 50·50µm² contact pads due to the tip positioning limitation in the micrometre range. The tip positioning is realized by four Newport Corporation micro manipulators. Special clamps were constructed to attach the tungsten tips for electrical measurements. The clamps are connected with a pico-ampere current source and a voltmeter. A microscope can be used to observe the contacting process.

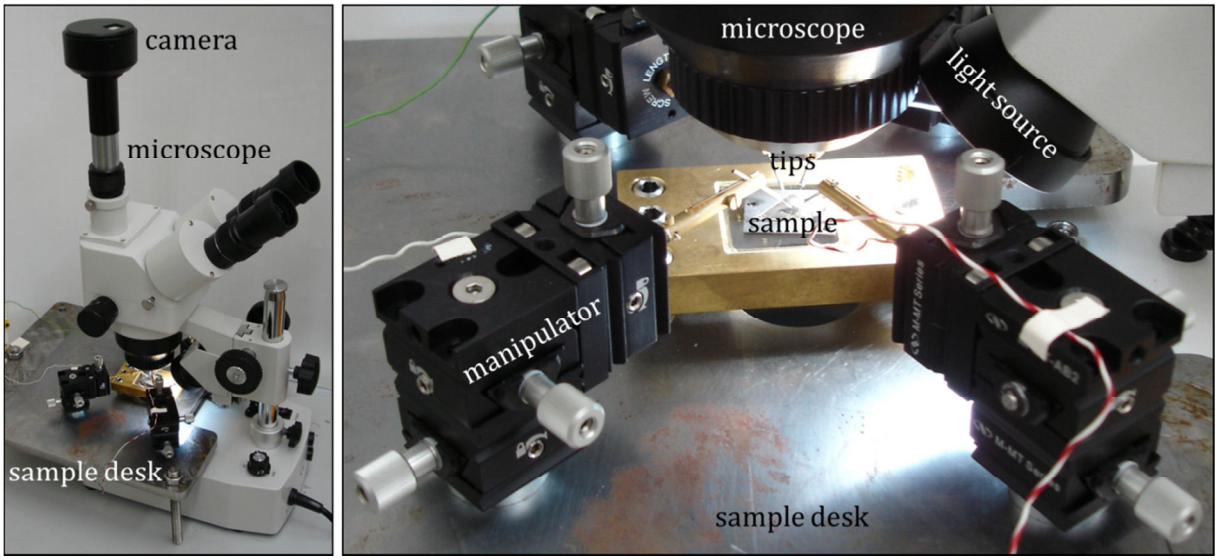

Figure 25: Overview of the designed four-point measuring device. The tips can be positioned by micro manipulators. By a microscope the contacting of the tips with the sample can be observed.

3.8.1 Tip production for four-point measurements

The used tips are made of a 0.1nm thick tungsten wire which was electrochemically etched in a potassium hydroxide dissolution. While the tungsten wire serves as the anode a platinum wire in the dissolution is used as the cathode. At voltages of 1.4V the tungsten oxidizes and reduces the water molecules in the dissolution to hydrogen gas and hydroxide ions like reported in references [103] or [104].

$$\begin{aligned} anode: &\quad W + 8OH^- \rightarrow (WO_4)^{2-} + 4H_2O + 6e^- \\ cathode: &\quad 6H_2O + 6e^- \rightarrow 3H_2 + 6OH^- \\ reaction: &\quad W + 2OH^- + 2H_2O \rightarrow (WO_4)^{2-} + 3H_2 \end{aligned} \tag{38}$$

The tungsten oxide separates from the wire. As this process happens over the whole tungsten wire in the dissolution the hydroxide concentration decreases at lower parts of the tungsten wire. In this case the wire part at the dissolution surface becomes oxidized faster. After a short time the lower part of the tungsten wire will break away from the thin wire part near the dissolution surface and falls down. This breaking can be registered by the etching electronic as a sudden resistance change that stops the etching process. The tip is now prepared with a diameter of only a few nanometres at the tip end.

Because these sharp tips will be deformed or destroyed while contacting the structure pads, a capacitor of 5.7µF is installed in the etching electronics so that the etching process will continue some seconds after the electronics register the resistance drop. By this technique the tip end becomes rounded and will be a few micrometres in diameter. This tip will not be deformed or destroyed after contacting the pads.

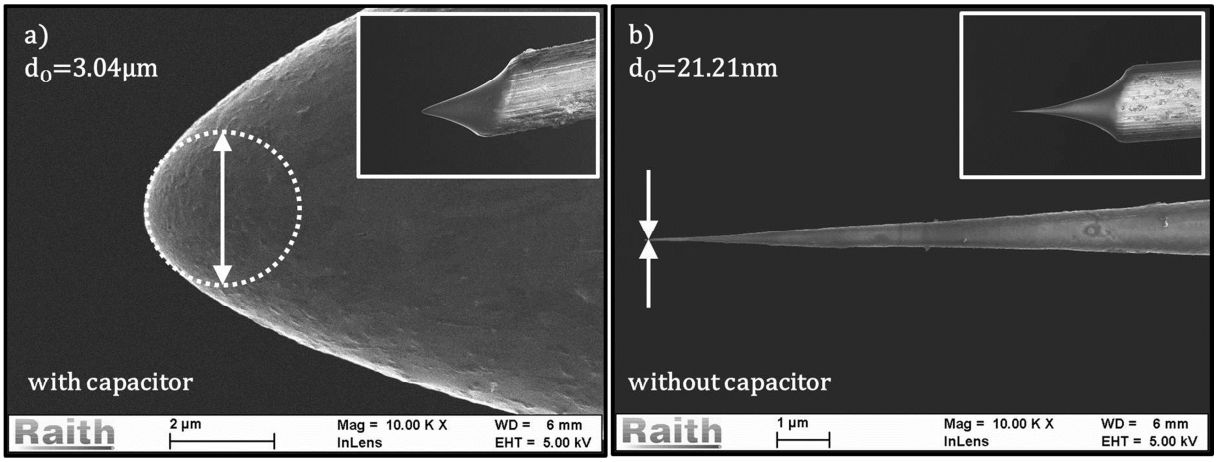

Figure 26: SEM images of the produced tungsten tips for electrical measurements. Since the etched tips have a thin tip end the tips will be damaged during the contacting process with the surface b), a capacitor can be used to continue the etching process after the etching is stopped by the electronics. In this context, the tips become rounded and are more resistant to deformations during surface contacting a).

After the etching process some tungsten oxide material will be deposited at the tip end and the tip conductivity will be reduced. By using hydrogen fluoride the tungsten oxide can be dissolved [105]. After the process a natural oxide film will be produced at the tip surface that does not perturb electrical measurements strongly.

3.8.2 Basics of the four-probe measurement

During electrical measurements not only the structure resistance R_s but also perturbing resistances are detected. In a simplified schema the perturbing resistances are the tip resistance R_t, the contact resistance between tip and surface R_c and other perturbing resistances that can be summed as R_a [106]. For small structures the structure resistance R_s is equal or smaller than the perturbing resistances and cannot be measured accurately by only two tips. Although, the tip resistance can be determined by additional

measurements, the contact and the perturbing resistances will change for every measurement and cannot be determined.

To solve this problem F. Wenner [107] developed a method where electrical measurements are performed with four probes. L. B. Valdes [108] extended this method for measurements of semiconductors. As shown in Figure 27 two tips are used for voltage measurements in a four-probe measurement.

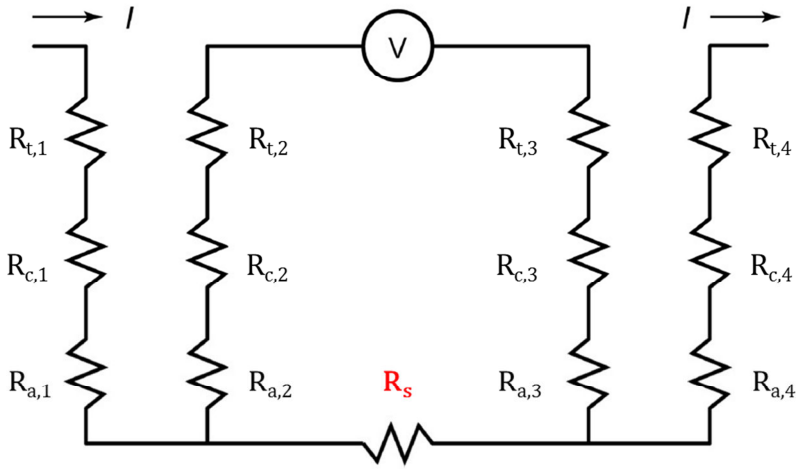

Figure 27: Overview of a four-probe measurement. The current flows through the structure resistance but additionally through perturbing resistances. When a high impedance voltmeter is used no current will flow through the inner electrical circuit. In this context, the perturbing resistances do not play a major role for electrical measurements of the structure resistance [106].

When a high impedance voltmeter is used there is up to no current will flow in the inner electric circle. Because of the Kirchhoff's rules $\sum_{i=1}^{n} I_i = 0$ at the nodes and $\sum_{i=1}^{n} U_i = 0$ within a mesh the current is mainly flowing through the sample resistance R_s. In this context, the perturbing resistances R_t, R_c and R_a now will not have any influence on the measurement. With four-point measurements Ohm's law can be investigated for the produced structures or the samples.

$$R_s = \frac{U}{I} \tag{39}$$

To calculate the electrical conductivity σ of the structures thick and thin samples have to be distinguished due to the different current distribution in the materials. It is common to place the tips in a single line at equal distances as the formula of the electrical conductivity will then be simplified. The evaluation of the electrical conductivity or rather the specific resistivity for thick and thin samples using four-probe measurements is described in reference [109].

Thick samples are samples with a thickness that is much greater than the tip-to-tip distance d. By assuming a resistance change ΔR as a function of the specific resistivity ρ and a varying tip-to-tip distance $d = \Delta x = x_2 - x_1$ the formula is

$$\Delta R = \rho \cdot \frac{\Delta x}{\Delta(y \cdot z)} \quad . \tag{40}$$

In thick samples the current distribution is spherical so that the resistance can be obtained by integration

$$R = \int_d^{2d} \frac{\rho}{2\pi x^2} dx = -\frac{\rho}{2\pi}\left(\frac{1}{2d} - \frac{1}{d}\right) = \frac{\rho}{4\pi d} \quad . \tag{41}$$

Due to the superposition of the current through the current tips, the real resistance is $R = U/2I$ and the specific resistivity becomes

$$\rho_{thick} = \frac{1}{\sigma_{thick}} = 2\pi d \frac{U}{I} \quad . \tag{42}$$

Samples with a thickness of $h \gg d$ have a current distribution that is ring-shaped and only two-dimensional. The integral will then be

$$R = \int_d^{2d} \frac{\rho}{2\pi h x} dx = \frac{\rho}{2\pi h}[\ln(2d) - \ln(d)] = \frac{\rho}{2\pi h}\ln(2) \quad . \tag{43}$$

In this case, the real resistance have to be corrected by a factor of 2, too, so the specific resistivity will be

$$\rho_{thin} = \frac{1}{\sigma_{thin}} = \frac{\pi h}{\ln(2)} \frac{U}{I} \quad . \tag{44}$$

If the arrangement of the tips is not equal and one-dimensional further corrections have to be made. For thick samples L. B. Valdes [108] showed that

$$\rho_{thick} = \frac{1}{\sigma_{thick}} = \frac{U}{I} \frac{2\pi}{\left(\frac{1}{d_{12}} + \frac{1}{d_{34}} - \frac{1}{d_{12} + d_{23}} + \frac{1}{d_{23} + d_{34}}\right)} \quad . \tag{45}$$

The electrical conductivity σ equals the reciprocal specific resistivity ρ. For materials with anisotropic conductivity the formulas have to be modified. For materials with a constant conductivity parallel to the surface $\sigma_x = \sigma_y$ but another conductivity perpendicular to the surface σ_z the formulas are [110]

$$\left(\sqrt{\sigma_{x,y} \cdot \sigma_z}\right)_{thick} = \frac{1}{2\pi d} \frac{I}{U} \tag{46}$$

$$\left(\sqrt{\sigma_x \cdot \sigma_y}\right)_{thin} = \frac{\ln(2)}{\pi h} \frac{I}{U} \tag{47}$$

for constant tip distances and a line arrangement of the tips. If the arrangement of the tips is changed this equations are not valid.

3.8.3 Procedure of an electrical four-probe measurement

For electrical analysis the sample is placed on the sample holder and the tips are put in the clamps of the micro manipulators. The sample holder is placed above the opening of the sample desk to allow the use of transmitted light. With the help of the microscope and the attached camera the tips are moved roughly with the micromanipulators until they are visible under the microscope.

All tips are initially contacted with each other to ensure their functionality. In some cases the current while a tip-tip contact has to be increased to melt the tips slightly together. After this check the tips will be placed one after another on the sample surface or on the generated structures. The current flow can be checked for two tips each. If there is no current flow the current can be increased also to melt the tips slightly with the surface. When all tips have an electrical contact with the surface electrical measurements can be performed.

3.9 SEM-four-probe measuring device

During this project some measurements were performed using an SEM-four-probe measuring facility of the Omicron Nanotechnology GmbH [111]. Because of the SEM also nano structures can be contacted due to the high resolution of the SEM images. The used tips are very sharp and only a few nanometre at the tip end. Because of the precise positioning the tips will not be damaged during the contacting process. In this context, also structures without contact pads could be investigated.

The electrical measurements procedure is almost analogues to the procedure presented in the last subchapter. Unfortunately, the SEM-four-probe facility could not be used during the whole project.

3.10 Chapter summary

The devices in this project can be separated according to their function into devices for structure production, structural analysis and electrical analysis. For structure production the ionLiNE of the Raith GmbH, an oxidation furnace and an ozone-generator-UV-lamp combination were used.

The ionLiNE was used to produce, focus and accelerate single charged gallium ions on sample surfaces for structure production. Various structures like dots, lines and areas

can be planned using the GDSII software. In this context, the dot-, line- and area-dose were introduced that equal a certain amount of ions that have to be deposited.

Besides a direct structure production process after high-dose irradiation a low-dose irradiation process can be combined with a subsequent oxidation process for structure generation. The oxidation process was performed by two methods. Either an oxidation furnace or an ozone generator combined with a UV-lamp is used. In the oxidation furnace the samples are heated at 500°C for 200min under an Ar-O_2 atmosphere with 2% of oxygen. During the heating process mainly irradiated areas become oxidized due to a carbon-oxygen reaction. Because heat sensitive samples, like thin HOPG, will be destroyed at too high temperatures an oxidation process at temperatures of up to 110°C can be performed where ozone is used as an oxidant. An ozone generator was used that produces ozone from oxygen by gas discharge. Additionally, an UV-lamp was used to produce ozone by photo absorption at λ=185nm. For higher reaction speed the sample was heated up to 110°C that is the maximum temperature for heat sensitive samples.

For the structural analysis of the samples and the generated structures an atomic force microscope, a scanning tunnelling microscope, a scanning electron microscope and optical microscopes were used. In atomic force microscopy a tip scans a sample surface area and interacts with the sample surface by attractive and repulsive forces. Since the tip is bounded to a cantilever, the cantilever deflects due to the attractive and repulsive forces. This deflection can be measured using a laser system, so that a surface and structure profile can be determined. A tip is also used in the scanning tunnelling microscopy. Here, at short tip-sample distances, and an applied voltage a current can be measured due to the quantum mechanical tunnelling effect. Because there is an exponential current-to-distance dependency the STM measurements are strongly sensitive. STM and AFM measurements can investigate structure geometries quantitatively. A qualitative analysis is given by the scanning electron microscopy. Here, a focused electron beam is moved in a grid over the sample surface. After the interaction of the beam electrons with the sample secondary electrons are emitted and analysed. Depending on the local surface characteristics the emission of secondary electrons varies in intensity. The SEM and the optical microscopes can be used for extensive examinations of the samples.

The generated structures and the samples were investigated concerning electrical properties. A four-probe measuring device was designed where four tips can be used for electrical measurements. The experimental results can be used to calculate the electrical conductivity or rather specific resistance of thin and thick HOPG samples or structures. Unfortunately, the self-designed device can only be used for structures with contact pads. Structures without contact pads could only be electrical investigated by an SEM-four-probe device of the Omicron Nanotechnology GmbH. This facility could not be used during the whole project.

4. Sample systems

In this chapter the sample material, graphite, will be discussed in more detail. In this project highly oriented pyrolytic graphite, HOPG, was used. First the structure of HOPG and of single graphite layers, of graphene, will be explained. Second the electrical properties of these materials will be described. Furthermore, the preparation of an HOPG sample and especially of a thin HOPG sample for ion beam lithography will be explained. For the classification of the sample thickness AFM measurements will be shown and compared to a calculation method where the sample thickness is determined by microscope images. Additionally, experiments for the investigation of the electrical conductivity of HOPG samples will be explained.

4.1 HOPG – Highly oriented pyrolytic graphite

All nano and micro structures were produced on graphite surfaces. Graphite is one of the allotropes of carbon and has an hcp, hexagonal close package, structure where single layers, the so-called basal planes, are stacked in an ABAB stacking sequence. HOPG, highly oriented pyrolytic graphite, is almost contamination-free and the misorientation angle between the basal planes, the so-called mosaic spread, is less than 2°. HOPG has a relatively large grain size of about 3-10µm [112]. Graphite can be produced synthetically by graphitization at temperatures above 2500°C and will change to HOPG under high pressure conditions during the production process.

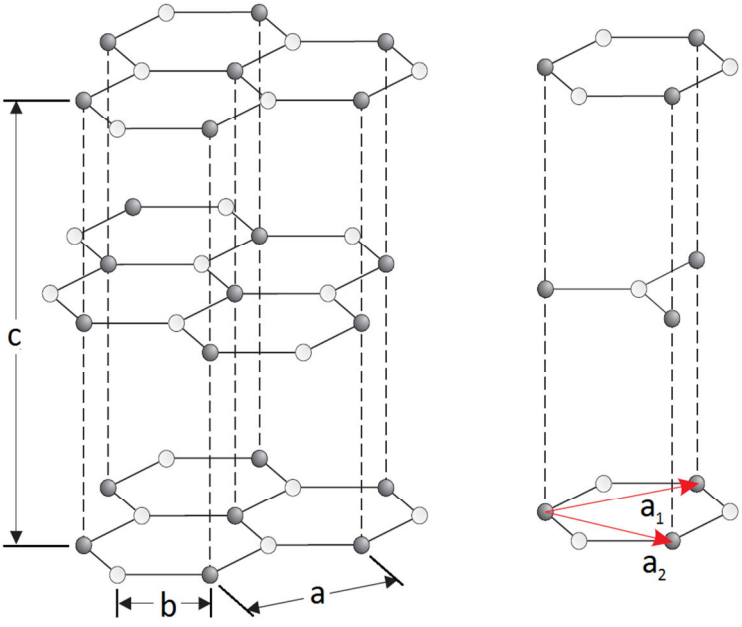

Figure 28: Lattice structure of HOPG: a) in-plane lattice constant: 2.46Å, b) next neighbour distance: 1.42Å, c) c-axis lattice constant: 6.70Å. The unit cell is build up by the plane vectors a_1 and a_2. Grey coloured carbon atoms have a direct neighbour along the c-axis [113].

In the honeycomb arrangement of the basal planes the carbon atoms are single covalently bonded with a nearest neighbour distance of 1.42Å. The in-plane lattice constant is 2.46Å. The basal planes are held together by weak interlayer interaction forces and are spaced 3.35Å.

The lattice arrangement is a result of the sp^2 hybridization in the graphite solid [20] where the 2s- and the $2p_{x,y}$-orbitals form three sp^2 molecule orbitals at an angle of 120° in the basal plane direction. The carbon atoms in the basal planes are bonded by strong σ bonds with 4.3eV per atom by the molecule orbitals while the remaining p_z-orbitals of the carbon atoms form delocalized π-orbitals with 0.07eV per atom in the c-axis direction [20], [114]. The π-orbitals belong to a half occupied energy band, so that the conductivity parallel to the basal planes is much higher than in c-axis direction due to a quantum mechanical hopping of the π-orbital electrons. The anisotropic conductivity is one of the most interesting facts on graphite solids because the conductivity parallel to the basal planes is of the order of metal conductivity and much higher than the conductivity perpendicular to the basal planes. Many investigations on the conductivity in graphite solids were made. Depending on the quality of the HOPG the electrical conductivity can vary. The conductivity σ is the reciprocal of the specific resistivity ρ with $\rho=\sigma^{-1}$ in units of Ω·cm. In [115] the HOPG resistivity is given as a function of the temperature.

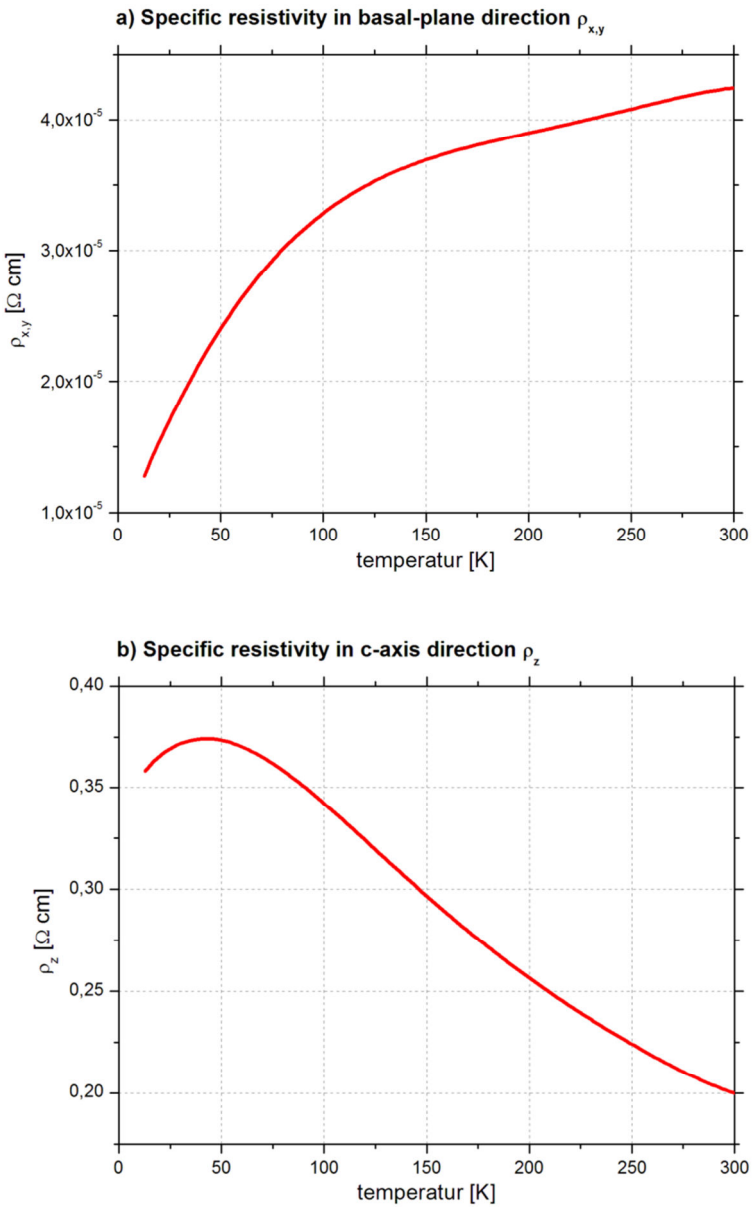

Figure 29: Specific resistivity of a HOPG solid parallel and perpendicular to the basal planes depending on the sample temperature as it is reported in [115].

At room temperature the specific resistivity of HOPG parallel to the basal planes $\rho_{x,y}$ is 3.5-4.5 x 10^{-5} Ωcm. In the perpendicular direction along the c-axis the specific resistivity ρ_z is 0.15-0.25 Ωcm [116]. The plots in Figure 29 show the specific resistivity in c-axis direction increases while the specific resistivity in the basal-plane direction decreases for lower temperatures. For low temperatures the current flow in the basal-plane direction is even higher than it is already at room temperature. In general the electric current mainly flows in the basal-plane direction for temperatures up to room temperature and will be localized near the HOPG surface when a current is applied at two surface points.

As mentioned before, the conductivity or specific resistivity of the sample especially near the surface also depends on other physical properties like the grain size or on the amount of surface step edges [117] so generally on the quality of the graphite or HOPG sample. HOPG is mainly produced in three quality grades ZYA, ZYB and ZYH. The ZYA is the highest quality HOPG with a mosaic spread of 0.4-0.7° and was used in this project. Although, the quality is very high the HOPG consists of small graphite crystals with a diameter of several micrometres. While all crystals have the presented hcp-lattice arrangement they are displaced one to another.

In the next sub chapter the physical properties of a single layer of graphite, of graphene, will be described briefly due to its interesting electrical behaviour and its high importance for recent science investigations and possible future applications.

4.2 Graphene – A single layer of graphite

Graphene is a single graphite layer and has the same structural properties like a single basal plane of the graphite bulk. That means that the honeycomb structure and the next neighbour distances such as the bond angles due to the sp^2 hybridization are the same for graphene as for a single graphite basal plane.

Because graphene is a so-called two-dimensional material it should be unstable due to thermodynamic aspects presented in the theoretical work by L. D. Landau in the year 1937 [118]. Although, most graphene samples were studied while supported by a bulk substrate some investigations were made on suspended graphene sheets so that the stability of two-dimensional graphene could be explained by a lattice deformation where the graphene layer becomes corrugated [119]. The mechanical and electronic properties of graphene make this material interesting for possible future applications.

Graphene has a very high Young's modulus of about 1020GPa along the basal plane direction which is nearly as high as the Young's modulus of diamond. The ultimate tensile strength is 1.25×10^{11}Pa and 125 times greater than for steel like reported in reference [120]. Additionally, graphene is nearly transparent for light in the visible spectrum. Investigations presented in references [121] show that the transmittance of visible light decreases by 2.3% for each additional layer for the first few graphene layers. In this context, the thickness of thin graphene samples that consist of only a few layers can be estimated using light microscopes and transmission measurements. This method will be discussed later in this chapter.

Especially for possible applications the electrical properties of graphene are important. Using the tight-binding Hamiltonian electrons in graphene can hop to both the nearest- and the next-nearest-neighbour. The energy band structure derived from the Hamiltonian leads to the energy spectrum presented in the next figure.

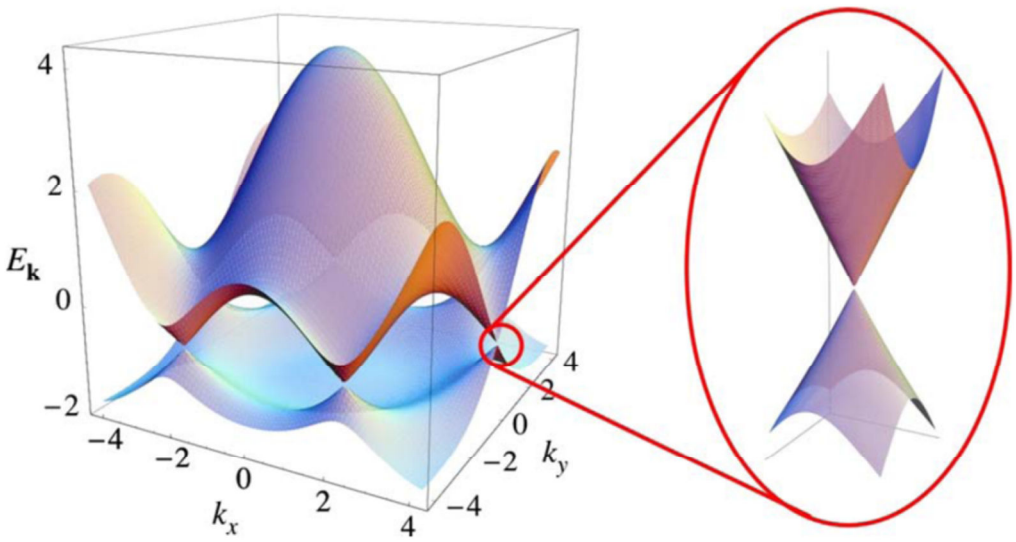

Figure 30: Overview of the energy band of graphene. At the Dirac points the conductance and the valence band touch each other like the zoom-in shows [4].

The K and K´ points at the corners of the graphene Brillouin zone are called the Dirac points where the π and the π* energy bands touch the Fermi level [4]. At the Dirac points the conductance and the valence band merge. This type of material is called zero-gap semiconductor [122].

Because the electron energy is linear dependent on the wave vector *k* the graphene electrons behave like quasi massless relativistic particles and can be described by the Dirac equation as mentioned in [122]. Electrons in graphene are only scattered at lattice defects up to room temperature. Because the defect density is low in graphene the carrier mobility is high and the mean free path of electrons in graphene can be higher than 2µm as reported in [123].

Unfortunately, the energy band structure will change for multiple graphene layers. Already two graphene layers have a parabolic spectrum around the Fermi energy with a band overlap of 0.16meV (graphite: 41meV). The semi-metallic behaviour rises with the amount of graphene layers. For more than ten graphene layers the difference in band overlap compared to graphite is less than 10% [124]. Because the edges of graphene layers additionally influence the energy band structure so that the benefit of Dirac-like electrons cannot or can only partially be used.

In summary, the interesting electric properties of graphene cannot be transferred on graphite samples. Additionally, problems would occur if graphene sheets would be structured using a focused ion beam. The deposition of the incident ions and the resulting graphene edge destruction would result in changed electrical properties.

In this project HOPG bulk was used for structure production. The sample preparation of the HOPG samples is discussed in the following sub chapter.

4.3 Sample preparation

For the production of nano and micro structures on surfaces 12·12·5mm³ HOPG bulks were used. The samples where either sliced into thick HOPG samples of 12·12·2mm³ sample parts and were then cleaned by exfoliation or the sample parts were used to prepare thin HOPG samples with only a few nano- or micrometres in thickness by a more complex preparation process. The preparation of this two sample classes will now be explained.

4.3.1 Thick HOPG samples

The preparation of thick HOPG samples for the use in ion beam lithography is simple. Due to the low interaction forces in c-axis direction graphene layers can be removed either by exfoliation or by slicing with a razor blade along the basal planes. The slicing with the razor blade is mainly used for a rough preparation of the HOPG samples. The exfoliation technique will create homogeneous sample surfaces with a low amount of step edges. For the exfoliation a simple adhesive tape can be used. The tape is stuck on the HOPG surface along the basal plane direction. When the adhesive tape is peeled off again at an angle of about 45° to the sample surface a few microns of the surface graphene layers will be removed.

The sample surface is chemically inert. Nevertheless, the sample can be contaminated with impurities and should be stored in a vacuum chamber.

Before the sample will be inserted into the ion beam facility it has to be mounted on a metal plate. As the sample will be charged during the irradiation process the sample will be grounded due to the metal plate that is connected electrically with the sample holder. To fix the sample on the metal plate tantalum stripes are used that are weld on the metal plate.

4.3.2 Thin HOPG samples

While the structural properties can be investigated for structures on thick HOPG samples it is necessary to prepare thin HOPG samples of a few nano- or micrometres in thickness to investigate the electrical properties of the produced structures.

Although, the current flow in a structure will mainly be located in the basal-plane direction at structure dimensions of several micrometres in width and length only a few nanometres in depth the current will also flow through the underlying HOPG bulk and will not only be located in the produced structures.

To locate the current flow in the structures they have to be produced on thin HOPG samples that are placed on an insulator. If the cavities produced around the micro- and nano structures are deeper than the sample thickness the produced structures will be electrically isolated from the rest of the HOPG sample.

The insulator material that was used for thin HOPG production was the so-called mica. Mica materials are sheet silicate minerals that have a highly perfect basal cleavage similar to HOPG. Muscovite is a mica material and was exclusively used in this project. Muscovite has the chemical formula $KAl_2(Si_3Al)O_{10}(OH,F)_2$ and can be cleaved by a razor blade easily along the basal planes to obtain clean and flat surface [125]. Muscovite is yellowish, flexible and high visual light transparency. Single mica plates were sliced along the basal planes so that the resulting mica slices were about 50x20x0.1mm^3.

For the production of thin HOPG samples a mechanical exfoliation method was developed with a subsequent chemical cleaning process. This process was first described in [102].

The HOPG sample is cleaved into several thin samples of about 0.5mm thickness. One sample has now a size of about 12x12x0.5mm^3. The sample will now be exfoliated with an adhesive film so that the sample surface will be clean and flat. The sample residues on the adhesive film cannot be used as samples because they are torn after the exfoliation.

The freshly cleaved sample is then covered with hot liquid resin. The used resin is glycol phthalate of the Logitech Ltd. and its melting point is at 120°C. As the resin cools down it becomes hard. When the sample is removed from the resin ideally a big and thin sample residue will remain on the hard resin. This sample residue is mostly not damaged concerning the lattice structure of the graphite. After the sample residues with the resin are put into liquid acetone, the resin will be dissolved and thin sheets of graphite will swim in the acetone.

The thin sample sheets or rather the thin HOPG samples were up to 25mm^2 large and had a thickness of about 30-150nm. Because of the dissolving process in acetone the surface of the thin sample is contaminated mostly with dissolved resin residues. To clean the surface the thin sample is transferred three to four times in new and clean acetone and rest in acetone for about one day in the last step to dissolve the remaining resin residues on the sample. After that the thin samples will be heated in acetone at about 55°C for one to two hours. The heating process is carried out under an extractor hood due to the low boiling point of acetone at 56°C.

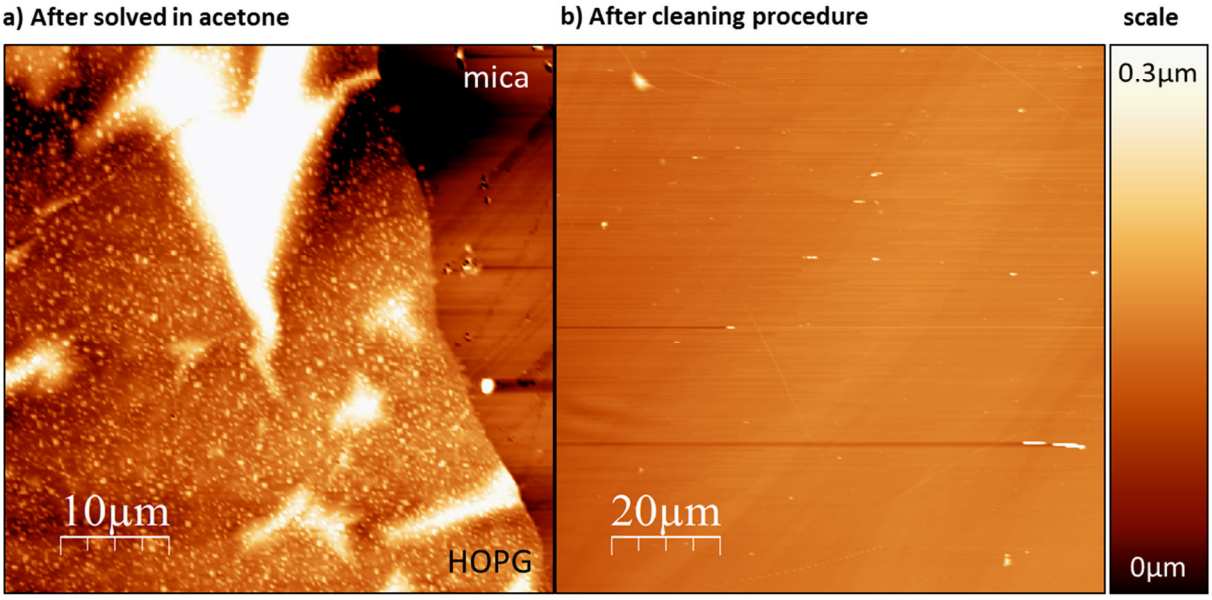

Figure 31: AFM images as an example for the cleaning process using heated acetone. While the thin HOPG sample is highly contaminated with resin residues after the first solving step in acetone a) the contamination will be reduced using multiple cleaning steps. Both pictures are height scaled equally.

Although, the sample surface is now cleaned from resin the acetone will itself residue on the sample surface when the sample is removed from the liquid acetone. The thin HOPG sample must be transferred into isopropanol in a three step dilution series. To put the cleaned thin HOPG sample onto the mica substrate the sample is transferred into distilled water where it will swim flat on the liquid surface after the isopropanol was dissolved due to the hydrophobicity of HOPG. The HOPG can then be fished up with one of the mica slices.

The mica slice is now cut up into a smaller piece, so that the mica together with the thin HOPG sample can be mounted on a metal plate (20x16x1mm^3) by tantalum stripes. In a last step the HOPG is electrically contacted with the metal plate by a silver colloid dissolution (Quick drying silver paint – G3691 – Agar Scientific Ltd.) to prevent sample charging during the irradiation process in the ion beam facility. The mounted sample is now retained under vacuum conditions to keep the sample surface clean until the lithography process is performed.

4.4 Sample classification

The samples were investigated in view of their surface quality and lattice structure, electrical conductivity and their sample thickness concerning thin HOPG samples. The results will be presented in the following sub chapters.

4.4.1 Surface and lattice quality

The sample quality was investigated for some representative samples. Measurements in the centi-, milli-, micro-, and nanometre range were performed. Therefore, camera, microscope, AFM and STM images were made and are presented in the next figure.

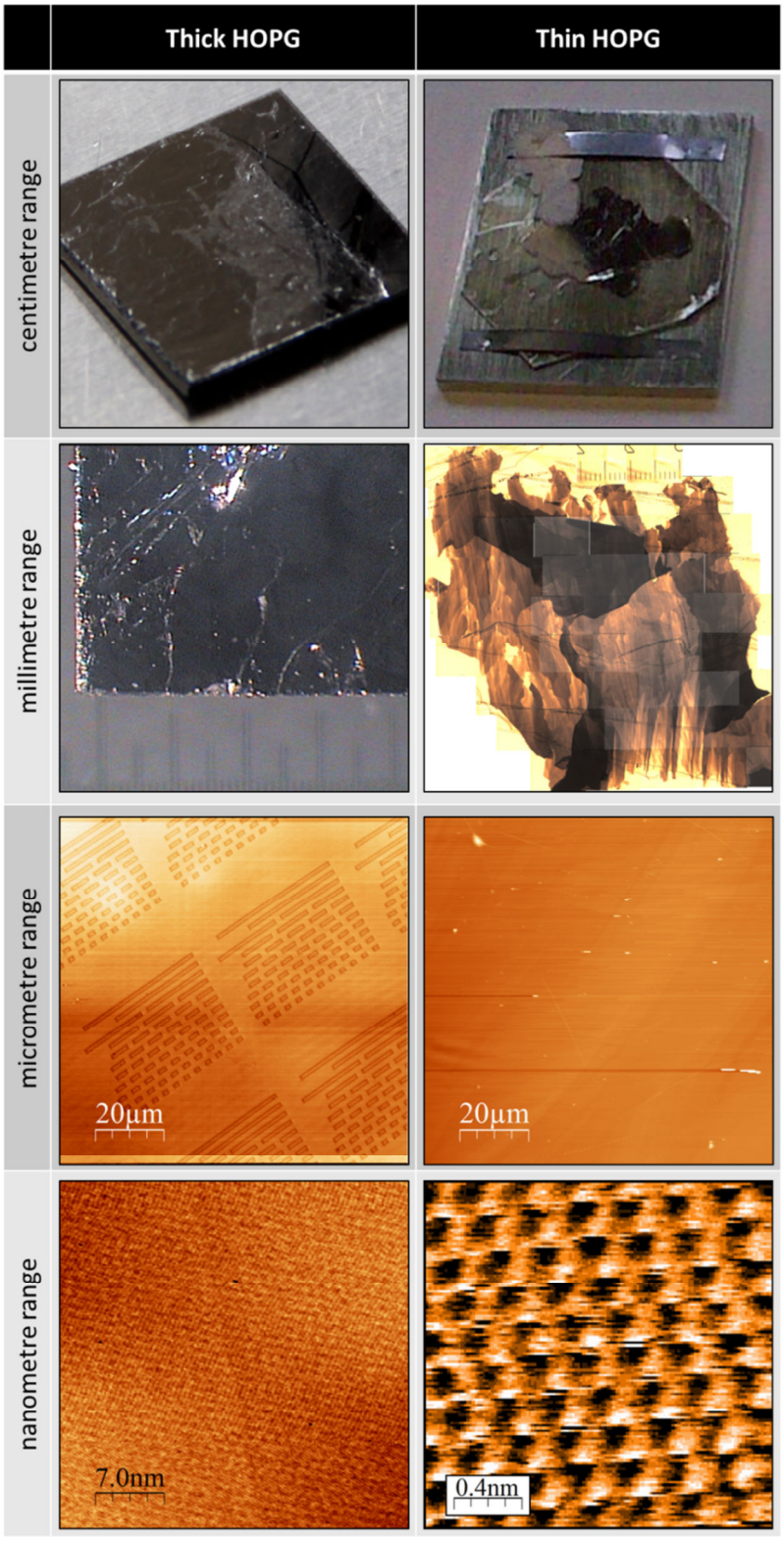

Figure 32: Classification of the quality of thin and thick HOPG samples. For both sample types camera, microscope, AFM and STM image were performed to obtain an overview about the quality from nano- to centimetre range. The micrometre range image of the thick HOPG shows a nano structured surface.

Thick HOPG samples seem to have a clean and nearly flat surface after the mechanical exfoliation in the centimetre range. On the right side an image of the thin HOPG sample on a mica slice on a metal plate is shown. The mica slice is mounted on the metal plate using tantalum slices. In the left upper corner of the metal plate the silver colloid is visible that connects the HOPG with the metal plate electrically. The sample size (metal plate size) is about 12x12mm² (20x16mm²).

Microscope images show that at the corners of the thick HOPG sample some peeled off areas exist while the sample surface is mostly flat in the middle of the sample surface. The thickness of thin HOPG samples can vary strong along the sample surface after the ex-

foliation process as the right microscope image shows. Here, more transparent sample parts are thinner than dark sample areas of the images.

For thin samples impurities can be observed on the sample surface on the micrometre range also after the performed cleaning process. Partially, some step edges can be observed in AFM measurements. Because thick samples have not been cleaned in liquids the surface remains clean even after the irradiation or rather structure production process as the left image shows. Both AFM images in the micrometre range are scaled from 0-0.3µm in the z-direction.

The lattice arrangement of the sample surface was investigated by STM. The thick sample image shows that the lattice order is long-range. The hexagonal arrangement of the carbon atoms was confirmed by STM measurements presented in the right image. It should be noted that the distance between two white hills equals the in-plane lattice constant. Due to the ABAB stacking sequence not all carbon atoms are scaled equally in z-direction because of the influence of the orbitals in the second graphene layer.

4.4.2 Thickness of thin HOPG samples

The thickness of thin HOPG samples was investigated by AFM measurements at the HOPG/mica step edges. Because the sample thickness varies with the sample position a method was developed to calculate the thickness distribution over the whole HOPG sample using microscope images. This method was compared to the AFM measurements to determine the accuracy of the calculation. By AFM measurements the thickness at selected sample positions could be investigated by the height difference at HOPG/mica edges as it is shown in the following figure.

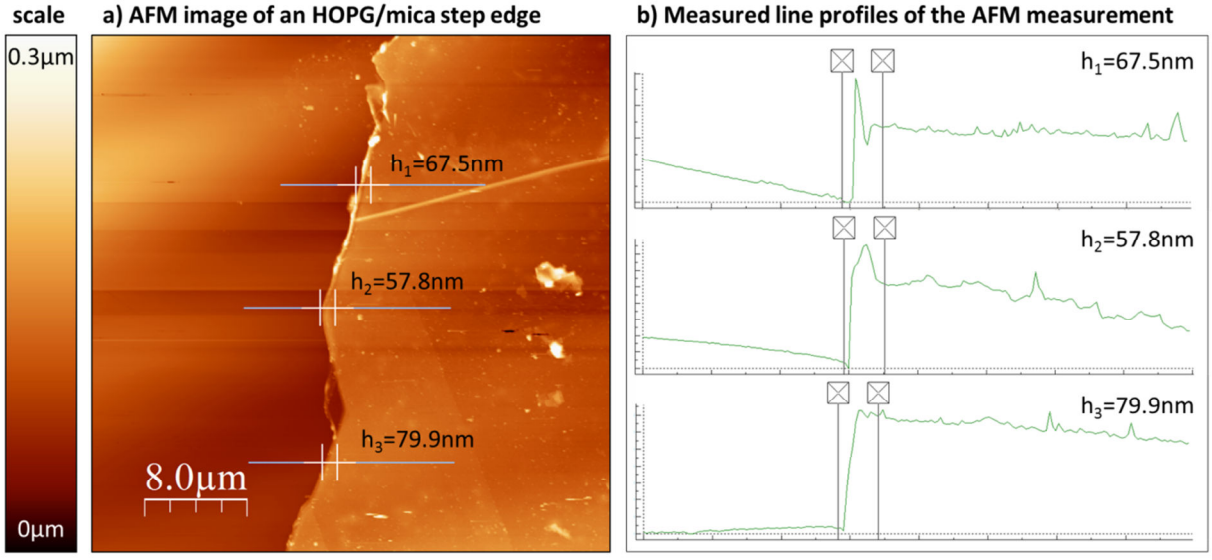

Figure 33: Determination of the sample thickness of thin HOPG samples by the measurement of the height difference at HOPG/mica step edges at three different positions. The AFM data was evaluated using the WSXM v.4 freeware program [126].

The measured thickness can only be obtained at HOPG/mica step edges where the mica surface serves as the reference height. As the figure shows the thickness varies strongly even for small sample areas. Most nano and micro structures were produced far away from the sample edges so that an alternative method had to be performed to determine the sample thickness at the structured surface areas.

Because single graphene layers transmit 97.7% of the visible light spectrum [121] and the transmittance of multiple graphene layers can be calculated, microscope images of thin HOPG samples were used to determine the sample thickness.

For the calibration of the sample images a grey scale foil was used with 24 different grey fields. The transmittance of every grey field could be measured with a UV/VIS spectrometer. After all grey fields were imaged in the bitmap format the green colour channel of the bitmaps were extracted. The average green colour value of every grey field was determined so that at the end the green colour values could be assigned to a transmittance (green colour value - transmittance). A formula for the transmittance of green light as a function of the sample thickness can be derived using the formulas presented in [127] (transmittance – sample thickness).

In summary, the green colour values over the whole sample can be used to estimate the sample thickness at every surface point. The details for the thickness determination by the calculation will be presented now.

A formula for the transmittance coefficient of a thin layer on an infinite thick substrate is presented in reference [127] and can be transferred for the graphite/mica sample system. Because the mica is finite in our experiments the formula of [127] has to be modified so that the transmittance coefficient will be

$$\tilde{t} = \frac{2\sqrt{N_{mica}}\cos(\alpha)}{\{\cos(\alpha) + N_{mica}\}\cos(N_g\delta_g) - i\left\{N_g + N_{mica}\frac{\cos(\alpha)}{N_g}\right\}\sin(N_g\delta_g)} \tag{48}$$

Here, α is the incident angle of the light to the sample surface, δ_g is relative graphite thickness given in units of $2\pi d_g/\lambda$ with $d_g$as the graphite thickness and λ as the wavelength of the incident light. N_{mica} and N_g are the generalized refraction indexes of mica and graphite. While N_{mica} only consists of the mathematically real part n_{mica}, N_g consists of real and imaginary part and equals therefore $(n_g + ik_g)$.

The presented formula can be checked, for example, by assuming no graphite layer $\delta_g = 0$. The transmittance T is the square of the transmittance coefficient $T = |\tilde{t}|^2$ and the sum of the transmittance T and the reflection R should be 1.

$$T + R = |\tilde{t}|^2 + R = \left[\frac{2\sqrt{N_{mica}}}{1 + N_{mica}}\right]^2 + \frac{[N_{mica} - 1]^2}{[N_{mica} + 1]^2} = \frac{{N_{mica}}^2 + 2N_{mica} + 1}{[N_{mica} + 1]^2} = 1 \tag{49}$$

The incident angle is perpendicular while using the microscope in transmitted light mode and so $\cos(\alpha) = 1$. Because the graphite thickness $d_g$is small compared to the incident light wavelength ($N_g\delta_g \ll 1$) the formula can additionally be simplified by $\cos(N_g\delta_g) \approx 1$ and $\sin(N_g\delta_g) \approx N_g\delta_g$.

$$\tilde{t} = \frac{2\sqrt{n_{mica}}}{(1+n_{mica}) - i\left\{(n_g + ik_g) + \frac{n_{mica}}{(n_g+ik_g)}\right\}(n_g+ik_g)\delta_g} \tag{50}$$

$$\tilde{t} = \frac{2\sqrt{n_{mica}}}{(1+n_{mica}) - i\left\{\delta_g(n_g+ik_g)^2 + \delta_g n_{mica}\right\}} \tag{51}$$

$$\tilde{t} = \frac{2\sqrt{n_{mica}}}{(1+n_{mica}) - i\delta_g n_{mica} - i\delta_g(n_g^2 + 2in_gk_g - k_g^2)} \tag{52}$$

$$\tilde{t} = \frac{2\sqrt{n_{mica}}}{(1+n_{mica}) + 2\delta_g n_g k_g - i\delta_g(n_g^2 - k_g^2 + n_{mica})} \tag{53}$$

The transmittance T is the square of the modulus of the transmittance coefficient and can be declared as

$$T = |\tilde{t}|^2 = \frac{4n_{mica}}{\left[(1+n_{mica}) + 2\delta_g n_g k_g\right]^2 + {\delta_g}^2\left[n_g^2 - k_g^2 + n_{mica}\right]^2} \quad . \tag{54}$$

In reference [128] values for the graphite bulk are reported as $n_g = 2.6$ and $k_g = 1.3$. The refractive index of mica (muskovit) is $n_{mica} = 1.563$ [129] perpendicular to the basal planes. The inverse function can be determined so that the relative graphite thickness can be given as a function of the transmittance.

$$\delta_g = \frac{2\pi d_g}{\lambda}$$

$$= \frac{\sqrt{\left\{\left[2n_gk_g\right]^2 + \left[n_g^2 - k_g^2 + n_{mica}\right]^2\right\} \cdot \left\{\frac{4N_{mica}}{T} - (1+n_{mica})^2\right\} + \left\{(1+n_{mica})2n_gk_g\right\}^2}}{\left[2n_gk_g\right]^2 + \left[n_g^2 - k_g^2 + n_{mica}\right]^2} \tag{55}$$

$$- \frac{(1+n_{mica})2n_gk_g}{\left[2n_gk_g\right]^2 + \left[n_g^2 - k_g^2 + n_{mica}\right]^2}$$

For incident green light with a wavelength of λ=500nm and the values for n_g, k_g and n_{mica} the formula for the transmission T as a function of the sample thickness d_g and the inverse function are approximately

$$T \approx \frac{6.252}{\left[2.563 + 8.495 \cdot 10^{7} d_g\right]^2 + 6.948 \cdot 10^{15} {d_g}^2} \tag{56}$$

$$d_g \approx 7.958 \cdot 10^{-8} \left[\sqrt{\frac{0.070}{T} - 0.036} - 0.193\right] [m] \ . \tag{57}$$

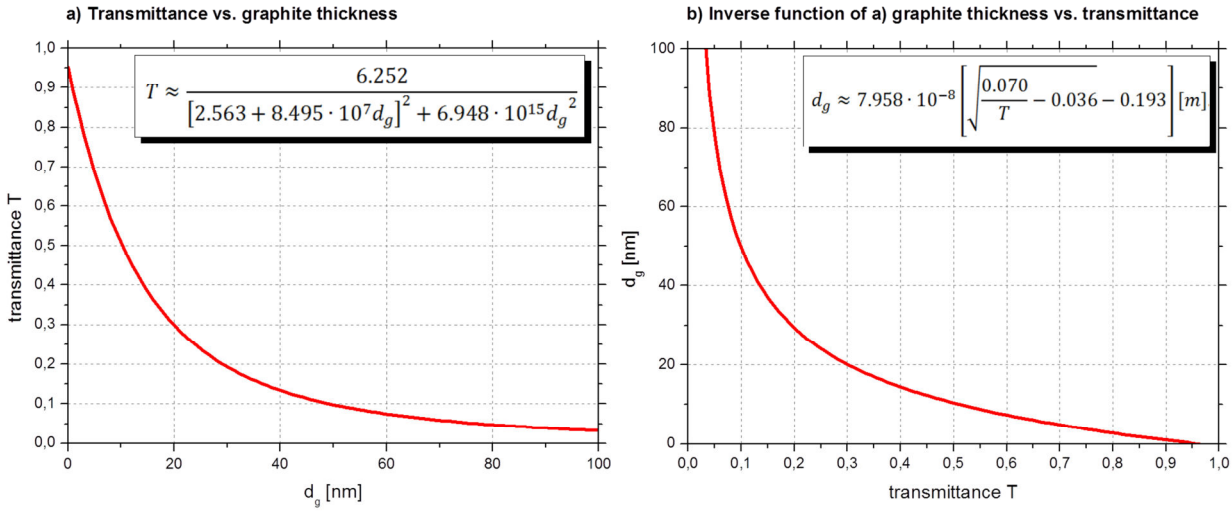

Figure 34: Transmittance as a function of the sample thickness and the inverse function derived from the formula presented in reference [127]. Without a sample on the mica substrate the transmission of green light is about 95.17%.

Using the evaluated formulas the mica transmittance is 95.17%. For an increasing graphite thickness the transmittance will decrease by the formulas presented in the figure.

There is a relation between the HOPG/mica transmittance $T_{HOPG+mica}$ and the mica transmittance T_{mica} given by

$$\frac{T_{HOPG+mica}}{T_{mica}} = \frac{T}{0.9517} \quad \Leftrightarrow \quad T = 0.9517 \cdot \frac{T_{HOPG+mica}}{T_{mica}}. \tag{58}$$

In equation (56) the transmittance T can be replace if the HOPG/mica and the mica transmittances are known. Because the transmittance of the HOPG/mica and the mica cannot be measured for every small sample area a calibration was performed to determine the transmittance using optical microscope images.

The images obtained from the optical microscope measurements are saved in RGB (red, green, blue) bitmap images in a 24bit format where every colour channel (red, green, blue) have values between 0 and 255. When the green colour channel is filtered pure black has a colour value of 0 and pure green has a colour value of 255. A grey scale foil with 24 (numbered: 0-23) different grey fields was investigated by optical microscope measurements. Here, the average green colour value of every grey field was determined. Additionally, the grey field areas are big enough (1·1cm²) to use a spectrometer that will

measure the transmittance to determine the dependency between a green colour value and a transmittance value.

The spectrometer (AVA AvaSpec-20048x14-USB2 – Avantes BV) uses a deuterium halogen light source (AVA AvaLight-DH-S-Bal-DUV --- 190-2500nm) to irradiate single grey field areas. All 24 grey fields were irradiated and the transmittances for wavelengths of 380-780nm are presented in the next plot. The transmittance of green light (λ=500nm) of every grey field was used for further calibration.

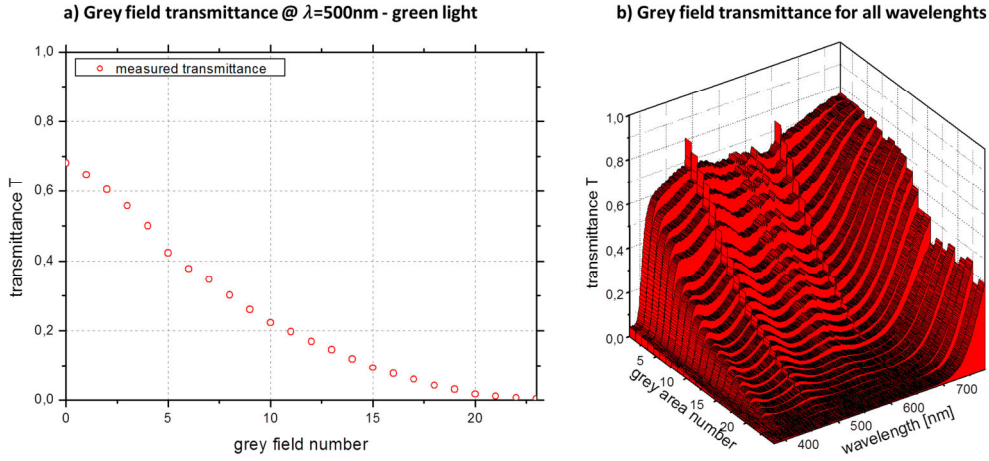

Figure 35: Transmittance of the grey fields on the grey scale foil. In b) all transmission values are shown for wavelengths between 380-780nm. In a) the transmittance of the grey fields for a wavelength of 500nm (green light) is shown.

The grey fields transmit 0-68% of the incoming green light. As mentioned before, every grey field was additionally investigated by optical microscope measurements. An average green colour value of every grey field was determined.

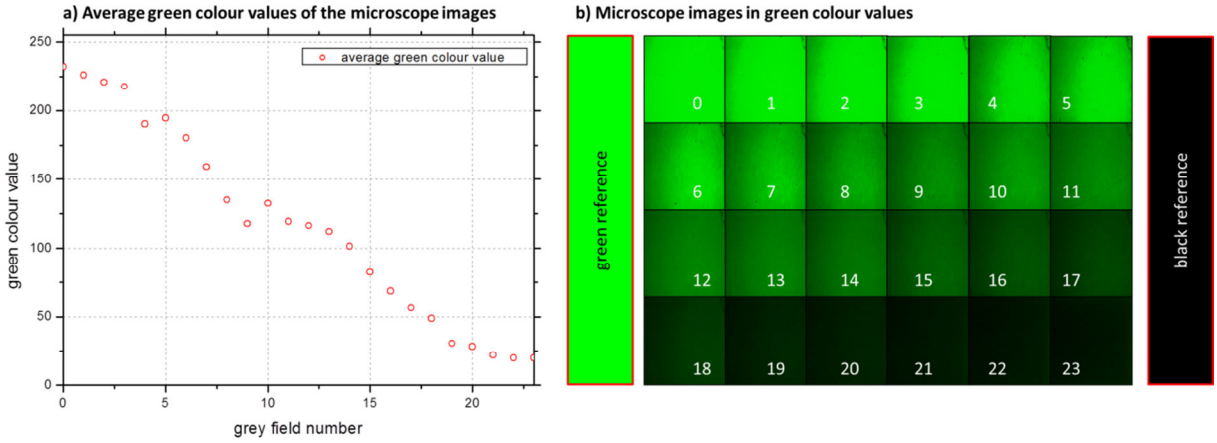

Figure 36: Results of the optical microscope measurements to obtain a dependency between the average green colour value and the grey field number. In b) all calibration images were resized from 760x572 pixels to show the measured colour gradient. The average green colour values were calculated for every image and plotted against the grey field number in a).

The results of the spectrometer measurements and the optical microscope measurements can be used to determine the transmittance as a function of the green colour val-

ue. The formula of the transmittance as a function of the green colour value (GCV) can be determined by fitting the values shown in Figure 37.

In the figure two data points were added manually. At a GCV of 0 (black) the transmittance is 0%. Furthermore, a reference measurement using the optical microscope was performed where no material was imaged. The parameters of the optical microscope were set so that image was not overexposed. In this context, the GCV of the image was 235.87 in average and the transmittance was 100%. The formula is

$$T_{HOPG+mica,mica} = 0.07 \cdot e^{\left(\frac{GCV}{93.6}\right)} - 0.07 \tag{59}$$

and the fitted line fits very well concerning real GCV-transmittance values (0-0%, 255-99.73%).

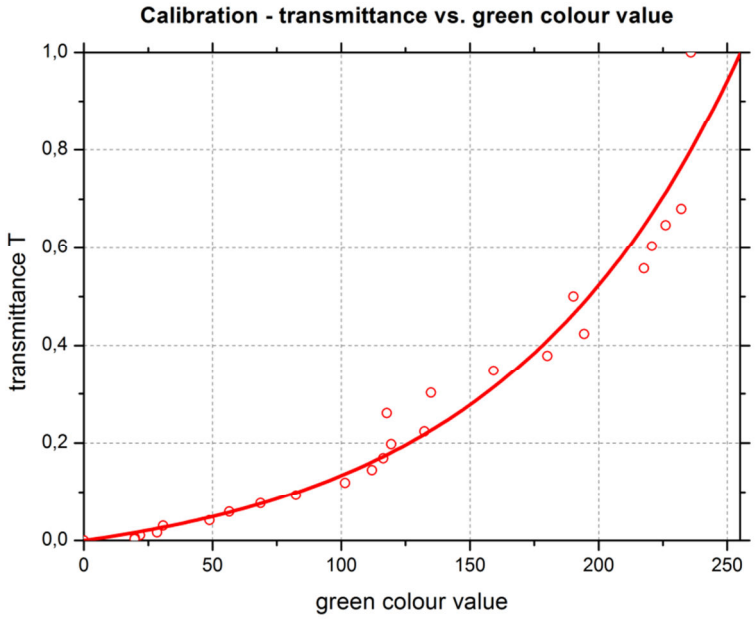

Figure 37: Transmittance as a function of the green colour value determined by optical microscope and spectrometer measurements.

The fitting formula is a good but also rough approximation of the data points. The deviation mostly has its origin in the microscope calibration presented in Figure 36. The equations (57-59) can be combined to obtain the sample thickness d_g as a function of the GCV of HOPG/mica and mica. The formula is

$$d_g \approx 7.958 \cdot 10^{-8} \left[\sqrt{0.074 \cdot \frac{\exp\left(\frac{GCV_{mica}}{93.6}\right) - 1}{\exp\left(\frac{GCV_{HOPG+\,mica}}{93.6}\right) - 1} - 0.036} - 0.193 \right] [m] \ . \tag{60}$$

As an example, the GCV of mica will be set to 250 ($T_{mica} = 94.17\% < 95.17\%$) to plot the sample thickness as a function of the GCV of HOPG/mica. In this context the GCV of HOPG/mica can only have values between 0 and 255.

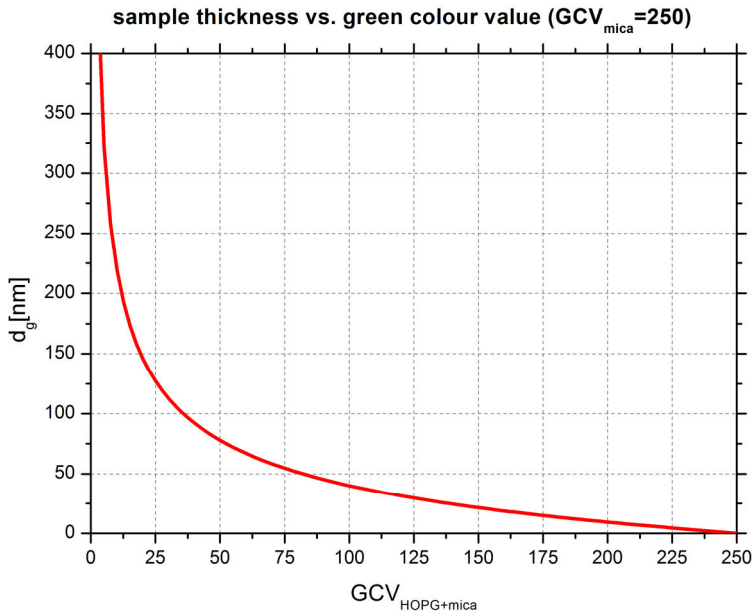

Figure 38: Thickness of the HOPG sample as a function of the green colour value (GCV) of HOPG/mica and an assumed GCV of mica of 250.

The calculation of the sample thickness for each pixel of an image was made by the MATLAB (matrix laboratory) program. An image was loaded by the program and the green colour value of every pixel was extracted which is the $GCV_{HOPG+mica}$ value. Because GCV_{mica} could not be determined for areas of HOPG/mica the average GCV_{mica} value of a free mica area in an image was used. Now, the graphite thickness could be determined by the formula for every image pixel. An example of the calculation results is presented in Figure 39.

To determine the accuracy of the calculation formula AFM measurements on the HOPG sample thickness were performed at different sample positions and compared to calculated HOPG sample thicknesses. The measured and calculated values are listed in the table of Figure 40.

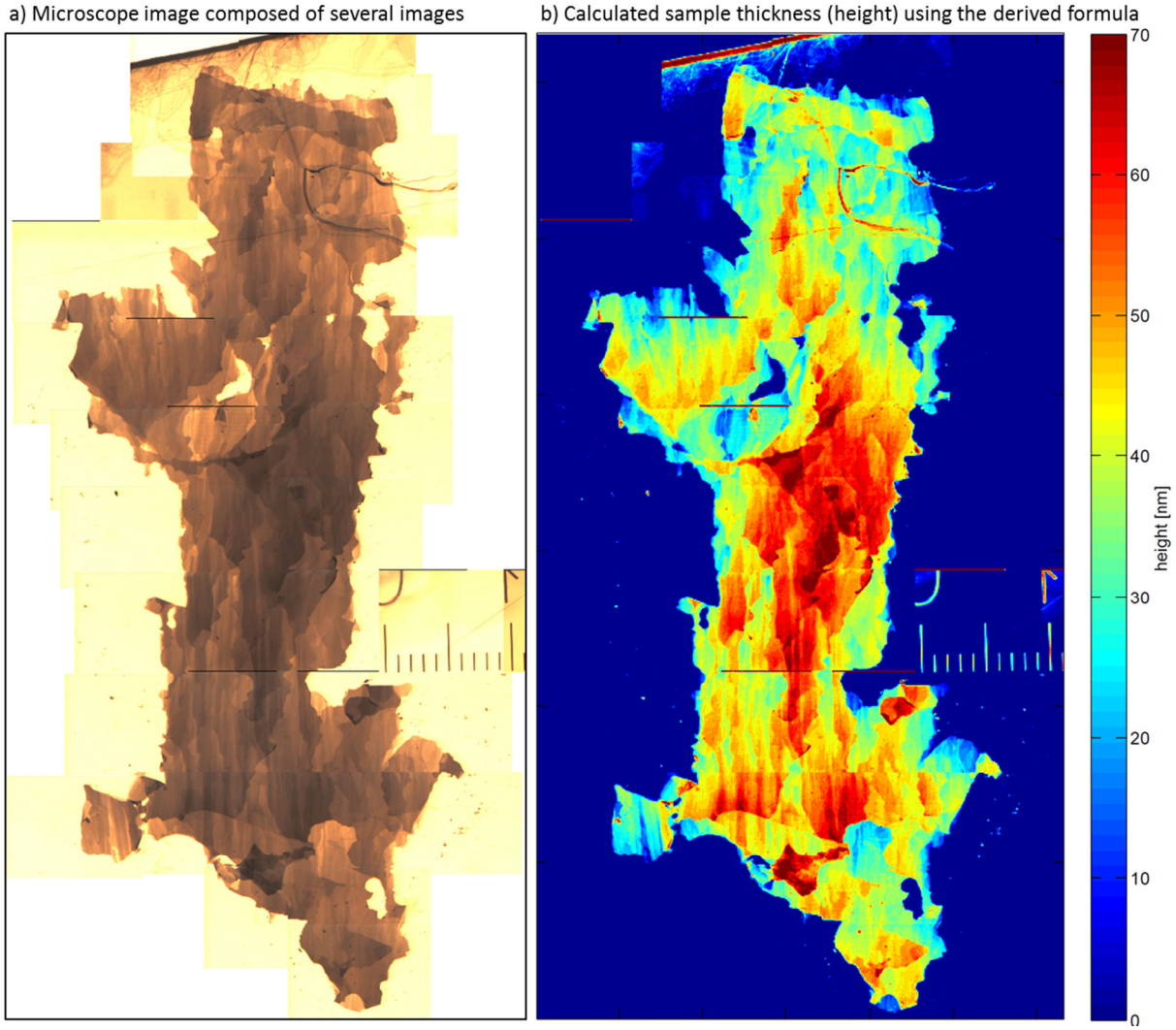

Figure 39: Example for the sample thickness determination. The height distribution was evaluated using a programmed MATLAB code to determine the sample thickness distribution over the whole sample and is presented in the right image.

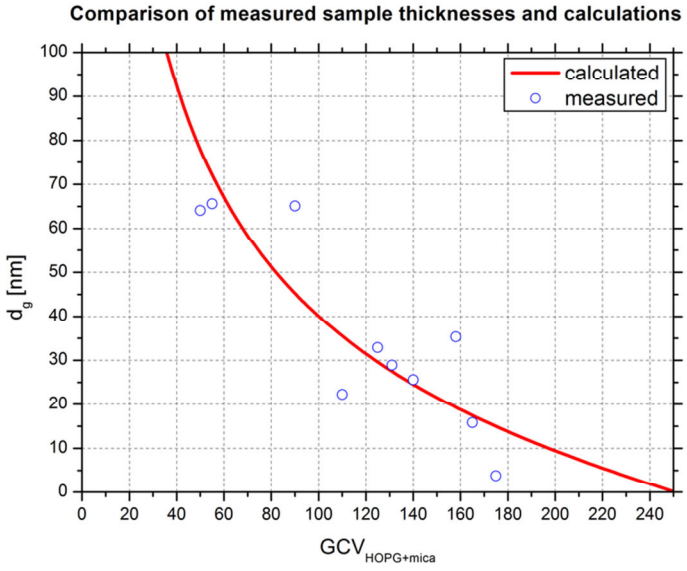

sample no.	measured: d_g [nm]	calculated: d_g [nm]	measured / calculated
1	32.9	28.21	1.17
	65.1	45.13	1.44
2	3.8	14.73	0.26
	35.3	19.80	1.78
3	64.1	78.51	0.82
	65.6	72.61	0.90
4	28.9	27.36	1.06
	15.8	17.43	0.91
5	25.6	24.27	1.05
	22.3	34.82	0.64

Figure 40: Comparison between calculated and measured sample thickness at two sample points for five different samples.

The measured data differs from the calculated data but is consistent with the fit of formula (60). The deviation between calculated and measured data can be partly explained by the AFM image presented in Figure 33. The AFM image shows that the sample thickness can vary strongly even in micrometre scale. Because pixels in the microscope images equal square micrometre fields the measured HOPG thicknesses using optics would have to be compared with an average over a number of AFM data.

However, the calculations can be used to approximately determine the thickness distribution over the whole sample. In this context, the needed ion dose for milling can be approximated for every sample position. Also thick sample areas can be determined where a milling process would be too much time-consuming.

4.4.3 Electrical conductivity and specific resistivity of HOPG samples

The electrical conductivity of the used HOPG was investigated both in the basal plane direction $\sigma_{x,y}$ and in the c-axis direction σ_z by four-probe measurements.

Four-probe measurements were performed to calculate the conductivity by the formulas introduced in chapter 3.8.2. The conductivity along the basal planes could be measured using thin HOPG samples. For the investigation of the conductivity along the c-axis thick HOPG samples were used. Because for thin and thick HOPG samples the same HOPG bulk material, the ZYA HOPG, was used the conductivity should be the same for both sample types.

For the use of four-probe measurements the sample thickness h has to be obtained for thin HOPG samples and the distance between the tips d for thick HOPG samples. Because the four-probe measurements have to be performed far away from HOPG/mica edges as it is described in chapter 3.8.2 no AFM measurements could be performed. In this context, the sample thickness was obtained by calculations presented in the last sub chapter 4.4.2. At the sample position where the four-probe measurements have been performed the sample thickness is approximately $h=95nm$. To determine the probe distance the four-probe measurements were performed using the self-constructed four-probe measuring device and the connected optical microscope. The microscope images were saved using the microscope camera. The images could be calibrated in the x- and y-direction by imaging sample surface features or structures with a known x-y-scale for every microscope magnification used.

The image size calibration is presented in the next figure where the size of the structures is known. Also an example of the four-probe measurement is shown where the tip distance is determined using the image size calibration for a microscope magnification of 1.

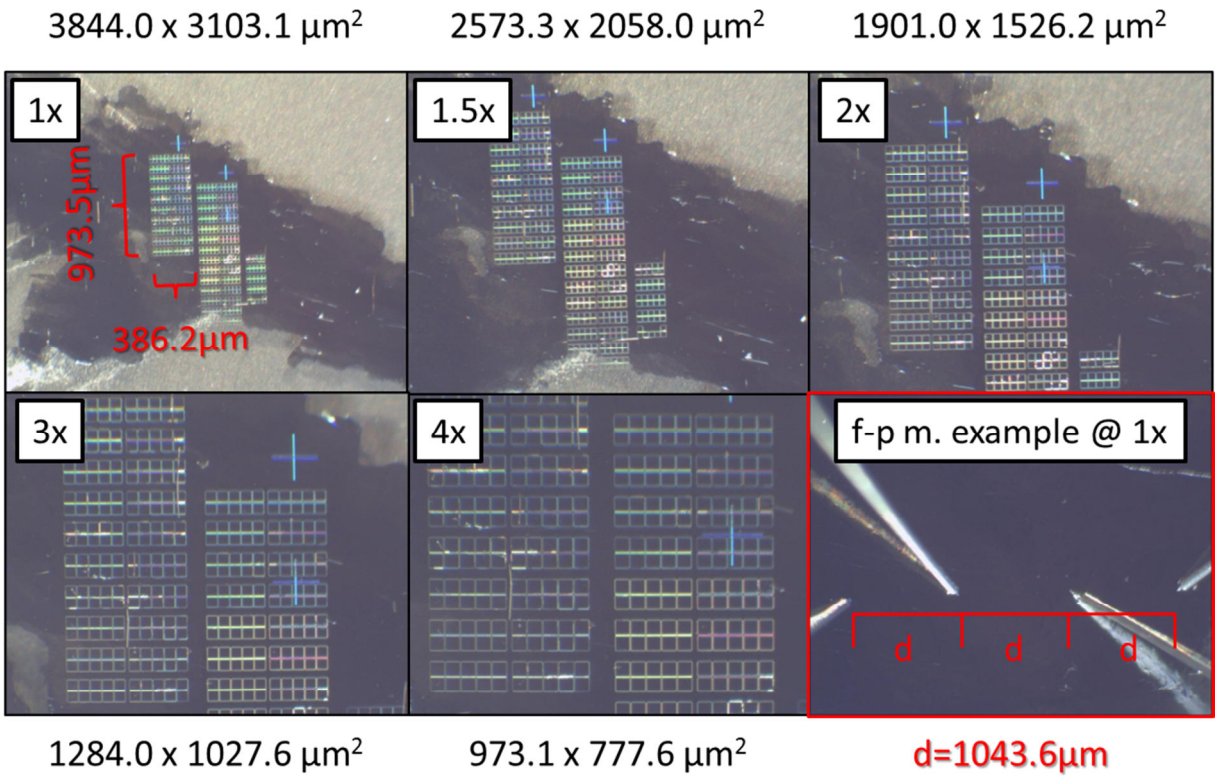

Figure 41: Image size calibration for different microscope magnifications 1x-4x using surface structures with a known size of 386.2 x 973.5 µm². The image size calibration is needed to determine the tip distance in a four-probe measurement for different microscope magnifications. Additionally, an example for a four-probe measurement at 1x microscope magnification is shown in the bottom right corner where the tips are arranged in a line with a constant distance of d=1043.6µm.

By four-probe measurements the voltage between the voltage tips was measured as a function of the current applied between the current tips. To determine the conductivity the formulas derived in chapter 3.8.2 can be used due to the linear tip arrangement during the measurements. Because the conductivity is constant in the basal plane direction $\sigma_x = \sigma_y = \sigma_{x,y}$ the formula for thin HOPG samples can be used to determine $\sigma_{x,y}$ or rather the specific resistivity $\rho_{x,y}$ where U/I is the slope $d\,U/dI$ using the line of best fit and the sample thickness h=95nm as mentioned before.

$$\left(\sqrt{\sigma_x \cdot \sigma_y}\right)_{thin} = \frac{\ln(2)}{\pi h}\frac{I}{U} \tag{61}$$

$$\sigma_{x,y} = \frac{\ln(2)}{\pi h}\frac{1}{\frac{dU}{dI}} \tag{62}$$

$$\rho_{x,y} = \frac{\pi h}{\ln(2)}\frac{dU}{dI} \tag{63}$$

The conductivity or rather the specific resistivity along the c-axis direction can be calculated using the slope dU/dI of the four-probe measurements and the tip distance d for thick HOPG samples and the calculated basal plane conductivity or rather specific resistivity out of thin HOPG sample measurements.

$$\left(\sqrt{\sigma_{x,y} \cdot \sigma_z}\right)_{thick} = \frac{1}{2\pi d}\frac{I}{U} \tag{64}$$

$$\sigma_z = \frac{1}{\left(2\pi d \cdot \frac{dU}{dI}\right)^2} \cdot \frac{1}{\sigma_{x,y}} \tag{65}$$

$$\rho_z = \left(2\pi d \cdot \frac{dU}{dI}\right)^2 \cdot \frac{1}{\rho_{x,y}} \tag{66}$$

The measured data for the determination of the conductivity or rather specific resistivity of the HOPG using four-probe measurements is shown in the next figure.

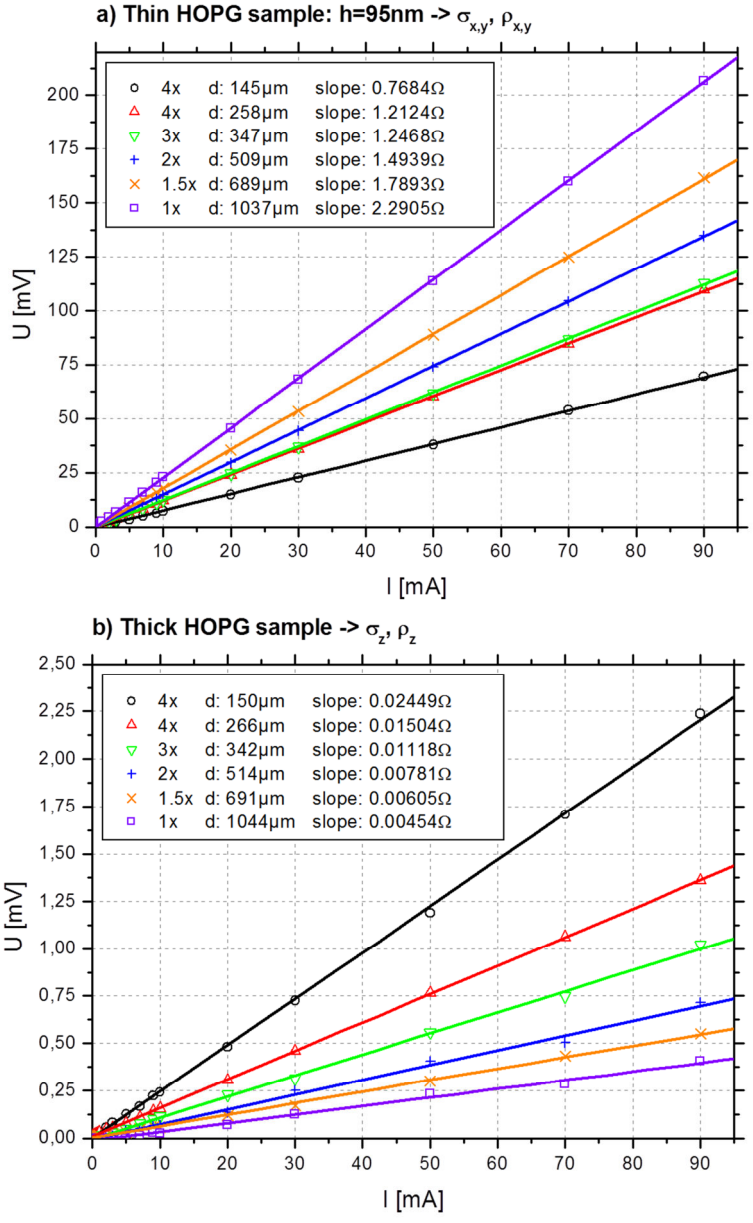

Figure 42: Results of the four-probe measurements to determine the conductivity or rather the specific resistivity of the HOPG used in this project. The voltage was measured as a function of the current at different tip distances while the tips were linear arranged. Four-probe measurements were performed both on a thin and a thick sample to determine the anisotropic conductivity.

In Figure 42 a) the measured slope dU/dI increases with the tip distance for thin HOPG samples. This behaviour contradicts the prognosis presented in reference [110] and the formula for the conductivity in basal plane direction that should be independent from the tip distance. In comparison, the slope dU/dI decreases with the tip distance for thick HOPG samples as presented in Figure 42 b). Although, this behaviour is predicted the resulting conductivity or rather specific resistivity in c-axis direction depends on the results for the values in basal plane direction where the values must not be dependent on the tip distance. To insert $\sigma_{x,y}$ and $\rho_{x,y}$ into the formulas for σ_z and ρ_z the tip distances must be about the same for the measurements on thin and thick HOPG samples because for the calculation of σ_z and ρ_z the corresponding values for $\sigma_{x,y}$ and $\rho_{x,y}$ have to be known that vary with the tip distance. The values for $\sigma_{x,y}$, $\rho_{x,y}$, σ_z and ρ_z are shown in the next figure.

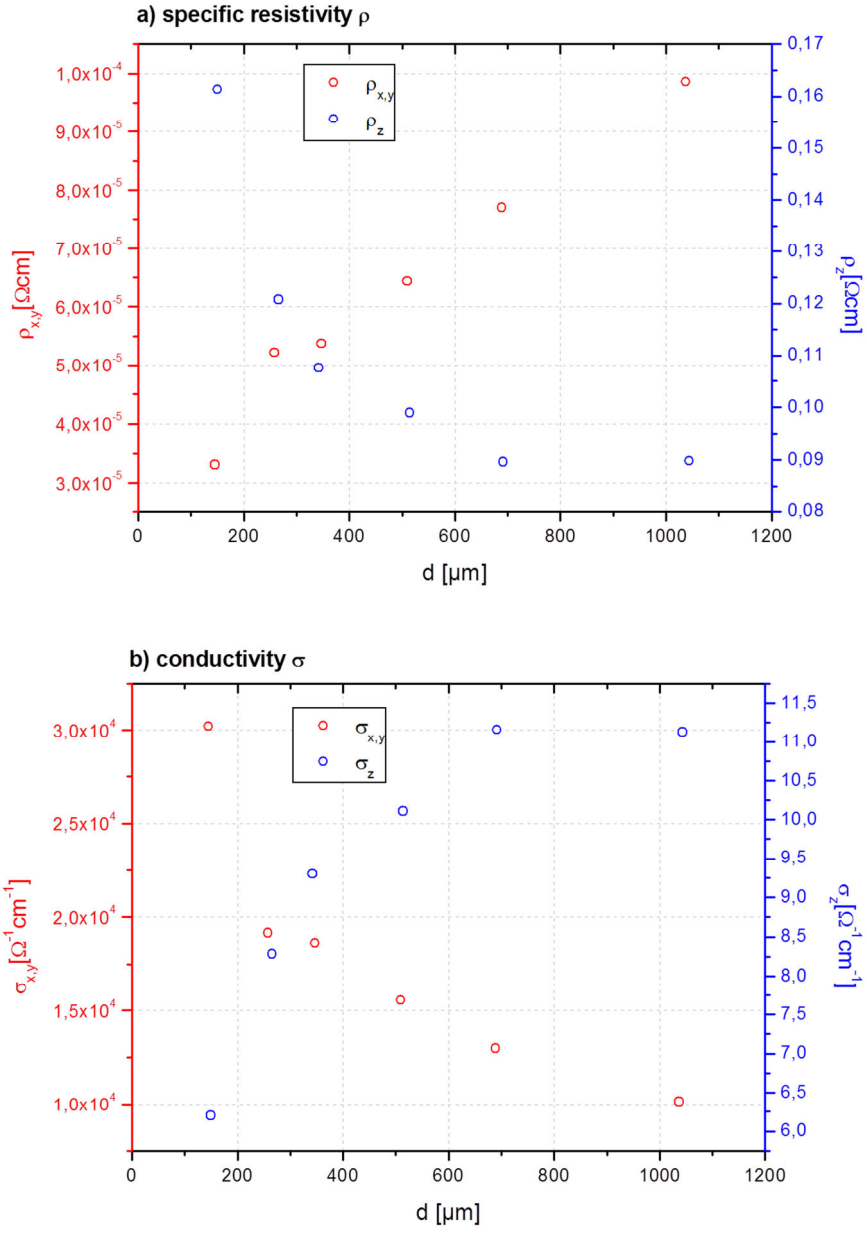

Figure 43: Measured conductivity and specific resistivity along the basal planes and in c-axis direction of the used HOPG samples investigated by four-probe measurements.

As mentioned before in reference [116] the conductivity and the specific resistivity of HOPG in basal plane direction are $\sigma_{x,y} = 2.2 - 2.9 \cdot 10^4\ \Omega^{-1}\,\mathrm{cm}^{-1}$ and $\rho_{x,y} = 3.5 - 4.5 \cdot 10^{-5}\ \Omega\,\mathrm{cm}$. In the c-axis direction the literature values $\sigma_z = 4.0 - 6.7\ \Omega^{-1}\,\mathrm{cm}^{-1}$ and $\rho_z = 0.15 - 0.25\ \Omega\,\mathrm{cm}$. For very short tip distances of 150µm the measured values correspond to the literature values. The conductivity along the basal planes decreases while the conductivity in c-axis direction increases with increasing tip distances.

One explanation could be the structure of the HOPG. Because even high quality ZYA-HOPG consists of several slightly shifted micro crystals the current will flow through a number of these crystals for tip distances of up to 1000µm. The current transition from one crystal to another causes an additional resistance so that in the case of basal plane current flow the conductivity $\sigma_{x,y}$ will decrease and the specific resistivity $\rho_{x,y}$ will increase with increasing tip distances. For high tip distances additional micro crystals will change the absolute amount of micro crystals only slightly. In this case, the values for $\sigma_{x,y}$, $\rho_{x,y}$, σ_z and ρ_z will also increase or rather decrease slightly. Because there is a strong change for tip distances <200µm the dimension of the HOPG crystals can be in the dimension of several cubic micrometres.

4.5 Chapter summary

In this project highly oriented pyrolytic graphite was used to prepare thin and thick HOPG samples for further ion beam structure production. Carbon atoms are arranged in graphite due to the sp^2 hybridization in a hexagonal close packaged lattice where the atoms are covalently bonded in the basal plane direction in a honeycomb arrangement. Perpendicular to the basal planes, in the c-axis direction, only weak interaction forces hold the basal planes together. Because of the lattice arrangement the conductivity in HOPG is anisotropic. In this case the conductivity along the basal plane direction is about 5000 times larger than in c-axis direction at room temperature.

Graphene is a single layer of graphite and has been strongly investigated during the last few years due to its mechanical but mostly due to its electrical properties. At the K and K´ points of the Brillouin zone the conductance and valence band merge so that the electrons of the graphene behave like quasi massless relativistic particles and can be described by the Dirac equation. Graphene electrons have group velocities near the speed of light and due to the graphene properties the mean free path of electrons can be very high. Although, the electric properties of graphene could provoke new opportunities for semiconductor applications they cannot be transferred to a graphite bulk of many graphene layers.

The high conductivity of HOPG along the basal planes should be transferred to the nano and micro structures produced by ion beam lithography. While the structural properties of these structures can be investigated for structures on thick HOPG sample surfaces

thin HOPG samples have to be prepared in the case of electrical property investigations. While thick samples are prepared by slicing or by exfoliation along the basal plane direction and are ready to use instantly the production process of thin samples requires a special cleaning process in acetone and isopropanol to clean the sample surface.

The prepared and cleaned thin HOPG samples are only about 30-150nm in thickness and are placed on a mica (muscovite) insulator. If the cavity depth is higher than the HOPG thickness the produced structures will be electrically isolated from the rest of the HOPG sample. The structures can then be electrically investigated without the influence of the HOPG sample by four-probe measurements.

The produced samples have to be classified concerning the surface quality and cleanness. The sample thickness has to be measured in the case of thin HOPG samples and the anisotropic conductivity or rather specific resistivity has to be analysed.

The surfaces of the prepared samples were investigated by microscope, AFM and STM measurements and show in most cases a good surface quality and lattice arrangement. Thin HOPG samples are slightly contaminated due to the production process.

Because the local thickness of thin HOPG samples has to be known for structure production and structure investigation the sample thickness was investigated by AFM measurements at HOPG/mica step edges. Because the sample thickness could only be determined at sample edges by AFM measurements an additional possibility was developed to determine the sample thickness distribution over the whole sample surface by the use of optical microscope images. While the sample thickness as a function of the transmittance could be derived theoretically the transmittance as a function of the image colour value was derived using an image calibration with the help of a calibration grey scale foil. In result, the dependency between the sample thickness and the image colour value (green colour value or GCV) could be derived to obtain the sample thickness for every sample surface point. The prepared thin HOPG samples are up to 150nm in thickness.

For the determination of the anisotropic conductivity of the prepared samples four-probe measurements were performed where the tips were arranged along a line at known tip distances so that the formulas presented in chapter 3.8.2 could be used to calculate the conductivity or rather specific resistivity in basal plane and c-axis direction. While the measured values are equal to the literature values for tip distances below 150µm in basal plane and c-axis direction the conductivity increases in basal plane direction and decreases in c-axis direction for tip distances above 150µm. One explanation could be the HOPG structure. HOPG consists of several small crystals of a few cubic micrometres in size. If a current is applied between two points an additional resistance will occur at crystal transition points. The summed additional resistance will be large for large tip distances and small for small tip distance. This means that the conductivity along the basal planes will be higher for small than for large tip distances.

5. Structural properties

In this chapter the structure production and the structural properties as a function of the kinetic ion energy and the ion dose will be discussed for the impact of gallium ions into HOPG surfaces. Additionally, the influence of process parameters like the ion current, the sample type, the aperture size and the amount of loops will be investigated.

Both, the low-dose and the high-dose irradiation process were investigated concerning the resulting depth and width of produced structures by AFM and optical microscopy. While for the high-dose irradiation the structure production can be performed on thin and thick HOPG samples the low-dose irradiation process was combined with a subsequent oxidation process performed in the oxidation furnace or by ozone. For the investigation of structural properties so-called test structures were produced that will be introduced in the following section.

5.1 Test structures

Test structures were produced for the structural properties investigation. Area test structures are 500·500nm² and are arranged in a 6·6 patterning field. Every test structure of the patterning field was irradiated with an individual area dose to investigate structural properties as a function of the ion dose. Figure 44 shows a schematic ion distribution in the sample for possible dot, line and area test structures.

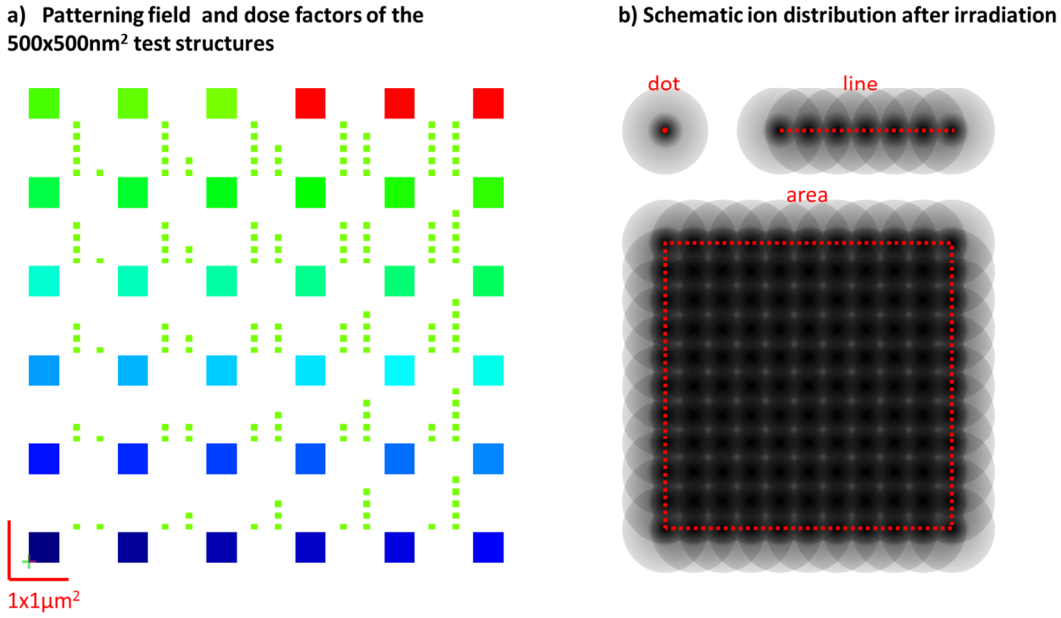

Figure 44: a) Shows the patterning field of the area test structures. The colours indicate an increasing dose factor. The small squares were irradiated as markers for orientation. In b) a schematic ion distribution after the irradiation is shown for a dot, a line and an area.

The dose factor for test structures in the patterning field increases from left-bottom to top-right and is indicated by the colour scale.

Figure 44 b) shows an important thing for the irradiation process. Although, all structures are produced by dots as explained in chapter 3.1.3 the real deposited ion dose along a line or in a dot can differ from the predefined ion dose. Because the ion beam has a Gaussian ion distribution the area dose along a line or in the centre of a dot will always depend on the focus size. Only in the centre of an area test structure the area dose will be equal to the predefined area dose because the ion distribution in the beam or rather the beam focus becomes unimportant. In the centre of the areas the ion distribution of every dot will overlap.

5.2 Low-dose irradiation and oxidation furnace

The presented test structures were produced using low-dose irradiation and a subsequent oxidation process by using the oxidation furnace at 500°C

After the production process the resulting area test structures were investigated concerning their structural properties, mainly concerning the structure depth, but also concerning the structure width. The structure depth was investigated depending on the deposited ion dose and the kinetic ion energy. First the results for the low-dose irradiation and a subsequent oxidation process in the oxidation furnace will be presented. The test structures were produced at kinetic ion energies of 15keV, 20keV, 25keV, 30keV, 35keV and 40keV at area doses up to 400µAs/cm^2. The range of the kinetic ion energy of 15-40keV is nearly the maximum kinetic ion energy achievable with the ionLiNE.

Because the oxidation was performed in the oxidation furnace the area test structures were mainly produced on thick HOPG samples. Although, for thin samples the ozone oxidation should be performed due to a sample and structure destruction one experiment was performed for thin HOPG at a kinetic ion energy of 40keV. The structures that were not destroyed during the heating process were investigated concerning their structural properties to compare the results with the structure production on thick HOPG samples and to identify possible differences between the structure productions of different sample types.

The investigations of the test structures were performed by AFM measurements. To give an overview of measurements concerning the structure depth an AFM image and the according line profiles are shown in the next figure.

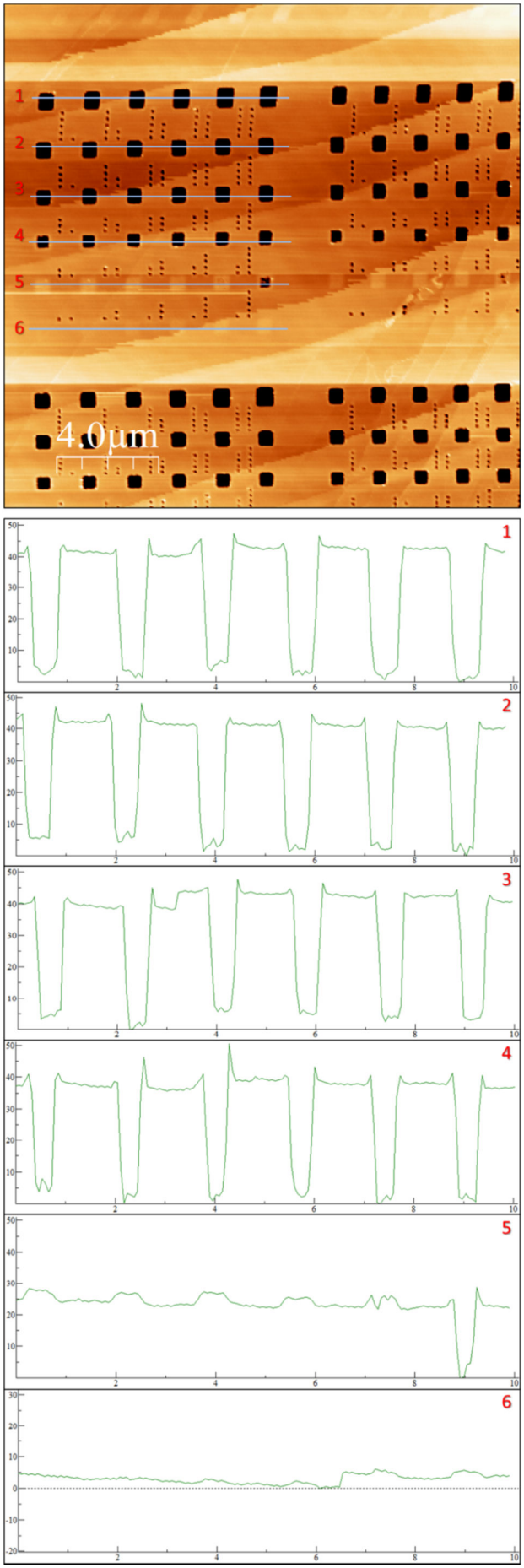

Figure 45: AFM image of the produced test structures that were evaluated with the WSXM software [126]. The produced 500·500nm² fields are arranged in a pattern of 6·6 fields. Under the AFM image the line profiles of the area test structures are shown and scaled equal in the z-direction for an optimal comparison (-20 to 30nm). The line profiles are scaled in nanometres along the z-direction and in micrometres along the x-direction (0-10µm).

The AFM measurement shows the produced structures using gallium ions with a kinetic ion energy of 30keV after low-dose irradiation and a subsequent oxidation process in the oxidation furnace at 500°C on a thick HOPG sample. Every area test structure in the patterning field was irradiated with an individual area dose of 0-400µAs/cm². As the image shows there is a critical ion dose below the test structures suddenly disappear.

The line profiles show a nearly constant structure depth in line profiles 1-4 of about 40nm. The structure depth decreases strongly below a critical area dose in line profile 5. Below a critical area dose no material is removed from the sample surface after the oxidation process at the irradiated areas. Areas that were irradiated with an area dose below the critical area dose form hills on the sample surface. This can be explained by the implanted gallium ions that deform the lattice arrangement of the solid atoms. The height of these hills decreases with smaller area dose. The hills are hardly visible for areas in line profile 6.

The structure width of the area test structures increase with increasing area dose. This can be explained by the recoil and ion trajectories after the impact of the gallium ions into the solid. The structure width of the structures will be discussed in chapter 5.2.3 in more detail.

5.2.1 Structure depth vs. area dose - experiments

The evaluation of the structure depth for all measured data was performed using a modified version of the so-called clusterizer software developed by Dipl.-Phys. N. Grönhagen during his diploma thesis at the Technische Universität Dortmund [130]. The software determines the structure depth of the AFM measurements semiautomatic using the HOPG surface as the reference height.

The results of the measured structure depth of the area test structures as a function of the area does for different kinetic ion energies are shown in the following figure. For all experiments a 30µm aperture was used. The ion currents during the irradiation processes are shown in the figure too.

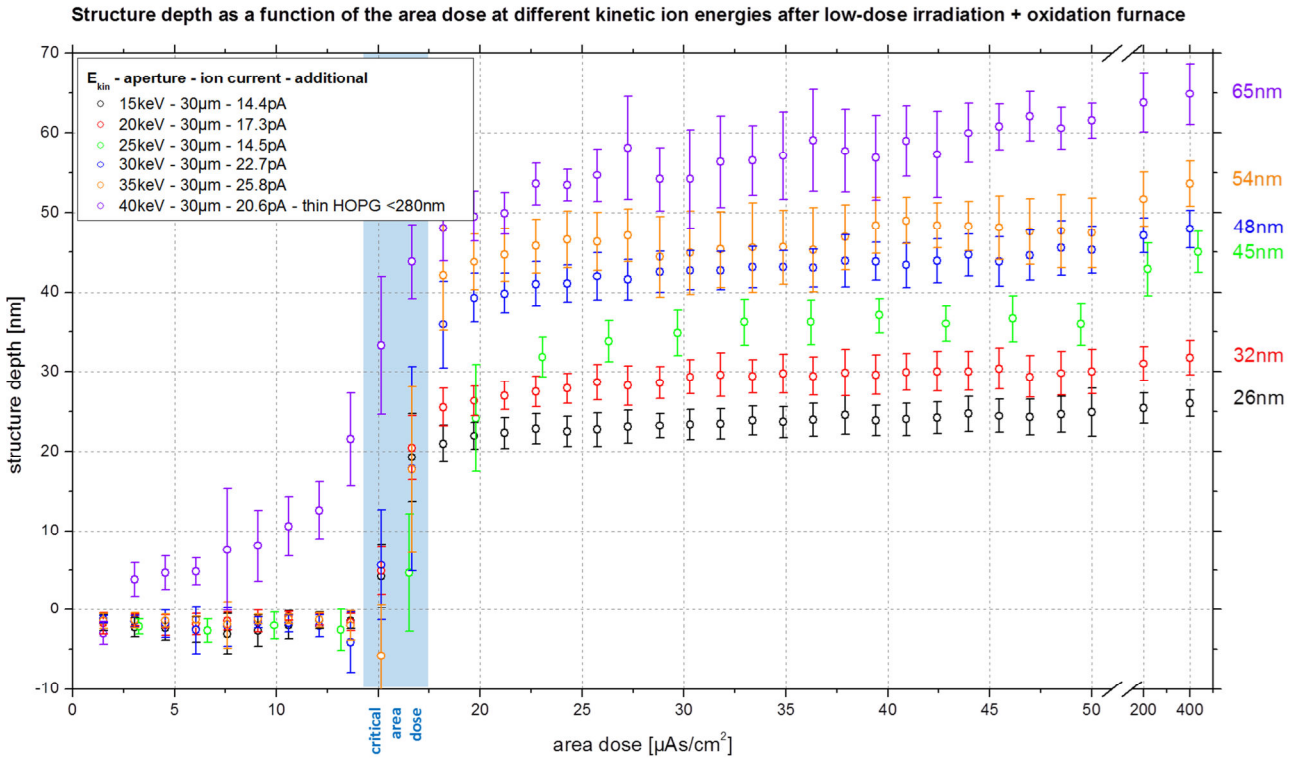

Figure 46: The structure depth of the test structures was investigated for area doses of 0-400µAs/cm² at kinetic ion energies of 15keV, 20keV, 25keV, 30keV, 35keV and 40keV. The area test structures were produced on thick HOPG samples except the 40keV process where a thin HOPG sample was used with a sample thickness below 280nm.

While at low area doses below 14µAs/cm² no area test structures are produced and only small hills appear at the irradiated areas shown in line profile 5 of Figure 45 and indicated by the negative structure depth values in Figure 46 there is a critical area dose at 14.0-17.5µAs/cm² (15.75µAs/cm² in average) where the structure depth increases strongly.

The critical area dose is equal for all experiments on thick HOPG samples and does not depend on the kinetic ion energy or the ion current. The defect or the so-called vacancy

density reaches a critical value so that the irradiated areas can be removed from the sample by an oxidation in the oxidation furnace.

The critical area dose for test structures on the thin HOPG sample is about 2.5-17.5µAs/cm² and differs from the critical area dose of the area test structures produced on thick HOPG. A first assumption could be a systematic error that occurred during the lithography process. Other explanations for the difference relative to the results for thick HOPG samples could be the low amount of basal plane layers, the sample surface quality, thickness variations and the local lattice structure of the thin HOPG sample. Because all other data is more consistent the critical area dose for low-dose irradiation processes will be assumed as 15.75µAs/cm².

Above the critical area dose the structure depth increases slightly. Even for an area dose of 400µAs/cm² the average structure depth is nearly the same as it is for an area dose near the critical area dose for all experiments.

Important to notice is that the maximum structure depth increases with the kinetic ion energy. This behaviour can be explained by the increasing penetration depth of the incident ions with increasing kinetic ion energy that TRIM simulations do predict and that is explained in the next subchapter.

Because the kinetic ion energy range of 15-40keV is the maximum range achievable the ionLiNE the resulting structure depths of 20-70nm presented in Figure 46 are the only structure depths that can be produced by low-dose irradiation production processes.

5.2.2 Structure depth vs. area dose – TRIM simulations

The structure depth as a function of the area dose and the kinetic ion energy can be explained by TRIM simulations. First investigations of our group were performed and presented in reference [131]. As mentioned in chapter 2.6.2 the TRIM program can calculate the ion and recoil trajectories dynamically and therefore the ion and recoil distributions. The results of the TRIM simulation for a graphite sample irradiated with 5000 gallium ions at different kinetic ion energies are presented in the next figure.

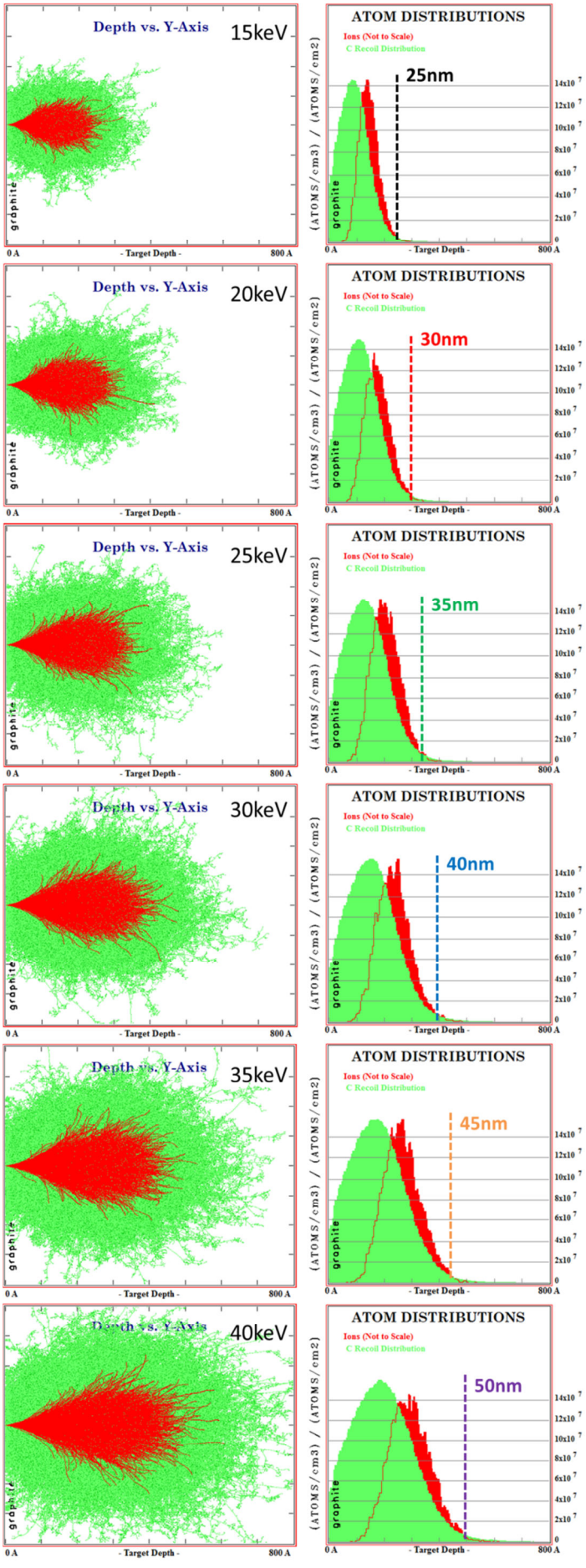

Figure 47: Ion and recoil trajectories and distribution as a function of the kinetic ion energy simulated by the TRIM program for the impact of 5000 gallium ions into a graphite solid. The atom distribution plots show a rescaled ion distribution due to clarity reasons. The real scale of the ion distributions are by a factor of 126(15keV), 134(20keV), 188(25keV), 208(30keV), 238(35keV) and 237(40keV) smaller than shown in the plots. The shown target depth of all plots is 0-80nm.

While the plots in chapter 2.6.2 show the ion and recoil trajectories for various ions and solids Figure 47 shows the trajectories for various kinetic ion energies.

The maximum penetration depth of ions and recoils increases with increasing kinetic ion energy as the trajectory plots but also the distribution plots show. The distribution plots are given in units of atoms/cm^3 per atoms/cm^2 and are normalized concerning the ion dose. If the data is multiplied by the ion dose used in the experiments in units of atoms/cm^2 the distributions will be given in atoms/cm^3.

The distribution plots show a shift of the maximum distribution values of ions/recoils and an increase of the distribution width as a function of the kinetic ion energy. Because the ion distribution is much smaller than the recoil distribution the resulting lattice disorder is mainly caused by the recoils and not by the implanted ions.

In a first approximation the maximum structure depth depends on the ion and recoil density due to the lattice destruction after the irradiation process. The approximat-

ed structure depths are shown in the distribution plots of Figure 47. Compared to the measured structure depths for high area doses presented in Figure 46 the approximated values of the TRIM calculations are always smaller. The approximated (measured) values are 25nm(26nm), 30nm(32nm), 35nm(45nm), 40nm(48nm), 45nm(54nm) and 50nm(65nm).

While the structure depth can be explained by trajectory and atom distributions in a first approximation the critical area dose and the structure depth can be explained by TRIM simulations concerning the vacancy distribution in the solids after the irradiation process. Vacancies occur when a solid atom is removed from its original site and the original site stays unoccupied. The number of vacancies is equal to the sum of the interstitials and the atoms that were removed from the target volume [69]. The vacancy distribution was calculated by the TRIM program for the impact of 5000 gallium ions into a graphite solid at kinetic ion energies of 15-40keV and is shown in the following figure.

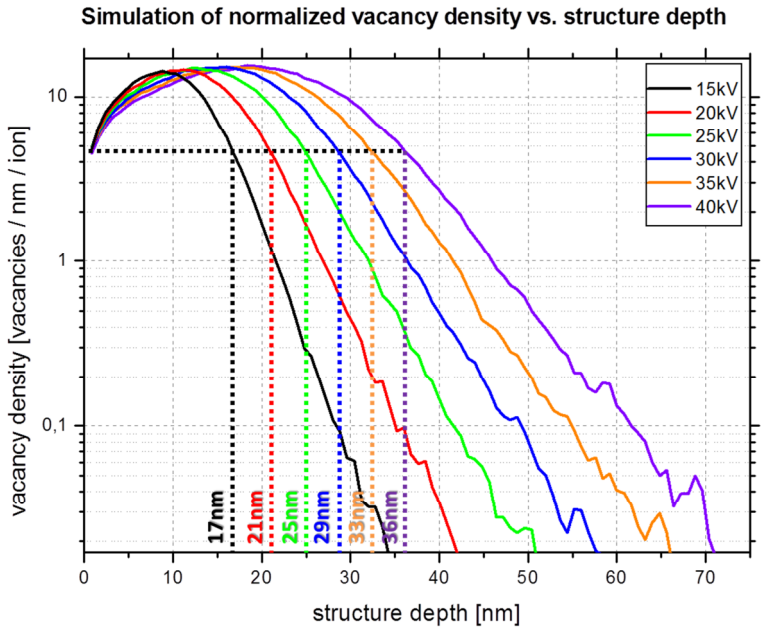

Figure 48: The TRIM simulated and normalized vacancy density as a function of the structure depth and the kinetic ion energy. For all calculated data the vacancy density is highest a few layers below the sample surface.

Assuming that the structure depth also dependents on the vacancy density in the HOPG sample there must be a critical vacancy density. Because the amount of vacancies depends on the amount of incident gallium ions, the critical vacancy density is a function of the critical area dose. Only when the area dose at the first surface layer is higher than the critical area dose the first layer can be oxidized.

As Figure 48 shows the vacancy density near the sample surface is always smaller than in the next few layers. If the area dose at the sample surface is higher than the critical area dose all next layers will be oxidized, too, so there has to be a strong structure depth increase when the surface area dose equals the critical area dose of 15.75µAs/cm^2. This behaviour was measured and shown in Figure 46 where a strong increase in the structure depth at the critical area dose was observed. In comparison the calculated (and

measured) structure depth slightly above the critical area dose (18.0µAs/cm²) are 17nm(21nm), 21nm(25nm), 25nm(24nm), 29nm(36nm), 33nm(42nm) and 36nm(48nm).

The vacancy distributions per ion presented in Figure 48 can also explain the slightly increase for area doses above the critical area dose. Because the vacancy density decreases strongly in deeper regions a high amount of additional gallium ions would be needed to raise the structure depth. To increase the structure depth by for example 20% (17nm→20nm, 21nm →25nm, 25nm →30nm, 29nm →35nm, 33nm →40nm, 36nm →43nm) the vacancy density has to be increased for all data in Figure 48 by a factor of 3.2.

Because the vacancy density per ion is constant near the surface for all kinetic ion energies the critical area dose has to be constant and independent from the kinetic ion energy. This behaviour was shown in Figure 46 where the critical are dose could be determined and is in the range of 14.0-17.5µAs/cm² (15.75µAs/cm² in average).

As mentioned before and presented in reference [131] the normalized vacancy density ρ_n of Figure 48 can be used to calculate a critical vacancy density ρ_c in units of vacancies/nm³ by a known critical area dose $D_{c,area}$. The normalized vacancy density at the surface is 4.81 vacancies/nm/ion for all kinetic ion energies. The critical area dose is 15.75µAs/cm² or 0.98 ion/nm². The critical vacancy density is then

$$\rho_c = \rho_n \cdot D_{c,area} = 4.81 \frac{vacancies}{nm \cdot ion} \cdot 0.98 \cdot \frac{ion}{nm^2} = 4.73 \frac{vacancies}{nm^3} \quad . \tag{67}$$

The relation of vacancies to solid atoms that is needed for an oxidation can be calculated. The critical vacancy density is known and only the amount of atoms per cubic nanometre must be calculated. For a honeycomb arrangement like in HOPG the amount of atoms per nm³ can be calculated by the formula

$$atoms\ per\ nm^3 = \frac{2}{V_{\text{honeyc.}}} = \frac{2}{\frac{3}{2} \cdot \sqrt{3} \cdot (0.142nm)^2 \cdot 0.335nm} = 113.96 \frac{atoms}{nm^3} \quad . \tag{68}$$

The minimum vacancy to solid atom relation η_{min} can now be calculated and is

$$\eta_{min} = \frac{4.73 \frac{vacancies}{nm^3}}{113.96 \frac{atoms}{nm^3}} = 0.04 \frac{vacancies}{atoms} \Longrightarrow 4.15\%\ vacancies \quad . \tag{69}$$

Already at this point the difference in the ion dose concerning the low-dose and high-dose structure production can be approximated. While for low-dose structure production the local vacancy density must be above 4.15% and already one gallium ion can produce 427.3 vacancies for high-dose structure production in a direct milling process the sputter yield is only 1.423 sputtered atoms per incident ion as presented in Figure 10 and Figure 11 in chapter 2.6.2 for the impact of 40keV gallium ions into graphite. The

low amount of ions that is need for low-dose structure production processes will therefore also reduce the irradiation time strongly in comparison to high-dose structure production processes.

Using the vacancy density distribution structure depth as a function of the area dose can be determined by the simulation results. As presented in Figure 48 the vacancy density is higher for basal plane layers just below the surface than for the first surface basal plane layer. The vacancy density decreases strongly in deep solid regions. From the measured average critical area dose of 15.75µAs/cm² or 0.98 ion/nm² a critical vacancy density with 4.73 vacancies/nm³ was calculated.

Assuming that the vacancy density will increase linear with the ion or area dose the structure depth will increase if the vacancy density in deeper regions of the solid will rise above the critical vacancy density shown in the following figure.

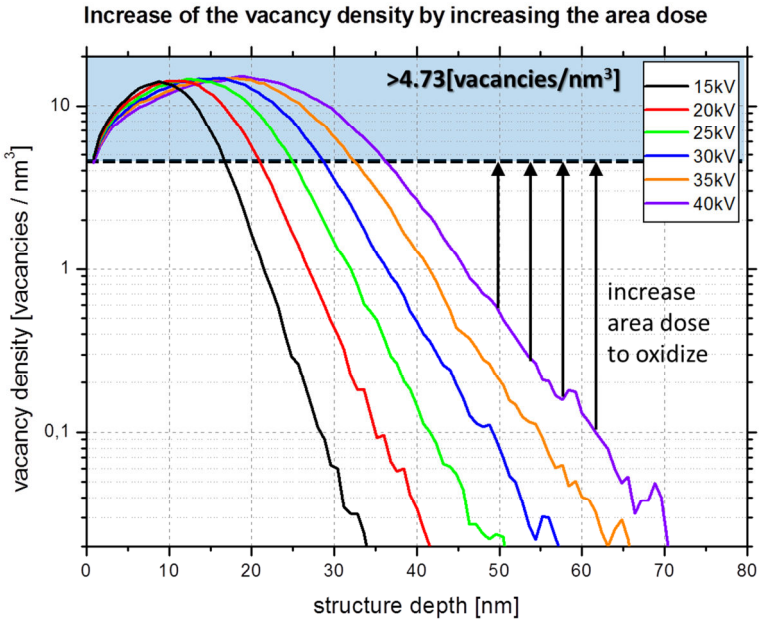

Figure 49: Schematic overview of the critical vacancy density that is needed for oxidation. The structure depth will increase if the vacancy density grows above the critical vacancy density. The vacancy density increases with the amount of incident ions given by the area dose.

To calculate the structure depth as a function of the area dose the vacancy density in deep solid regions has to be multiplied by a factor so that the resulting vacancy density will be higher than the critical vacancy density. These factors were calculated for every structure depth. Because the critical vacancy density equals the critical area dose the calculated factors must be multiplied with the critical area dose to determine a structure depth vs. area dose dependency.

The results of the TRIM simulations concerning the structure depth as a function of the area dose are shown in the following figure.

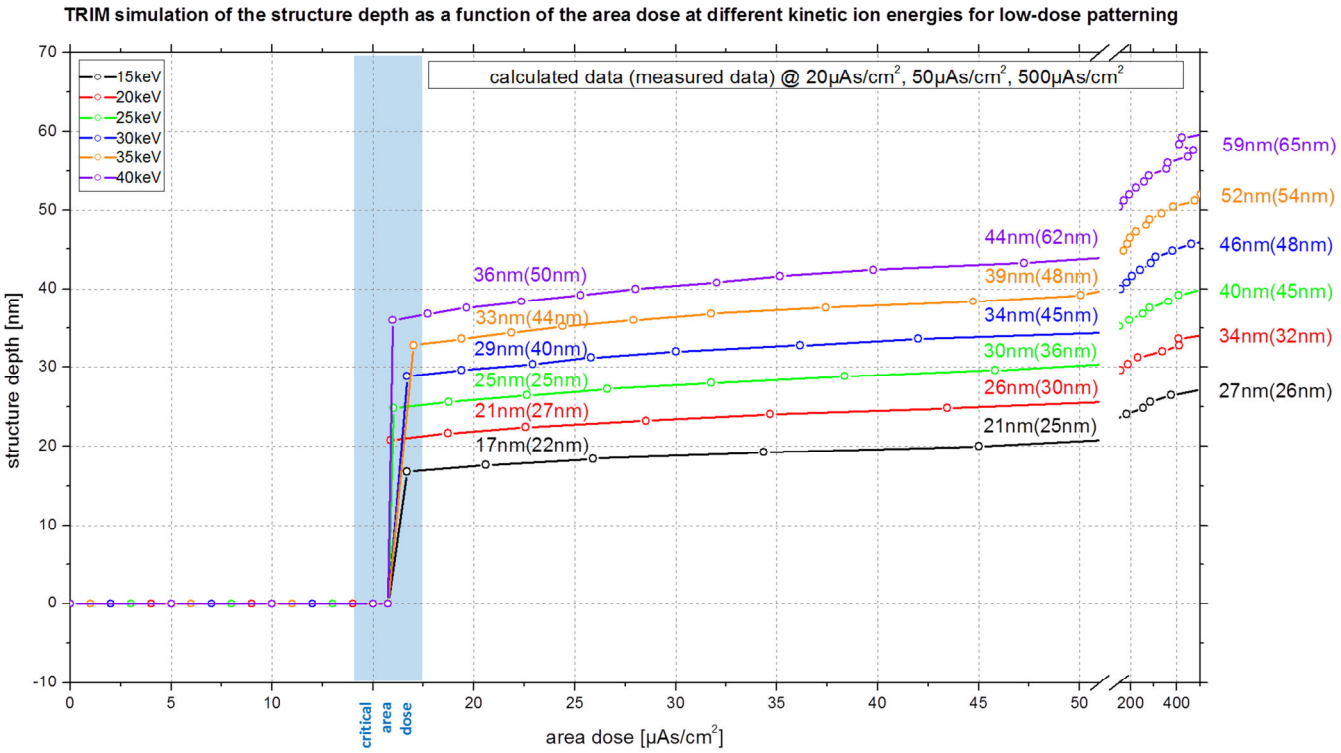

Figure 50: Calculation of the structure depth as a function of the area dose using TRIM simulation results concerning the vacancy distribution shown in Figure 49. Below the critical area dose of 15.75µAs/cm² the vacancy distribution data could not be used for the calculation but the theoretical structure depth should be zero. The plot shows the calculated and measured values for the structure depth at area doses of 20, 50 and 500µAs/cm². The plot is scaled as Figure 46 for better comparability.

Due to the vacancy distribution presented in Figure 49 the TRIM simulation results presented in Figure 50 can only be used for area doses above the critical area dose of 15.75µAs/cm². Theoretically, the structure depth for area doses below the critical area dose should always be zero. The heightened areas for area doses below the critical area dose cannot be calculated by TRIM.

The simulations show that the structure depth as a function of the area dose is qualitative the same for the experiments as well as for the simulated data. At the critical area dose the structure depth increases strongly and increases slightly for area doses above the critical area dose. But in comparison to the measured data the slope of the calculated data is higher than for the measured data. This is best visible for area doses above 200µAs/cm².

The plot in Figure 50 shows a comparison of the measured and calculated data at 20, 50 and 500µAs/cm². For these area doses the measured values are always higher than the calculated values. The measured data in comparison to the calculated data at this area doses is in average higher by 28%, 25% and 4%. So for higher area doses the measured data differs less from the calculated data due to the mentioned slope differences between measured and calculated data. The difference between the calculated and simulated data can be explained by the TRIM simulation algorithm itself. Effects like channeling [37] are not included in the simulation that would increase the simulated penetra-

tion depth of ions and recoils into solids and therefore also the structure depth. Additionally, the lattice structure but also the mosaic spread in HOPG is not included in the simulations.

5.2.3 Structure width and length vs. area dose – experiments

Although, the investigation of the structure depth as a function of the area dose was the main part of the structural investigation also the structure width was investigated as a function of the area dose.

The dependency of the structure width vs. the area dose can already be seen in Figure 45 and can be partially explained by the ion and recoil trajectories simulated by TRIM and shown in Figure 47. Although, the assumed ion beam diameter in the simulation is zero the incident gallium ions, the recoils and so the produced defects will be distributed along the x- and y-direction parallel to the HOPG surface. From Figure 47 an increased structure width can be estimated due the ion and recoil distribution. Produced structures will therefore be of the order of 40-60nm broader than the predefined structure width. Additionally, the beam diameter is about 10nm. Thus, the structure width and length will be increased as shown schematically in Figure 44 b). The dependency of the structure width as a function of the area dose is shown in the next figure.

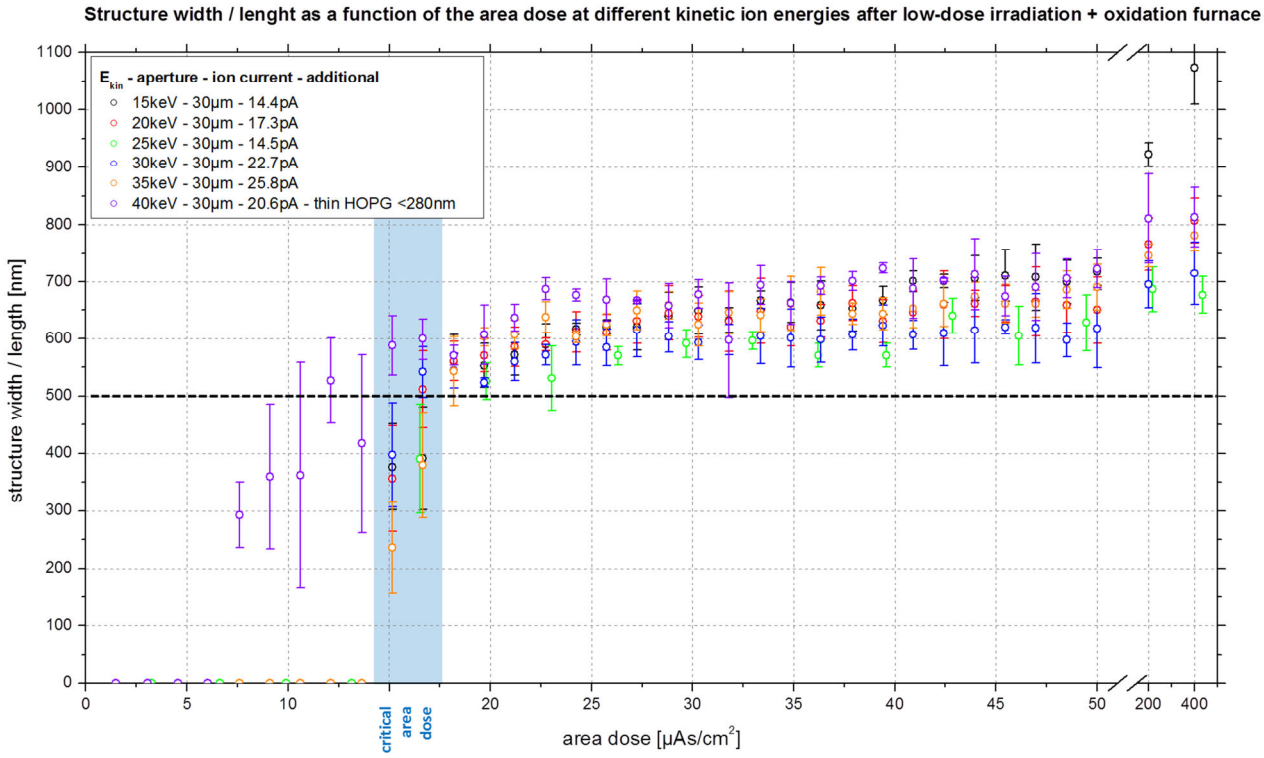

Figure 51: The structure width as a function of the area dose was investigated for test structures by AFM measurements and were evaluated with the WSXM software. The test structures were produced using gallium ions with a kinetic energy of 15-40keV.The critical area dose range was adopted from the structure depth investigations and is included in the plot.

Below the critical area dose no test structures were produced so that no structure width was determined or rather set to zero. Above the critical area dose the structure width increases. The plot shows that the structure width is not a function of the kinetic ion energy.

Most of the measured structure widths are between 550-700nm at area doses of 17.5-50.0µAs/cm^2. The structure width should be 500nm as predefined in the GDSII software and is therefore 50-200nm larger as set. As mentioned before, the increased structure width has its main origin in the x- and y-scattering of the incident ions and the recoils. Furthermore, also the ion beam diameter must be taken into account. Although, the oxidation process should only increase the structure width by 2nm after 200min at 500°C (chapter 3.2.1, Figure 18) a structure-broadening could also be caused by this process.

There is a slight increase in the structure width for increasing area doses in the range of 20-50µAs/cm^2 while for area doses above 200µAs/cm^2 the structure width increases to 700-800nm for a kinetic ion energy of >15keV. The high structure width for 15keV of 900-1100nm can be explained the nuclear stopping theory. Due to the low kinetic energy an increased scattering of the ions in x- and y-direction near the surface can be assumed. Besides systematic errors, this fact could be the reason for an increased structure width at a kinetic ion energy of 15keV.

Because no vacancy distribution on x- and y-direction can be quantitatively extracted from the TRIM simulation no simulation results can be determined for the structure width and length.

5.3 Low-dose irradiation and ozone generator + UV-lamp

Thin HOPG samples will be destroyed after the heating process in the oxidation furnace. Therefore, another oxidation method has to be performed for thin HOPG samples after low-dose irradiation. Thin HOPG samples are needed to produce electrical isolated structures and are therefore necessary. In this subchapter the thin HOPG destruction at high temperatures and the oxidation process using ozone will be discussed.

5.3.1 Thin HOPG sample destruction at high temperatures

The oxidation of thin samples at high temperatures cannot be performed due to two main reasons. One reason is the different thermal expansion of the thin HOPG sample and the mica substrate and the other reason is a water inclusion between the thin HOPG sample and the mica substrate. Both reasons are also discussed in reference [102].

The thermal expansion is material-, temperature- and also quality-dependent and is described by the thermal expansion coefficient. While the thermal expansion coefficient of HOPG is positive in c-axis direction for temperatures above 0°C the expansion coefficient along the basal plane direction is negative for temperatures of about 0-400°C and positive for temperatures above 400°C determined by experiments [132] and theory [133]. Additionally, the quality of the HOPG can change the thermal expansion coefficient as a function of the temperature as reported in reference [134]. The thermal expansion coefficient for muscovite is positive [135] for all temperatures. During the heating process the thin HOPG samples will contract and the mica substrate will expand until 400°C. Above this temperature both materials will expand.

A possibility for the sample destruction could be the stress in the HOPG during the heating process. Because the HOPG contracts and the muscovite expands the HOPG sample will be torn apart in smaller parts of several square micrometres. This disruption was observed in former performed experiments at temperatures above 110°C. For smaller temperatures the thin HOPG samples stayed stable. At temperatures above 110°C the HOPG changes its original position on the muscovite slightly. When the sample and the muscovite are cooled down to room temperature the muscovite contracts and the small HOPG pieces form wrinkles at the edges.

As mentioned before, also water inclusions between the HOPG sample and the muscovite substrate were observed by SEM measurements. Due to the production process of thin HOPG samples water can be included between sample and substrate during the last step of the cleaning process in distilled water. During the heating process the water vaporizes at temperatures above 100°C and can destroy parts of the sample.

In the following figure optical microscope, AFM and SEM images of the sample destruction are shown for thin HOPG samples that were heated above 110°C.

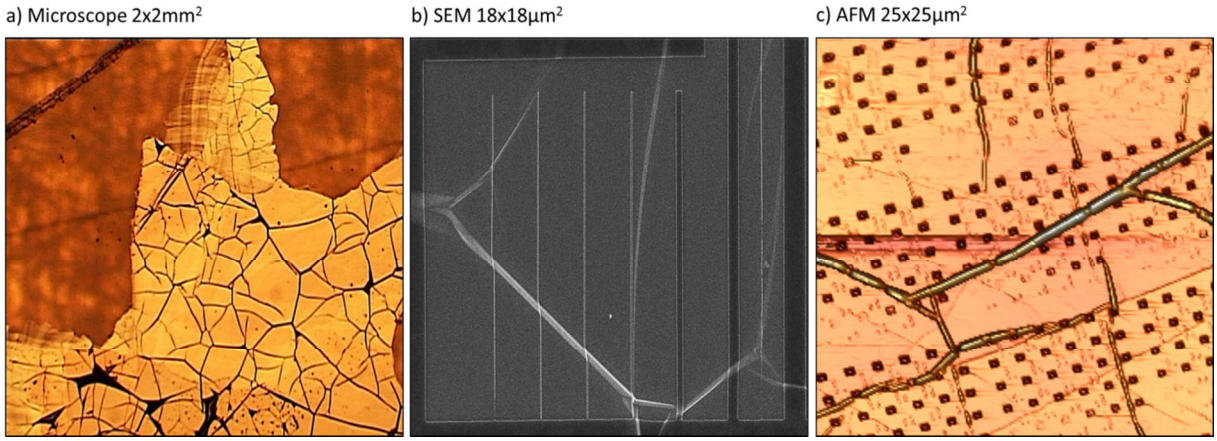

Figure 52: Optical microscope, SEM and AFM images of sample and structure destruction shown in millimetre, micrometre and nanometre range after the heating of thin HOPG samples at 500°C for 200min. Due to the mechanical stress during the heating process the sample is torn into pieces of several square micrometres. After cooling down to room temperature the HOPG pieces form wrinkles at the edges so that the sample and the produced structures become damaged or destroyed.

5.3.2 Oxidation and structure production with ozone generator and UV-lamp

In several experiments it was tried to oxidize the low-dose irradiated areas on the thin HOPG samples by the use of ozone and additionally by heating the sample at T=110°C.

First, the maximum temperature for which thin HOPG samples stayed stable and were not destructed was determined in former experiments. The experiments were performed by heating a sample holder where a thin HOPG samples was mounted. The temperature was increased by a heating filament and the temperature of the HOPG sample was directly measured on the sample surface. During the heating process the samples were imaged by a high-resolution camera. The temperature was measured parallel so that the sample surface structure could be investigated at different temperatures. Above 110°C a disruption of the sample surface could be observed. For all following oxidation processes with ozone a maximum heating temperature of 110°C was used.

Second, the oxidation of sample edges was investigated using the ozone generator. In this case, a thin HOPG sample was imaged with an optical microscope before and after 1h, 2h, 3h and 6h of oxidation using the ozone generator. An example of the oxidation process is shown in the following figure.

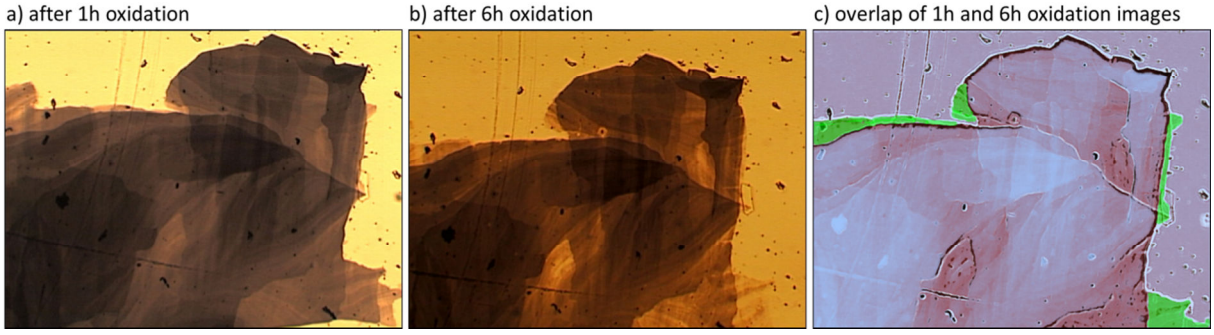

Figure 53: a) and b) show two microscope images of a part of a thin HOPG sample before and after the oxidation process using the ozone generator. c) shows an overlap of a) and b) to highlight the oxidation of the sample. The oxidized areas after the oxidation process were marked green.

Finally, the structure production on thin HOPG samples using was investigated. To accelerate the oxidation process and to reduce the time needed for oxidation the ozone generator was combined with an UV-lamp and the samples were heated. The samples were irradiated with an area dose of 50µAs/cm² that is 3-4 times more than the critical area dose.

In several experiments and at different oxidation parameters it was tried to initiate the structure production by oxidation. AFM measurements show that even after 11h of oxidation using the ozone generator with an ozone flow rate of 40l/h, the UV-lamp and after heating the samples on 110°C the irradiated areas did not become oxidized in all performed experiments.

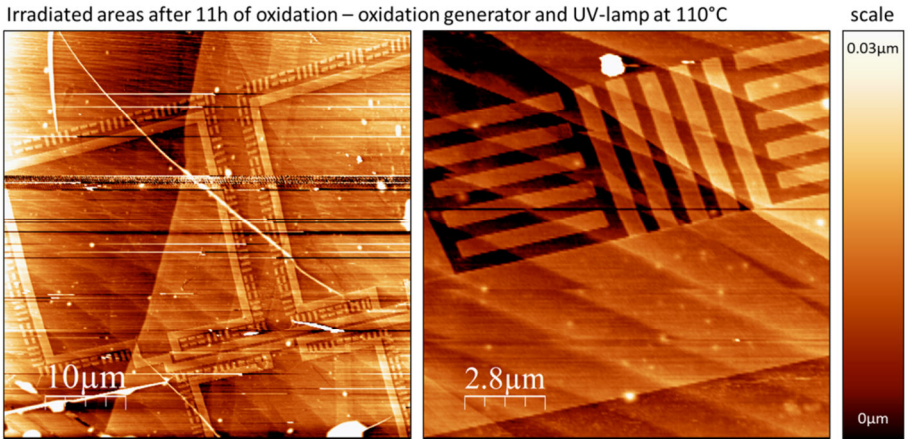

Figure 54: AFM images after oxidation using the ozone generator and the UV-lamp after 11h at 110°C. The irradiated areas were not oxidized. The areas are higher than the un-irradiated areas.

The oxidation of the irradiated areas by ozone was not achieved. The irradiated areas are higher than the un-irradiated areas for all irradiation experiments. The sample surfaces become mainly contaminated because of the gas flow of the ozone generator. At temperatures of 110°C there should be no water film that would protect the irradiated areas from oxidation. Because the samples edges become oxidized during the experiments the results of the failed structure production using ozone cannot be explained at this point of investigation. Additional experiments for the structure production after low-dose irradiation and the oxidation by ozone might be performed in future.

5.4 High-dose irradiation

Area test structures were produced by high-dose irradiation processes for structural properties investigation just like for the low-dose irradiation process presented in chapter 5.2 before.

The structure depth as a function of the area dose was investigated for kinetic ion energies of 20keV, 30keV and 40keV. For kinetic ion energies of 30keV the test structures were investigated in four experiments at different conditions. In this case, conditions mean different aperture sizes and different ion currents (70-100µm, 153-300pA), thin or thick HOPG samples and loops or no loops.

Because the structure depth can be different for line production in comparison to area production due to focus properties shown in Figure 44 b) the structure depth as a function of the line dose was investigated too. The patterning field of line test structures is the same as for area test structures in which the areas have been replaced by lines.

To give an overview about the AFM measurements two representative AFM images and the according line profiles are shown in the next figure.

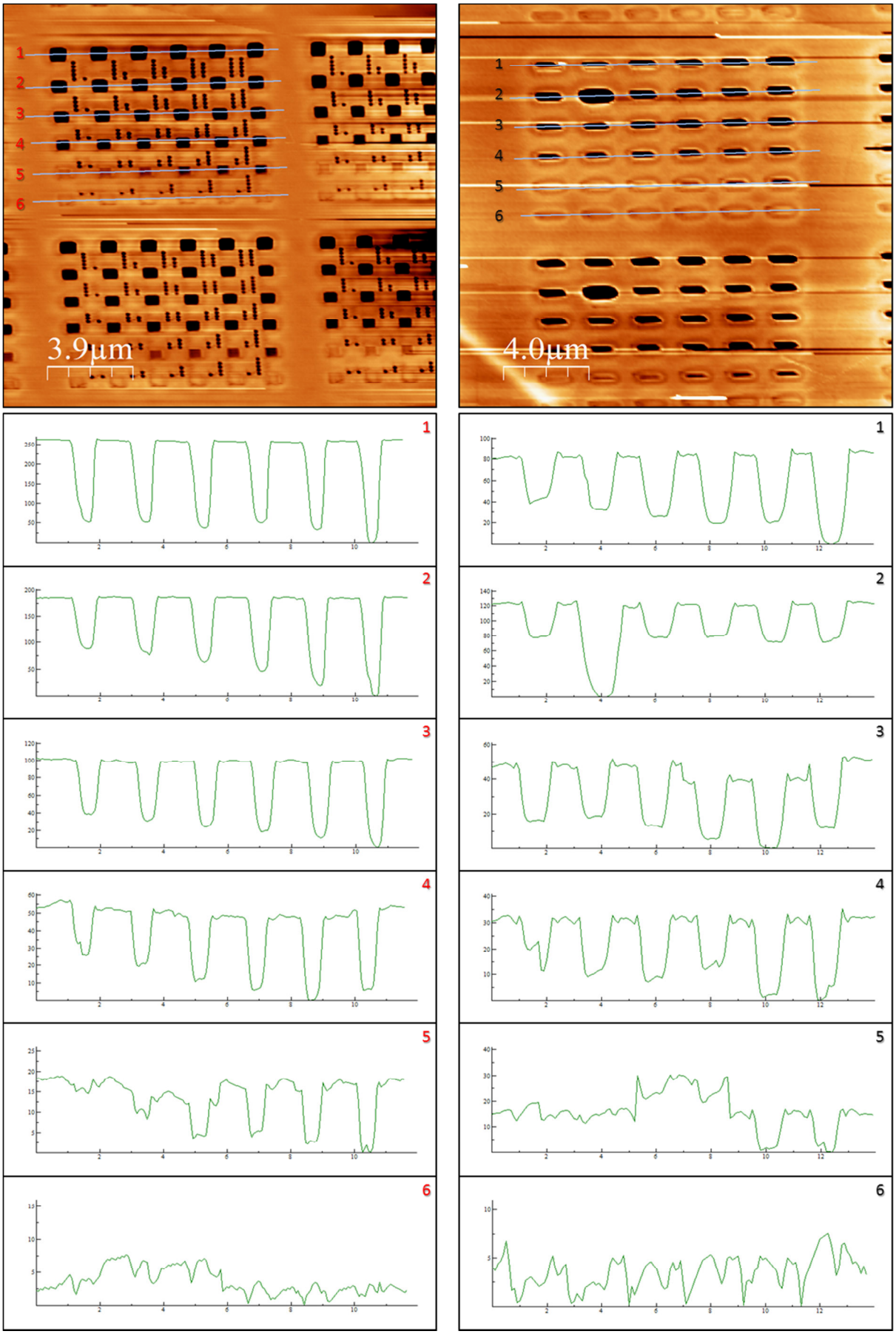

Figure 55: AFM images and line profiles of areas and lines produced by high-dose irradiation at 30keV on thick HOPG. The line profiles are scaled in nm along the z- and in µm along the x-direction.

Every area test structure was irradiated with an individual area dose of 0-162000µAs/cm². The line test structures were irradiated with a line dose of 0-2.7µAs/cm. The structure depth increases strongly in line profile 5 for area and line test structures. For high doses the structure depth increases linear for area and line test structure. In comparison to the low-dose irradiation there are no heightened areas or lines after the high-dose irradiation. As for the low-dose investigations there seems to be a critical milling area and line dose where the structure depth suddenly increases (profile line 5). The structures according to line profiles 5 and 6 do not have a regular structure depth. This is a problem for the investigation of the structure width so that the structure width for this test structures was determined measuring the width of the deepest cavity. There seems to be a patterning error in line 2 of the line test structures. This line test structure was accidently produced at an extreme high line dose of 21.5µAs/cm. Nevertheless, this line test structure will show an interesting effect discussed in chapter 5.4.1. Especially in the line profiles 4 and 5 the destruction of the structure edges can be observed where the area around the test structures appears heightened.

5.4.1 Structure depth vs. area dose – experiments

For area test structures the structure depth as a function of the area dose was investigated as for the low-dose investigations before. For kinetic ion energies of 20keV, 30keV and 40keV and different parameters like ion current, aperture size, sample type and loops the test structures were produced on thick HOPG samples.

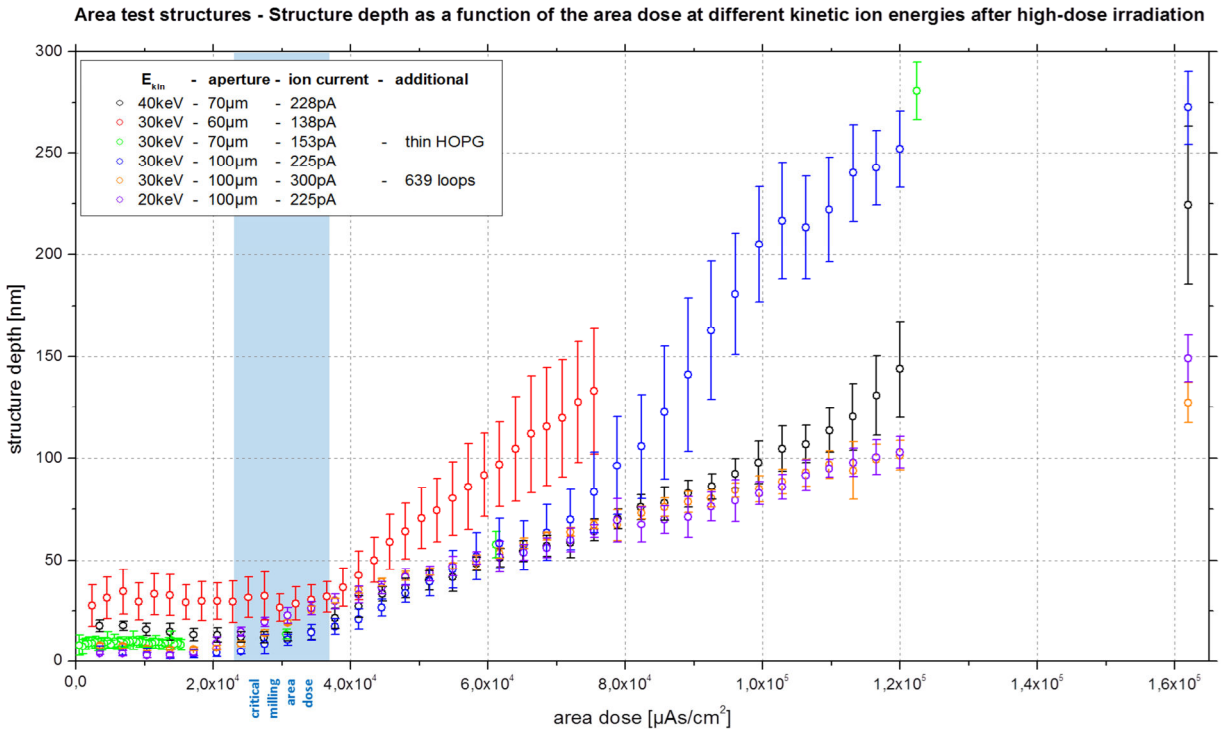

Figure 56: Structure depth of area test structures after high-dose irradiation as a function of the area dose.

For area doses up to 20mAs/cm² the structure depth is constant. In this area dose range the depth increase due to the sputtering process is compensated because of the ion implantation. There is a critical area milling dose of 22-37mAs/cm² (29.5mAs/cm² in average) for all experiments where the sputter effect starts to dominate and the structure depth increases linear for further dose increase. The critical area milling dose is independent from all other investigated parameters.

The structure depth increase above the critical milling area dose can be explained by the lattice destruction. The lattice destruction must cause a reduction of the displacement energy E_d and the surface binding energy E_b. Above the critical milling area dose the reduction of the displacement and the surface binding energy will stop the compensation of the structure depth increase by the ion implantation. The effective sputtering yield must therefore increase with the area dose. Additionally, the reduced displacement and surface binding energy has to be constant after reduction due to a constant slope of the measured data presented in Figure 56.

Except for the area dose no other parameters have a measureable influence on the structure depth. The structure depth varies strongly for every experiment like especially the results for the 30keV experiments show. There is also no dependency of the structure depth to the kinetic ion energy visible that is in contrast to low-dose irradiation experiments.

In summary, a critical milling area dose can be identified but the influence of parameters except the area dose could not be identified. More investigations will perhaps show more detailed results but at this point of the investigation the high-dose production process seems to be not well controllable. Nevertheless, the maximum possible structure depth in the experiments is about 250nm and therefore several times larger than the maximum structure depth after low-dose irradiation production processes.

5.4.2 Structure width and length vs. area dose - experiments

Below the critical milling area dose the area test structures could be produced although they are irregular in shape as also the investigation of the structure width will show.

Above the critical milling area dose the structures are regular and can be measured easily concerning the structure width. Because the structure shape is irregular for low doses as shown in Figure 55 the structure width of the deepest cavity was measured.

The structure width as a function of the area dose for the high-dose irradiation experiments is shown in the following figure.

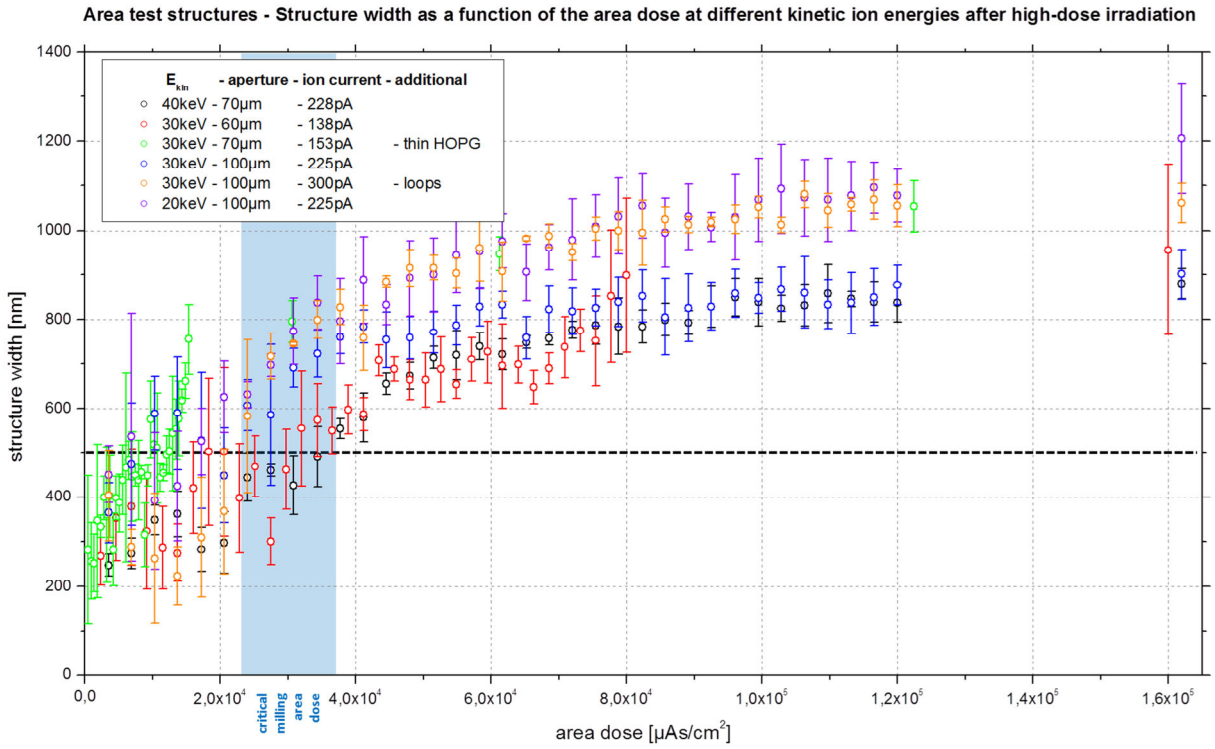

Figure 57: Structure width as a function of the area dose of area test structures. The critical milling area dose range was adopted from the structure depth investigations and is included in the plot.

Below the critical milling area dose the structure width deviates strong because of the irregular shape of the milled structures. Additionally, the structure width is nearly equal to the predefined structure width. The structure width deviation decreases at the critical milling area dose where the structure shape becomes regular. Nevertheless, the structure width is different for every performed experiment. Slightly above the critical milling area dose at $4.0 \cdot 10^4$µAs/cm² the structure width is 550-1000nm and therefore up to two times larger than the predefined structure width. For area doses of $1.6 \cdot 10^5$µAs/cm² the structure width even increases to 800-1300nm.

In summary, the difference between the predefined and the real structure width is a disadvantage of the high-dose production process that is caused mainly because of the ion and recoil distribution in the solid. The structural properties of area test structures are better for the low-dose than the high-dose production process (see Figure 51 for comparison). In this context, the milling process should only be used if the increase in structure width by 300-800nm is not significant, for example, when micrometre structures are produced.

The measured data also shows that the structure width is not clearly dependent from the kinetic ion energy or other parameters. Although, an increase of the kinetic ion energy seems to reduce the structure width for area doses above the critical milling area dose the measured data differs strongly in all experiments so that no dependency of the structure width and the kinetic ion energy can be assumed at this point of investigation.

5.4.3 Structure depth vs. line dose – experiments

Line test structures were produced and investigated concerning the structure depth and width. The results will be presented briefly and mainly new aspects will be discussed in the following subchapters.

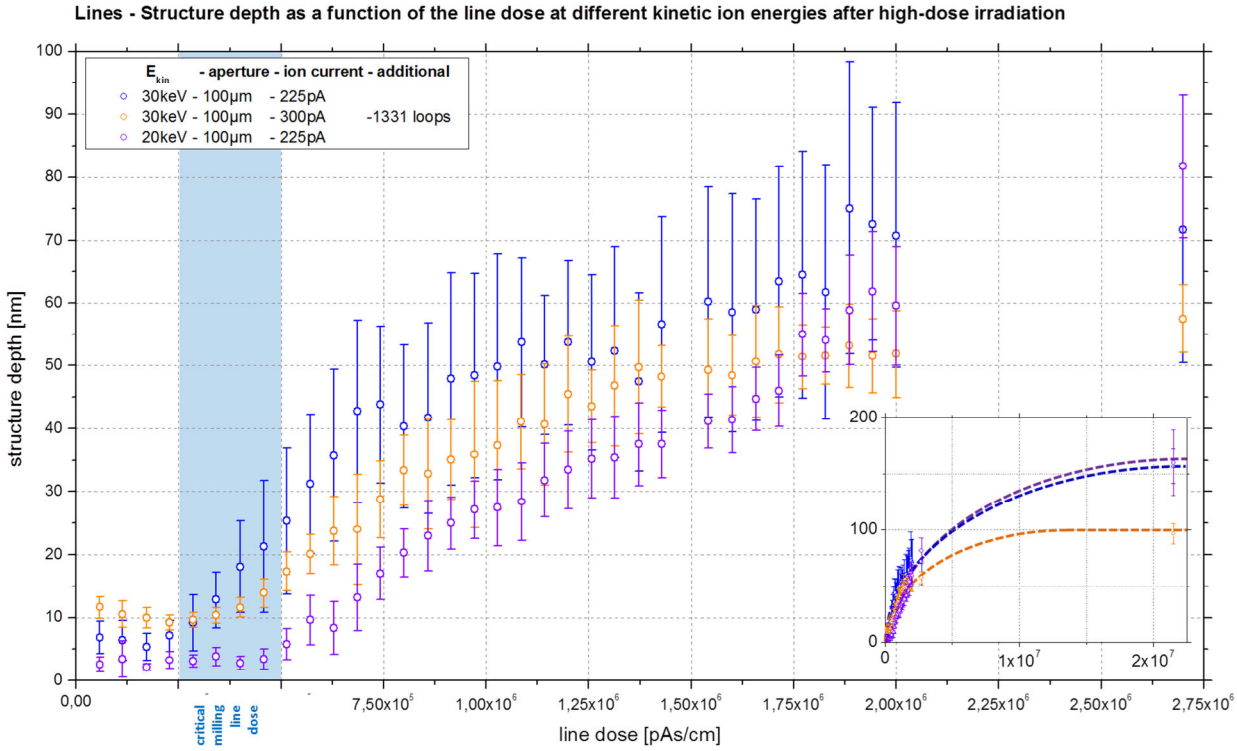

Figure 58: The structure depth of the line test structures after high-dose irradiation was investigated for line doses up to 21.5µAs/cm at kinetic ion energies of 30keV and 40keV. The small plot shows the measured data of the big plot and additionally the measured structure depth after the irradiation at an extreme high line dose of 21.5µAs/cm that was accidently produced and was shown in Figure 55 before.

During the production of area and line test structures the same ion current was used but the dwell time for the line structure production was about 16 times larger than for area structure production. Because of the increased dwell time the structure depth should be multiple times larger for lines than for areas. But, when the big plot of Figure 58 is compared to Figure 56 a smaller structure depth for lines than for areas was measured. This fact can be explained by the ion distribution presented in Figure 44 b). Because the ion beam diameter is finite the real ion dose will always be smaller for lines than for areas where the ion and recoil distributions overlap. This will result in a reduced sputter effect for lines although the dwell time will be higher for line than for area production at a constant ion current.

Also for line test structures a critical dose, the critical milling line dose, can be observed and is in the range of 2.5-5.0·10^5pAs/cm or 0.25-0.5µAs/cm (0.375µAs/cm in average). Above the critical dose the structure depth increases linear like for the investigations of the area test structures before. The accidently produced lines at an extreme high line

dose of $2.15 \cdot 10^7$pAs/cm or 21.5µAs/cm shows that the structure depth deviates from the linear increase with the ion dose for extreme high line doses. While sputtered atoms for the first surface layers have an escape angle of 180° the escape angle decreases with the structure depth. For a high structure depth the sputtered atoms can adsorb at the structure edges so that the effective sputtering yield will decrease for deep structures.

The results of the structure depth of line and area test structures can be used to calculate the focus width of the ion beam. In both experiments there is a critical dose where the sputter process begins. The quotient of the critical doses equals the focus width and is about $3.75 \cdot 10^5 \left[\frac{\text{pAs}}{\text{cm}}\right] : 29.50 \left[\frac{\text{mAs}}{\text{cm}^2}\right] = 127\text{nm}$. As mentioned before and shown in Figure 44 b), the resulting structure depth will always be smaller for lines than for areas for the same current, dwell time and focus width because of the finite ion beam diameter and the ion and recoil distribution in the solid.

5.4.4 Structure width vs. line dose – experiments

The results of the structure width measurements for line test structures are presented in the following figure. Like for the test structure production by high-dose irradiation also the line test structures are irregular in width for line doses below the critical milling line dose. In this context, the largest structure width was measured for the relevant line test structures.

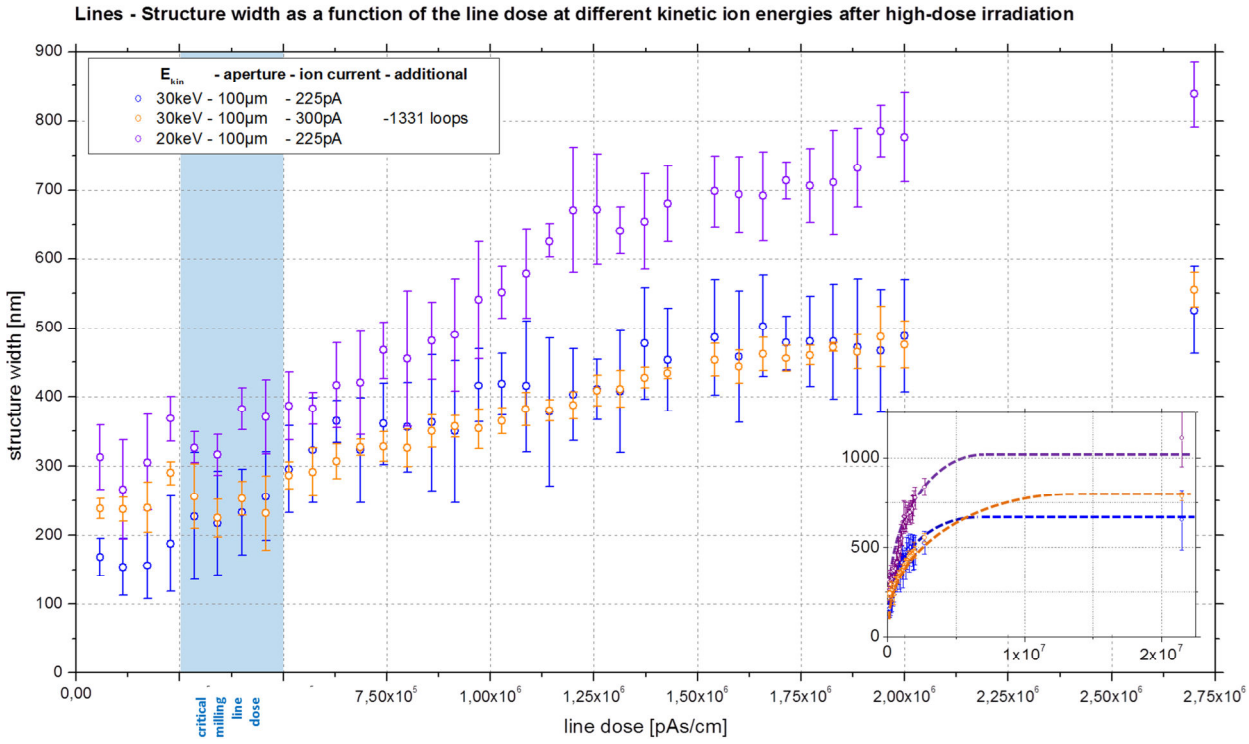

Figure 59: The structure width as a function of the line dose was investigated for line test structures by AFM measurements and were evaluated with the WSXM software. The test structures were produced using gallium ions with a kinetic energy of 20keV and 30keV. The critical milling line dose range was adopted from the structure depth investigations and is included in the plot.

The investigation results of the structure width of line test structures confirm the results for the structure width of area test structures. The structure width is 150-400nm below the critical milling line dose and increases linear for line doses above the critical milling line dose to 500-850nm or even to 700-1100nm for extreme high line doses. This high structure width values cannot be explained by TRIM simulations quantitatively shown in Figure 47. Due to the simulations only a structure width of 160nm could be assumed for line test structures.

The structure width is always larger than the structure depth for line structures shown in Figure 58. At kinetic ion energies of 20keV and 30keV the ion and recoil trajectories were shown in Figure 47 before where the ion and recoil distribution was nearly spherical. The low structure depth to structure width ration can be explained by the ion and recoil distribution and by the low sputtering yield during a high-dose irradiation shown in chapter 2.6.2. Only atoms near the sample surface can be sputtered so that the graphene layers of the HOPG have to be sputtered layer by layer. The area the surface atoms become sputtered is discoidal and several hundreds of nanometre in diameter due to the interaction of the surface atoms with ions and recoils. Because the sputter yield decreases with the structure depth the maximum structure depth for line structures is about 150nm like shown in Figure 58. The ion and recoil distribution is up to 1000nm in diameter parallel to the sample surface so that the low structure depth to structure width ration can be explained. Although, the structure width seems to be inversely proportional to the kinetic ion energy this would be contradict to the TRIM simulations in Figure 47. The simulations show that the structure width should increase proportional with the kinetic ion energy.

5.5 Comparison and improvement for the structure production

The low-dose and the high-dose irradiation have different advantages and disadvantages concerning the structure production and the structural properties. The high-dose irradiation process is not fully understood at this point of investigation due to a variety of open questions. The structure depth varies strong due to different focus widths for every performed irradiation. The variations seem not to be dependent on conditions like the kinetic ion energy, the sample type, the current and the amount of loops.

The structure depth for area test structures is always higher than for the structure depth of line test structures mostly due to the focus width. Furthermore, the structure width for area and line test structures is larger than TRIM simulations predict. It can be assumed that not all processes can be explained by the simulation data like for example interaction processes between sputtered atoms and incident ions or solid atoms. Because the simulations do not include a dynamic sputtering process the ion, solid and recoil dynamics cannot be calculated when the milling process is in progress.

In summary, the milling process is not well controllable at this point of investigation but it has certain important advantages. The milling process can be performed at any temperature so that temperature sensitive samples or structures would not be destroyed. This is a strong advantage concerning multi material samples that will not become stressed or destroyed due to different material expansion coefficients. The milling process is also important for the production of structures with large structure depths. The structure depth can be multiple times larger than for the structures produced by low-dose irradiation. Here, the structure depth can be tuned by the deposited dose and thus during the irradiation process and not by the kinetic ion energy and thus only before the irradiation process.

The advantages of structure production using the high-dose irradiation are simultaneously the disadvantages of structure production using the low-dose irradiation. The structure production by low-dose irradiation must always be combined with an oxidation process that can only be performed at high temperatures at this point of investigation. Thereby, this technique cannot be used for temperature sensitive samples or structures. The structure depth of the produced structures is limited to <70nm and cannot be tuned during the irradiation process.

The advantages of the structure production using the low-dose irradiation are the better control of the production process and the structural properties of the produced structures. The deviation of the structure depth and width is much smaller for this production process and all values fit well to simulated TRIM data.

Because of the limitation in structure depth the structure production using low-dose irradiation is better for nano structures. The structure production using high-dose irradiation is better for the production of large nano or micro structures. A strong improvement of the structure production by ion beam lithography would be combination of the advantages concerning the low-dose and the high-dose irradiation.

	advantages (+)	disadvantages (-)
low-dose	- Controllability and predictability - Structural properties - Experiments ↔ theory - Irradiation time	- Limited structure depth - Oxidation process ↔ time, temperature - No direct structure production - Samples stay stable - Only oxidizable materials can be used
high-dose	- High Structure depth - No oxidation process - Direct structure production - Samples stay stable - Most materials can be structured	- Controllability and predictability - Structural properties - Experiments ↔ theory - Irradiation time

Table 2: Overview of the advantages and the disadvantages concerning the low-dose and high-dose irradiation processes. An assumed improved production process has to combine the advantages of the low-dose and the high-dose structure production process.

A first attempt to improve the production process was a low-dose irradiation combined with an oxidation process by the use of ozone. This process would have combined most of the advantages of the low-dose and high-dose irradiation except an adjustable structure depth and the possibility to structure all materials. Unfortunately, in most cases only sample edges and none of the irradiated areas were oxidized by this production process. More investigations are necessary to optimize the structure production using ozone.

For the possibility to produce structures with adjustable or high structure depths combined with the advantages listed in table 2 the irradiation process in the FIB-facility should be modified. Beside the use of highly charged ions explained in chapter 2.7 oxidants could be used during the irradiation process. In this case, the irradiated areas could be oxidized continuously so that the maximum structure depth would increase strongly. Although, only oxidizable materials could be structured this first upgrade could improve the applicability of the ion beam facility. In this context, the vacuum conditions need still be good so that there might be limitations using a combined irradiation and oxidation process.

5.6 Chapter summary

The structure production was performed using low-dose and high-dose irradiation processes. Concerning the low-dose irradiation a subsequent oxidation process was initialized using an oxidation furnace under an Ar-O_2 atmosphere and at 500°C. Additionally, experiments were performed with ozone as an oxidant to oxidize irradiated sample areas at room temperature. In contrast, the structure production by high-dose irradiation is a direct structure production method. The sputtering yield of ions low so that concerning the low-dose irradiation the solid lattice destruction was used to mainly oxidize irradiated solid surface areas. If the solid atoms have to be sputtered despite the low sputtering yield a high amount of ions, a high-dose irradiation, must be used to create structures. For the structure production thick and thin HOPG samples were used.

Both methods were investigated concerning the resulting structure depth and width of the produced nanostructures as a function of the deposited ion dose at different kinetic ion energies. For this, area test structures of 500·500nm² were produced using both methods on thin and thick HOPG samples. In a patterning field of 6·6 the area test structures were produced using different area doses. Additionally, line test structures were produced at different line doses and kinetic ion energies by high-dose irradiation. All investigations were performed by AFM measurements.

While test structures can be produced after a low-dose irradiation and a subsequent oxidation process in the oxidation furnace and also after a direct milling process using high-dose irradiation the structure production using low-dose irradiation and ozone

failed. In this context no additional investigations of the structure production using low-dose irradiation and ozone were performed.

Produced area test structures using low-dose irradiation and a subsequent oxidation process in the oxidation furnace showed that the resulting structure depth is a function of the area dose and of the kinetic ion energy. Above a critical area dose of 15.75µAs/cm^2 structures are produced by low-dose irradiation and the oxidation process in the oxidation furnace for all kinetic ion energies. The structure depth rises only slightly for higher area doses but is strongly dependent on the kinetic ion energy. This behaviour can be explained by the ion and recoil trajectories and the vacancy distribution in the solid surface simulated by TRIM.

The structure depth is dependent on the maximum ion or recoil range in the sample. Because the lattice destruction of the solid is caused by ions and recoils irradiated areas can be oxidized at a maximum depth that equals the maximum ion or recoil range into the sample. The sudden increase of the structure depth as a function of the area dose is caused by the vacancy distribution in the solid. All simulation data show that the vacancy density increases for the first few layers near the sample surface and then decreases strongly for deep sample layers. If the vacancy density in the sample surface layer is larger than the critical vacancy density of 4.73 vacancies per cubic nanometre the oxidation process and so the structure production can be performed. Because the vacancy density increases for the next few layers near the sample surface also this layers will be oxidized until a layer that has a vacancy density below the critical vacancy density.

In summary, the resulting structure depths of the low-dose irradiation process can be explained well by the simulations. In this case, also the results of the structure width as a function of the area dose can be explained well by the simulated data. The ion and recoil distribution and so the vacancy distribution parallel to the sample surface can explain the increased structure width of 100-200nm.

There is a critical milling area and line dose that was determined by the experiments for high-dose irradiation processes. Although, at area and line doses below the critical doses the area and test structures are produced they are mostly irregular shaped. Above the critical milling area doses of 29.5mAs/cm^2 and the critical milling line dose of 0.375µAs/cm the produced structures become regular concerning the structure depth and width.

Unfortunately, the milling process and so the structure depth and the structure width are not predictable or controllable well. Although, some experiments were performed at nearly same conditions the structure depth and width differ strongly. Furthermore, no dependency of the structure depth or width as a function of the kinetic ion energy, the sample type or the amount of loops could be determined. Because of the focus width the structure depth for areas will always be higher than the structure depth of lines for constant ion current, dwell time and focus width.

Important to notice is that there seems to be a maximum structure depth at extreme high ion doses where the structure depth is constant even after a further dose increase.

In summary, the structure depths and widths obtained from the high-dose experiments are in contradiction to the TRIM simulations. One reason could be that the ion, recoil and sputtered atom dynamics that cannot be simulated for milling processes.

One reason why low-dose and high-dose irradiation processes were investigated is that both methods have advantages and disadvantages concerning the structure production and the structural properties. The low-dose irradiation structure production, for example, cannot be performed for temperature sensitive samples.. Additionally, the maximum structure depth is limited to <70nm due to the kinetic ion energies.

A problem of the high-dose irradiation process is the controllability and predictability of the structure production process. The structural properties are poor due to an increased structure width of 700-1100nm. The results of the high-dose irradiation are not comparable with TRIM simulations and the irradiation time is much high than for low-dose irradiation processes.

A combination of the advantages of both methods would lead to an improved process. The oxidation with ozone would reduce the oxidation temperature and can probably be used after further investigations in the future. Another possibility is the use of highly charged ions and was discussed in chapter 2.7 before. In this context, the sputtering yield would be much higher than by the use of single charged ions and the critical milling ion dose would be decreased strongly. Perhaps the use of oxidants during the irradiation process could be beneficial because the oxidation could be performed parallel to the irradiation process. But there will be limitations because of the needed vacuum conditions during the irradiation process.

6. Electrical properties

In this chapter the results on the electrical properties of nano and micro structures are presented. In the last chapter test structures and their structural properties were presented concerning a low-dose or a high-dose irradiation process. These test structures can be specified as cavities created on HOPG surfaces. The production of cavities can be used to create free-standing conductors on sample surfaces like it is presented in the next figure. The cavities can be produced by low-dose and high-dose irradiation either on thick or thin HOPG samples with advantages and disadvantages concerning the production process, the structural and the electrical properties of the resulting conductors.

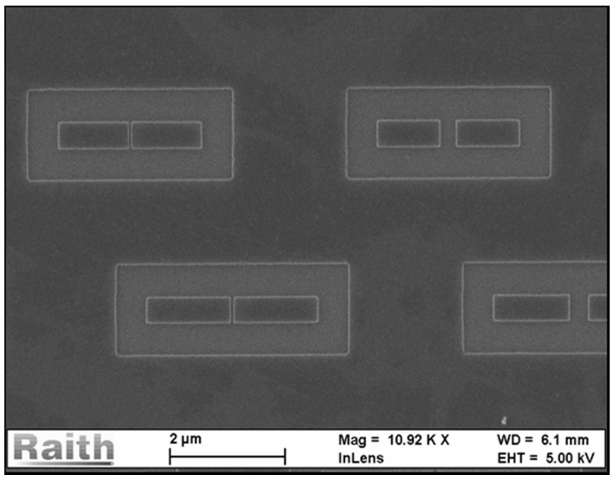

Figure 60: SEM image of some of the free-standing structures with gaps.

Concerning the electrical properties of the free-standing structures several aspects have to be taken into account when the structures are produced by low-dose or high-dose irradiation processes. The free-standing structures should be

- electrical conductive
- electrical isolated from the rest of the sample
- ideal and not damaged or destroyed partially
- free of contaminations or impurities
- contactable

Before the free-standing structures are produced possible disadvantages for the electrical properties investigation can be listed for structures produced by low-dose and high-dose irradiation processes.

In general, the HOPG sample and so the free-standing structures are electrical conductive along the basal plane direction parallel to the sample surface. Because of the implanted ions and the lattice destruction the conductivity of the graphite material will decrease. This is due to the fact that lattice defects will scatter electrons and the current will be reduced because of a decreased electrical conductivity. Especially for high-dose

irradiation processes a high amount of ions and recoils exist in the solid and the lattice destruction is much higher than for low-dose irradiation processes. It can be assumed that for free-standing structures created by high-dose irradiation a decreased electrical conductivity will be measured.

Because the free-standing structures have to be electrical isolated from the rest of the sample the use of thick HOPG samples is critical. The cavity depth can only be <70nm for low-dose and <200-300nm for high-dose production processes. It is possible that the applied current will not always be localized in the free-standing structures. Although, the electrical conductivity in basal-plane direction is much higher than in c-axis direction at free-standing structure dimensions of for example 40µm·300nm·70nm the applied current will also flow in the HOPG bulk under the free-standing structures as later simulations will show. If thin HOPG samples with a thickness of about <70nm are deposited on a mica insulator the produced cavities will be deep enough to separate the free-standing structures from the rest of the HOPG.

Ideal and not damaged or destroyed free-standing structures can be produced by high-dose and low-dose processes on thick HOPG samples but only by high-dose processes on thin HOPG samples. Due to the sample destruction at high temperatures after using the oxidation furnace and due to the failure of structure production using ozone at low temperatures the low-dose process cannot be used to create a high amount of ideal and not damaged or destroyed free-standing structures on thin HOPG samples.

For the electrical investigation the free-standing structures should be free of contaminations or impurities. Implanted ions can be considered as impurities. As mentioned before, they can have an influence on the conductivity of the free-standing structures. For small free-standing structures the current flow is mainly localized near the structure surface. Impurities on the sample surface can lead to a change of the current flow. Additionally, impurities can be deposited in the produced cavities. The deposition can lead to an electrical contact between the free-standing structures and the rest of the HOPG bulk that can be named as electrical conductive bridges. Although, impurities in the cavities can be identified well using an SEM the identification of small impurities is nearly impossible using optical microscopes. After the cavities were produced the structure edges are areas for impurity adsorptions due to the lattice destruction and free chemical bond partners. At standard atmosphere the sample and structure surface can be contaminated by water particles or films that can additionally complicate electrical investigations.

Although, four-probe measurements are performed where no contact resistance will influence the measurements, the contact resistance is still present and is a general problem for contacting different materials in the nano scale range. Surface impurities at the samples, structures and four-probe tips can prevent an electrical current flow. During the measurements partially high currents had to be applied to melt the tips with the structures. In this context, the structures became damaged which have influenced the results of the performed experiments.

In the next sections the free-standing structures produced by low-dose and high-dose processes will be presented. The investigation results concerning the electrical properties will be discussed for these structures and a simulation program will be introduced so that the experimental results can be compared to simulations.

6.1 Nano structures for electrical properties investigations

For the first investigations simple line-like free-standing conductors were produced. Cavities were created to produce free-standing structures of 1-50µm in length, 40-1000nm in width and 30-75nm in depth. The diameters can additionally vary due to the used low-dose or high-dose process because of a variation in the resulting cavity width presented in chapter 5.

Because of the conductor size of several nano to micrometres they have to be investigated using the SEM-four-probe measuring device of the Omicron GmbH presented in chapter 3.9. Since the facility could not be used during the whole project free-standing structures were also produced with so-called contact pads of 20·20µm² up to 50·50µm² to get contacted using optical microscopes and to perform electrical investigations with the self-designed four-probe measuring device presented in chapter 3.8. Examples of the produced conductors are shown in the following figure.

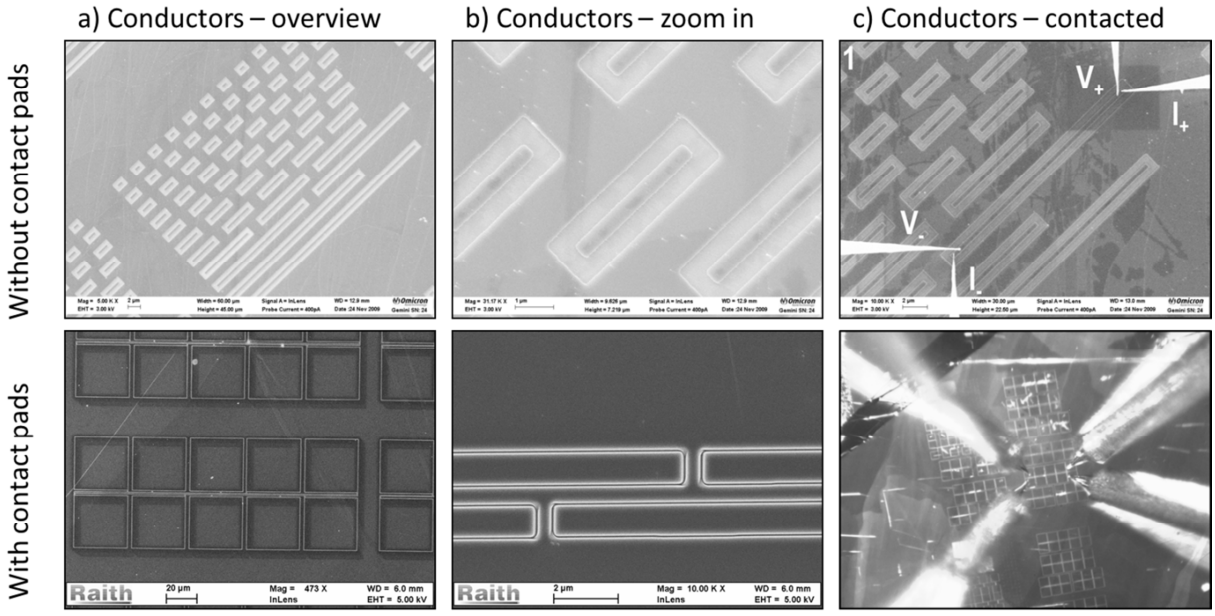

Figure 61: Examples of the produced conductors with and without contact pads that were electrically investigated in the SEM-four-probe and the self-designed four-probe facility.

The conductors without contact pads were produced by low-dose irradiation and a subsequent oxidation process in the oxidation furnace on thick HOPG samples. The conductors were 1-40µm in length, 500nm in width and about 35nm in depth. They were electrically investigated using the SEM-four-probe facility of the Omicron GmbH.

The conductors with contact pads were produced by a high-dose milling process where cavities were produced by line writing. These conductors are up to 100µm in length, 400-1000nm in width and up to 70nm in depth. They were electrically investigated using the self-designed four-probe device.

Although, the presented structures are simple many effects have influenced the electrical measurements and the results of the investigations were often unexpected. To compare the results with theory and to interpret the measured data a simulation program was designed to obtain the three dimensional potential and current distribution in free-standing structure on sample surfaces during four-probe measurements. Before the results of the electrical measurements are presented the potential and current simulation program will be presented in the next section.

6.2 Simulation program for the potential and current distribution

The potential and current distribution of free-standing structures on sample surface was simulated using the MATLAB programming language. The algorithm of the simulation will be described briefly in this subchapter and simulation examples concerning the advantages and disadvantages for four-probe measurements will be presented at the end of this subchapter.

The simulation program can be classified as a finite elements calculation. A three dimensional structure is divided into multiple equal cuboids. If a voltage is applied between two cuboids a current will flow and spread in the cuboid system. In the simulation the current can flow exclusively in x-, y- or z-direction. That means that the current will flow from one cuboid to the next neighbour cuboid in x-, y- or z-direction.

The produced conductors are cuboid shaped. The resistance R of a conductor along the x-, y- or z-axis is a function of the specific resistivity $\rho_{x,y,z}$ multiplied with the length and divided by the width and height

$$\begin{aligned} R_x &= \rho_x \cdot \frac{\Delta x}{\Delta y \cdot \Delta z} \\ R_y &= \rho_y \cdot \frac{\Delta y}{\Delta x \cdot \Delta z} \\ R_z &= \rho_z \cdot \frac{\Delta z}{\Delta x \cdot \Delta y} \end{aligned} \quad . \tag{70}$$

If the conductor is divided into multiple equal small cuboids, every single cuboid has a new resistance along the x-, y- and z-direction $R_{c,x}$, $R_{c,y}$ and $R_{c,z}$. The conductor can now be replaced through an electrical network including the resistances $R_{c,x}$, $R_{c,y}$ and $R_{c,z}$. In the following figure the descriptions are shown schematically.

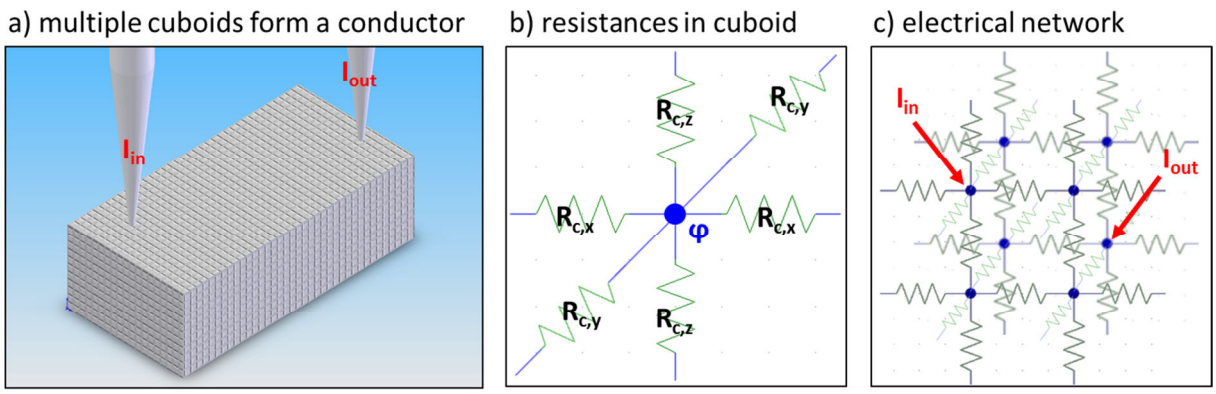

Figure 62: a) A conductor is divided into several equal shaped cuboids. b) Every cuboid has a resistance along the spatial directions. c) Multiple cuboids are connected in an electrical network. In the simulation the node for the current in- and output can be set.

Every node in the electrical network is a centre of a cuboid. Every cuboid has a potential φ_i. The difference between the potential of two nodes is the voltage $U_{ij} = \varphi_j - \varphi_i$. A current or a voltage can be applied between two nodes by the current tips.

For the calculation or simulation of this electrical network the cuboid resistances $R_{c,x}$, $R_{c,y}$ and $R_{c,z}$ have to be calculated. Although, the nodes are connected in all spatial directions by resistances single resistances R_c can be calculated by the following assumption.

Along the x-direction the nodes are only connected in a series circuit together. The equivalent resistance R_{E1} is the product of $R_{c,x}$ and the amount of resistances $R_{c,x}$ along the x-direction n_x. Along the y-direction the resistances R_{E1} are parallel connected. Using the formulas for parallel circuits an equivalent resistance R_{E2} can be calculated. Along the z-direction the resistances R_{E2} are also parallel connected so that the equivalent resistance R_{E3} can be calculated that is equal with the conductor resistance R_x.

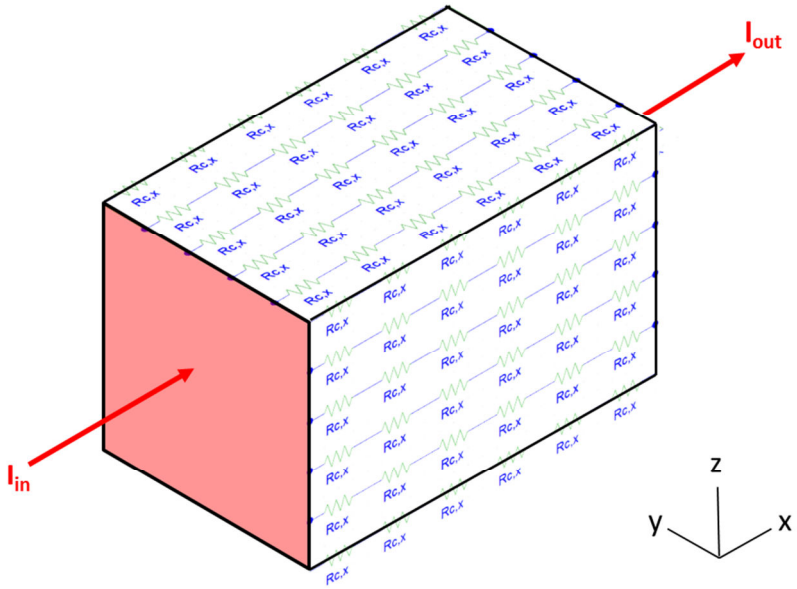

Figure 63: Schematic overview of the determination of the cuboid resistance $R_{c,x}$ in x-direction. If a current is applied at the area along the y- and z-direction the current mainly flows parallel to the x-axis. In this case, the cuboid resistance $R_{c,x}$ can be calculated easily. The calculation of $R_{c,y}$ and $R_{c,z}$ can be performed similar.

The current flows parallel to the x-direction so that the cuboid resistance $R_{c,x}$ can be calculated. Here, n_x, n_y and n_z are the amount of the cuboid resistances $R_{c,x}$, $R_{c,y}$ and $R_{c,z}$ along the x-, y- and z-direction.

$$\begin{aligned} R_{E1} &= n_x \cdot R_{c,x} \\ \frac{1}{R_{E2}} &= \frac{(n_y+1)}{R_{E1}} \\ \frac{1}{R_x} = \frac{1}{R_{E3}} &= \frac{(n_z+1)}{R_{E2}} = \frac{(n_y+1)\cdot(n_z+1)}{n_x \cdot R_{c,x}} \end{aligned} \tag{71}$$

The calculation of the cuboid resistances $R_{c,y}$ and $R_{c,z}$ can be performed similar. After equation (70) and (71) are combined the cuboid resistances can be given as a function of the specific resistivity ρ in x-, y- and z-direction. Furthermore, the reciprocal value of the cuboid resistance is the conductance $1/R = G$.

$$\begin{aligned} R_{c,x} &= \rho_x \cdot \frac{\Delta x}{\Delta y \cdot \Delta z} \cdot \frac{(n_y+1)\cdot(n_z+1)}{n_x} = \frac{1}{G_x} \\ R_{c,y} &= \rho_y \cdot \frac{\Delta y}{\Delta x \cdot \Delta z} \cdot \frac{(n_x+1)\cdot(n_z+1)}{n_y} = \frac{1}{G_y} \\ R_{c,z} &= \rho_z \cdot \frac{\Delta z}{\Delta x \cdot \Delta y} \cdot \frac{(n_x+1)\cdot(n_y+1)}{n_z} = \frac{1}{G_z} \end{aligned} \tag{72}$$

Now, the electrical network is classified concerning all resistances and the connections between all nodes. Additionally, the current in- and output can be included by selection of certain node points. Since the electrical network is fully determined, a network analysis for electrical circuits can be used to calculate the current or potential distribution. There are several network analysis algorithms that have certain advantages or disadvantages for the calculation of individual networks. Examples for network analysis algorithms are the mesh analysis method, the node analysis method and the superposition method that are mentioned and described in references [136] and [137]. All methods use the Kirchhoff's rules that are $\sum_{i=1}^{n} I_i = 0$ for nodes and $\sum_{i=1}^{n} U_i = 0$ within a mesh. The used algorithm for the network simulation is the nodal analysis method [138], [139] because of a short calculation time of the electrical networks presented in this subchapter. The calculation algorithm is explained using the example shown in the next figure.

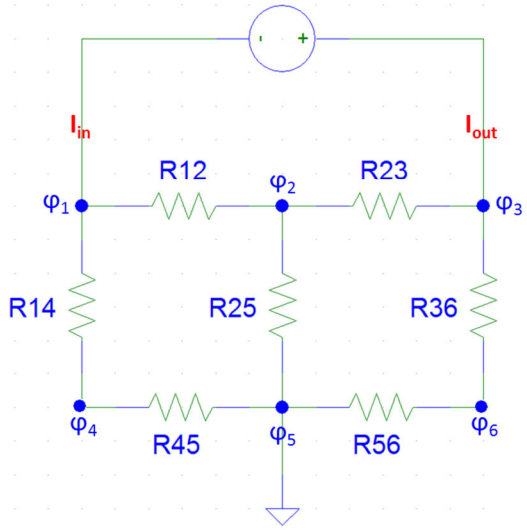

Figure 64: Example of an electrical circuit for the simulation of the potential and current distribution using the node analysis method.

For every node in the electrical circuit the sum of the currents is zero $\sum_{i=1}^{n} I_i = 0$. Using Ohm's law the currents I_i can be replaced by the voltages U_i and the resistances R_i or rather the conductances G_i. The indices of the conductance are equal to the corresponding resistances. The equations of this electrical circuit are:

$$
\begin{aligned}
-I_{in} &= I_{12}+I_{14} &&= G_{12}(\varphi_1-\varphi_2)+G_{14}(\varphi_1-\varphi_4) &&= (G_{12}+G_{14})\varphi_1 - G_{12}\varphi_2 - G_{14}\varphi_4 \\
0 &= I_{21}+I_{23}+I_{25} &&= G_{12}(\varphi_2-\varphi_1)+G_{23}(\varphi_2-\varphi_3)+G_{25}(\varphi_2-\varphi_5) &&= -G_{12}\varphi_1 + (G_{12}+G_{23}+G_{25})\varphi_2 - G_{23}\varphi_3 - G_{25}\varphi_5 \\
-I_{out} &= I_{32}+I_{36} &&= G_{23}(\varphi_3-\varphi_2)+G_{36}(\varphi_3-\varphi_6) &&= -G_{23}\varphi_2 + (G_{23}+G_{36})\varphi_3 - G_{36}\varphi_6 \\
0 &= I_{41}+I_{45} &&= G_{14}(\varphi_4-\varphi_1)+G_{45}(\varphi_4-\varphi_5) &&= -G_{14}\varphi_1 + (G_{14}+G_{45})\varphi_4 - G_{45}\varphi_5 \\
0 &= I_{52}+I_{54}+I_{56} &&= G_{25}(\varphi_5-\varphi_2)+G_{45}(\varphi_5-\varphi_4)+G_{56}(\varphi_5-\varphi_6) &&= -G_{25}\varphi_2 - G_{45}\varphi_4 + (G_{25}+G_{45}+G_{56})\varphi_5 - G_{56}\varphi_6 \\
0 &= I_{63}+I_{65} &&= G_{36}(\varphi_6-\varphi_3)+G_{56}(\varphi_6-\varphi_5) &&= -G_{36}\varphi_3 - G_{56}\varphi_5 + (G_{36}+G_{56})\varphi_6
\end{aligned}
$$

The equations can be converted into a matrix.

$$
\begin{pmatrix}
G_{12}+G_{14} & -G_{12} & 0 & -G_{14} & 0 & 0 \\
-G_{12} & G_{12}+G_{23}+G_{25} & -G_{23} & 0 & -G_{25} & 0 \\
0 & -G_{23} & G_{23}+G_{36} & 0 & 0 & -G_{36} \\
-G_{14} & 0 & 0 & G_{14}+G_{45} & -G_{45} & 0 \\
0 & -G_{25} & 0 & -G_{45} & G_{25}+G_{45}+G_{56} & -G_{56} \\
0 & 0 & -G_{36} & 0 & -G_{56} & G_{36}+G_{56}
\end{pmatrix}
\bullet
\begin{pmatrix} \varphi_1 \\ \varphi_2 \\ \varphi_3 \\ \varphi_4 \\ \varphi_5 \\ \varphi_6 \end{pmatrix}
=
\begin{pmatrix} -I_{in} \\ 0 \\ -I_{out} \\ 0 \\ 0 \\ 0 \end{pmatrix}
$$

The advantage of the conversion into a matrix is a fast calculation of the unknown potentials. The matrix is symmetrically and contains only conductance values of the electrical network. The rows and columns of the matrix can be numbered. Because of the symmetry the matrix entries m_{ij} and m_{ji} are equal and indicate that two nodes *i* and *j* are connected by a resistance R_{ij} with the conductance G_{ij}. Along the main diagonal all resistances or rather conductances are summed for a certain node *i* or *j* and their connection nodes.

Before the potentials can be calculated one of the potentials φ_i has to be set to zero. For the example in Figure 64 this would be φ_5. Now the row and column *i* can be eliminated from the matrix and the calculation speed will improve.

The presented conversion of the Kirchhoff's current laws of an electrical circuit into a matrix of conductances and the solvation of the matrix to determine the potentials is the mentioned node analyse method.

After the potentials have been calculated the voltage between two nodes can be calculated by $U_{ij} = \varphi_j - \varphi_i$. The currents between two nodes can be calculated by Ohm's law $I_{ij} = U_{ij}/R_{c,x,y,z}$. The calculated data can be displayed along two of the three axis x, y and z. To obtain three dimensional images a front-view (x, y), side-view (y, z) and top-view (x, z) can be shown. Additionally, the free dimension axis (front-view: z, side-view: x, top-view: y) can be set manually to show the potential and current distribution for different layers for example on the surface or in the third layer parallel to the surface.

The voltage measured during a four-probe measurement can also be simulated. Therefore, the position of the voltage tips and so the connection points with the solid have to be transferred into the simulation. Like for the current in- and output in the simulation, also the voltage as the potential difference between two nodes can be separately calculated. Because in the simulation every node can be set as a current in- or output and as a

voltage measure node a lot of possibilities occur. Additionally, images can be loaded into the simulation where colour values correspond to current in- and output, voltage tip contact points or blank positions. Furthermore, a substrate can be simulated too.

To determine the accuracy of the simulation a simple experiment was setup where four-point measurements were performed. The comparison of the simulated and the experimental data is shown in the next figure.

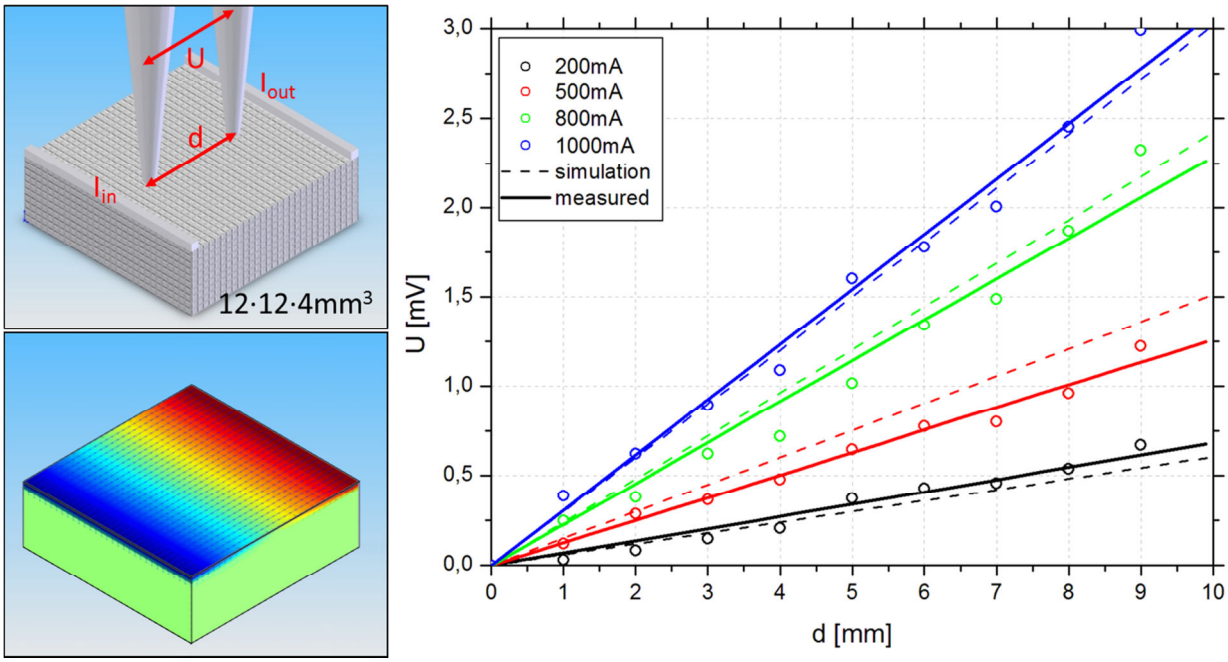

Figure 65: Example of the measurement and the simulation on a HOPG bulk of 12·12·4mm³. The bulk was contacted by wires at the bulk edges where a current was applied between 0.2-1A. Two tips measured the voltage at different surface positions symmetrically from the centre of the bulk surface at distances d between 1-10mm. The same setup was simulated and the obtained data was compared to the measured values.

The calculated potentials show a homogeneous distribution along the HOPG surface. The current flows in a direct line from one wire contact to the other. Additionally, the penetration depth of the current is low as the side-view and the front-view show.

The simulation overview shows a potential and current distribution that was assumed for the experiment before. The plot in the figure shows the measured and simulated voltage as a function of the tip distance *d* for currents of 0.2-1A. For this experiment the measured and simulated data deviate up to 16%.

For all performed simulations in this project the literature values for $\rho_{x,y}$ and ρ_z of HOPG were used [115] and are $\rho_{x,y} = 4.5 \cdot 10^{-5}$ Ω·cm and $\rho_z = 0.2$ Ω·cm at room temperature.

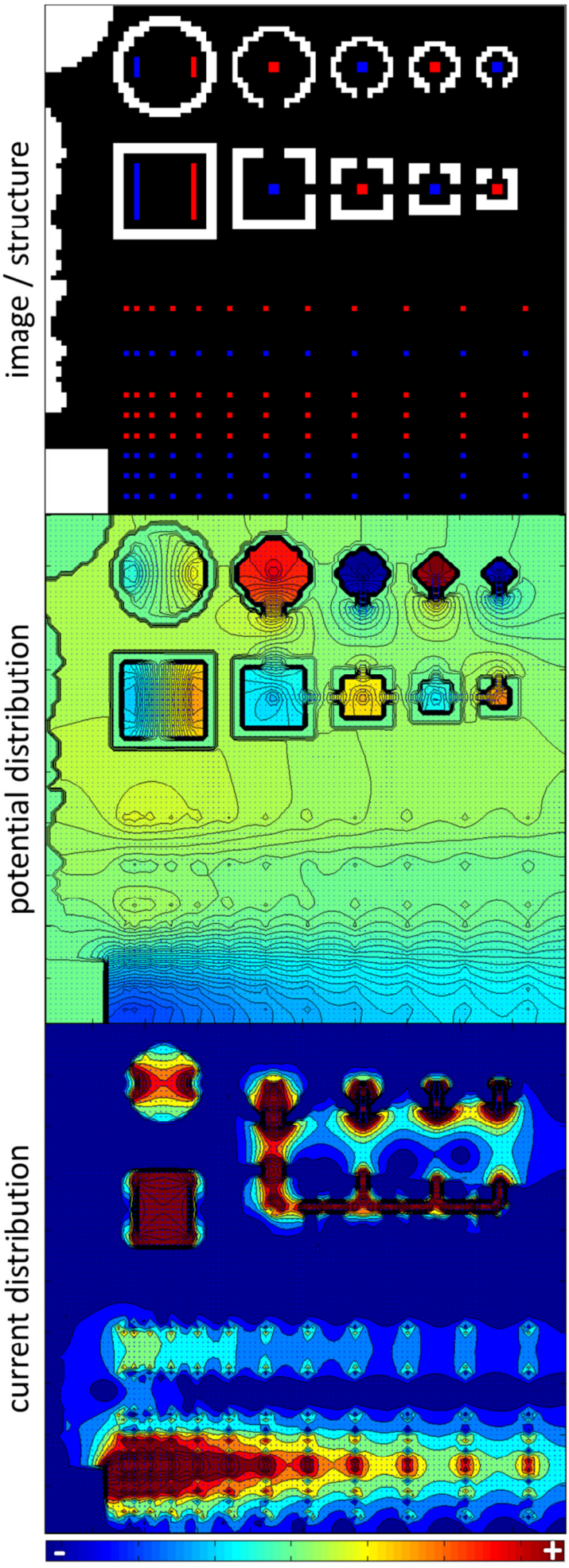

Figure 66: Simulation example of a structure (black) with defects (white) that was contacted with multiple current in- (red) and current out tips (blue). The image contains of 100·100 pixels and has a thickness of 2 pixels (minimum thickness).

Although, the presented simulations were very symmetric concerning the shape of the simulated structures Figure 66 shows a potential and a current distribution of an system with defects and multiple current in- and outputs to present additional possibilities of the simulation that can be used for comparison with future experiments.

Square and circle shaped structures were simulated and multiple current in- and output points as well as defects were implemented in the simulation. The potential and current distribution for the array of current in- and outputs shows a realistic behaviour.

At the edges of the structure the potential lines are perpendicular. The asymmetry of the defect edges perturbs the symmetry of the potential and current distribution. The isolated circle and square structure show a realistic and symmetric potential and current distribution. The other circles and squares are connected through open gates. Here, the current mainly flows directly from current in- to output nodes.

Some unsolved problems are a wrong potential or current distribution direct at the edges or defect centres. Because at defect centres the potentials have to be set as zero potentials there is a potential difference at the

edges that will perturb the evaluation of the potential and current distribution at defect points but that has no influence on the simulation or the simulation results. Unfortunately, the resistances $R_{c,x}$, $R_{c,y}$ and $R_{c,z}$ will not be calculated exactly when defects are included in the simulation. Although, the node potential method is a fast algorithm, the matrix dimension will increase by one additional row and column when one potential is added so the calculation time will increase strongly. The actual version of the simulation can calculate up to 40000 potentials at moderate calculation times of about 40min at the used computer system (Windows 7 64bit, Intel i3 CPU 3.33GHz, 16GB RAM). Additionally, the MATLAB code is limited concerning the maximum usable computer memory on some operation systems so that in future the program code will probably be transferred into another programming language. This will increase the amount of potentials that can be calculable and so the resolution of the potential and current distribution.

The presented potential and current simulation is used to support the measured data of experiments concerning the electrical properties of free-standing conductors that will be discussed in the following subchapters.

6.3 Electrical properties of conductors on thick HOPG samples

First electrical properties of free-standing conductors were performed in cooperation with the Omicron Nanotechnology GmbH using their SEM-four-probe facility [111]. The free-standing conductors have no contact pads and are shown in Figure 61. They were produced on thick HOPG samples using a low-dose irradiation and a subsequent oxidation process in the oxidation furnace.

As mentioned before, these conductors are not electrically isolated from the rest of the HOPG bulk. The conductor height is about 35nm. They are 500nm in width and their length varies from 1-40µm. Although, the electrical conductivity along the basal-plane direction is about 10^{-5}-10^{-4} higher than in z-axis direction the current will flow through the HOPG bulk for very long conductors due to a very low ratio of conductor height to conductor length of 35nm / 40000nm that is about 10^{-5}. Electrical measurement results will be shown for two conductor types of 5µm and 20µm length and compared to the simulation results.

6.3.1 Four-point measurements of conductors on thick HOPG - experiments

Using the SEM-four-probe facility the current and voltage tips were contacted along the 5µm and 20µm conductors at various positions along a line on the conductor surfaces. In the next figure the results of the measurements are presented.

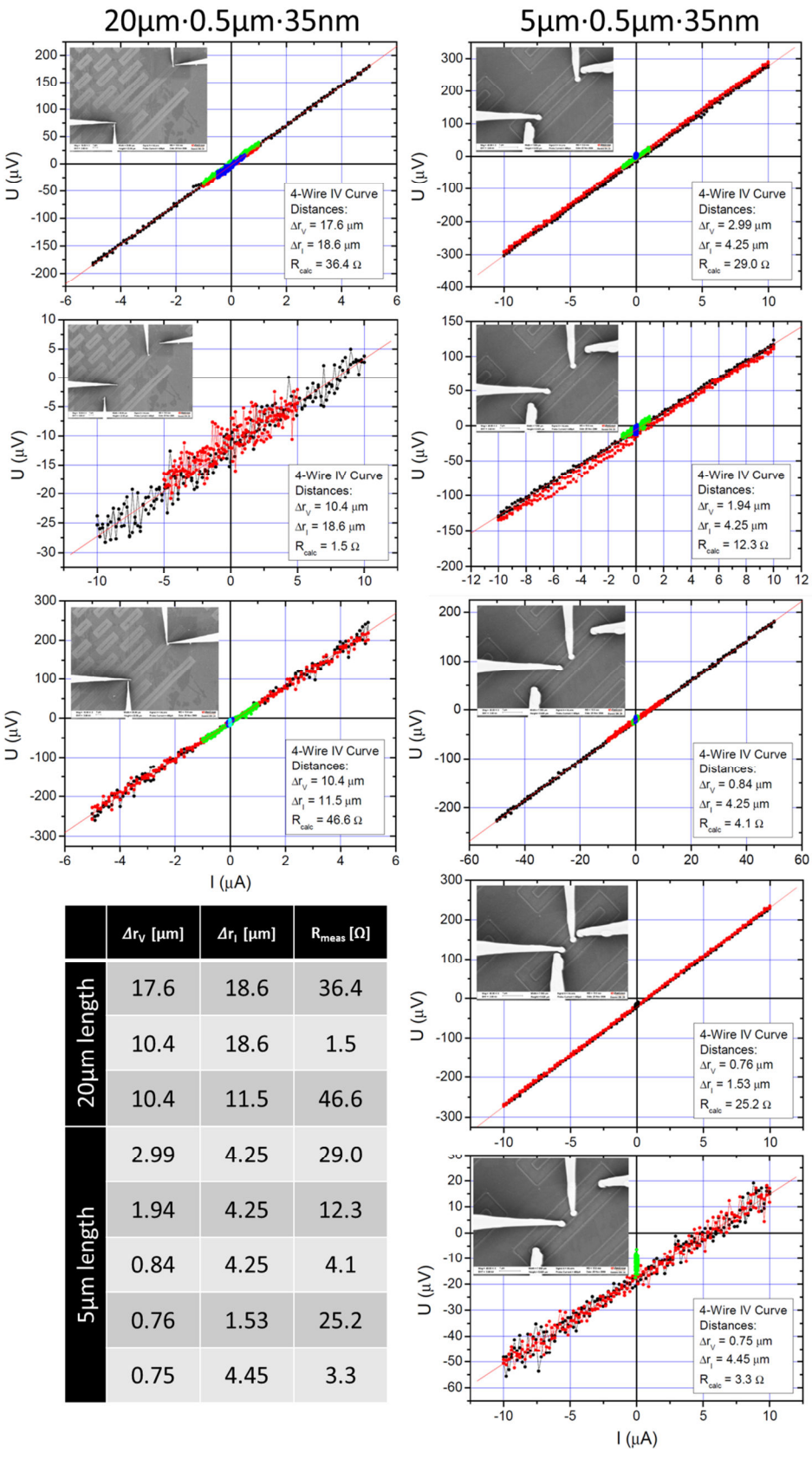

	Δr_V [µm]	Δr_I [µm]	R_{meas} [Ω]
20µm length	17.6	18.6	36.4
	10.4	18.6	1.5
	10.4	11.5	46.6
5µm length	2.99	4.25	29.0
	1.94	4.25	12.3
	0.84	4.25	4.1
	0.76	1.53	25.2
	0.75	4.45	3.3

Figure 67: Four-probe measurements on 5µm and 20µm long conductors with a height of 35nm and a width of 500nm. The shown table gives an overview about the measured parameters Δr_V: voltage tip distance, Δr_I: current tip distance, R_{calc}: slope U / I.

The measurements on the 20µm conductors show a strong decrease of the resistance after the voltage tip distance is decreased. When the current tips are approached to the voltage tips the resistance increases and can be higher than in the first measurement. This behaviour cannot be explained for electrical isolated conductors but by additional leak currents in the HOPG substrate.

For the measurements on the 5µm conductor the voltage tip distance is decreased in the first three measurements by 1/3 stepwise. The resistance decrease is not 1/3 and can only be explained by additional bulk conductance too. Additionally, the dependency of the resistance to the current tip distance shown in measurements 4 and 5 support the assumption of additional leak currents.

The measured data of the 5µm conductor measurements can be used to plot the resistance as a function of the voltage tip distance Δr_V at constant current tip distance Δr_I (measurements 1, 2, 3, 5) and as a function of the current tip distance Δr_I at constant voltage tip distance Δr_V (measurements 3, 4, 5) to highlight the discrepancy of the evaluation of the resistance.

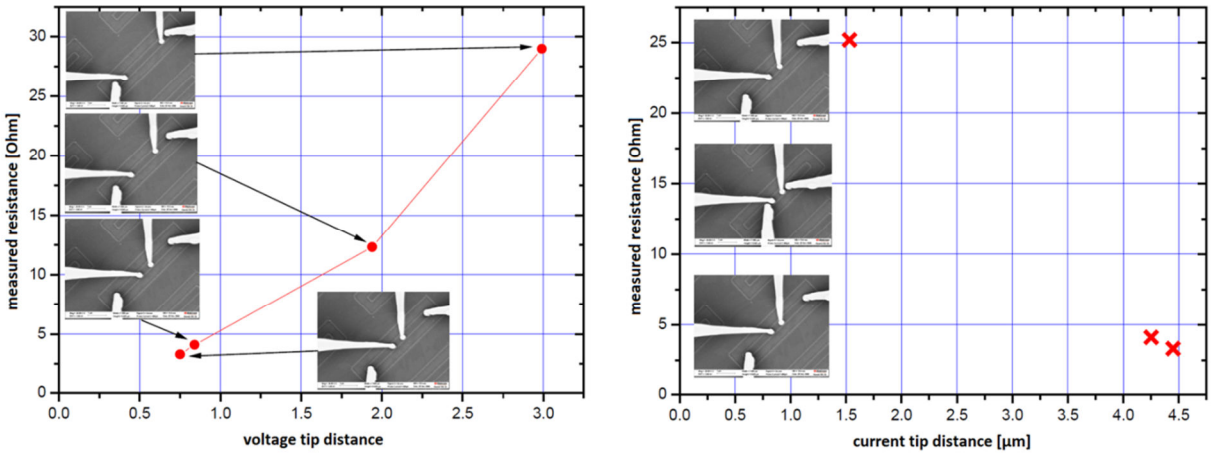

Figure 68: Resistance as a function of the voltage and current tip distances. The data was extracted from the measurements presented in Figure 67 before to show the discrepancy of the resistance measurements of the conductors.

The overview shows in detail the non-linear behaviour of the resistance increase for increasing voltage tip distances that cannot be explained by a simple conductor current flow. The right plot additionally shows that the measured data is reproducible. The measurements at current tip distances of Δr_I =4.25mm and Δr_I =4.45µm were measured before and after the measurement of the current tip distance measurements at Δr_I=1.53µm. Unfortunately, the behaviour of the resistance as a function of the current tip distance cannot be observed due to too less measured data.

6.3.2 Four-point measurements of conductors on thick HOPG – simulations

The experimental data can be compared to calculation data using the specific resistivity ρ of the HOPG and the conductor dimensions. Later the simulation results can be compared to experimental and calculated data. The resistance of a separated conductor on an isolating substrate can be determined by the formula

$$R_{x,y,z} = \rho_{x,y,z} \cdot \frac{\Delta length}{\Delta width \cdot \Delta height} \tag{73}$$

along the three axes as it was mentioned before in chapter 6.2 and chapter 3.8.2. For a cubic structure the resistance depends on the side the current is applied, the x-y, y-z and x-z surface area. Although, the current flows from one current tip to the other during a four-probe measurement, the current flow is mainly along one direction after the cur-

rent has spread in the conductor. In this context, the presented formulas can be used and compared with the measured data of the four-point measurements.

Because the current is distributed in the conductor the width and the height are equal with the factors Δwidth and Δheight if a current flows in x-direction. If the current flows along the x-direction the potentials are equal at the y-z-area at a given x-value. If a four-probe measurement is performed the voltage tips measure the potential difference at two surface points. The value Δlength is therefore the voltage tip distance Δr_V. The specific resistivity is given by the current flow direction in x-, y- or z-direction $\rho_{x,y,z}$.

In the following table the measured and calculated resistances are presented and compared to each other.

	Δr_V [µm]	Δr_I [µm]	R_{meas} [Ω]	R_{calc} [Ω]
20µm length	17.6	18.6	36.4	402.3
	10.4	18.6	1.5	237.7
	10.4	11.5	46.6	237.7
5µm length	2.99	4.25	29.0	68.34
	1.94	4.25	12.3	44.3
	0.84	4.25	4.1	19.2
	0.76	1.53	25.2	17.4
	0.75	4.45	3.3	17.1

Table 3: Comparison between measured and calculated resistance values. The calculated values were obtained using the formulas for an electrically isolated conductor with a specific resistivity with known length, width and height values.

The calculated data for an electrical isolated conductor differs strong from the measured data obtained from four-probe measurements. The discrepancy can be explained by leak currents in the HOPG sample that influence the measured data as mentioned before.

The fact that the measured data for the 20µm conductor differ stronger (factor < 160) from the calculated data in comparison to the values obtained from the 5µm conductor measurements (factor < 6) is an indication for increasing leak currents with increasing length-height ratio of the conductors.

The simulation presented in chapter 6.2 can be used to calculate the voltage between the two voltage tips by including the HOPG bulk and the cavities in the calculation. The simulations were performed for the 5µm and 20µm conductors for room temperature. The top-, front- and side-views of the potential and current distributions are shown in the next figure. The cavity width is 500nm and the cavity depth is 35nm. The front- and side-views are represented by the red dashed lines shown in the images. Here, the potentials of the cavities had to be set to zero to make the plots visible with the MATLAB plot program which does not change or influence the simulation results.

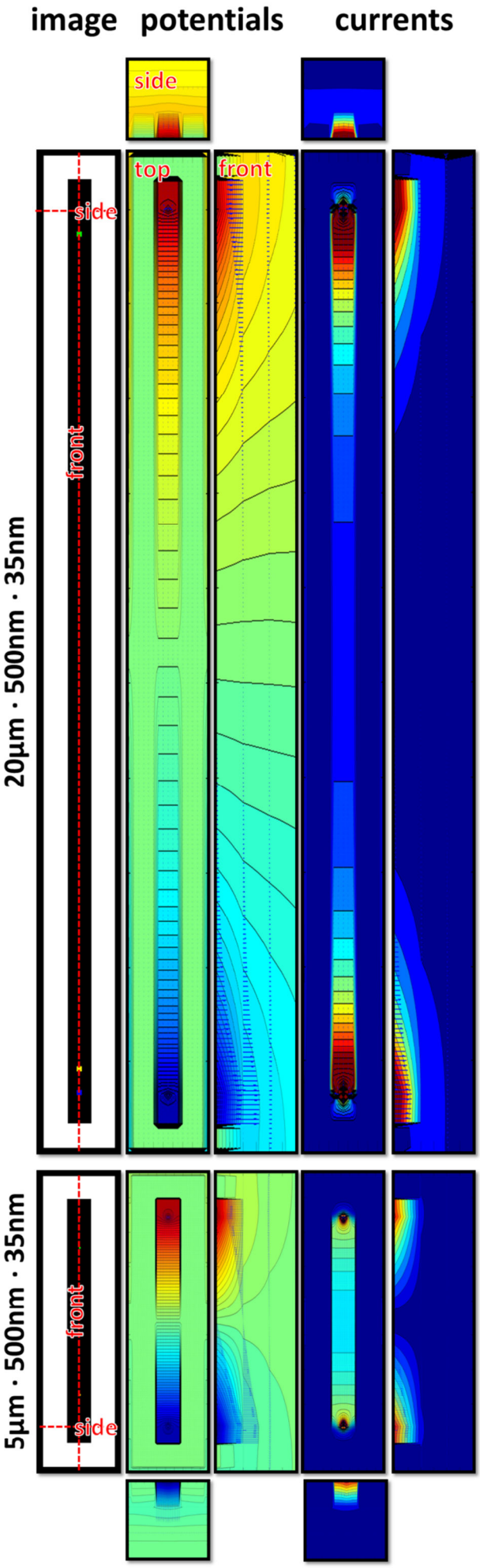

Figure 69: Simulations for the 5µm and 20µm conductors with 500nm width. The cavity depth was 35nm. The potentials of the cavities had to be set to zero due to the used plot program. The top-, front- and side-view concerning the potential and current distribution is shown for the 5µm and the 20µm conductors. The simulation included the HOPG substrate and the cavities.

The simulations were performed using about 40000 potential nodes which are nearly the maximum of the possibilities of the program code. Each image pixel of the 5µm simulations equals 35nm in x-, y- and z-direction. For a better visibility the z-scale in the front- and side-view was stretched. Along the z-direction 35nm conductor material and 70nm HOPG bulk material was simulated. Concerning the 20µm conductors each pixel in x- and y-direction equals 100nm due to the maximum of potentials that can be calculated with the program. For a better comparability with the simulations of the 5µm conductor the z-direction was scaled by 35nm per pixel too. Also here 35nm conductor and 70nm of HOPG bulk was simulated along the z- direction.

The top-view images of the potentials and currents for 5µm and 20µm conductors show a realistic and homogeneous distribution for a four-probe measurement with current tips positioned on the red and blue pixel shown in the images. The green and yellow pixels are the positions of the voltage tips that were used for the determination of the U/I-values or rather the resistance (see next table).

Most important results of the simulation are the front- and side-views. Especially for the 20µm conductor the potentials in the HOPG bulk are not equal. This results in leak currents during four-probe measurements with a high current tip distance Δr_I. The current flow through the HOPG bulk can explain the discrepancy of the performed four-probe experiments on the conductors.

The leak currents can also be observed for the simulation of the 5µm conductor especially in the potential distribution in front-view. Here, the effect of the leak currents is much lower. In this context, the measured resistances should be more like the calculated or simulated resistances. This was shown in Table 3 before.

Four-probe measurements with different current and voltage tip positions presented in Figure 67 were simulated. The positions of the current and voltage tips were included into the simulation program through coloured pixels (red, blue, yellow, green) in the images shown in Figure 69. Table 4 adds the simulated resistance values to Table 3.

	Δr_V [µm]	Δr_I [µm]	R_{meas} [Ω]	R_{calc} [Ω]	R_{sim} [Ω]
20µm length	17.6	18.6	36.4	402.3	86.8
	10.4	18.6	1.5	237.7	28.1
	10.4	11.5	46.6	237.7	56.2
5µm length	2.99	4.25	29.0	68.34	47.78
	1.94	4.25	12.3	44.3	29.4
	0.84	4.25	4.1	19.2	13.2
	0.76	1.53	25.2	17.4	15.8
	0.75	4.45	3.3	17.1	11.0

Table 4: Measured, calculated and simulated resistances for the 5µm and 20µm conductors.

The simulated resistances fit better to the measured experiments as the calculated resistances do. The simulated values differ by a factor of <19 for the 20µm conductor and by a factor of <4 for the 5µm conductor. Additionally, the simulated data shows a higher decrease of the resistance than 1/3 while decreasing the voltage tip distance by 1/3 that can only be explained by leak currents.

Especially the values for 20µm length become strongly corrected using the simulations. Because the leak currents are stronger for the 20µm than for the 5µm conductor it can be assumed that leak currents influence the measured resistance values strongly.

Although, the simulated values still differ from the measured values the leak currents can be identified using the simulation program. One reason could be that only a small part of the HOPG bulk could be simulated. Additionally, the simulation does only include bulk properties and no size-effects, HOPG crystals, edge defects or other nano and micro physics.

It can be assumed that at length to height ratios $\Delta l/\Delta h$ that are smaller than ~100/1 the current flow will mainly be located in the conductors due to the small leak currents for the 5µm conductor with a length to height ratio $\Delta l/\Delta h$ of $5000/35 \approx 143$.

Because the conductivity along the basal-plane and c-axis direction is a function of the temperature the minimum length-height ratio $\Delta l/\Delta h$ will rise above 100/1 for a localized current flow in the conductors at low temperatures. While the ratio of the conduc-

tivities in basal-plane and c-axis direction $\sigma_{x,y}/\sigma_z$ is 4700 at room temperature (see Figure 29) the ratio will rise to about $\sigma_{x,y}/\sigma_z$=28800 at 5K using liquid helium. For this example the minimum length-height ratio $\Delta l/\Delta h$ will increase probably to about 400/1 like the following simulation example shows.

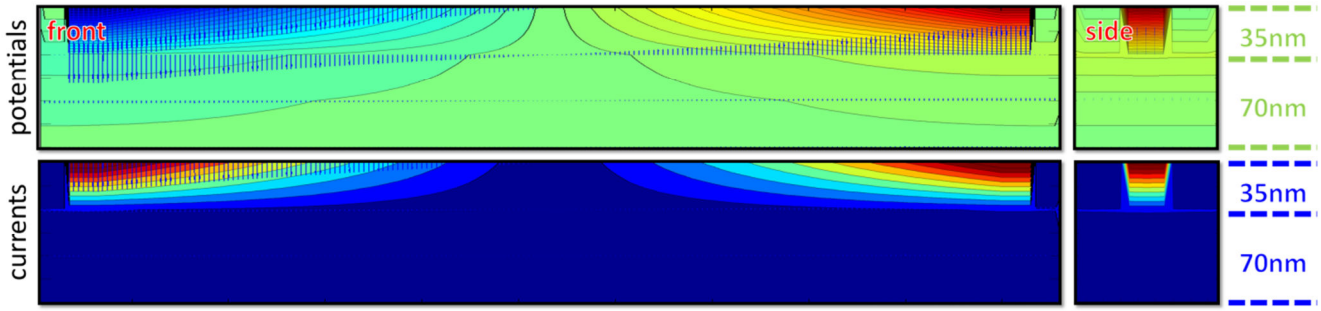

Figure 70: Simulation example of the 20µm conductor presented in Figure 69 before at 5K. The potential and current distribution changes due to a new conductance ratio of $\sigma_{x,y}/\sigma_z$=28800 that is about 6 times larger than at room temperature.

Here, the same simulation was performed as in Figure 69 for the 20µm conductor but at a temperature of 5K. Because conductance ratio $\sigma_{x,y}/\sigma_z$ is 6 times higher than at room temperature the current flow is more localized in the basal-plane direction and there are up to no leak currents for the 20µm conductor on thick HOPG.

Because the leak currents will be a problem for large structures on thick HOPG thin HOPG substrates were irradiated in a high-dose irradiation process to produce electrical isolated free-standing structures. The electrical investigation of these structures is presented in the next subchapter.

6.4 Electrical properties of conductors on thin HOPG

Especially for large structures the leak currents will make experimental results unusable. Additionally, for complex structures or even electrical networks it is necessary that the structures are all electrical isolated.

For this reason electrically isolated conductors were produced by high-dose irradiation on thin HOPG samples. They were investigated concerning their electrical properties mainly to determine the use of this method for later productions of electrical isolated networks on HOPG surfaces with included complex structures.

The conductors presented in this chapter were produced by a line-like production of cavities with a high-irradiation process like presented in Figure 61. Additionally, contact pads were produced that are in contact with the conductors to perform electrical properties investigations using the self-designed four-probe device.

Simulations show that the additionally produced contact pads do not or only slightly influence the current flow through the conductors like the following top-views of the current and potential distribution show.

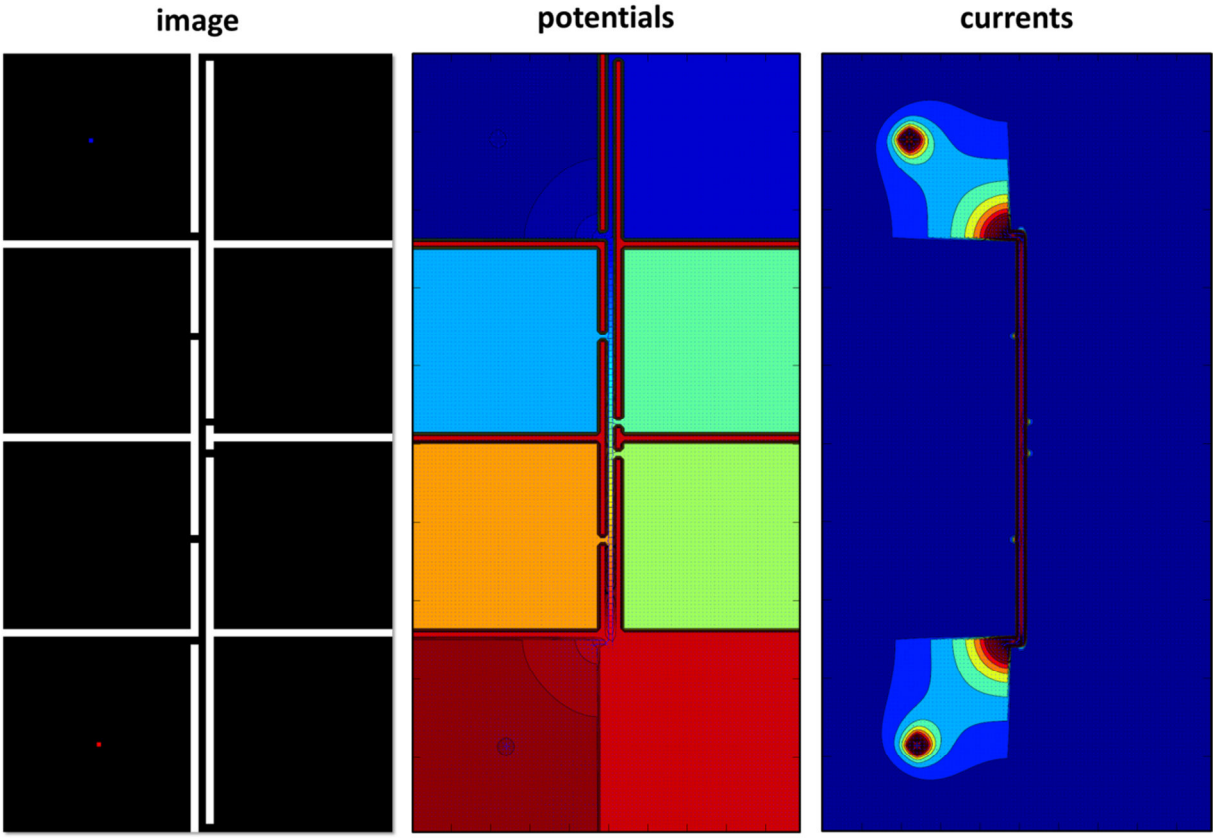

Figure 71: Example of the simulated potential and current distribution after applying a current between two contact pads of the produced structure.

A conductor with eight contact pads was simulated. Here, a current flow was simulated between the top left and bottom left contact pads.

The second image of Figure 71 shows that the potential distribution is homogeneous for contact pads. The potential of a contact pads is nearly equal with the potential at the corresponding conductor position. In this context, the voltage tips can be contacted on the contact pads to measure the voltage between two conductor positions.

The image of the current distribution shows that the current flow is mainly concentrated in the conductor. Only at the connection points between the conductor and the contact pads the current is slightly unsymmetrically. Because the current flows through the conductor it can be assumed that the current in the conductor is equal to the current applied into the structure trough the current tips.

In summary, the simulations show that the contact pads will not influence the four-probe measurements.

6.4.1 Four-probe measurements of conductors on thin HOPG – setup

Several thin HOPG samples were prepared and about 150 conductors with contact pads were produced and electrically investigated using the self-designed four-probe device.

Cavities in line mode were produced to isolate the structures from the rest of the HOPG. A line dose of 1.6µC/cm was used to obtain cavity depths of 40-80nm like presented in chapter 5.4.3. In this context, samples with sample areas thinner than the cavity depth had to be identified by optical microscope measurements and the simulation program for the thickness determination of thin HOPG samples presented in chapter 4.4.2.

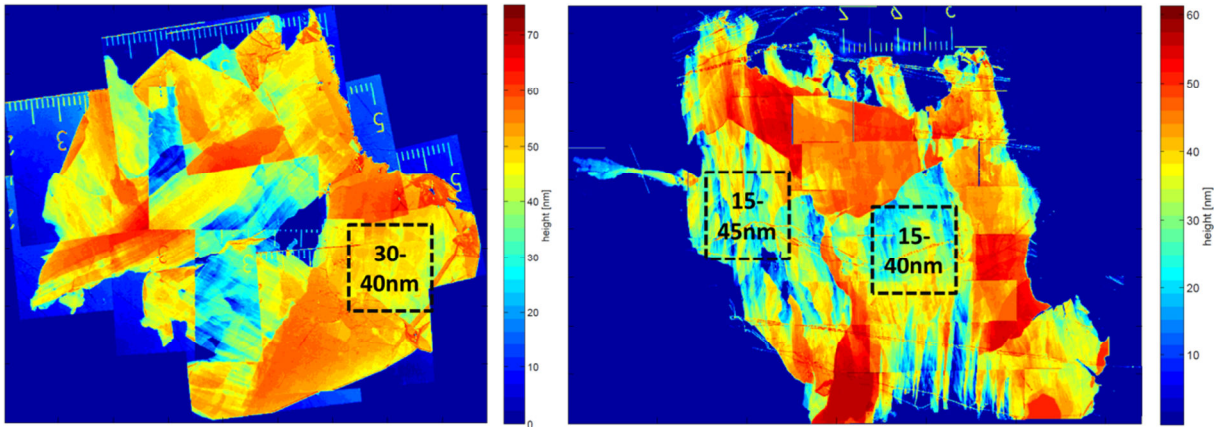

Figure 72: Examples of the sample thickness obtained by the simulation program introduced in chapter 4.4.2 for some of the used samples. The height of an area can be determined by the displayed height minus the reference height at the mica surface that is shown in blue.

At the beginning of this chapter five requirements were listed for the electrical properties investigation.

Most of the produced structures were not electrically isolated fully from the rest of the HOPG sample. The electrical isolation was tested by measuring the resistance between every contact pad with the rest of the HOPG. If the measurements showed an overload or rather resistances above several of MΩ the pads were classified as electrical isolated. Some measurements showed effects like 5 of 6 isolated structures but an electrical contact of all isolated contact pads to the non-isolated pad. Additionally, some contact pads were isolated but became electrical conductive to the HOPG after several repeated measurements. Furthermore, some contact pads were isolated from the HOPG but also from some or all other contact pads. Only two of the produced structures fulfil all requirements concerning ideal structures for an optimal electrical properties investigation.

These complications occur mainly due to the production process and sample inhomogeneity. The thickness of the irradiated sample areas varies. The last figure shows that the thickness can vary several of nanometres in small areas of 500·500µm. AFM measurements show that in the micro- or nanometre scale the thickness can vary up to 50-100nm probably generated during the exfoliation process. In this context, the sample

thickness can be higher than the cavity depth so that a current can flow between the structures and the surrounding HOPG. Additionally, the produced cavities vary strongly concerning their depth that is due to the irradiation process showed in chapter 5.4.3. So the cavity depth will not be larger than the sample thickness for the whole structure in most cases. An applied voltage or current during the measurements can additionally lead to a reorganisation at the produced cavities so that electrical conductive bridges between the contact pads and the HOPG can occur. Impurities on the sample surface can also cause conductive bridges at cavities. Although, stitching effects can be excluded due to the production of the structures only in write fields some structures were produced with slight deformations that can cause additional conductive bridges. Furthermore, some structures became damaged after they were produced. These are the main reasons for the production of non-perfect structures.

6.4.2 Four-Probe measurements on non-perfectly isolated conductors

Although, these structures were not considered for the electrical properties investigation some of the results of the four-probe measurements will be shown in the following figures to explain some details of the measurements.

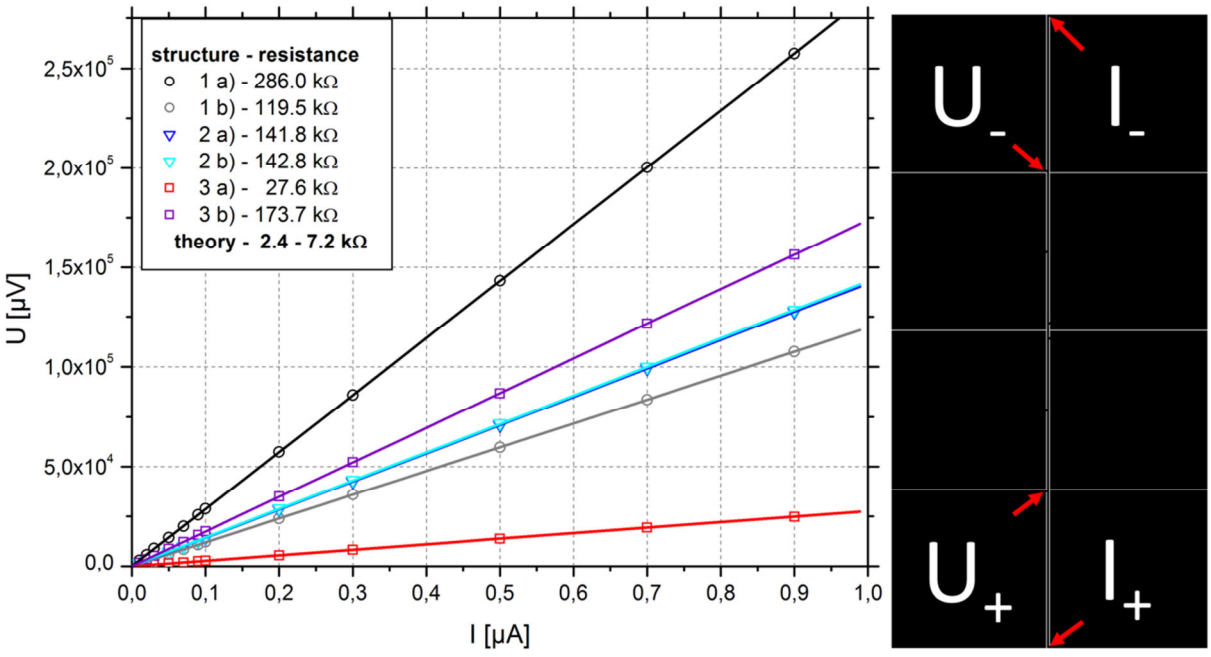

Figure 73: Experimental results concerning four-probe measurements of 6 non-perfect structures. The conductor is 200µm in length, 400nm in width and 15-45nm in depth. The conductor is contacted with contact pads where four-probe measurements were performed using the four marked contact pads. The contact bridge between the marked contact pads and the conductor are shown by red arrows. The distance between the two conductor positions where voltage measurements were performed is 101µm.

In Figure 73 six measurements are shown. The measurements are grouped where two measurements a) and b) are in a group 1-3. Structures in one group are located closely

together on the sample surface so that the sample thickness is nearly equal for structures of one group. All measurements were performed on structures presented on the right side of the figure. Additionally, all measurements were performed using the shown current and voltage tip positions. A current up to 0.9µA was applied and the voltage was measured using the voltage tips.

For all four-probe measurements on these non-perfect-structures the slope $\Delta U/\Delta I$ is constant up to 0.9µA. In this context, the deviation of the measured values is very small for non-perfect structures. But the obtained resistances vary for every measurement also for structures of the same group. The difference in the resistance could be an indication for additional leak currents. The resistances are about 1-2 orders of magnitude larger than predicted by the theory. Additionally, the contamination of the sample with gallium ions and the destruction of the structure edges change the resistance of a conductor strongly. The presented resistance vary from 27.6-286.0kΩ for equal structures but probably different structure depths.

The resistances between the voltage and the current tips were measured when they were contacted on the contact pads. The measured resistances are, for example, 54.5kΩ (I-I), 151.0kΩ (U-U) for structure 3b) and 150.0kΩ (I-I), 272kΩ (U-U) for structure 2a). As expected for contact resistances which are not extremely large these values are of the order of the resistance measured with the four-probe device but up to now no clear relationship to the measured resistances could be determined.

Mainly because the conductive bridges of the structures cannot be identified simulations cannot be performed for a comparison with the presented non-perfect structures. Positive results of the measurements are the constant slope of every data and so a low deviation. In this context, the self-designed four-probe device is operative and measurements on perfect structures will be performed with low deviations.

6.4.3 Four-Probe measurements on two perfectly isolated conductors

Due to the measurements of non-perfect structures it could be expected that the obtained resistances on perfect structures will be nearly equal to the theory value. But, the measurements of the perfect structures that were electrically isolated from the rest of the HOPG bulk show a higher resistance than predicted through theory with leak currents as shown in the next figure.

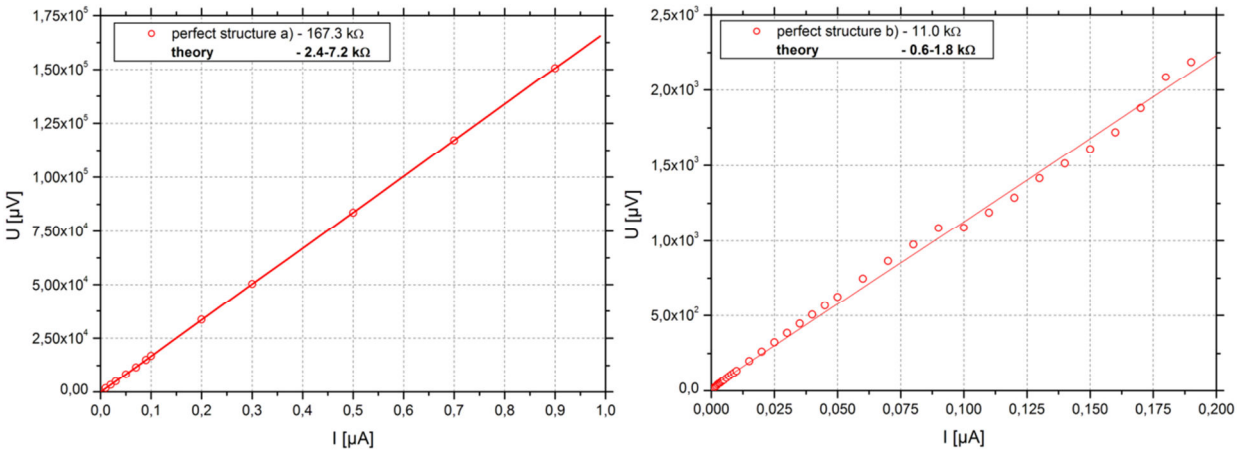

Figure 74: Results of the four-probe measurements on the perfect structures. The theory values were determined using a diameter of 101µm·400nm (15-45)nm for structure a) and of 25µm·400nm·(30-40)nm for structure b) with bulk conductivities. The structure depth was determined using the height distribution of the samples presented in Figure 72. Structure a) was produced on the right sample and structure b) on the left sample.

The results of the electric measurements show a large discrepancy between the theory values and the measured data. For structure a) the values are 23-70 times higher than the theory values. For structure b) the measured data is a factor of 6-18 times higher than the theory. Also the simulations presented in chapter 6.2 predict a resistance of 2.7-8.0kΩ for structure a) and a resistance of 0.7-2.0kΩ for structure b). The simulated values will always be larger than the calculated values because only tip or area contacts could be simulated on the top of the sample surface but no area contacts on the sides of the conductor that would make the simulated values more precise. It should be noted, that for the calculation and simulation the electrical conductivity of the HOPG bulk were used. The electrical properties will probably change for small structures after irradiation as shown in the following table.

	R_{meas} [kΩ]	R_{calc} [kΩ]	R_{sim} [kΩ]	$\rho_{x,y}$ [Ω·cm] measured	$\rho_{x,y}$ [Ω·cm] literature	$\sigma_{x,y}$ [Ω^{-1}·cm^{-1}] measured	$\sigma_{x,y}$ [Ω^{-1}·cm^{-1}] literature
a)	167.3	2.4 – 7.2	2.7 – 8.0	$99\cdot10^{-5}$ - $298\cdot10^{-5}$	$4.25\cdot10^{-5}$	$0.03\cdot10^{4}$ - $0.1\cdot10^{4}$	$2.35\cdot10^{4}$
b)	11.0	0.6 – 1.8	0.7 – 2.0	$53\cdot10^{-5}$ - $70\cdot10^{-5}$	$4.25\cdot10^{-5}$	$0.14\cdot10^{4}$ - $0.19\cdot10^{4}$	$2.35\cdot10^{4}$

Table 5: Comparison between measured, calculated and simulated data concerning the resistance, the specific resistance and the electrical conductivity along the x- and y-direction.

The increase of the resistance can be explained by the ion implantation and lattice destruction mainly at the structure edges. Probably more investigations are necessary to explain this effect in full detail but at this point of investigation one conclusion could be that using a high-dose irradiation process the electrical properties of the produced structures will differ from the bulk properties due to the ion irradiation.

One main effect might be that the ion irradiation produces defects which reduce the electrical conductivity. Additionally, the ion implantation can be seen as a doping effect. Gallium atoms have 3 valence electrons and will behave like an acceptor after implanted in silicon or graphite that is the so-called p-doping. Silicon has a diamond structure with 4 sp^3-orbitals and only covalent bonds. The doping causes additional positive or negative charge carrier (n- or p-doping) in the silicon bulk. Graphite has 3 covalent bonds due to the 3 sp^2-orbitals and one electron for the van der Waals interaction along the c-axis. If graphite is p-doped the positive charge carriers will probably interact with or rather neutralize the “free” electron along the c-axis direction and the conductivity along the basal-plane direction will be reduced.

Results of boron-doped HOPG bulks are presented in references [140] and [141]. The investigation results in these references show that the carbon atoms are replaced by the boron atoms which do not occupy intercalate states but carbon atom lattice positions. Carbon-boron bonds occur and the density of π electrons is reduced which results in a decreased electrical conductivity. Unfortunately, no references were found concerning gallium-doped HOPG.

Although, no investigations could be performed on electrical isolated structures after low-dose irradiation process it can be assumed that for low-dose production processes the electrical properties of the produced structures will be more similar to the electrical bulk properties of HOPG due to less implanted ions and less destructed structure edges.

6.5 Chapter summary

To perform electrical measurements on free-standing conductors certain requirements concerning the produced structures are necessary. The produced structures should be electrical isolated from other conductive material, the structures have to be free of damages or contaminations and the ability to contact the structures have to be given.

Because the low-dose and high-dose production processes both have advantages and disadvantages not all requirements can be achieved concerning the resulting structure properties. Low-dose produced structures cannot be produced on thin HOPG samples at this point of investigation and are therefore not electrically isolated. High-dose produced structures can be electrically isolated when produced on thin HOPG samples but become damaged at the edges concerning the lattice arrangement. Additionally, they become doped by the high amount of implanted ions. That will reduce the electrical conductivity of the structures.

Four-probe measurements were performed to measure the resistance or the electrical conductivity of structures produced by low-dose irradiation on thick HOPG samples and by high-dose irradiation on thin HOPG samples. The structures were conductors with 500nm in width and several micrometres in length. The structure depth was dependent

on the irradiation process. Because the SEM-four-probe facility could only be used for one sample system in cooperation with the Omicron Nanotechnology GmbH some conductors were produced with contact pads to perform measurements using the self-designed four-probe device.

A current and potential distribution simulation was simulated with MATLAB to compare the measured data with simulation data. The program uses a node potential analysis algorithm for calculation. Compared to other calculations and to macroscopic measurements on HOPG the simulation results differ only slightly. The program can also load images to simulate three dimensional objects on substrates with defects.

The electrical measurements of low-dose produced conductors on thick HOPG and the simulation results showed that there are leak currents above a certain conductor length to depth ratio that influence the electrical properties of the conductors. For all measurements the obtained experimental data for the resistance is lower than the simulated and calculated data. The simulation takes into account a certain part of the bulk material and is in qualitative agreement even if the simulation results differ not as strongly from the values obtained for isolated conductors than the experiments. Because the electrical conductivity along the basal-plane and the c-axis direction depends on the temperature the length to height ratio might be raised for low temperatures like for example at 77K or 4K by cooling with liquid nitrogen or helium as predicted by simulation results.

Some of the produced structures on thin HOPG samples by high-dose irradiation are electrical isolated but the electrical measurements show much higher resistances than simulations and calculations predict using leak currents. During the high-dose irradiation many ions are implanted in the graphite bulk and into the conductors. Additionally, the conductor edges and the lattice arrangements of the conductors are destructed. Both effects lead to an increase of the specific resistance along the basal-plane direction. One explanation of the increase can be the doping effect caused by the gallium ions where “free” electrons of the carbon atoms are neutralized by positive charge carriers, the gallium ions.

7. Conclusion and outlook

Ion beam lithography was investigated concerning the possibilities of structure production as an alternative to other lithography methods like for example electron beam lithography. The physics of the structuring process were investigated theoretically by simulations and experimentally by measuring the structural properties of the produced structures. Highly oriented pyrolytic graphite (HOPG) was used as material for these investigations. In addition to the direct milling process by high-dose irradiation an indirect production process was investigated where a low-dose irradiation was combined with a subsequent oxidation. Structures that were produced by both processes were not only studied concerning their structural but also concerning their electrical properties.

Compared to other lithography methods ion beam lithography has advantages and disadvantages concerning the structure production. These were studied and additionally determined by experiments and simulations. No resist is needed for ion beam lithography and all materials can be used for the structure production using the high-dose milling process. No chemical etching is necessary that is an advantage in comparison to electron beam lithography. The disadvantages are a long structure production time for serial ion beam lithography, the contamination and destruction of the produced structures due to ion implantation. The disadvantages can be minimized using the low-dose irradiation process for the structure production on graphite. The irradiation time becomes very small. Much less ions are needed and implanted in the sample so that the contamination of the sample is minimized and the structural properties of the produced structures are more controllable and predictable. A problem of the low-dose irradiation structure production process is the necessity of a subsequent oxidation process of the graphite at high temperatures. Only sample substrates can be used which are stable at these temperatures. Additionally, the structure depth is limited. To make this process more competitive to other lithography methods an oxidation at low temperatures is needed that should be engaged parallel to the irradiation process. First improvements could be achieved by using ozone as an oxidant.

Simulations show that the structuring processes and so the structural properties of produced structures depend strongly on the used ion material and only slightly on the used sample material. In this context, an ion material can be chosen that is needed for individual or special structures that should be produced. The physics and the theory of the interaction between the ions and the sample material are included in free accessible software programs that are continuously improved and whose deviation to experiments is generally small.

The ion beam facilities have been improved parallel to other lithography, for example electron beam lithography devices. For the ionLiNE and the eLiNE systems of the Raith GmbH the same software programs (for example GDSII) can be used for ion beam and electron beam devices.

The investigations of the structural properties of the produced structures show critical parameters for the structure production using both methods, the high-dose and the low-dose irradiation processes. A critical ion dose could be identified for the structure production. The investigations of the developed low-dose structure production process show better structural properties concerning the deviation in structure width and depth in comparison to the direct milling process using high-dose irradiation. For the low-dose process the properties of the produced structures mainly depend on the kinetic ion energy. The low-dose production process and the critical parameters can be compared to simulation results and fit well to theory. This is an improvement in comparison to the high-dose irradiation process that is less controllable and predictable the structural properties of produced structures. Although, the low-dose irradiation process has certain disadvantages in comparison to the high-dose irradiation process the results of the investigations will help to develop a new production method in the future which will probably combine the advantages of the high-dose and the low-dose production processes.

In this work not only structural but also electrical properties were investigated on structures produced on HOPG surfaces. HOPG has an interesting anisotropic behaviour concerning the electrical conductivity and especially single graphite layers, the so-called graphene, is a hot topic in recent investigations. This was, together with favourable chemical and other properties, the major reason for the choice of this material.

Four-probe measurements of the produced structures using high-dose and low-dose irradiation processes on thick and thin HOPG show interesting electrical properties. Concerning the low-dose production process on thick HOPG samples the conductor length-to-height ratio is critical to avoid leak currents in the HOPG substrate which cause decreased resistances compared to calculations for an isolated conductor. Simulations are in qualitative agreement with these leak currents. In the case of high-dose production processes the conductors are electrically isolated from the HOPG bulk but the ion implantation and the lattice destruction of the conductors cause an increase of the measured resistance. Concerning the lattice destruction a gallium-doping effect can be probably assumed where positive charge carriers interact with the p_z-orbital electrons so that the electrical conductivity decreases. Both irradiation processes have therefore advantages, disadvantages and limitations concerning the structure production.

The performed investigations and experiments helped to classify current possibilities concerning ion beam lithography and improvements for the future. The low-dose production process is a first step for better structural and electrical properties of produced structures in comparison to the high-dose production process. Improvements were listed concerning the use of multiple charged ions and parallel running irradiation and oxidation processes to obtain more deep, clean, controllable and predictable structures that are less destructed. A further improvement would be the use of chemical processes independent from oxidation processes to expand the possibilities of structure production using the ion beam facility. Right now, the ion beam lithography is an alternative

lithography method for special applications, but it will be more important if improvements for the structuring processes can be applied.

Additionally, the obtained project results will be used to combine lithography methods with cluster physics experiments performed by our group. For example structured surfaces could be used to influence the growth of islands, wires or clusters. Structured surfaces can also be used to fix deposited clusters for further electrical investigations. Furthermore, samples can be structured using the ion beam facility after cluster deposition. A continuation of the cooperation with industry partners will offer additional opportunities at the Technische Universität Dortmund.

Appendix

I. Bibliography

[1] Nobelprize.org. (2011, February) The Official Web Site of the Noble Prize - Physics. [Online]. http://nobelprize.org/nobel_prizes/physics/laureates/2010/

[2] K. S. Novoselov et al., "Electric Field Effect in Atomically Thin Carbon Films," *Science*, pp. 306, 5696, 666-669, 2004.

[3] A. K. Geim and K. S. Novoselov, "The Rise of Graphene," *Nature Materials*, pp. 6, 183-191, 2007.

[4] A. H. Castro Neto, F. Guinea, N. M. R. Peres, K. Novoselev, and A. K. Geim, "The electronic properties of graphene," *Reviews of Modern Physics*, pp. 81, 109, 2009.

[5] S. Stankovich et al., "Graphene-based composite materials," *Nature*, pp. 442, 282-286, 2006.

[6] S. Sivakumar, "Lithography Challenges for 32nm Technologie and Beyond," *Portland technologie Development, Intel Corporation, Hillsboro, OR 97124, USA*, 2006.

[7] Physikalisch Technische Bundesanstalt. (2011, February) [Online]. http://www.ptb.de/de/publikationen/download/pdf/einheiten.pdf

[8] Wikipedia. (2011, March) physical constants. [Online]. http://en.wikipedia.org/wiki/Physical_constant

[9] C. Kittel, *Einführung in die Festkörperphysik*. München: Oldenbourg Wissenschaftsverlag GmbH, 2006.

[10] S. Hunklinger, *Festkörperphysik*.: Oldenbourgh Wissensverlag GmbH, 2007.

[11] N. W. Ashcroft and N. D. Mermin, *Festkörperphysik, 2. korrigierte Auflage*. München: Oldenbourg Wissenschaftsverlag GmbH, 2005.

[12] G. Czycholl, *Theoretische Festkörperphysik*. Berlin, Heidelberg: Springer-Verlag, 2008.

[13] Wikipedia - Lithografie. (2011, April) Lithographie und Steindruck. [Online]. http://de.wikipedia.org/wiki/Lithografie

[14] M. Panhorst. (2011, April) Lithografiemethoden. [Online]. http://www.panhorst.com/s-layer/s-layer-HTML/node13.html

[15] P. W. H de Jager and P. Kruit, "Applicability of focused ion beams for nanotechnology," *Microelectronic Engineering*, pp. 27, 1-4, 327-330, 1995.

[16] D. Lietz - Dissertation, *A New Deep X-Ray Lithography Beamline at DELTA - Setup and Performance* -. Dortmund, 2010.

[17] H. I. Smith et al., "X-ray nanolithography: Extension to the limits of the lithographic process," *Microelectronic Engineering*, pp. 32, 1-4, 143-158, 1996.

[18] L. L. Sohn and R. L. Willett, "Fabrication of nanostructures using atomic-force-microscope-based lithography," *Applied Physics Letters*, pp. 67, 11 1552-1554, 1995.

[19] S. Y. Chou, P. R. Krauss, and P. J. Renstrom, "Imprint Lithography with 25-Nanometer Resolution," *Science*, vol. 272, 5258, 85-87, 1996.

[20] C. E. Mortimer and U. Müller, *Das Basiswissen der Chemie*. Stuttgart: Georg Thieme Verlag, 2001.

[21] Periodensystem.info. (2011, February) [Online]. http://www.periodensystem.info/periodensystem/

[22] N. Bohr, "On the Constitution of Atoms and Molecules, Part I," *Philosophical Magazine*, pp. 26, 1-25, 1913.

[23] N. Bohr, "On the Constitution of Atoms and Molecules, Part II Systems Containing only a Single Nucleus," *Philosophical Magazine*, pp. 26, 476-502, 1913.

[24] W. Heisenberg, "Über den anschaulichen Inhalt der quantentheoretischen Kinematik und Mechanik," *Zeitschrift für Physik A, Hadrons and Nuclei*, pp. 43, 3-4, 172-198, 1927.

[25] E. Schrödinger, "Quantisierung als Eigenwertproblem I-III," *Annalen der Physik*, pp. 79, 361-376 --- 79, 489-527 --- 80, 734-756, 1926.

[26] (2011, February) ChemGlobe. [Online]. http://www.chemglobe.org/general/atomeigenschaften/ionisierung.php

[27] Prof. Dr. Hofsäss. (2011, April) Ion-Festkörper-Wechselwirkung - Lecture. [Online]. http://physik2.uni-goettingen.de/zope/Members/hofsaess/folder.2006-04-20.2327614369/Einleitung%201.pdf

[28] S. Duffe, N. Grönhagen, L. Patryarcha, and B. Sieben, "Penetration of thin C60 films by metal nanoparticles," *Nature Nanotechnology*, pp. 5, 335-339, 2010.

[29] A. S. El-Said et al., "Creation of Nanohillocks on CaF2 Surfaces by Single Slow Highly Charged Ions," *Physical Review Letters*, pp. 100, 237601, 2008.

[30] N. A. Marks, "Evidence for subpicosecond thermal spikes in the formation of tetrahedral amorphous carbon," *Physical Review B*, pp. 56, 5, 2441-2446, 1997.

[31] T. Diaz de la Rubia, R. S. Averback, R. Benedek, and W. E. King, "Role of the thermal spikes in energetic displacement cascades," *Physical Review Letters*, pp. 59, 1930-1933, 1987.

[32] M. von Ardenne, G. Musiol, and U. Klemradt, *Effekte der Physik und ihre Anwendungen*. Frankfurt: Wissenschaftlicher Verlag Harri, 2005.

[33] H. W. Koch and J. W. Motz, "Bremsstrahlung Cross-Section Formulas and Related Data," *Reviews of modern Physics*, pp. 31, 920–955, 1959.

[34] A. B. Migdal, "Bremsstrahlung and Pair Production in Condensed Media at High Energies," *Physical Review*, pp. 103, 6, 1811-1820, 1956.

[35] J. V. Jelley, "Cerenkov radiation and its applications," *British Journal of Applied Physics*, pp. 6, 227, 1955.

[36] R. M. Sternheimer, "The Energy Loss of a Fast Charged Particle by Cerenkov Radiation," *Physical Review*, pp. 89, 1148, 1953.

[37] D. S. Gemmel, "Channeling and related effects in the motion of charged particles through crystals," *Review of Modern Physics*, pp. 46, 1, 129-227, 1974.

[38] P. Sigmund, *Stopping of Heavy Ions*.: SpringerVerlag, 2004.

[39] M. Nastasi, J. Mayer, and J. Hirvonen, *Ion-Solid Interaction - Fundamentals and Applications*. Cambridge: Cambridge University Press, 1996.

[40] Wikipedia. (2011, April) Threshold displacement energy. [Online]. http://en.wikipedia.org/wiki/Threshold_displacement_energy

[41] H. H. Andersen, "The Depth Resolution of Sputter Profiling," *Applied Physics*, pp. 18, 131-140, 1979.

[42] N. Bohr, "On the theory of the decrease of velocity of moving electrified particles on passing through matter," *Philosophical Magazin*, pp. 25, 10, 1913.

[43] F. Bloch, "Bremsvermögen von Atomen mit mehreren Elektronen," *Zeitschrift für Physik A*, pp. 81, 5-6, 293-299, 1932.

[44] H. Bethe, "Bremsformel für Elektronen relativistischer Geschwindigkeit," *Zeitschrift für Physik A*, pp. 76, 5-6, 293-299.

[45] Prof. Dr. Spaan. (2005) Lecture on nuclear and particle physics.

[46] PDG - particle data group. (2011, February) [Online]. http://pdg.lbl.gov/2009/reviews/rpp2009-rev-passage-particles-matter.pdf

[47] J. Lindhard, "The Barkas effect - or Z3, Z4-corrections to stopping of swift charged particles," *Nuclear Instruments and Methods*, pp. 132, 1-5, 1976.

[48] J. F. Ziegler, "The Stopping of Energetic Light Ions in Elemental Matter," *Journal of Appliied Physics*, pp. 85, 1249-1272, 1999.

[49] M. Stiftinger. (2011, April) LSS-Theory. [Online]. http://www.iue.tuwien.ac.at/phd/wimmer/node12.html

[50] J. Lindhard, M. Scharff, and H. E. Schiott, "Range concepts and heavy ion ranges," *Kgl. Danske Videnskab. Selskab, Mat.-Fys. Medd.*, pp. 33, 14, 1963.

[51] J. Lindhard and M. Scharff, "Energy Dissipation by Ions in the keV Region," *Physical Review*, pp. 124, 1, 128-130, 1961.

[52] A. Hoessinger. (2011, February) Simulation of Ion Implantation for ULSI Technology. [Online]. http://www.iue.tuwien.ac.at/phd/hoessinger/node40.html

[53] J. F. Ziegler, J. P. Biersack, and U. Littmark, *The Stopping and Range of Ions in Solids*. New York: Pergamon Press, 1985.

[54] H. Bethe and W. Heitler, "On the Stopping of Fast Particles and on the Creation of Positive Electrons," *Royal Society of London - Series A*, pp. 146, 856, 83-112, 1934.

[55] C. Grupen and B. A. Shwartz, "*Particle Detectors".* New York: Cambridge University Press, 2008.

[56] A. H. Sorensen, "Pair production and bremsstrahlung contributions to the stopping of relativistic heavy ions," *Nuclear Instruments and Methods in Physics Research Section B: Beam Interactions with Materials and Atoms*, pp. 203, 1-4,12-16, 2005.

[57] MELF-GOS. (2011, February) MELF-GOS Model. [Online]. http://bohr.inf.um.es/MELF-GOS.html

[58] M. J. Berger, J. S. Coursey, M. A. Zucker, and J. Chan. (2011, Feb) National Institute of Standarts and Technology - Physical Measurement Laboratory. [Online]. http://www.nist.gov/pml/data/star/index.cfm

[59] J. F. Ziegler, M. D. Ziegler, and J. P. Biersack, *SRIM - The Stopping and Range of Ions in Matter*. Maryland, USA: LuLu Press, 2008.

[60] J. F. Ziegler, M. D. Ziegler, and J. P. Biersack. (2011, Feb) SRIM - Programm. [Online]. http://www.srim.org/

[61] J. F. Ziegler and J. M. Manoyan, "The Stopping of Ions in Compounds," *Nuclear Instruments and Methods in Physics Research Section B: Beam Interactions with Materials and Atoms*, pp. 35, 3-4, 215-228., 1988.

[62] J. F. Ziegler, M. D. Ziegler, and J. P. Biersack, SRIM(TRIM) program - explanation about the Compound Correction, 2011, Compound Correction Tutorial.

[63] J. F. Ziegler, M. D. Ziegler, and J. P. Biersack. (2011, Feb) SRIM - calculations and experimental results. [Online]. http://www.srim.org/SRIM/SRIMPICS/STOPPLOTS.htm

[64] J. F. Ziegler, M. D. Ziegler, and J. P. Biersack. (2011, Feb) SRIM - calculations and experimental results - ions in carbon. [Online]. http://www.srim.org/SRIM/SRIMPICS/STOP-TGTS/STOPxx06.gif

[65] G. H. Kinchin and R. S. Pease, "The Displacement of Atoms in Solids by Radiation," *Reports on Pogress in Physics*, pp. 18, 1, 1955.

[66] P. Sigmund, "A note on integral equations of the Kinchin-Pease Type," *Radiation Effects*, pp. 1, 15-18, 1969.

[67] M. J. Norgett, M. T. Robinson, and I. M. Torrens, "A proposed method of calculating displacement dose rates," *Nuclear Engineering and Design*, pp. 33, 1, 50-54, 1974.

[68] K. Binder and D. W. Heermann, *Monte Carlo simulation in statistical physics : an introduction*. Berlin, Heidelberg: Springer-Verlag, 2010.

[69] J. F. Ziegler, M. D. Ziegler, and J. P. Biersack. SRIM - Tutorials. [Online]. http://www.srim.org/SRIM/SRIM%2008.pdf

[70] W. Meissl et al., "Electron Emission from Insulators Irradiated by Slow Highly Charged Ions," *e-Journal of Surface Science and Nanotechnology*, pp. 6, 54-59, 2008.

[71] A. Arnau, F. Aumayr, P.M. Echenique, M. Grether, and W. Heiland, "Interaction of slow multicharged ions," *Surface Science Reports*, pp. 27,4-6,113-239, 1997.

[72] NanoFIB project 2001 - EC growth project Contract No. G5RD-CT2000-0034. [Online]. www.nanofib.com

[73] Raith GmbH - Ionenstrahlanlage ionLiNE - Broschüre. [Online]. www.raith.com

[74] R. G. Forbes, "Understanding how the liquid-metal ion source works," *Vacuum*, pp. 48, 1, 85-97, 1997.

[75] J. J. Van Esa et al., "An improved gallium liquid metal ion source geometry for nanotechnology," *Microelectronic Engineering*, pp. 73-74, 132-138, 2004.

[76] J. Gierak et al., "Exploration of the ultimate patterning potential achievable with high resolution focused ion beams," *Applied Physics A*, pp. 80, 1, 187-194, 2005.

[77] G. I. Taylor, "Disintegration of Water Drops in an Electric Field," *Proceedings of the Royal Society A*, pp. 280, 1382, 382-397, 1964.

[78] W. Gilbert and Translation by P. F.Mottelay, *On the Loadstone and Magnetic Bodies*. New York, 1958.

[79] J. F. Mahoney, A. Y. Yahiku, H. L. Daley, R. D. Moore, and J. Perel, "Electrohydrodynamic Ion Source," *Journal of Applied Physics*, pp. 40, 5101, 1969.

[80] J. Gierak et al., "Exploration of the ultimate patterning potential of focused ion beams," *Journal of Microlithography, Microfabrication and Microsystems*, pp. 5, 011011, 2006.

[81] J. Orloff, J. Li, Z. Li, and M. Sato, "Experimental study of a focused ion beam probe size and comparison with theory," *Journal of Vacuum Science Technology B: Microelectronics and Nanometer Structures*, pp. 9, 5, 2609-2612, 1991.

[82] D. R. Olander, W. Siekhaus, R. Jones, and J. A. Schwarz, "Reactions of Modulated Molecular Beams with Pyrolytic Graphite. I. Oxidation of the Basal Plane," *The Journal of Chemical Physics*, pp. 57, 408, 1972.

[83] G. Blyholder, J. S. Binford, and H. Eyring, "A Kinetic Theory for the Oxidation of Carbonized Filaments," *The Journal of Physical Chemistry*, pp. 62, 263-267, 1958.

[84] H. Hövel et al., "Controlled cluster condensation into preformed nanometer-sized pits," *Journal of Applied Physics*, pp. 81, 1, 154-158, 1997.

[85] C. Wong R. T. Yang, "Kinetics and mechanism of oxidation of basal plane on graphite," *Journal of Chemical Physics*, pp. 75, 4471, 1981.

[86] X. Chu and L.D. Schmidt, "Gasification of graphite studied by scanning tunneling

microscopy," *Carbon*, pp. 29, 8, 1251-1255, 1991.

[87] G. v. Bünau and T. Wolff, *Photochemie. Grundlagen, Methoden, Anwendungen*. Weinheim: VCH Verlagsgesellschaft, 1987.

[88] G. Binnig, C. F. Quate, and Ch. Gerber, "Atomic Force Microscope," *Physical Review Letters*, pp. 56, 930-933, 1986.

[89] V. L. Mironov, "Fundamentals of the scanning probe microscopy," *Journal of Nanoscience and Nanotechnology*, pp. 4, 7, 647-90, 2004.

[90] Wikipedia - Probe images Rasterkraftmikroskopie. [Online]. http://de.wikipedia.org/wiki/Rasterkraftmikroskop

[91] IUPAC. (2011, July) Compendium of Chemical Terminology, 2nd ed. [Online]. http://goldbook.iupac.org/V06597.html

[92] Universität Mainz - Institut für phys. Chemie. Fortgeschrittenenpraktikum zur Rasterkraftmikroskopie. [Online]. http://www.uni-mainz.de/FB/Chemie/fbhome/physc/Dateien/Rasterkraftmikroskopie_10_11.pdf

[93] R. Howland and L. Benatar, *A Practical Guide to Scanning Probe Microscopy*.: Park Scientific Instruments, 1993.

[94] B. T. Matthias, "Dielectric Constant and Piezo-Electric Resonance of Barium Titanate Crystals," *Nature*, pp. 161, 325-326, 1948.

[95] "The Piezo-Electric Loud-Speaker," *Nature*, 1934.

[96] J. M. Soler, A. M. Baro, N. Garcia, and H. Rohrer, "Interatomic Forces in Scanning Tunneling Microscopy: Giant Corrugations of the Graphite Surface," *Physical Review Letters*, pp. 57, 444-447, 1986.

[97] J. G. Simmons, "Generalized formula for the electric tunneling effect between similar electrodes separated by a thin insulating film," *Journal of Applied Physics*, pp. 34, 1793, 1963.

[98] Raith GmbH eLiNE. [Online]. http://www.raith.com/?xml=solutions|Lithography+%26+nanoengineering|e_LiNE+plus

[99] J. Goldstein et al., *Scanning Electron Microscopy and X-Ray Microanalysis.*: Springer Verlag, 2003.

[100] L. Reimer, *Scanning Electron Microscopy*. Berlin, Heidelberg, New York: Springer

Verlag, 1998.

[101] T. E. Everhart and R. F. M. Thornley, "Wide-band detector for micro-microampere low-energy electron currents," *Jounal of Scientific Instruments*, pp. 37, 7, 246, 1960.

[102] K. Bauer - Diploma thesis, *Leiterbahn-Strukturen durch FIB-Strukturierung auf Graphit-Schichten*. Dortmund, 2010.

[103] R. R. Schulz - Dissertation, *Ein neues Tieftemperatur-Ultrahochvakuum-Rastertunnelmikroskop zur Untersuchung von Hochtemperatursupraleitern*. University of Saarbrücken, 1994.

[104] J. P. Ibe et al., "On the electrochemical etching of tips for scanning tunneling microscopy ," *Journal of Vacuum Science & Technologie A*, pp. 8, 3570, 1990.

[105] L. A. Hockett and S. E. Creager, "A convenient method for removing surface oxides from tungsten STM tips," *Review of Scientific Instruments*, pp. 64, 263, 1993.

[106] D. K. Schroder, *Semiconductor Material and Device Characterization, 2nd Edition*. New York: John Wiley & Sons, 1998.

[107] F. Wenner, "A method of measuring earth resistivity," *Bulletin of the Bureau of Standards (U.S.A.)*, pp. 12, 258, 478-496, 1915.

[108] L. B. Valdes, "Resistivity Measurements on Germanium for Transistors," *Proceedings of the IRE 42*, 1954.

[109] J. Chan. (2011, June) EECS 143 - microfabrication Technology - Four-Point Probe Manual. [Online]. http://microlab.berkeley.edu/ee143/Four-Point_Probe/

[110] S. Kalinin and A. Gruverman, *Scanning Probe Microscopy - Electrical and Electrochemical Phenomena at the Nanoscale - Volume I*. New York: Springer-Verlag, 2007.

[111] Omicron Nanotechnology GmbH. (2011, August) UHV Nanoprobe. [Online]. http://www.omicron.de/en/products/uhv-nanoprobe/instrument-concept

[112] H. J. Güntherodt and R. Wiesendranger, *Scanning Tunneling Microscopy I.*: Springer Verlag, 1994.

[113] G. Moos - Dissertation, *Dynamics of photoexcited electrons in metals and semimetals*. University of Berlin, 2003.

[114] Wikipedia. (2011, March) Graphit. [Online]. http://de.wikipedia.org/wiki/Graphit

[115] O. El-Shazly, S. G. Tawfik, A. K. Ibrahim, I. H. Ibrahim, and E. F. El-Wahidy, "Electrical resistivity and Hall effect of K-FeCI3 graphite," *Journal of Materials Science*, pp. 28, 5040-5044, 1993.

[116] tectra. (2011, May) HOPG. [Online]. http://www.tectra.de/hopg.htm

[117] S. Banerjee, M. Sardar, N. Gayathri, A. K. Tyagi, and B. Raj, "Conductivity landscape of highly oriented pyrolytic graphite surfaces containing ribbons and edges," *Physical Review B*, pp. 72, 075418, 2005.

[118] L. D. Landau, "Zur Theorie der Phasenumwandlungen II," *Phys. Z. Sowjetunion 11*, p. 11, 1937.

[119] J. C. Meyer et al., "The structure of suspended graphene sheets," *Nature*, pp. 446, 60-63, 2007.

[120] Wikipedia. (2011, May) Graphen. [Online]. http://de.wikipedia.org/wiki/Graphen

[121] R. R. Nair et al., "Fine Structure Constant Defines Visual Transparency of Graphene," *Science*, pp. 320, 5881, 1308, 2008.

[122] F. Ghaleh - Dissertation, *Characterization of Surface Defects Produced with Focused Ion Beams and Exploration of Applications for Controlled Growth of Nano-structures*. TU Dortmund, 2008.

[123] J. Chen, C. Jang, S. Xiao, M. Ishigami, and M. S. Fuhrer, "Intrinsic and extrinsic performance limits of graphene devices on SiO2," *Nature Nanotechnology*, pp. 3, 206-209, 2008.

[124] B. Partoens and F. M. Peeters, "From graphene to graphite: Electronic structure around the K point," *Physical Review B*, pp. 74, 075404, 2006.

[125] Mineralienatlas. (2011, May) [Online]. http://www.mineralienatlas.de/lexikon/index.php/MineralData?mineral=Muskovit

[126] I. Horcas et al., "WSXM: A software for scanning probe microscopy and a tool for nanotechnology," *Review of Scientific Instrumuments*, pp. 78, 013705, 2007.

[127] B. Heinz, *Optische Konstanten von Halbleiter-Mehrschichtsystemen - Dissertation*. RWTH Aachen, 1991.

[128] P. Blake et al., "Making graphene visible," *Applied Physics Letters*, pp. 91, 6, 063124, 2007.

[129] Wikipedia. (2011, May) Muskovit. [Online]. http://de.wikipedia.org/wiki/Muskovit

[130] N. Grönhagen - Diploma thesis, *Wachstum von Nanostrukturen auf strukturiertem Graphit*. TU Dortmund, 2008.

[131] S. Balk - Diploma thesis, *Untersuchung der Dosisabhängigkeit bei der Nanostrukturierung von Graphit mit fokussierten Ionenstrahlen*. TU Dortmund, 2009.

[132] J. B. Nelson and D. P. Riley, "The thermal expansion of graphite from 15°C to 800°C: part I. Experimental," *Proceedings of the Physical Society*, pp. 57, 477, 1945.

[133] D. P. Riley, "The thermal Expansion of Graphite: part II. Theoretical," *Proceedings of the Physical Society*, pp. 57, 486, 1945.

[134] R. H. Knibbs and I. B. Mason, "Thermal expansion of pyrolytic graphite and its variation due to non-alignment of the crystallites," *Nature*, pp. 203, 58-60, 1964.

[135] H. A. McKinstry, "Thermal expansion of clay minerals," *The American Mineralogist*, pp. 50, 212, 1965.

[136] Wikipedia - Network analysis. (2011, June) [Online]. http://en.wikipedia.org/wiki/Network_analysis_%28electrical_circuits%29#cite_note-1

[137] J. W. Nilsson and S. A. Riedel, *Electric Circuits*, 8th ed.: Pearson Prentice Hall, 2007.

[138] Wikipedia - Nodal analysis. (2011, June) [Online]. http://en.wikipedia.org/wiki/Nodal_analysis

[139] P. Dimo, *Nodal Analysis of Power Systems*. Kent, England: Abacus Press, 1975.

[140] M. Endo, T. Hayashi, S. Hong, T. Enoki, and M. S. Dresselhaus, "Scanning tunneling microscope study of boron-doped highly oriented pyrolytic graphite," *Journal of Applied Physics*, pp. 90, 11, 2001.

[141] E. Kim, I. Oh, and J. Kwak, "Atomic structure of highly ordered pyrolitic graphite doped with boron," *Electrochemistry Communications*, pp. 3, 608-612, 2001.

II. List of abbreviations

List of words:

abbreviation	***meaning***
AFM	atomic force microscopy / microscope
FBMS	fixed beam moving stage
FEG	field emission gun
FIB	focused ion beam
GCV	green colour value
GDSII	graphical design station II
Hcp	hexagonal close-package
HOPG	highly oriented pyrolytic graphite
LMIS	liquid metal ion source
MATLAB	matrix laboratory
MELF-GOS	mermin-type energy loss function - generalized oscillator strenghts
PMMA	polymethylmetacrylate
RGB	red, green, blue
SEM	scanning electron microscopy / microscope
SRIM	stopping and range of ions in matter
STM	scanning tunneling microscopy / microscope
TRIM	transport of ions in matter
UV/VIS	ultraviolet-visible spectroscopy
WSXM	windows scanning x microscope

List of some physical constants, reference [7], [8]*:*

physical constant	***symbol or formula***	***value***
atomic mass unit	u	$1.660\ 538\ 86\ (28) \cdot 10^{-27}$ kg
Avogadro constant	N_A	$6.022\ 1415\ (10) \cdot 10^{23}$ mol^{-1}
Boltzmann constant	k_B	$1.380\ 6505\ (24) \cdot 10^{-23}$ J·K^{-1}
elementary charge	e	$1.602\ 176\ 53\ (14) \cdot 10^{-19}$ C
magnetic constant	μ_0	$4\pi \cdot 10^{-7}$ N·A^{-2}
Planck constant	$h=2\pi \cdot \hbar$	$6.626\ 0693\ (11) \cdot 10^{-34}$ J·s
rest mass - electron	m_e	$9.109\ 3826\ (16) \cdot 10^{-31}$ kg
rest mass - proton	m_p	$1.672\ 621\ 71\ (29) \cdot 10^{-27}$ kg
speed of light in vacuum	c	$2.997\ 924\ 58 \cdot 10^{8}$ m·s^{-1}
Bohr radius	$a_0 = \alpha/(4\pi R_\infty)$	$5.291\ 772\ 1092\ (17) \cdot 10^{-11}$ m
classical electron radius	$r_e = e^2/(4\pi \varepsilon_0 m_e c^2)$	$2.817\ 940\ 3267\ (27) \cdot 10^{-15}$ m
electric constant	$\varepsilon_0 = 1/(\mu_0 c^2)$	$8.854\ 187\ 817\ 62\ldots \cdot 10^{-12}$ F·m^{-1}
fine-structure constant	$\alpha = e^2/(4\pi \varepsilon_0 m_e c)$	1/137.035 999 11 (46)
Rydberg constant	$R_\infty = \alpha^2 m_e c/(2h)$	$1.097\ 373\ 156\ 8525\ (73) \cdot 10^{7}$ m^{-1}

III. Glossary

K

L

M

N

O

P

Q

R

S

T

U

V

W

Z

IV. Acknowledgement

Mein Dank geht an alle, die zu einem Gelingen dieses Projektes beigetragen haben. In erster Linie danke ich PD Dr. Hövel für eine exzellente Betreuung dieser Arbeit, Prof. Dr. Tolan für die Aufnahme in den Lehrstuhl und eine sehr gute Unterstützung, sowie beiden für ihre fachliche und menschliche Kompetenz, die mich während meiner Ausbildung an der Technischen Universität Dortmund gefördert hat.

Ich danke Herrn Balk und Herrn Bauer für eine gelungene Zusammenarbeit, ihre Ideen und die große Motivation, die sie in dieses Projekt gesteckt haben. Durch die Zusammenarbeit konnten zusätzliche und vor allem wichtige Aspekte hinzugefügt werden, wodurch das Projekt an Qualität und Vielseitigkeit hinzugewonnen hat.

Weiterhin geht mein Dank an die Kooperationspartner dieses Projektes, die durch Kompetenz und den Austausch von Ressourcen die Herstellung und die Untersuchung der erzeugten Strukturen überhaupt möglich gemacht haben. In diesem Zusammenhang danke ich vor allem Herrn Bruchhaus, Herrn Bauerdick, Herrn Rudzinsky, Herrn Nadzejka, Herrn Jede (Raith GmbH), Herrn Köble, Frau Anargirou (Omicron Nanotechnology GmbH), Herrn Rademacher (TU Dortmund - Maschinenbau), Herrn Schemionek und Frau Pike (Präparationslabor), sowie allen weiteren Kooperationspartnern für das große Interesse und die sehr gute Zusammenarbeit.

Bei allen Mitarbeitern des Lehrstuhls möchte ich mich herzlich für die angenehmen Jahre bedanken, die von sehr gutem wissenschaftlichen Austausch und einer konstant guten Arbeitsatmosphäre geprägt waren. Mein besonderer Dank geht hierbei an die Kolleginnen und Kollegen Frau Duffe, Herr Grönhagen, Herr Mende und Frau Miroslawski. Ein großer Danke auch an Frau Hoffmann, Herr Holz, Herr Latussek, Herr Nyrow, Herr Schwamberger, Herr Steffen, Herr Wirkert, Herr Witt und an die ehemaligen Mitarbeiter Herr Conrad, Herr Ghaleh, Herr Irawan, Frau Lietz und Herr Wortmann.

Zudem möchte ich betonend meiner Familie, meiner Freundin und meinen Freunden für die Jahre der Geduld, Unterstützung und Freundschaft während meiner Doktorarbeit danken. Euch allen: Vielen Dank!

Den Prüfern und Lesern dieser Arbeit danke ich für das Interesse an diesem Projekt und an den wissenschaftlichen Ergebnissen der Fakultät für Physik – EIa – der Technischen Universität Dortmund zum Thema Ionenstrahllithographie.

V. Affirmation

Ich, Dipl.-Phys. Lukas Patryarcha, versichere hiermit an Eides statt, dass ich die vorliegende Dissertation mit dem Titel *„Experiments and simulations on the structural and electrical properties of nano and micro structures on graphite surfaces produced by ion beam lithography“* selbständig und ohne unzulässige fremde Hilfe erbracht habe. Ich habe keine anderen als die angegebenen Quellen und Hilfsmittel benutzt sowie wörtliche und sinngemäße Zitate kenntlich gemacht. Die Arbeit hat in gleicher oder ähnlicher Form noch keiner Prüfungsbehörde vorgelegen.

_____

Dortmund, den 09.08.2011